UTS UNIVERSITY OF TECHNOLOGY SYDNEY

Investigating the mechanisms underlying cachexia in pulmonary diseases

by Karl Joseph Hegarty

Thesis submitted in fulfilment of the requirements for the degree of

Doctor of Philosophy

under the supervision of
Professor Philip Hansbro
Professor Andrew Philp
Dr. Elinor Hortle
Dr. Ashleigh Philp
Dr. Nicole Hansbro

University of Technology Sydney
Faculty of Science

January 2025

Declaration by author

Certificate of original authorship:

I, Karl Hegarty declare that this thesis, is submitted in fulfilment of the requirements for the award of Doctor of Philosophy in Science, in the Faculty of Science at the University of Technology Sydney.

This thesis is wholly my own work unless otherwise referenced or acknowledged. In addition, I certify that all information sources and literature used are indicated in the thesis.

This document has not been submitted for qualifications at any other academic institution.

This research is supported by the Australian Government Research Training Program

Signature: Production Note:
Signature removed prior to publication.

Date: 10/01/2025

Ever tried. Ever failed. No matter. Try Again. Fail again. Fail better.

- Samuel Beckett

Acknowledgements

I am deeply thankful for all the helping hands and words of wisdom that have shaped my path. Throughout my PhD, my supervisors, colleagues, friends, and family have been by my side through a rollercoaster of highs and lows. Numerous projects were started and finished during these 3.5 years, in the way that only happens with science: it leads the academic down a road only to show them the new cul-de-sac sign it has erected.

I would like to sincerely thank Philip and Nicole Hansbro for providing me with the opportunity to pursue my PhD in Sydney. I appreciate the chance to be part of a vibrant lab environment that facilitated my academic and personal development. The experiences I've gained during this time have been invaluable and will undoubtedly shape my future endeavours.

Elinor Hortle, during the first shift in my project you were there to provide me support that I couldn't have done without and I'm eternally grateful that I've had you on my side backing me up over these last few years. You have been incredibly kind and patient with me during a tough few years (even when I seemed to be picking the hardest possible routes!) and you were there to have my back, so I thank you from the bottom of my heart.

To Ashleigh and Andrew Philp, you both played a crucial role in stabilizing my candidature, especially towards the end of 2023, when yet another project had come to an unexpected halt. Your mentorship, despite my lack of prior experience working with muscle research, was incredible. Ash, I've enjoyed our countless conversations and the fun banter during endpoints, but I won't miss your endless rants about tea bag strings, and claims of Bob Geldof's supposed English ancestry! Andy, our discussions on muscle physiology and cell signaling opened my eyes to a world I was previously unaware of. Your insights have not only shaped my research but have also inspired me and those around me to improve our physical well-being.

I'd also like to extend my gratitude to everyone at the Centenary Institute who has supported me with advice and friendship, particularly Bernadette Saunders, Patrick Bertolino and Guy Lyons. Bernadette, lab demonstrating with you in your classes was by far the most enjoyable demonstrating experience I had in UTS. I'll forever be inspired by the care and attention to detail you poured into those classes. Patrick, you've been a source of invaluable wisdom and a fellow enthusiast for pints, which never goes unappreciated! You've also been there during difficult times of my candidature to offer advice and guidance. Guy, I'm sure my partner thanks you too - our lunch chats about rugby spared her from hearing about it endlessly at home! You were also a fantastic support during my PhD and were always there to improve my day or listen and talk about my latest project change.

A special thank you goes to Centenary's building manager, Matthew Murarotto, whose positive disposition was a constant inspiration throughout my time at Centenary. Tyson Blanch from Bioresources, you brought laughter and levity to my breaks, and your patience and care when managing my mice were greatly appreciated. Sarah Robinson, although it has only been just over a year since we first started hanging out in the tearoom, I feel like I've gotten to know you so well, and I will always appreciate the deep friendship that we have forged. It is difficult to start up in a new country without knowing anyone so to have someone at work I could rely on being my friend and to talk utter nonsense with made coming into work that much easier. Jamberoo awaits!

This lab could not function without all the cogs spinning in unison and it was only with the collective effort and help from my colleagues in CFI that many of the experiments we do are accomplishable. Our endpoints which require all-hands-on-deck! Elinor Hortle, Matt Johansen, Ashleigh Philp, Angelica Katsifis, Jacqueline Marshall, and Tsung-Yu (Johann) Pai were integral to my own studies and helped in my endpoints.

I'd also like to thank the many friends I've made in the Hansbro lab, particularly the current and former RAs and TOs and lab managers who supported me. Justin Lee for being a histological pro. Duc Nguyen, you were always patient and positive, and your good humour and seemingly endless work ethic has kept level 3 humming for the last 5 years. Solomon Odgers who unfortunately left us for supposed greener pastures, I would like to thank him for his organisational know-how which saved me on way too many occasions but also for being a great source of the chats on any given day and a good, honest friend.

There's absolutely no way of describing the help and support I've received from Matt Johansen, though I'm sure he'll be glad to no longer be worried about me playing pranks on him anymore. I'll miss our coffee strolls around the oval in our meagre attempts at getting some fresh air and sunlight! I feel very privileged to have worked beside such a caring and hard-working scientist who is going to do amazing things in his field. Jinx Moore, I'm so lucky to have made such a wonderful friend, and I look forward to more pints and risqué jokes in the future! You still owe me for that building FOB and key though! (Re)Beccaaaah (Shipley), though you've only recently joined the lab I feel like you've also become an integral part of it and I've appreciated having a fellow European (oops) to chat nonsense with!

Everyone in the Philp lab: Camila Padilha, Dean Campelj, Elya Ritenis and Isabelle Alldritt. Thank you so much for immediately opening your arms to me (with a brewery crawl) when I came to CPC to work amongst you, and especially to Elya, who showed me the Western Blot ropes and provided no shortage of Eastern European factoids and GenZ brain rot humour.

To the Luke O'Neill lab in Dublin, and to Luke in particular, your mentorship laid the foundation for my scientific journey. When COVID-19 hit, I was working night shifts as a gum removal cleaner in Dublin. Without your generosity and welcoming spirit, I might have stayed in that job indefinitely,

as opportunities in Ireland were scarce at the time. Being surrounded by brilliant minds passionate about immunometabolism helped me forge my own interests and inspired me to pursue this field further. I would also like to thank Tristram Ryan and Alex Hooftman for your sage advice and your friendship over the course of my PhD candidature. Hopefully we'll catch up again sooner than last time!

To my friends back in Dublin, I've missed you all so much. One trip home during these four years is nowhere near enough, but I hope to visit more often now that I'm off the PhD stipend. Jack MacNamara, I'm not sure how we've managed it, but a 1475 snapstreak deserves its own acknowledgment. Thank you for the daily reminder that I've got the best mate in the world back in Ireland and for being such a good friend to me over these years even though I'm on the other side of the world! Charlie Walsh and May Higgins, thank you for coming to live with myself and Soleille in Oz, we've had such an amazing time and you have both been incredible Sydney roomies, travel buddies, sesh heads and friends.

I would also like to thank my Australian family, especially my relatives in Newcastle: Margaret, Brett, and Conor Haswell, and Alex and Clare McCloy, and my Sydney family: Oscar, Marie-France, Liam, Ciara, and Emer. I'll never get over how welcoming all of you were and how quickly you made myself and Soleille feel a part of the family. I am grateful for your love and support. Brett and Maggie, I can't wait for some surfing up north. Oscar, get the shrimpin' nets ready and Ciaran, Ciara, Mark, Emer and Cai, I look forward to our upcoming darts adventures, I hope you're ready...

To my extended family on the Cahill and Hegarty sides, your kindness has shaped me into the person I am today. I would not have had the confidence to pursue my academic dreams without all of you by my side. I'm especially grateful for my Nanny, Ursula Cahill. I've missed you dearly and will always cherish our chats over a cup of tea.

To my family in Ireland (the Hegartys) - Joe, Yvonne, Dad, and Anna - you've been my rock. Mum and Dad, your unwavering support and work ethic have inspired me to pursue my passions and always strive to do my best. I am privileged beyond measure to have you as parents, and I will always aim to live up to the example you've set. Anna, your passion for science and nature, especially in the face of adversity, has been a source of inspiration. Your ability to persist and carry on even during difficult times has helped guide me towards my own goals. You're all my inspiration and I hope to see you all soon—I'm always thinking of you.

Finally, to Soleille, my partner of six years—thank you for your unwavering love and support. I'll never be able to fully compensate you in words, for what you've given me over this time. Completing my PhD would genuinely not have been possible without you by my side, especially during the tough days when both of us were juggling PhDs and living on a shoestring budget. Despite the challenges, we've come out stronger, in no small part due your encouragement. Your own scientific ability, positive outlook on life and empathy for everyone around you are forever going to drive me to be a better person. I am grateful that we've been able to navigate this journey in Sydney together and look forward to all our exciting chapters ahead.

Abstract

Cachexia, characterized by skeletal muscle atrophy, is a frequent comorbidity in cancer and pulmonary diseases, including idiopathic pulmonary fibrosis (IPF), asthma, and chronic obstructive pulmonary disease (COPD). Skeletal muscle enables movement but is also a part of the endocrine system and plays a crucial role in maintaining systemic homeostasis. Its dysregulation in cachexia contributes to increased exacerbation rates, reduced quality of life, and worsened prognosis. In COPD, cachexia is associated with up to a 50% decrease in patient survival compared to non-cachectic patients. Currently there are no approved pharmacological interventions that address cachexia, and non-pharmacological interventions like improving diet and exercise can be difficult to implement. This highlights the need to test novel therapies for cachexia for which experimental mouse models of disease could be utilised.

In this thesis, experimental chapter 3 investigated murine models of IPF, asthma, and COPD for their ability to emulate cachexia, and disruption of atrophy-associated pathways. Among these models, only cigarette smoke (CS) exposure in IPF or COPD models induced significant skeletal muscle atrophy and demonstrated reduced mTORC1 pathway signalling in young (8-week-old) female and male C57BL/6 mice. Later chapters used CS exposure to induce cachexia and trial experimental therapies. Pathway enrichment analysis of publicly available human quadriceps microarray data revealed dysregulation of mitochondrion-associated pathways and increased local inflammation. This supported the decision to try and improve mitochondrial health and reduce inflammation in skeletal muscle as a treatment for cachexia.

Therapeutic models were carried out in CS-induced experimental mouse models of COPD and aimed to restore muscle mass and balance protein synthesis/degradation by targeting mitochondrial dysfunction and inflammation. In chapter 4, intranasal administration of H-151, a

stimulator of interferon genes (STING) inhibitor was used to prevent inflammatory signalling caused by mtDNA through cGAS-STING signalling. H-151 did not ameliorate the negative effects of CS on skeletal muscle or total body weight, failed to improve lung function and did not reduce a CS-induced increase in 4E-BP1 levels in the quadriceps. However, mitochondrial respiration analyses showed that H-151 treatment mitigated CS-induced complex I proton leak across the mitochondrial inner membrane and reduced ADP sensitivity.

In chapter 5, Urolithin A (UA), a dietary mitophagy inducer, was provided *ad libitum* to young (8-week-old) and adult (1-year-old) mice. UA treatment did not improve body and skeletal muscle mass outcomes in young or adult mice or prevent lung function decline. Mitochondrial respiration significantly differed with age and was modulated by UA. Additionally, CS exposure reduced phosphorylation of S6 ribosomal protein (rpS6) in young mice and decreased muscle fiber area. Adult mice exhibited significant muscle atrophy, whereas young mice plateaued in weight following CS exposure.

In conclusion, increased 4E-BP1 expression and decreased rpS6 phosphorylation in the quadriceps suggested alterations in protein balance in CS exposed mice. Furthermore, mitochondrial functions such as complex I proton leak and ADP sensitivity in the gastrocnemius were altered by CS exposure and both H-151 and UA treatments, though the changes were inconsistent between the two models. Collectively, this study demonstrates the potential utility of murine COPD models for investigating cachexia-targeted therapies as mice consistently lost significant gastrocnemius and quadriceps muscle mass with CS exposure. However, it also highlights significant limitations of these models, in particular the rapid, supra-physiological nature of CS induced muscle mass loss and the poor reproducibility of skeletal muscle outcomes such as mitochondrial respiration and mTORC1 signalling measurements. Overall, this suggests that targeting mitochondrial dysfunction

and inflammation could still provide therapeutic potential for COPD cachexia and indicates H-151 and UA have limited therapeutic efficacy.

Table of Contents

List of Tables

List of Figures

Abbreviations

Abbreviation	Meaning
ABR	Australian BioResources
ACTB	B-actin gene
AD	Alzheimer's Disease
ADP	Adenosine Diphosphate
AERD	Aspirin-exacerbated respiratory disease
AHR	Airway Hyperresponsiveness
Akt	Protein Kinase B
ALI	Acute Lung Injury
AMP	Adenosine monophosphate
AMPK	5' AMP-activated protein kinase
ANOVA	Analysis of Variance
ARC	Australian Research Council
ATP	Adenosine Triphosphate
ATF4	Activating Transcription Factor 4
BALF	Bronchoalveolar Lavage Fluid
Bleo	Bleomycin
BMI	Body-Mass Index
BSA	Bovine Serum Albumin
CASP3	Caspase-3
CCCP	Carbonyl cyanide m-chlorophenyl hydrazone
CD	Cluster of Differentiation
cGAMP	2'3'-Cyclic GMP-AMP
cGAS	cyclic GMP–AMP synthase
CHRNA1	Cholinergic Receptor Nicotinic α1 Subunit
CI-Leak	Complex I associated proton leakage
CI-P	Complex I associated ATP production
CI&II	Complex I and complex II associated ATP production
CMU	*Chlamydia Muridarum*

COPD	Chronic Obstructive Pulmonary Disease
Crs	Dynamic compliance
CS	Cigarette Smoke
CSA	Cross-sectional area
CSE	Cigarette Smoke Extract
Cst	Static Compliance
CUL1	Cullin 1
Cys	Cysteine
DC	Detergent compatible
Dex	Dexamethasone
DMSO	Dimethyl Sulphoxide
DNA	Deoxyribonucleic Acid
dsDNA	Double-stranded DNA
ECM	Extracellular Matrix
EDL	Extensor Digitorum Longus
EDTA	Ethylenediaminetetraacetic acid
EGR1	Early Growth Response Protein 1
eIF-4E	Eukaryotic Translation Initiation Factor-4E
ER	Endoplasmic Reticulum
ETC	Electron Transport chain
FACS	Fluorescence-activated Cell Sorting
FBXO32	F-box only protein 32 (gene name for Atrogin-1)
FEV1	Forced Expiratory Volume (in 1 second)
FFMI	Fat-free Mass Index
FMO	Fluorescence Minus One
FoxO	Forkhead box O
FVC	Forced Vital Capacity
GADD45A	Growth Arrect and FNA damage-inducible A
GAP	GTPase-activating protein
GC	Glucocorticoid

GDP	Guanosine Diphosphate
GDF-15	Growth/differentiation factor 15
GMP	Guanosine Monophosphate
GOLD	Global Initiative for Chronic Obstructive Lung Disease
GTP	Guanosine-5'-triphosphate
H&E	Haematoxylin and Eosin
HBSS	Hank's Balanced Salt Solution
HDAC4	Histone Deacetylase 4
HDM	House Dust Mite
HEPES	4-(2-Hydroxyethyl)piperazine-1-ethane-sulfonic Acid
HPRT	Hypoxanthine-guanine phosphoribosyltransferase
HRCT	High Resolution Computed Tomography Scan
HRP	Horseradish Peroxidase
ICS	Inhaled Corticosteroids
IFN	Interferon
IFU	Inclusion-forming Units
Ig	Immunoglobulin
IGF	Insulin Growth Factor
IL	Interleukin
ILC	Innate Lymphoid Cell
ILD	Interstitial Lung Disease
i.n.	Intranasal
i.p.	Intraperitoneal
IPF	Idiopathic Pulmonary Fibrosis
IR	Insulin Receptor
IRF3	Interferon Regulatory Factor 3
IRS	Insulin Receptor Substrates
ISG	Interferon stimulated gene
ISRE	Interferon stimulated response elements
KC	Murine homolog for CXCL1

KY	Kentucky
LABA	Long-acting β2 Agonists
LAMA	Long-acting Muscarinic Antagonists
LC3	Microtubule-associated Protein 1 Light Chain 3 α
LN	Liquid Nitrogen
LPS	Lipopolysaccharide
LRR	Leucine-rich Region
MAFbx	Muscle Atrophy F-box
MDM2	Mouse double minute 2 homolog
MFA	Muscle Fiber Area
mRNA	Messenger Ribonucleic Acid
MSTN	Myostatin
MTCO1	Mitochondrially Encoded Cytochrome c Oxidase I
mTOR	Mammalian Target of Rapamycin
mTORC	Mammalian Target of Rapamycin Complex
mtDNA	Mitochondrial DNA
mtROS	Mitochondrial reactive oxygen species
MuRF1	Muscle RING finger 1 (protein name for TRIM63)
N-A	Nose-Anus
NCBI	National Center for Biotechnology Information
NDUFB8	NADH dehydrogenase [ubiquinone] 1 beta subcomplex subunit 8
NET	Neutrophil Extracellular Traps
NF-κB	Nuclear Factor Kappa-light-chain-enhancer of Activated B cells
NJ	New Jersey
NLRP3	NOD-, LRR- and pyrin domain-containing protein 3
NOD	Nucleotide-binding and oligomerization domain
NPFE	Negative Pressure Forced Expiration
NRF2	Nuclear Factor Erythroid 2-related Factor 2
NSW	New South Wales
NTHi	Non-typeable *Haemophilus Influenzae*

OCT	Optimal Cutting Temperature
OMM	Outer Mitochondrial Membrane
Ova	Ovalbumin
OXPHOS	Oxidative Phosphorylation
PBS	Phosphate Buffered Saline
PCR	Polymerase Chain Reaction
PDK1	3-Phosphoinositide-dependent Kinase 1
PEF	Peak Expiratory Flow
PGC1α	PPARγ coactivator 1-α
PIC	Protease Inhibitor cocktail
PIP2	Phosphatidylinositol-4,5-bisphosphate
PIP3	phosphatidylinositol-3,4,5-trisphosphate
PI3K	Phosphoinositide 3-kinase
PM	Particulate Matter
PPARγ	Peroxisome proliferator-activated receptor γ
PRR	Pattern Recognition Receptor
PSMA2	Proteasome subunit alpha type-2
PSMD	26S proteasome non-ATPase regulatory subunit
QC	Quebec
RBC	Red Blood Cell
REML	Restricted maximum likelihood
Rheb	Ras homolog enriched in brain
RICTOR	Rapamycin-insensitive companion of mammalian target of rapamycin
Rn	Resistance of the central airways
RNA	Ribonucleic Acid
RPM	Rotations Per Minute
rpS6	S6 Ribosomal Protein
Rs	Resistance of the central and peripheral airways
RSV	*Respiratory Syncytial Virus*
RT	Reverse Transcription

RT-qPCR	Real Time – Quantitative Polymerase Chain Reaction
Sal	Saline
SABA	Short-acting β_2 Agonists
SD	Standard Deviation
SDHB	Succinate Dehydrogenase Subunit B
Ser	Serine
SIRT	Sirtuin
SMK	Cigarette Smoke Exposed
SOP	Safety Operating Procedure
SPG	Sucrose Phosphate Glutamate
STING	Stimulator of Interferon Genes
SS	Single Stain
S6K	S6 Kinase
TANK	TRAF family member-associated NF-κB activator
TBK1	TANK -binding kinase 1
TBS-T	Tris Buffered Saline – Tween20
TCR	T-cell receptor
TEM	Transmission electron microscopy
TFAM	Transcription factor A, mitochondrial
TFEB	Transcription factor EB
TGF-β	Transforming Growth Factor-Beta
Th	T helper
Thr	Threonine
TLC	Total Lung Capacity
TNF	Tumour Necrosis Factor
TRAF	TNF associated Factor
TRIM63	Tripartite Motif Containing 63 (gene name for MuRF1)
TSC	Tuberous Sclerosis Complex
UA	Urolithin A
UBE2Q2	Ubiquitin-conjugating Enzyme E2 Q2

UPS	Ubiquitin Proteasome System
UIP	Usual Interstitial Pneumonia
UQRC2	Ubiquinol-Cytochrome c reductase core protein 2
USA	United States of America
UV	Ultraviolet
WB	Western Blot
WHO	World Health Organisation
WT	Wild type
4E-BP1	eIF-4E Binding Protein 1

Chapter 1 Literature Review

1.1 Cachexia: Diagnosis, prevalence and impact in respiratory diseases.

Cachexia is defined as a complex metabolic syndrome associated with underlying illness and characterized by muscle and strength loss with or without loss of fat mass. [1, 2]. This definition is different from sarcopenia, which is ageing associated muscle loss [3], or muscle disuse atrophy/wasting syndrome which is muscle loss caused by sedentarism or muscle disuse [2, 4]. However, definitions of these terms vary in literature, and are often used inter-changeably, which has led to difficulties elucidating the epidemiology of cachexia [1]. Fundamentally, muscle mass is regulated by a balance of anabolism and catabolism or protein synthesis and degradation respectively (Figure 1.1) [5, 6].

The criteria for the diagnosis of cachexia in cancer, heart failure and COPD includes a loss of >5% body weight over a 12-month period, as well as needing to meet 3 of the following criteria: loss of strength, fatigue, anorexia, low fat free mass index (FFMI) or increased inflammatory markers [1].

According to a meta-analysis from 2022, the global prevalence of sarcopenia, defined by the authors as a “loss of muscle mass and strength”, was estimated to be between 10-27% of adults over the age of 60. The study acknowledged difficulties in providing an exact number due to issues arising from the different diagnostic criteria used between studies [7]. However, even with a modest estimate of 10%, the global burden of muscle atrophy is clearly a major issue, especially considering the estimated cost of cachexia and other physiological conditions relating to muscle atrophy on the cost of healthcare [8-11]. This is because patients with increased muscle loss are more likely to be hospitalised, require longer periods of care, are more likely to be readmitted and have a higher incidence of complications [12, 13].

Although there is consensus that sarcopenia and cachexia carry significant economic costs, a 2019 meta-analysis by Bruyère et al. highlighted the difficulty of assessing their exact economic burden [11]. This challenge stems from variations in diagnostic criteria and substantial study heterogeneity, underscoring the need for consistent methods to define sarcopenia and cachexia. However, one U.S.-based study examined the cost of hospitalization for patients with sarcopenia and found they were more likely to be hospitalized than those without sarcopenia, with an annual marginal cost increase of $2,315.70 per patient [14].

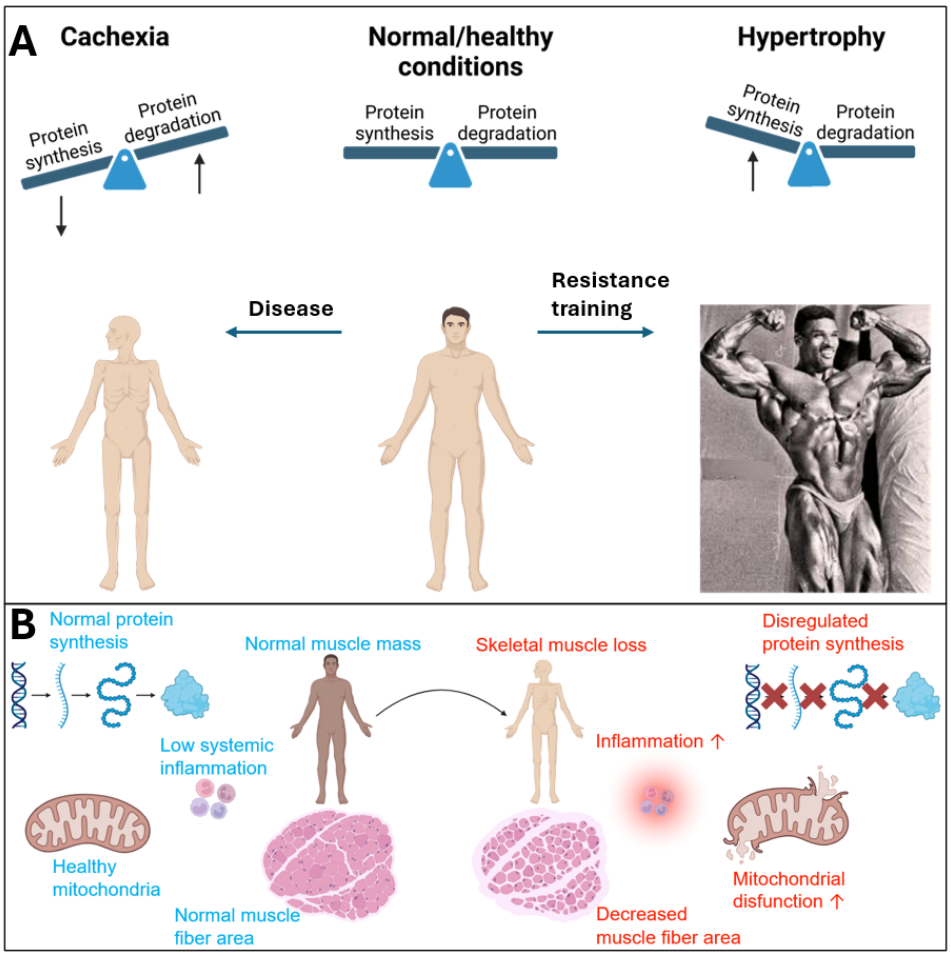

Figure 1.1 An overview of the main physiological effects of cachexia.

A: Under normal conditions, protein synthesis and degradation are in equilibrium in skeletal muscle. Muscle growth or hypertrophy involves an increase in protein synthesis that results in positive net protein synthesis/protein degradation. During many illnesses, cachexia may be induced through dysregulation of this equilibrium, resulting in decreased protein synthesis and

increased protein degradation. Photo credit: Ronnie Coleman **B:** Cachexia is associated with skeletal muscle loss, malnutrition, systemic inflammation, decreased muscle fibre area, mitochondrial dysfunction and dysregulated protein synthesis/degradation. Image made using BioRender.

Cachexia can negatively impact prognosis in many diseases especially in cancer where it is commonly reported and studied. The impact of cachexia in pulmonary diseases is less understood and, aside from in COPD, has not been widely investigated [15]. However, studies that have shown a link between muscle loss, function and wasting in the chronic pulmonary diseases COPD, asthma and IPF. It has been observed that in COPD approximately 10-40% of patients will develop cachexia [16], resulting in a 50% decrease in median survival [17-19] and mortality rate of 10-15% per year [15]. In IPF, muscle atrophy, especially in the erector spinae muscles was associated with increased mortality in IPF patients [20-25]. In moderate and severe asthma, low muscle mass and strength were associated with worse patient symptoms [26] and overall disease outcome [27].

1.1.1 Skeletal muscle is required for maintaining homeostasis

Skeletal muscles play a critical role in maintaining whole body homeostasis by regulating and providing essential physiological services [28-31]. They serve as the body's primary glycogen storage site, followed by the liver, with glycogen readily converted into glucose and subsequently into ATP through glycolysis and the tricarboxylic acid (TCA) cycle [32, 33]. Glycogen stored in skeletal muscle is used during exercise, as ATP production is required for contraction [33]. However, skeletal muscles are highly metabolically adaptable, and capable of shifting rapidly to alternative fuel sources such as fats, amino acids, and ketones for ATP production under different physiological conditions (e.g. exercise, disease) or depending on the abundance of bioenergetic substrates [34].

In addition, skeletal muscles function as detoxifying systems. They manage toxic byproducts such as ammonia by converting it into glutamine, which is safely transported to the liver [35, 36]. Similarly, increased lactate, H^+, P_i and Mg^{2+} which are increased in the cytosol during periods of intense exercise or hypoxemia, is buffered by muscles to prevent acidosis [37]. Buffering allows muscles to maintain efficient energy metabolism [38], and for lactate to be safely transported to the liver where the Cori cycle can convert it back to glucose to be used in the muscles again [39].

Muscles are an integral part of the endocrine system [40, 41], producing and releasing signalling molecules known as myokines into the circulatory system that exert systemic effects on energy metabolism, inflammation, and overall homeostasis [42]. These myokines include classical inflammatory mediators such as interleukin-6 (IL-6) and tumour necrosis factor (TNF), as well as other regulators like myostatin, that promote protein degradation and contributes to muscle atrophy [43]. Myokines enable communication between muscles and other organs, dynamically adjusting their function based on physiological conditions.

A crucial role of skeletal muscle is to serve as a reservoir for amino acids, the building blocks of proteins. During periods of physiological stress, such as illness, aging, or malnutrition, muscles activate pathways for protein degradation within myofibers, releasing amino acids into circulation. Amino acids are essential for repairing damaged tissues, supporting immune responses, fuelling metabolism, and maintaining organ function and systemic homeostasis [29]. This has been previously demonstrated during emphysema, a major hallmark feature of COPD [44].

Many studies investigating the role of skeletal muscle in homeostasis and disease in humans have been conducted following dietary, exercise, or pharmacological interventions and are frequently performed in the context of diseases where skeletal muscle wasting is a comorbidity. Despite this, animal models remain essential for studying skeletal muscle in both homeostasis and disease, with

their efficacy well established [45, 46]. This is largely due to the critical role of protein synthesis and degradation mechanisms in regulating fundamental cellular processes and development [47]. As a result, these mechanisms have become highly conserved across mice, humans, and other species [47, 48]. Mouse models have been widely used to study human muscular dystrophies [49], as well as conditions such as atrophy, cachexia, and sarcopenia [45, 50-52]. Additionally, experimental mouse models offer common advantages associated with animal studies, including the use of genetically modified mice to investigate specific genes, their high-throughput nature, and the ability to conduct *in vivo* treatment experiments. This provided a strong foundation for investigating the skeletal muscle phenotype in mouse models of respiratory disease.

1.2 Cachexia in respiratory diseases

Major advancements in the last few decades have identified many risk factors for the development of muscle atrophy across a range of illnesses but mainly in the context of cancers, COPD and myopathies: Systemic inflammation [53-55], inactivity [17, 56], malnutrition [57, 58], dysfunctional and unhealthy mitochondria [59, 60], denervation [61-63], hormonal changes (decreased growth factors e.g. testosterone, insulin growth factor (IGF)) [6, 64], corticosteroid treatment [65, 66], hypoxia [67] and ageing [63, 68] have all been demonstrated as co-contributors in cachexia [6]. These risk factors ultimately operate via downregulating protein synthesis and increasing protein degradation [6]. As outlined above, protein degradation and supply of amino acids is important to maintain homeostasis during illness and are needed for the immune response to disease and tissue repair. However, it is likely that chronic pulmonary diseases like COPD, IPF and asthma can perpetuate this cycle of muscle degradation.

There is a current lack of pharmacological interventions that try to directly improve skeletal muscle health in and attenuate cachexia in pulmonary diseases [69, 70]. This has been in part due to the difficulties in finding good therapeutic targets through the identification of key mechanisms.

Unfortunately, the underlying mechanisms of cachexia in asthma and IPF have not been elucidated as cachexia has not received much attention in these diseases, despite high estimated prevalence in both diseases [23, 26], although risk factors relating to worse spirometry measurements in patients with asthma or IPF seem to be associated with muscle atrophy in these diseases [23, 26]. Cachexia in COPD on the other hand has been better characterised in both an experimental and clinical setting, and some risk factors have been established though not fully elucidated [16, 71, 72].

While it is true that the prevalence of cachexia in asthma patients is not well reported, there have been studies in the past few years that have highlighted a need for further investigation into the association and impact of muscle loss in asthma. A study by Visser et al. 2023 [27], looking at a cohort 114 of asthma patients, observed that asthma patients with low muscle mass had lower muscle strength and worse clinical outcomes. They also identified an association with lower muscle mass and a decrease in FEV1, 6-minute walking distance, overall quality of life and a higher number of ER visits. A separate study by Hu et al. [26], found that asthmatics had a 17.6% and 5.5% of being diagnosed with sarcopenia or severe sarcopenia respectively. Sarcopenic asthmatics had a higher prevalence of shortness of breath, airway obstruction and lower compared to non-sarcopenic asthmatics. Furthermore, this study highlights an increased likelihood of developing COPD in sarcopenic asthmatics than in non-sarcopenic asthmatics. This implies the development of sarcopenia in asthmatics as a risk factor for the development of COPD. Asthma-COPD overlap prevalence has an estimated range of between 12.6% and 55.7% among COPD patients [73]so it is important to understand how one may relate or lead to the other.

There are also difficulties in distinguishing between COPD and asthma diagnoses in older adults. Is cachexia in asthma going underreported due to an association between COPD and cachexia? Indeed, one of the distinguishing factors of COPD that is highlighted in the GOLD 2025 guidelines is

weight loss, muscle mass loss and anorexia. These are considered “common factors” in COPD with “prognostic importance”. The report does caveat this by saying it could be the sign of other diseases such as lung cancer or tuberculosis, but crucially there is no mention of asthma [75].

Considering the association between asthma and muscle loss in the discussed epidemiological studies, the prevalence of asthma-COPD overlap, and the difficulty in distinguishing between asthma and COPD, It was deemed reasonable to investigate the skeletal muscle phenotype in our mouse model of moderate and severe asthma.

Indeed, Studies investigating the risk factors for cachexia in COPD have implicated a variety of mechanisms. As reviewed by Sanders et al., COPD-induced cachexia is associated with numerous factors, including increased catabolic signaling mediated by nuclear factor κ-light-chain-enhancer of activated B cells (NF-κB) and forkhead box O transcription factors (FoxOs). These transcription factors regulate the ubiquitin-proteasome system (UPS), atrogene induction, and inflammation in the limb muscles of patients [16]. Interestingly, a study examining protein synthesis signaling in COPD found an increase in protein synthesis pathway activity, but only in cachectic COPD patients [76]. Sanders et al. also hypothesized that reduced muscle quality contributes to cachexia. This reduction in muscle quality is evidenced by a loss of the oxidative phenotype, which is mediated by fiber type shifting (type I to type II), reduced muscle strength and endurance, and diminished mitochondrial capacity observed in the skeletal muscle of COPD patients [16].

To investigate disruption to protein synthesis and degradation in COPD, some studies have analysed the metabolome of COPD patient serum using techniques such as isotope labelling of metabolites, and liquid chromatography-mass spectrometry. In one such study, postabsorptive whole body protein balance was reduced in COPD patients and was associated with increased systemic inflammation, high blood pressure, low protein intake and reduced physical activity [77].

A separate study observed an increase in protein synthesis/breakdown in COPD patients in the postabsorptive state, indicating an increase in whole-body protein turnover but not a net increase in protein catabolism [78]. However, a non-targeted metabolomics study using samples from 178 COPD patients of varying severities observed higher protein degradation products in patient serum, even in non-cachectic patients [79]. Increased serum methylhistidine, a product of muscle actin and myosin degradation, was also observed, suggesting active protein degradation in the skeletal muscle [79].

The role of autophagy in the skeletal muscles of COPD patients remains poorly characterized. Many studies have focused on static markers of autophagy, such as microtubule-associated protein 1 light chain 3 alpha (LC3) and p62 abundance, or the LC3BI/LC3BII ratio [80, 81]. However, these measurements do not provide a comprehensive indication of autophagic flux, which is essential to understanding whether myofibers are effectively clearing dysfunctional organelles, such as mitochondria, to improve muscle health. Autophagic flux also reflects key cellular signaling pathways mediated by mammalian target of rapamycin complex 1 (mTORC1) and 5'-adenosine monophosphate (AMP)-activated protein kinase (AMPK), which have opposing actions [82].

Furthermore, mitochondrial dysfunction has been implicated in both myopathies and cachexia [83]. Impaired glucose metabolism is a shared feature of the skeletal muscle and lungs in COPD highlighting the importance of mitochondrial health in COPD-induced muscle wasting [84]. This further implicates dysfunctional autophagy as reduced clearance of dysfunctional mitochondria may result in their accumulation, inefficient metabolism and mitochondrial induced inflammation.

To further understand the mechanisms of pulmonary disease-induced cachexia, this review outlines the key characteristics of COPD, IPF and asthma, relevant clinical interventions, and the experimental murine models in which these mechanisms can be examined and targeted with

therapies. Following this, an overview of the signalling pathways that prevent or contribute to muscle atrophy such as the protein synthesis and degradation pathways respectively, and their modulation by inflammation will be highlighted. Finally, therapeutic targets for addressing cachexia in pulmonary diseases will be discussed.

1.3 COPD

According to a 2024 WHO report, COPD is the 4th leading cause of illness and death globally, and was responsible for 3.5 million deaths in 2021 [85]. It has many associated risk factors and is phenotypically diverse, which makes treating or curing COPD very challenging [85]. The predominant cause of COPD is cigarette smoke (CS) exposure, cessation of which is the only known treatment that can help reduce disease progression [75, 86]. CS is the cause of 70% and 30-40% of COPD cases in high-income and low-income countries respectively [85]. High household or ambient air pollution is also a major risk factor, especially in low-middle-income countries compared to high-income countries. Pollutant exposure such as occupational hazards (e.g. dust, chemicals, and fumes), air pollutants from industry (e.g. particulate matter (PM)2.5, smoke from coal or vehicles), and co-morbidities like infections and asthma are also known to cause COPD [87-90]. CS exposure and household air pollution remain the top known causes. Outside of environmental risk factors, genetic factors including endotypes such as α-1 antitrypsin deficiency and telomerase polymorphisms account for 2% of COPD cases [91], although there are possibly other factors not yet fully characterised like hypoxia inducible factor-2 related COPD [92].

Hallmarks of COPD include chronic bronchitis, obstruction of the small airways and emphysema (destruction of the alveolar structure) [93]. Exposure to risk factors results in a breakdown of the epithelial barrier of the lung airways, and airway remodelling. Increased mucus secretion, cell composition of the epithelium and changes to the immune landscape are some of the main factors associated with COPD airway remodelling [93]. Forced spirometry measurements that demonstrate

a post-bronchodilator FEV1/FVC < 0.7 is required for a COPD diagnosis [74, 75]. Mucus production, dyspnoea, chronic cough and a history of exposure to risk factors are also taken into account but not required for diagnosis [74].

Inflammation in COPD: Accumulation of innate immune cells like granulocytes, macrophages and innate lymphocyte cells (ILCs), in the lung is a hallmark pathology in COPD and their contribution to chronic inflammation and emphysema have been well documented [94-98]. Mouse models of COPD have demonstrated early recruitment of neutrophils to the lung lumen which coincides with early loss of epithelial barrier integrity [99]. Macrophages residing in the lung lumen can be functionally impaired and demonstrate reduced phagocytic capacity, resulting in increased bacterial burden during infection, causing increased chronic inflammation [100]. The increased presence of ILCs, ILC1, ILC3 and NK cells, indicate COPD severity and can drive activation of macrophages through IFN-γ production [101]. ILC2s have also demonstrated plasticity and can convert into ILC1s in response to viral infection [97]and IFN-γ signalling [98], further driving pathogenesis in COPD. Eosinophils are of major importance in COPD as they are potentially implicated in inflammation but are also useful from a clinical perspective as they can be predictive of a patient ability to respond to inhaled corticosteroids (ICS) [102, 103].

Inflammation in COPD can be driven by different adaptive immune types and are responsible for the heterogeneity seen in COPD. Broadly, there are four types: 1. Type 1 (Th1 cell mediated; interferon driven), 2. Type 2 (Th2 cell mediated; IL-4, IL-5, IL-13 driven), 3. Type 17 (Th17 mediated; IL-17 and IL-22 driven), 4. Regulatory T cells (Treg mediated; anti-inflammatory; TGF-β driven) [93].

Exacerbations are an important factor to consider during COPD. Increased exacerbations are linked to poor prognosis and can perpetuate muscle loss [104, 105]. Exacerbations can be driven by different immune mechanisms in different patients and are often associated with co-morbidities

like infection or asthma [106]. Exacerbation associated immune phenotypes can be broken down into four groups: 1. High airway IL-1β and TNF, 2. T1 mediated (high airway CXCL10 and CXCL11), 3. T2 immunity mediated (high airway IL-5 and CCL17) 4. Low airway inflammation [107].

Murine models of COPD: The most widely used murine models of COPD are the intranasal (i.n.) elastase-induced, i.n. LPS-induced and CS-induced COPD models [108]. LPS and elastase models are relatively acute models compared to the CS model and don't typically span more than 4 weeks [108]. These models induce severe, acute airway inflammation that results in emphysema, a key phenotype of COPD [109-113]. However, LPS and elastase are not causes of COPD in humans and the short duration for the induction of emphysema is not reflective of human development of COPD. Chronic CS-induced models of COPD are considered the gold-standard model for COPD as CS is a cause of COPD in humans, the model slowly induces emphysema relative to elastase- and LPS-induced models and produces hallmark features of human COPD [111]. CS exposure can be administered via two routes, whole-body exposure and nose-only exposure. There are minor differences between the two routes of administration. One study that investigated the differences between the routes showed an increased whole-body inflammation using whole-body exposure, and some small increases were observed in bronchial epithelial layer, mucus secretion and emphysema (determined by mean linear intercept) using nose-only exposure compared to whole body exposure [114]. An increasing emphasis on the COPD microbiome also highlights the need for murine models of COPD that minimise non-relevant disruption to the microbiome [115-119]. In the case of whole-body CS exposure models, smoke that settles on the fur of the mice may be ingested during grooming, effecting the gut microbiome. However, neither route has been studied directly so it is currently unclear which method best reflects the human COPD microbiome. Although the cigarette smoke (CS)-induced murine model of COPD is widely regarded as the gold standard, it has limitations that highlight the challenges of replicating human disease features in animal models.

These limitations are particularly relevant when designing therapies targeting specific aspects of COPD, such as chronic bronchitis and airway remodelling, which are not always evident in some murine COPD models [112, 120]. Therefore, to improve therapeutic development, animal models must accurately capture hallmark features of human COPD, including lung function decline, chronic bronchitis, emphysema, microbiome dysbiosis but also cachexia, considering its significant impact on disease prognosis.

Few studies that have examined the impact of the CS-induced experimental COPD on muscle mass or health. One study that looked at the effect of acute exercise in a 90-day CS-induced murine COPD model, exercised mice from days 60 to 90. The result of exercise was a somewhat surprisingly potent improvement of pulmonary inflammation, systemic inflammation and reduced airway remodelling [121]. Unfortunately, the authors did not examine the effect of exercise on muscle health or hypertrophy, nor did they provide any information on whole body or skeletal muscle weight fluctuations [121]. A repeat of this study is required to confirm the impressive improvements to COPD symptoms that exercise provided in this model, and to further examine the effects of exercise on muscle health in COPD, and the role it has in improving symptoms.

There have been some studies that have used alternative models to investigate muscles in the context of COPD. One examined the impact of pulmonary emphysema on muscle health and function. The model used genetically inducible IL-13 to drive emphysema as opposed to CS-induced emphysema as the authors state that CS can influence the muscle response to injury, and they wanted to remove this as a confounding factor [122]. This provides a more precise avenue for examining the effects of pulmonary emphysema alone on muscle atrophy, however it removes the highly relevant impact of CS on COPD induced cachexia, as this is a major etiological factor for COPD patients. Another emphysema/COPD murine model that employed porcine pancreatic elastase to induce emphysema demonstrated reduced exercise tolerance, weight loss and atrophy of the

diaphragm [123]. Thus, the use of murine COPD models requires therapeutic goals that address specific overlapping aspects of both specific murine and human COPD.

1.4 Asthma

Asthma is a major non-communicable respiratory illness that effects approximately 300 million people globally and is responsible for approximately half a million deaths/year [124, 125]. On average, adults over the age of 65, females and non-Hispanic blacks have a much higher death rate [126]. In contrast to the epidemiology of COPD, asthma is more prevalent in high-income countries (~10%) compared to low-income countries (6-7%) [127]. Asthma severity is sometimes described in terms of a patient's response to ICS, with steroid sensitive patients considered mild-moderate asthmatics and steroid resistant patients is severe asthmatics [128]. Steroid resistant asthma, despite being an estimated 3.6-10% of total asthma cases [129], accounts for amount of the total healthcare costs of asthma (50-80%) [128, 130, 131]. There are many known risk factors that can cause/ contribute to the development of asthma including environmental factors like CS exposure and household air pollution, which overlap with risk factors associated with COPD [89]. Other risk factors include genetics, exposure to allergens (e.g., house dust mites (HDM)) and infections (influenzae, early life exposure to beneficial microbes, socioeconomic factors, sex (boys have higher likelihood of developing asthma before puberty but this trend reverses post-puberty) and age [125].

Asthma is used as an umbrella term for a group of phenotypically different airway diseases that can vary in cause, severity and treatment method, but retain similar disease features. Hallmarks of asthma are wheezing, dyspnoea, mucus hypersecretion, chest tightness, tightening of the airway and variable expiratory flow limitation [132, 133]. Exposure to risk factors can cause a breakdown of the airway epithelium, airway remodelling, changes to the immune landscape. Notably, these changes result in bronchial hyperresponsiveness and smooth muscle remodelling that cause airway tightening and thus, breathing difficulties [134, 135].

The diagnosis of asthma is non-trivial, and it can be difficult to pinpoint the exact type of asthma a patient has without longitudinal monitoring [136, 137]. Diagnosis is usually based on a demonstrated history of characteristic asthma symptoms, ICS use, but most importantly confirmation of variable expiratory airflow limitation using spirometry or peak expiratory flow (PEF) measurements[138]. FEV1, FEV1/FVC and PEF are decreased in asthma patients and increased FEV1 and FVC ≥12% and 200ml respectively, or an increase in PEF≥20% in response to bronchodilators or ICS are required for confirmation of variable expiratory airflow limitation [138, 139]. Thus, patient history of variable respiratory symptoms and a post treatment increase in FEV1 and PEF are used to confirm asthma diagnosis.

Inflammation in asthma: Asthma can be broadly divided into two endotypes based on their dominant CD4+ T cell response, type 2 (Th2 mediated) and non-type 2 [132, 140]. Type 2 endotypes of asthma can be divided into three phenotypes, atopic, late onset and AERD (aspirin-exacerbated respiratory disease). They are characterised by a high Type 2 T helper (Th2) cell mediated immune response. Th2 cells, along with group 2 innate ILCs, produce IL-4, IL-5 and IL-13 that mediate airway eosinophilia, Goblet cell metaplasia, mucus hypersecretion, and B cell isotype switching to produce IgE [141]. IgE production causes mast cell and basophil degranulation and is typically triggered in response to an allergen [142]. Type 2 asthma accounts for approximately half of all asthma cases [132].

Non-type 2 endotypes of asthma can be divided into four phenotypes, non-atopic, smoking related, obesity related, and late onset asthma that typically occurs in patients >50 years of age. These phenotypes usually lack a high Th2 cell presence or airway eosinophilia and instead can have a high Th1/Th17 cell presence, high levels of neutrophils in the sputum, paucigranulocytic and resistant to corticosteroid therapy [132].

Murine models of asthma: Murine models of asthma can help investigate underlying mechanisms, future therapeutic targets, and response to experimental therapies in asthma [143]. BALB/c and C57BL/6 mice are commonly used in these models, along with knockout (KO) variants [144], however BALB/c mice are most common because of their heightened type 2 response vs other strains making them the preferred option for studying type 2 endotypes of asthma [145]. Challenges like using physiological allergens (HDM, cockroach, pollen, fungal spores), artificial allergens (ovalbumin (Ova), LPS, cyclic-di-GMP) and infections (non-typeable *haemophilus influenzae (*NTHi*), chlamydia muridarum (*CMU*), respiratory syncytial virus (*RSV*)*) and multi-challenges have been used to induce asthma in murine models [144].

The type of challenge used in the model dictates the asthma phenotype. For example, HDM-induced asthma in BALB/c mice induces airway hyperresponsiveness (AHR), eosinophilia, and airway remodelling [146, 147]. Ova-induced models in BALB/c mice are a commonly used model of asthma due to their reproducibility and ability to reflect many aspects of human type 2 asthma [144]. Ovalbumin sensitisation, with an adjuvant like aluminium hydroxide, followed by Ova-challenge can induce type 2 mediated airway inflammation, epithelial remodelling, increased airway and serum IgE, and AHR in response to an agonist (e.g. methacholine, histamine, leukotrienes) [148, 149].

Recently, co-challenge models that use an allergen or stimulus like HDM or ovalbumin along with an infection have demonstrated the potential for more precise induction of asthma phenotypes. These co-challenge models retain clinical relevancy as infections like NTHi, CMU and RSV are all common isolates from the airways of asthma patients and presents an opportunity for studying mechanisms within different phenotypes [128]. For example, CMU and NTHi respiratory infections, with ovalbumin sensitisation and challenge induced a murine model of severe steroid-resistant-asthma. In this model, increased AHR, neutrophilia and NOD-, LRR- and pyrin domain-containing

protein 3 (NLRP3)-induced IL-1β was observed in the airway. This was reversed by neutrophil depletion [150].

Diet and obesity have also been shown to increase asthma severity and the likelihood of steroid resistance. A study that examined the sputum of 25 obese asthmatics found an increase in type-2 responses, increased NLRP3 inflammasome activity and eosinophilia [151]. These findings were replicated in a model with BALB/c mice that were given a high fat diet (HFD) and ovalbumin sensitised. Interestingly, HFD alone (without Ovalbumin sensitisation) was enough to induce AHR, and HFD/ovalbumin sensitised mice became steroid insensitive [151]. As expected, the HFD mice gained weight over the 13 weeks of the model compared to the normal chow diet mice, but most of this weight was due to an increase in fat, not skeletal muscle mass. Therefore, targeted regimes that increase skeletal muscle mass, rather than just overall weight gain through HFD, may be the best route for improving cachexia in asthmatics, as the latter may lead to increased inflammation, AHR and likelihood of steroid insensitivity [151].

1.5 Idiopathic Pulmonary Fibrosis (IPF)

IPF is an interstitial lung diseases (ILD) defined as a "specific form of chronic, progressive fibrosing interstitial pneumonia of unknown cause, occurring primarily in older adults, limited to the lungs" which has a distinct histopathological/or radiologic pattern [152]. The epidemiology of IPF is not well known as there is heterogeneity between epidemiological studies when it comes to their methods, especially in how IPF is defined [153], but also because there are no large scale studies [152]. For these reasons it is difficult to say exactly the prevalence of IPF, however, systematic reviews of the current studies as of 2017 estimate that 3 million people suffer from the disease globally [154]. One literature review from 2021 that used data from 22 different studies estimated a prevalence of 0.33–4.51 per 10,000 persons [155]. Prognosis for patients with IPF is poor and most patients do not survive 5 years post-diagnosis [156].

The aetiology of IPF is difficult to define, however there are associated risk factors that correlate with incidence like CS exposure, environmental exposures (e.g. occupational dust from stone cutting, mining, farming), microbial infections and gastroesophageal flux, and genetic factors [152, 157]. The hallmarks of IPF disease are progressive cough, dyspnoea, and lung scarring (fibrosis). Diagnosis is based on three factors: 1. The exclusion of other ILDs, 2. Histological assessment of the lungs to confirm usual interstitial pneumonia (UIP) pattern (usually by high resolution computed tomography scan (HRCT)) and 3. Lung biopsy is recommended for patients where UIP is not confirmed by HRCT [152, 158, 159]. UIP histopathological features comprise of "honeycombed" lung areas (subpleural cystic spaces that give the appearance of a honeycomb structure due to their well-defined walls), fibrotic areas, as well as intermittent normal parenchymal areas [152]. There is usually mild to moderate immune cell infiltration, and patches of proliferating fibroblasts and myofibroblasts [160]. Fibroblasts that differentiate into myofibroblasts secrete ECM proteins which alter the lung interstitial space, reducing gas exchange, causing stiffness in the lungs and shortness of breath [161]. ECM deposition and changes to spirometry has so far been shown to be irreversible in humans and there are no treatments that fully halt progression [162].

Inflammation in IPF: The role of the immune system in inducing and perpetuating IPF is not well characterised compared to asthma and COPD, where there are clear immune endotypes and phenotypes. Neutrophils were found to be elevated in both the blood and bronchoalveolar lavage fluid (BALF) of IPF patients, and in a mouse model of bleomycin induced IPF and there is evidence of neutrophil extracellular traps (NET)osis in exacerbating fibrosis in the lung [163, 164]. Studies have suggested an increased Th2/Th1 cell ratio could be linked to increased fibrosis, however anti-IL-13 [165] and recombinant IFNγ administration [166] did not provide any improvement in human trials. M2 macrophages, cytotoxic T cells, Th17 cells and Treg cells could promote fibrosis [167].

Th1 cells, and tissue resident memory CD4+ T cells have demonstrated potential beneficial roles in IPF [167]. However, greater understanding of the role of immune cells in IPF is needed to properly direct future clinical trials. Thus, treatments remain focused on decreasing fibrosis by targeting the epithelium, fibroblasts and myofibroblasts.

Exacerbations in IPF patients can cause abrupt, step-wise, decreases in lung health. The cause of exacerbations in IPF remains unclear but have been compared to acute lung injury (ALI) as they share clinical features [168]. Increased immune cells infiltrations during exacerbations may not drive the exacerbation but may be responding to an infection. Infections, microaspirations, drugs intended to treat co-morbidities are known to cause ALI and thus may underly some exacerbations in IPF [168].

Murine models of IPF: Bleomycin-induced murine models of pulmonary fibrosis are the most commonly used model for the study IPF *in vivo* and typically precede human trials of new pharmacological interventions [169-172]. Bleomycin induces fibrosis, with immune cell infiltration, and collagen deposition. Inflammation induced by bleomycin injury occurs over 3 weeks after as seen by an increase in total BAL leukocytes [173] and the optimal time to observe fibrosis is about 1-2 weeks post-challenge [173-175]. Young mice typically resolve bleomycin-induced fibrosis within 3-4 weeks, but aged (1y old) mice do not [176], and aged mice have demonstrated increased NLRP3 inflammasome activation [177]. Aged male mice also develop more fibrotic disease than aged female mice and demonstrated increased TGF-β, IL-17A and CXCL1 in the bronchoalveolar lavage fluid [176]. One model of bleomycin-induced fibrosis also demonstrated increased NLRP3 inflammasome activation in old vs young C57BL6 mice, which may imply the NLRP3 inflammasome has more of a role in fibrosis than previously thought. Other models of fibrosis that don't recapitulate UIP histology in the same way as bleomycin-induced models and are thus, less used in the context of IPF studies, are asbestos, silica, and cytokine induced models

of IPF [178]. There are limitations associated with the use of Bleo-induced murine model that must be considered; bleomycin-induced fibrosis in young mice is resolved over time but is not resolved in humans and does not reflect the average age of IPF diagnosis [162]. Other bleomycin models that have used repeat bleomycin exposures in mice have reduced post-injury recovery and persistent fibrosis and epithelial remodelling, making them more suitable for the study of IPF than single dose exposure models [179]. A recent study highlighted several key differences between the spatially resolved transcriptomes of mouse bleomycin-induced and human pulmonary fibrosis [180]. These included the presence of aberrant epithelial cells that remained senescent in human IPF but retained some function in mice, allowing them to proceed with their differentiation into AT1 cells. This progression for mouse epithelial cells from AT2 to ADI and then AT1 cells supports previous studies that demonstrated postinjury healing in mice models. Other differences identified in the study included changes to immune cell populations and their interactions, as well as distinct signalling molecules like TGF-β and apolipoprotein E [180]. Though this study highlighted several key differences, there were still similarities identified such as the presence of pro-fibrotic macrophages with similar gene signatures, and similar signalling pathways [180].

Furthermore, therapies administered in bleomycin-induced IPF models typically occur prophylactically or at an early timepoint post-bleomycin challenge. These prophylactic models have yielded positive results in the past; the only two pharmacological interventions pirfenidone and nintedanib exhibited efficacy in preventive models prior to human trials [181, 182]. However, neither of these interventions prevent or reverse disease, or improve patient survival. Thus, a shift toward the use of aged, male and female, non-resolving animal IPF models, e.g. through the use of repeated bleomycin challenge, could better reflect the clinical reality of human pulmonary fibrosis.

Assessing Lung function in murine models of respiratory disease

Invasive plethysmography was used in my study to assess lung function in experimental mouse models of respiratory disease. This method used a Scireq Flexivent to measure respiratory mechanics (See figure 2.2). Spirometry assessment in humans requires patients to do breathing exercises such as forcefully breathing into a tube that measures FEV over time. This is not possible in mice. Instead, a tracheostomy is performed under anaesthesia and the Flexivent controls breathing whilst performing precise perturbations. This allows for greater control of variation between subjects as the machine breaths for the mouse at a precise rate (450bpm) and delivers the same programmed perturbations for each mouse. This removes the confounding factors of patient cooperation and the need for good breathing technique that are required for human spirometry assessment. However, this does not necessarily replicate natural respiratory mechanics that would be seen in humans and does not perfectly translate from animal model to clinical setting. One major difference between these two methods of assessing lung function is the opposing impact of COPD on FVC in mouse models and in humans. In mouse models, increased emphysema and compliance can lead to higher FVC [183], however this is not true in humans where a progressive decrease in FVC due to gas trapping is observed [184].

1.6 Skeletal muscle homeostasis, growth and depletion.

Understanding the underlying mechanisms of protein synthesis and degradation is crucial for the development of future therapeutics that specifically address cachexia. Dysregulation of these pathways can lead to an imbalance, resulting in muscle loss. Restoration of this balance or preventing dysregulation should be the goal of future therapies. Interestingly, disuse atrophy and disease mediated atrophy likely have different triggers that influence signalling for atrophy [56]. However, they ultimately utilise the same cellular machinery for protein degradation (proteasome/autophagy) and inhibit protein synthesis signalling and thus, have some overlap in their processes. Protein degradation can be influenced by a wide range of factors and is

investigated through examining the expression of “atrogenes”, or atrophy associated genes [6, 185]. The Phosphoinositide 3-kinase (PI3K)/Protein Kinase B (Akt)/mTORC1 pathway is the key signalling pathway that mediates protein synthesis, so investigating this pathway for dysregulation at different points along the signalling pathway could give insight into the mechanisms underlying pulmonary disease mediated cachexia (Figure 1.2).

1.6.1 PI3K/Akt/mTORC1 signalling pathway

The PI3K/Akt/mTOR signalling pathway mediates protein synthesis involved in muscle growth by regulating translational proteins [186]. This signalling cascade can be activated by mechanotransduction [187, 188] and endogenous growth factors like insulin, IGF-1/-2, amino acids [189, 190], which bind and activate the receptor tyrosine kinases insulin receptor (IR) and IGF1R respectively [191]. Activated IR phosphorylates IR substrates (IRS)-1/-2 at multiple tyrosine kinase residues [192-194], recruiting and phosphorylating phosphoinositide 3-kinase (PI3K) which docks at the IRS via its p85 subunit [195]. PI3K subunit p110 then catalyses the conversion of phosphatidylinositol-4,5-bisphosphate (PIP2) to phosphatidylinositol-3,4,5-trisphosphate (PIP3). PIP3 can then recruit 3-phosphoinositide-dependent kinase 1 (PDK1) and Akt to the plasma membrane, where PDK1 can phosphorylate Akt at Thr308, partially activating Akt activity. PIP3 also recruits mTORC2, a protein complex consisting of key subunits mTOR and Rapamycin-insensitive companion of mammalian target of rapamycin (RICTOR). mTORC2 can then fully activate Akt by phosphorylating Ser473 [196, 197].

Fully activated Akt can promote several key functions like cell survival, glucose uptake and protein synthesis. Protein synthesis is promoted by Akt through indirect activation of mTORC1. Akt inhibits the guanosine-5'-triphosphate (GTP)ase-activating protein (GAP) Tuberous Sclerosis Complex 2 (TSC2) by phosphorylation (Figure 1.2). This prevents TSC2 mediated conversion of Ras homolog enriched in brain (Rheb)-GTP to Rheb-GDP, which inhibits its function. Thr308 Akt phosphorylation

alone can result in TSC2 inhibition, however inhibition of FoxO transcription factors required Ser473 activation [198].

Rheb-GTP is then able to activate mTORC1 which can activate its downstream effectors like S6 kinase (S6K) and eukaryotic translation initiation factor-4E (eIF-4E) binding protein 1 (4E-BP1) [199]. S6K is phosphorylated by mTORC1 at Thr389, and p-S6K can go on to activate S6 ribosomal protein (rpS6) by phosphorylating Ser235/236. rpS6 is a component of the translational part of the ribosome, and phosphorylation of rpS6 increases ribosome capacity for translation [199]. mTORC1 phosphorylation of 4E-BP1 at Thr37/46 primes other sites for phosphorylation, which when phosphorylated create a conformational change to 4E-BP1, reducing eIF-4E affinity. eIF-4E is a subunit of the eIF-4F complex, which is needed for mRNA recruitment to the ribosome, driving mRNA translation and thus, protein synthesis [199].

Both mRNA recruitment to the ribosome and elongation are considered rate limiting for protein synthesis. Initiation of translation is considered the main rate-limiting step of translation and is controlled by eIF-4F complex [200]. mRNA sequences can have differential effects on their recruitment to the ribosome, with some sequences resulting in faster or slower ribosomal recruitment, and thus protein synthesis [201]. Codon choice can also affect elongation as some codons are decoded at a higher speed than others. The availability of a codons corresponding tRNA dictates elongation, as mRNAs with codons requiring tRNAs of lower concentration will have reduced rates of translation. Reduced translation speed results in decreased protein production and destabilisation of mRNA, further exacerbating translational issues [202].

1.6.2 Mediators of muscle atrophy and protein degradation

Activation of the PI3K/Akt/mTORC1 pathway canonically increases protein synthesis through activation of mTORC1 and its downstream effectors. However, there are circumstances where this

pathway results in increased expression of atrophy associated genes. Akt activation typically results in increased protein synthesis through indirect activation mTORC1 and inhibits FoxO mediated protein degradation by phosphorylating FoxOs, inhibiting their nuclear translocation, and subsequent transcription of the UPS genes (Figure 1.2) [203, 204]. These UPS genes include the E3-ubiquitin ligase proteins *TRIM63* (muscle RING finger 1 (MuRF1) and *FBXO32* (Atrogin-1), which are classically associated with muscle atrophy and protein degradation [205, 206]. However, there is evidence to show that mTORC1 activation can also promote muscle atrophy and myopathy by inhibiting autophagy in a way that is tightly regulated and tissue-dependent [207, 208]. mTORC1 has been shown to inhibit autophagy through Ulk1 phosphorylation and is also able to control autophagy independent of FoxO3 activation status, demonstrating its key role in regulating autophagy [207, 209]. In one study using a TSCmKO model, constitutive activation of mTORC1 resulted in negative regulation of Akt by mTORC1, resulting in Nuclear Factor Erythroid 2-Like 1 (Nrf1) mediated proteasome biogenesis and thus protein degradation [207, 210]. Constitutive mTORC1 activation also increased 72 of the examined 154 atrophy-associated genes, including *TRIM63* and *FBXO32*, and was normalised after 3 days of rapamycin treatment [210].

UPS genes can be considered part of a broader spectrum of genes that are differentially expressed atrogenes. Of these genes, the E3 ubiquitin ligases *TRIM63* and *FBXO32* are frequently upregulated in atrophy [205, 211]. *FBXO32* codes for MAFbx (Atrogin-1) protein, which can decrease protein synthesis by tagging eIF-4F, MyoD and myogenin for degradation [212-214] and *TRIM63* codes for MuRF1 protein which labels sarcomeric proteins for degradation [185, 215]. Atrogenes like *TRIM63* and *FBXO32* can be upregulated in many catabolic conditions outside of cachexia and are increased in many catabolic conditions including but not limited to ageing, CS-exposure, denervation, fasting and immobilisation [185].

Transcription of these genes can be regulated by several transcription factors like the FoxO protein family [206], activating transcription factor 4 (ATF4) [216, 217] and NF-κB [218] (Figure 1.2). The FoxO protein family of transcription factors have been shown to upregulate UPS proteins *TRIM63* and *FBXO32*, subunits of the 20S proteasome, and autophagy related proteins p62 and cathepsin-L [203]. This combined increase in UPS, proteasomal and autophagy proteins and their activity provide the catabolic environment required for protein degradation and muscle loss. FoxO transcription factor activity can be modulated at a transcriptional level but mainly through post translational modification of the different FoxO isoforms [219, 220] e.g. Akt phosphorylation of FoxO inhibits its function and translocation [221].

Growth arrest and DNA damage-inducible A (*GADD45A*) has been shown to be one of the earliest markers of neurogenic skeletal atrophy and remains upregulated for much longer (at least until 90 days post denervation) as opposed to other atrogenes like *TRIM63* and *FBXO32* which return to baseline within a week [222]. Several transcription factors can upregulate *GADD45A* expression including, but not limited to, ATF4, FoxO proteins and indirectly through NF-κB induced early growth response protein 1 (EGR1) [223], although predominantly by ATF4 in the context of atrophy [224]. The exact role of *GADD45A* in atrophy is controversial, with studies showing both protective and detrimental roles. Constitutively expressed GADD45A was found to decrease mitochondrial content, oxidative phosphorylation (OXPHOS) capacity and was selectively atrophic in glycolytic muscle fibres in a transgenic murine model [225]. This same study also found increased *GADD45A* expression correlated with muscle weakness in humans [225]. Conversely, *GADD45A* was found to be protective in another study, where loss of *GADD45A* expression in a murine model of atrophy resulted in loss of fibre type identity and increased neurogenic muscle atrophy [222] and can inhibit NF-κB [226]. Histone deacetylase 4 (HDAC4) has been shown to increase *GADD45A* during muscle denervation-induced atrophy [62]. Overall, Gadd45α is broadly

considered a mediator of atrophy through its repression of protein synthesis, metabolic pathways, association with denervation and mitochondrial biogenesis [62, 224, 227].

1.6.3 The role of inflammation in cachexia

Pulmonary diseases like COPD and certain asthma endotypes are partially characterised by chronic, systemic inflammation and there is evidence for inflammation in modulating muscle atrophy. Studies have shown that circulating cytokines and increased inflammatory signalling in the skeletal muscle can contribute to increased protein degradation, a reduction in protein synthesis and detrimental alteration of cellular metabolism [17, 53, 228].

IL-6, TNF, IL-1β induced activation of the transcription factor NF-κB has been shown to upregulate atrogenes including *TRIM63*, *FBXO32* and *GADD45A*, and block myoblast differentiation into myotubes [55, 229, 230]. Furthermore, IL-6, type I interferon (IFNα + IFNβ) [231-233] and type II IFN (IFNγ) [234] mediated activation of the janus kinase-signal transducer and activator of transcription proteins (JAK-STAT) pathway has also been shown to increase atrogenes *TRIM63*, *FBXO32*, *CASP3* (caspase-3) and *MSTN* (myostatin) [235-237]. Myostatin (a member of the transforming growth factor TGF-β family) is a myokine released by myofibers, and signals in an autocrine and paracrine fashion to inhibit muscle growth via the SMAD signalling pathway [238]. Akt is also inhibited during inflammation through myostatin activation of SMAD4 [239] but interestingly TNF activation of Tumour Necrosis Factor Receptor Associated Factor 6 (TRAF6) has been shown to increase Akt activation through facilitating Akt plasma membrane localisation [240].

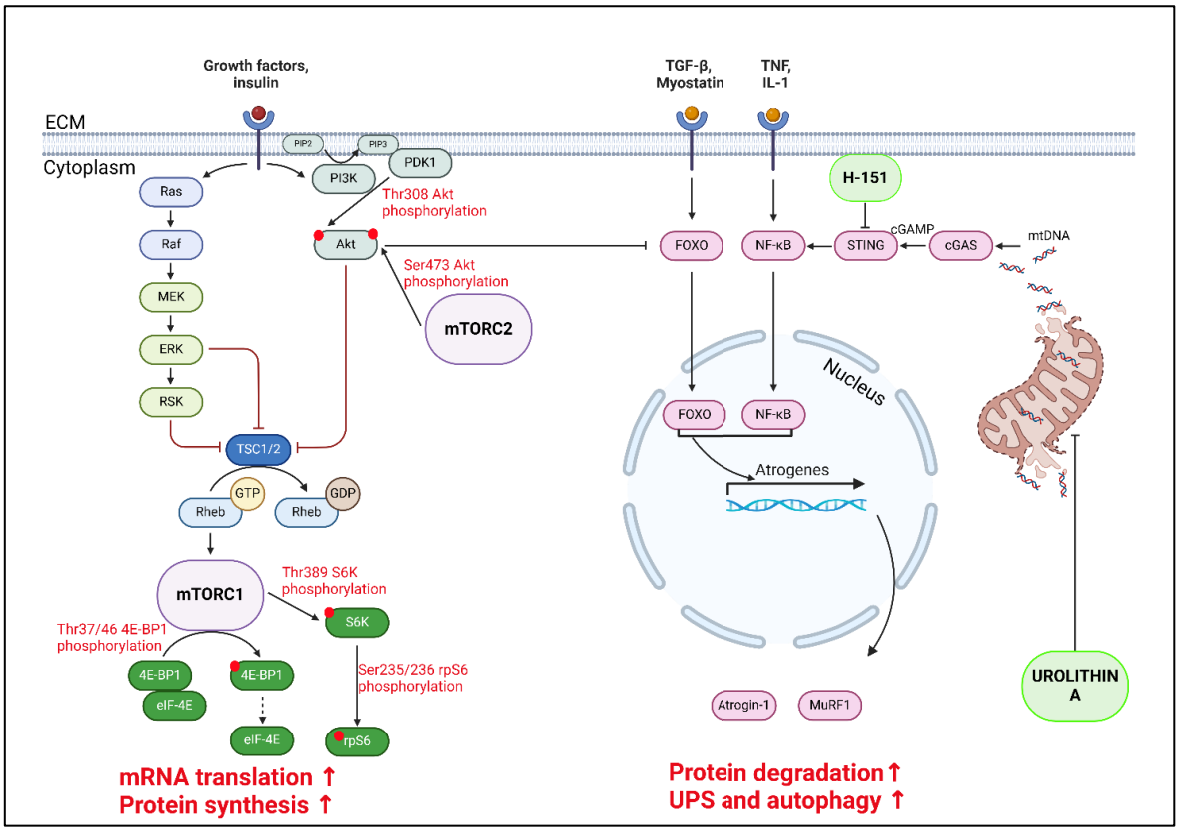

Figure 1.2 Summary of cell signalling pathways of protein synthesis and degradation

Growth factors like insulin, can activate Akt which goes on to activate mTORC1 by inhibiting TSC1/TSC2. Activated mTORC1 can then phosphorylate key proteins, like 4E-BP1 and S6K which can activate rpS6. The result of this is increased protein synthesis. Inflammatory factors like TNF and TGF-β can upregulate transcription factors FOXO and NF-κB, upregulating genes associated with protein degradation. The cGAS-STING pathway can potentially mediate these transcription factors through direct and indirect upregulation of NF-κB. Image made using BioRender.

1.7 Avenues for future therapies targeting cachexia in pulmonary disease.

1.7.1 Current pharmacological and non-pharmacological treatments for pulmonary diseases and cachexia.

COPD has no cure and current treatments only partially alleviate symptoms. However, they do not reverse or halt the decline in lung function. Bronchodilators are the most widely prescribed COPD treatments and can alleviate tightness in the chest by relaxing the airways. For patients with respiratory co-morbidities, such as allergic airway disease or type 2 high asthma, they can use

inhaled corticosteroids to help alleviate symptoms, however COPD symptoms are commonly corticosteroid resistant. Steroid resistance in COPD is a major roadblock to addressing symptoms as corticosteroids are effective, widely available treatments for the alleviation of many respiratory disease symptoms but provide limited relief to most COPD patients. Thus, they are only recommended for patients with asthma, or as part of a triple inhaled therapy with long-acting β2 agonists (LABAs) and long-acting muscarinic antagonists (LAMAs) [74]. Despite this, COPD patients were historically, and are still prescribed high doses of corticosteroids to address symptoms outside of these guidelines, which can negatively impact prognosis and increase risk of pneumonia [241]. For asthma treatment, inhaled corticosteroids are often used alongside other inhaled therapies such as short-acting β_2 agonists (SABA), LABA and leukotriene receptor antagonists. Like COPD patients, asthma patients can develop resistance to corticosteroid treatment and the prescription of increasingly higher doses of corticosteroids was historically common. For many reasons this can negatively impact patient prognosis in the long term due to the side effects of corticosteroids. Pirfenidone and nintedanib are the only approved drugs used to treat IPF in the US and non-pharmacological therapies include oxygen supplementation and pulmonary rehabilitation [242, 243].

These treatments fail to prevent disease progression, provide limited relief for patients, and fail to prevent cachexia. Moreover, it is possible that these treatments may contribute to muscle atrophy as has been the case with glucocorticoid (GC) induced muscle atrophy. The negative impact of GC therapy, particularly fluorinated GCs, on skeletal muscle has been well characterised in patients with rheumatological and inflammatory diseases [244, 245], as well as in diseases where there is high circulating GCs, such as in cachexia, sepsis, and insulinopaenia [65, 246]. This is likely due to GC upregulation of atrogenes, via activation of the UPS, and inhibition of PI3K/Akt/mTORC1 signalling [65, 247-249]. However, there is evidence of GC treatments being beneficial to muscle mass, as

symptom relief provided by their use can increase patient activity and subsequent muscle health [250].

Interestingly, the IPF treatment pirfenidone, which inhibits TGF-β production, may provide partial protection to muscle atrophy and function through inhibiting the SMAD mediated Akt inhibition [251], and reducing muscle skeletal muscle fibrosis [252]. Nintedanib can negatively regulate skeletal muscle growth as it is a tyrosine kinase inhibitor and can inhibit activation of the PI3K/Akt/mTORC1 signalling pathway [182, 253]. However, clinical studies have demonstrated both pirfenidone and especially nintedanib, can increase weight loss in IPF patients [254, 255]. A study which reviewed the effects of patients switching from pirfenidone to nintedanib treatment observed that low body-mass index (BMI) in patients was a risk factor for early termination of the nintedanib treatment and that anorexia induced by nintedanib treatment was more prevalent in patients switched from pirfenidone [255]. Due to limitations of the study, it is unclear whether pirfenidone was preventing IPF-induced weight loss, which was then exacerbated by the discontinuation of pirfenidone and nintedanib treatment, or whether pirfenidone was the cause of weight loss, although the latter seems less likely [255], since changing from pirfenidone to nintedanib treatment did accelerate weight loss. That being said, nintedanib has also demonstrated some ability to improve muscle heath and decrease *TGFB* expression and thus, may be appropriate for addressing cachexia under certain conditions e.g. Duchenne muscular dystrophy [256]. However, more investigation is needed to fully understand the impact of both drugs on muscle mass and function.

There are currently no approved drugs for the treatment of cachexia. However, a recent randomised double-blind phase 2 clinical trial looked at the impact of Ponsegromab on cachexia in 187 patients with cancer (non-small-cell lung carcinoma (40%), pancreatic (32%) and colorectal cancer (29%)). Ponsegromab is a humanised monoclonal antibody for growth/differentiation factor 15 (GDF-15)

(Ponsegromab) and was found to increase weight and activity, improve symptoms of cachexia and decrease in adverse events [257]. This promising result indicates the detrimental role of GDF-15 in cancer-associated cachexia and warrants further investigation in pulmonary disease induced cachexia.

1.7.2 Mitochondrial dysfunction as a therapeutic target in cachexia

Poor mitochondrial health and dysfunctional mitochondrial dynamics have been observed in the lungs of patients with COPD [258-260], moderate and severe asthma [261-264] and IPF [260, 265]. As such, improving mitochondrial health represents an attractive therapeutic target in these diseases. However, improving mitochondrial function in the skeletal muscle of cachectic patients with pulmonary diseases as a way of decreasing muscle atrophy poses significant hurdles.

The restoration of mitochondrial health involves the removal of damaged mitochondria via mitophagy and the subsequent biogenesis of new, functional mitochondria. However, mitophagy depends on the upregulation of protein degradation pathways, including autophagy and proteasome formation, while mitochondrial biogenesis typically requires AMPK activation and thus mTORC1 inhibition due to their bidirectional inhibition [266, 267]. This is mechanistically opposed to the activation of PI3K/Akt/mTORC1 signalling, which is critical for promoting protein synthesis and inhibiting muscle atrophy. Active mTORC1 can also phosphorylate the transcription factor EB (TFEB), inhibiting its transduction to the nucleus where it upregulates mitochondrial biogenesis, autophagy and lysosomal gene expression [268]. This process can be indirectly reversed by AMPK, and subsequently prevents mTORC1 mediated phosphorylation of 4E-BP1 and S6K [269].

This raises an important question: does the induction of mitophagy inhibit mTORC1 activation to the extent that it suppresses overall protein synthesis, exacerbating muscle atrophy? Alternatively,

does the restoration of mitochondrial function, through reduced inflammatory signalling, oxidative stress, and metabolic dysregulation, attenuate the downstream effects on the PI3K/Akt/mTORC1 pathway, ultimately preserving muscle protein synthesis?

These interactions require further investigation to determine the feasibility of targeting mitochondrial dysfunction as a therapeutic strategy in pulmonary disease-induced cachexia. The ongoing monoclonal antibody trials for GDF-15 in preventing cachexia is particularly interesting in this case, as GDF-15 is upregulated in the serum of patients with mitochondrial diseases [59], is used as a biomarker for mitochondrial dysfunction [270, 271], and is associated with the senescence-associated secretory phenotype (SASP), which is also associated with mitochondrial dysfunction [83]. This raises another question then as to whether mitochondrial dysfunction is contributed to by GDF-15 signalling, whether it co-occurs independently of GDF-15, or whether mitochondrial dysfunction drives GDF-15 production. Though the mechanism has not yet been fully elucidated, studies have provided evidence of skeletal muscle mitochondrial dysfunction as an inducer of GDF-15 production [272, 273], which highlights mitochondrial dysfunction as a novel therapeutic target in cachexia.

1.7.3 cGAS-STING pathway inhibition as a potential mechanism for improving muscle health in cachexia.

Recent studies have highlighted a potential role for the cyclic guanosine monophosphate (GMP)-AMP synthase (cGAS)-stimulator of interferon genes (STING) pathway in causing myopathies [60]. The cGAS-STING pathway is involved in the detection of cytosolic double-stranded DNA (dsDNA) [274-276] (Figure 1.2). dsDNA is detected by and causes a conformational change in the pattern recognition receptor (PRR) cGAS which catalyses the production of cyclic GMP-AMP (2’3’-cGAMP) [276]. This conformational change results in cGAS dimerising on the dsDNA. dsDNA can have many sources including viruses and bacteria but can also include host dsDNA originating from cellular

stress or damaged/dysfunctional mitochondria. 2'3'-Cyclic GMP-AMP (cGAMP) binds the STING protein dimer at the endoplasmic reticulum (ER) resulting in oligomerisation [277, 278]. The STING oligomer becomes de-anchored from the ER and moves through the Golgi where it then recruits TRAF family member-associated NF-kappa-B activator (TANK) -binding kinase 1 (TBK1). TBK1 autophosphorylates and activates interferon regulatory factor 3 (IRF3) and NF-κB signalling [279]. IRF3 translocates to the nucleus where it binds interferon stimulated response elements (ISRE), resulting in upregulated proinflammatory gene expression such as interferon-stimulated genes (ISG), like ISG15, and type I interferons. Interestingly, STING is also known to activate non-canonical NF-κB signalling through p52-RELB, which functions as a negative regulator of type I interferon production [280].

Mitochondrial dsDNA leakage into the cytosol where it activates the cGAS-STING pathway, increasing inflammation (Figure 1.2) [60, 274]. Targeting the cGAS-STING pathway offers a new approach for limiting inflammation driven cachexia in COPD. H-151 is a small molecule inhibitor that inhibits cGAS-STING signalling by irreversibly binding Cys91 in the transmembrane domain of STING, preventing palmitoylation and oligomerisation of the STING dimer, which is essential for activation of the type I interferon and ISG inflammatory response [281]. In previous *in vivo* studies, H-151 reduced phosphorylation of TBK1 and circulating IFNβ and IL-6 [281].

1.7.4 Urolithin A as a therapeutic for improving muscle health in cachexia.

Urolithin A (UA) is a gut metabolite produced from ellagitannins and ellagic acid by the gut microbiota in rodents and humans [282, 283]. These precursor compounds can be found in foods such as pomegranate, raspberries and walnuts [283, 284]. UA has generated excitement over its observed beneficial effects *in vitro* and in animal and human *in vivo* studies, and ability to improve mitochondrial health through mitophagy induction (Figure 1.2). Studies in rodents and *Caenorhabditis elegans* have observed increased longevity and mitophagy with UA treatment

[285]. In an Alzheimer's disease (AD) transgenic mouse model UA was shown to increase lysosomal function, improve learning, memory, and olfactory function, increase lifespan and reduce levels of β-amyloid and tau [286, 287]. Clearance of these commonly misfolded proteins that cluster in the central nervous system during AD was mediated by UA induced cathepsin normalisation and thus, increased lysosomal function [286, 287]. In a D-Gal induced murine model of ageing, UA was also found to improve learning and memory, decreased NLRP3 activation and increased mitochondrial biogenesis through an increase in p53-mediated peroxisome proliferator-activated receptor gamma (PPARγ) coactivator 1-alpha (PGC1α) expression [288]. Activated p53 is also known to increase transcription factor A, mitochondrial (TFAM) mediated transcription of mitochondrial genome, resulting in increased biogenesis [289]. Interestingly, impaired autophagy in the skeletal muscle of elderly mice was shown to increase denervation and muscle weakness and its rescue prevented age-related muscle loss [63].

Human trials have demonstrated beneficial effects of UA in improving skeletal muscle function, and disease symptoms. In one human trial, adults between the ages of 65-90 given UA (1000mg/d) in the diet showed improved muscle endurance, and reduced circulating acylcarnitine, ceramides, and C-reactive protein [290]. Another study looking at UA in healthy, but overweight, middle-aged patients, observed increased mitophagy, exercise capacity and muscle strength, as measured by hamstring strength and leg flexion strength [291]. UA has been shown to decrease signalling via the protein synthesis PI3K/Akt/mTORC1 pathway by inhibiting PI3K and Akt activation [292, 293]. In tandem to this, UA activates AMPK via activation of the Sirtuin (SIRT) pathway signalling, resulting in increased mitophagy and decreased mTORC1 activation [294].

Though dysregulated autophagy in the lungs of COPD patients is known to contribute to pathogenesis [295-297], the role of autophagy in muscles during COPD is somewhat controversial. Autophagy is required for maintaining homeostasis in muscles and for allowing cells to meet their

bioenergetic demands and preventing senescence, especially in muscle satellite cells [298] which are required for myogenesis [299]. The controversial role of autophagy in skeletal muscle of COPD patients stems from studies that showed both impaired [80] and upregulated [300]autophagy can drive atrophy. Studies looking at COPD patient skeletal muscle found markers of autophagy and increased autophagosome quantity inversely correlated with FEV1 [80] and that autophagosome numbers were increased only in cachectic COPD patients [81]. COPD patients with increased skeletal muscle autophagosome numbers also showed an associated increase in AMPK activity, FoxO transcription factors and inhibition of the Akt/mTORC1 pathway [80], suggesting autophagy coincides with an increase in protein degradation and simultaneous decrease in synthesis. However, impaired autophagy/mitophagy in COPD has been suggested as a driving factor in skeletal muscle dysfunction in COPD and improvements to autophagy could ameliorate muscle weakness and cachexia [301]. For example, in the aforementioned study of an IL-13^{TG} murine emphysema model, impaired autophagy in muscle satellite cells resulted in reduced myogenic and replicative capacity and resulted in increased muscle atrophy and contractile dysfunction [122]. This suggests that increased autophagy, although correlative with cachectic COPD, may not be a driving factor and could be important for maintaining muscle health and mass.

Despite decreasing signalling through the protein synthesis pathway, and evidence of AMPK upregulation which is correlated with cachexia in COPD, UA has demonstrated safe supplementation, improved muscle health, muscle function, decreased inflammation, increased mitophagy and reduced disease burden across a range of studies, with no reports of induced muscle atrophy. By improving mitochondrial health there should also be a decrease in cGAS-STING mediated inflammation/cachexia. This highlights the potential therapeutic benefit of improving mitochondrial health as a method of targeting cachexia.

1.8 Thesis Hypothesis and Aims

Hypothesis

Skeletal muscle mitochondrial dysfunction and inflammation contribute to cachexia in pulmonary disease. Inflammation is partially mediated by mitochondrial dysfunction and subsequent release of mtDNA into the cytosol where it activates cGAS-STING signalling. Activation of this pathway results in autocrine cytokine signalling which activates NF-κB mediated transcription of atrogenes and the UPS. Furthermore, STING activation of TBK1 causes TBK1 mediated inhibition of mTORC1, preventing protein synthesis. Thus, improving mitochondrial function through inducing mitophagy, or inhibition of the cGAS-STING signalling pathway will attenuate cachexia in pulmonary diseases (Figure1.3).

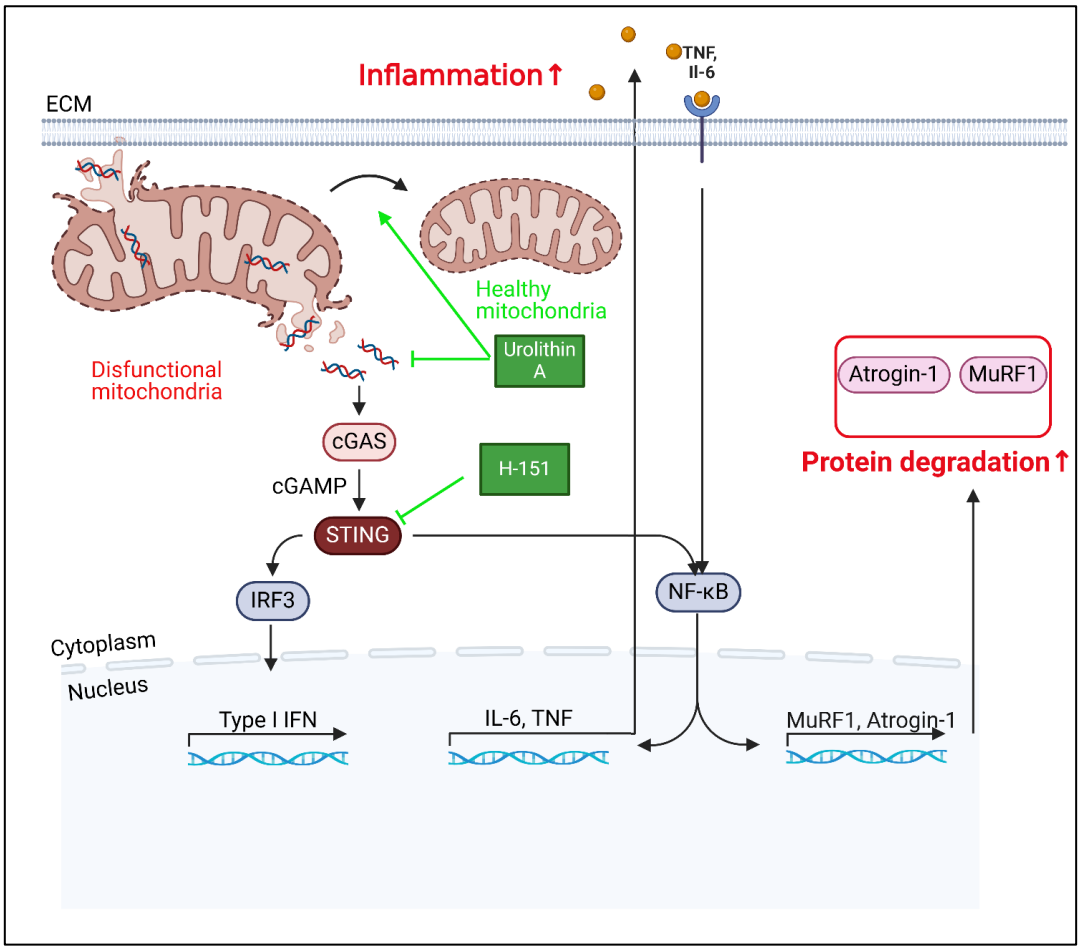

Figure 1.1 Hypothesis of H-151 and Urolithin A mediated prevention of mitochondrial dysfunction-induced protein degradation in skeletal muscle.

Mitochondrial dysfunction results in the release of mtDNA into the cytosol, where it can bind cGAS and induce cGAS-STING mediated inflammation. This gives rise to the transcription of factors of protein degradation like Atrogin-1 and MuRF1. Urolithin A attenuates mitochondrial dysfunction through increased mitophagy, thus preventing mtDNA leak into the cytoplasm. H-151 is a small molecule inhibitor of STING which prevents STING functions. Image made using BioRender

Aims

Provided below are the primary aims of this thesis:

1. To assess the prevalence of muscle atrophy across different experimental murine models of IPF, asthma, and COPD, and to identify the most suitable model for therapeutic studies targeting cachexia in a pulmonary disease.

2. To elucidate the effects of experimental IPF, asthma and COPD models on mediators of protein degradation and synthesis in skeletal muscle.

3. To compare skeletal muscle atrophy observed in experimental COPD models with that in human COPD and appropriately target overlapping mechanisms of disease.

4. To investigate the effects of STING inhibition on skeletal muscle protein degradation, synthesis, and mitochondrial respiration in experimental COPD.

5. To evaluate the impact of Urolithin A treatment on inflammation, skeletal muscle protein degradation, synthesis, and mitochondrial respiration in young and adult mice within the context of experimental COPD.

Chapter 2 Materials and Methods

2.1 Animals

Wild type (WT) female BALB/c and male and female C57BL/6 mice used in the mouse models of COPD and IPF were purchased from Australian BioResources (ABR) (Moss Vale, NSW, Australia). Aged female C57BL/6 mice (dob: 23/05/2023, purchased at ~6mo) were purchased from the OzGene-Animal Resource Centre (ARC) (Canning Vale, WA, Australia). Mice were kept in cages of 4 mice/cage, housed with a 12-hour light/dark cycle and allowed water and standard mouse chow *ad libitum.* Biological replicates ranged (n=6-8) depending on the model and number of mice available. This was based on previously published studies using these experimental mouse models of COPD, IPF and asthma from my lab and externally. [111, 169, 302].

2.2 Murine models of CS-induced COPD

C57BL/6 mice (n=8) were exposed to 12 cigarettes (3R4F reference cigarettes from the University of Kentucky, Lexington, KY, USA) twice/d, 5 d/w, for 2-12 weeks using a custom-built nose-only exposure system (CH Technologies, NJ, USA). This system was kept in a fume cupboard to avoid second-hand CS exposure. Each cigarette was fitted to the pump, lit using a heat lamp and burned for approximately 4-5 minutes. During this, the exposure system would pump smoke through to the mice 12 times (12 puffs). Each smoking session lasted approximately 45m, after which the mice were monitored for signs of stress or abnormalities for a minimum of 30m. Mice were returned to their racks only if no abnormalities were detected during the monitoring period. This was approved by our institutional animal ethics committee. Details for this experimental murine model of COPD have been previously published by my lab [111, 119]

CS-induced experimental COPD time course model (2, 4, 6, 8 and 12w; Figure 2.1): This model had 5 groups of female C57BL/6 mice that were either CS or room air exposed for 2, 4, 6, 8, 10 and 12w

(Figure 2.1; n=8 for each exposure condition). Exposures began when the mice were 8w old so mice from different groups were not age matched at endpoint. Therefore, each time point was a snapshot of the effects of exposure at that specific age. i.e. mice from the 2w time point were 10w old, mice from the 4w time point were 12w old etc.

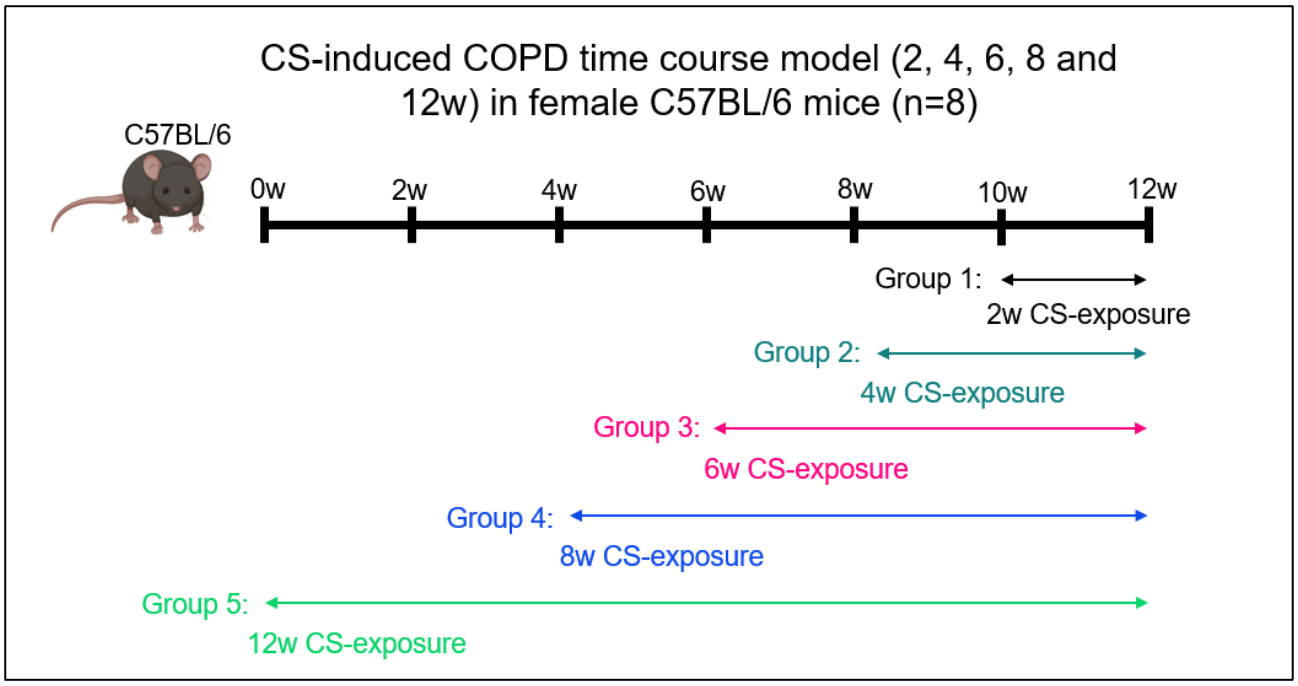

Figure 2.1 Overview of CS-induced COPD murine model in female mice at 5 timepoints

Female C57BL/6 mice (n=8) began CS-exposure at 8w old, and were exposed for 2, 4, 6, 8 or 12w. Each timepoint reflects the amount of time post the commencement of CS-exposure and the different timepoints were not age-matched at their endpoints.

CS-induced experimental COPD time course model (3, 8 and 12w) in male and female mice (Figure 2.2): This model had 3 groups of male and female C57BL/6 mice that were either CS or room air exposed for 3, 8, and 12w (Figure 2.2; n=8 for each condition). Mice from the 3, 8 and 12w time points began exposures at 17, 12 and 8w old, respectively. Thus, mice were the same age at endpoint.

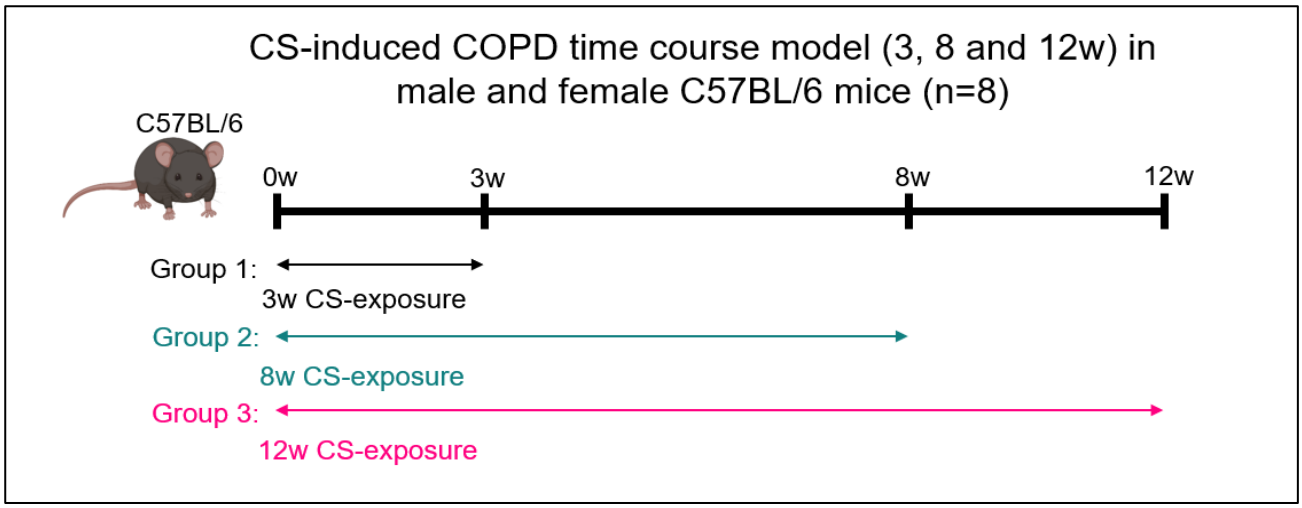

Figure 2.2 Overview of CS-induced COPD murine model in male and female mice at 3 timepoints

C57BL/6 mice (n=8) began CS-exposure at 8w.o., and were exposed for 3w, 8w or 12w. Each timepoint describes the amount of time post the start of either room air or CS-exposure and the different timepoints were not age-matched at their endpoints.

2.3 Murine models of IPF

4w and 10w bleomycin-induced experimental IPF model (Figure 2.3): C57BL/6 mice (n=10) were given a single i.n. dose of bleomycin sulphate (Bio-strategy; CAS 9041-93-4) to induce fibrosis and control mice were given i.n. dose of phosphate buffered saline (PBS). Bleomycin was dissolved in 1X PBS and given at a dose of 0.05U/mouse. Timepoints of 4 and 10w post-bleomycin were investigated. The model began when the mice were 8 weeks old.

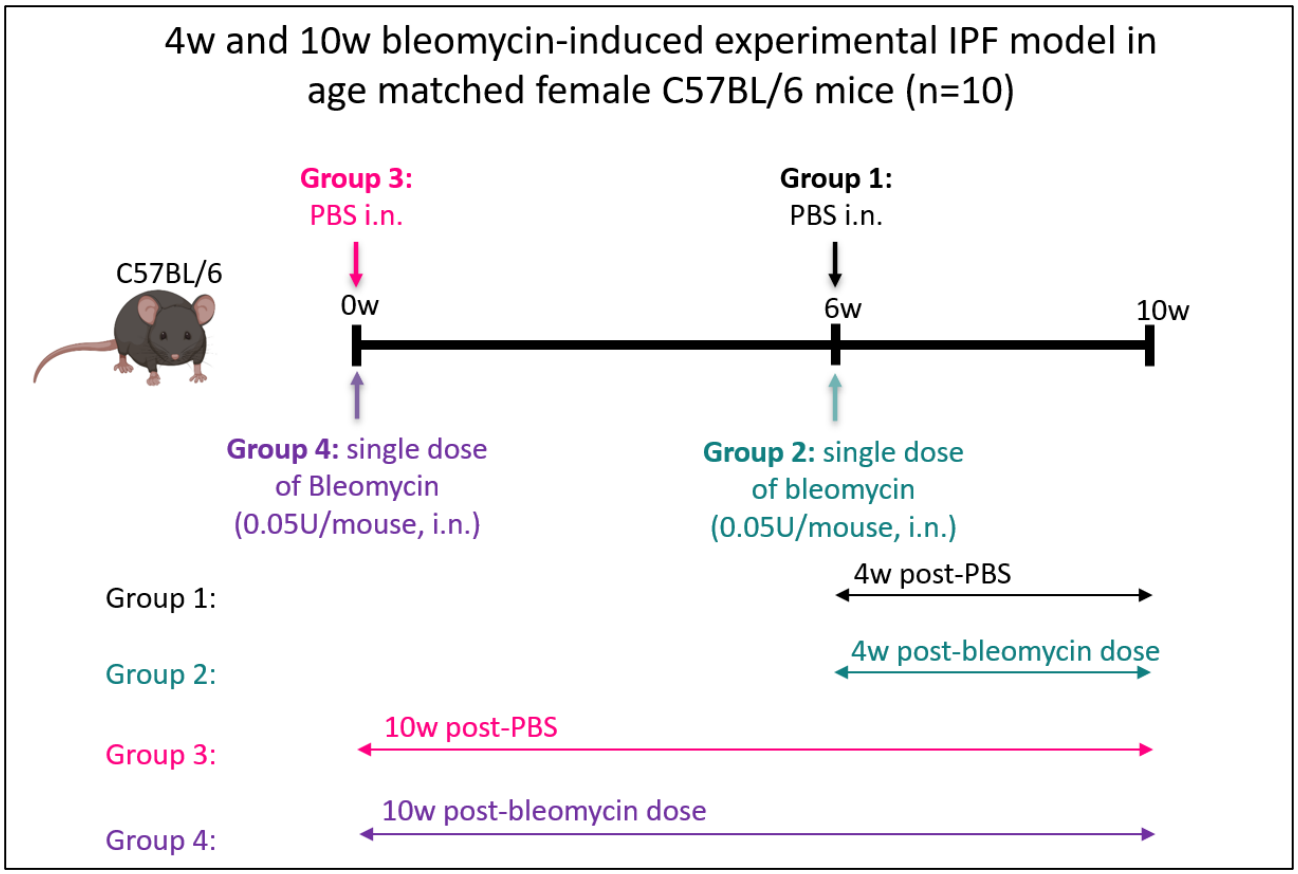

Figure 2.3 Overview of a single dose i.n. bleomycin-induced 4w and 10w IPF time course murine model

C57BL/6 mice (n=8) were given a single dose i.n. bleomycin or PBS at different time points over a 10w period, to produce two cohorts of a 4w and 10w age matched IPF model. At the start of week 0, groups 3 and 4 were given a single dose of bleomycin or PBS respectively and sacrificed at the end of week 10. At the 6-week timepoint, groups 1 and 2 were given a single dose of bleomycin or PBS respectively and sacrificed at the end of 10w.

Bleomycin and CS induced experimental IPF model (Figure 2.4): 8-week-old C57BL/6 mice (n=8) were CS or room air exposed for 8 weeks. Mice were given a single i.n. dose of either bleomycin or PBS after 4w of CS exposure. The model ended after 8w of total CS exposure (4w after single dose of i.n. bleomycin)

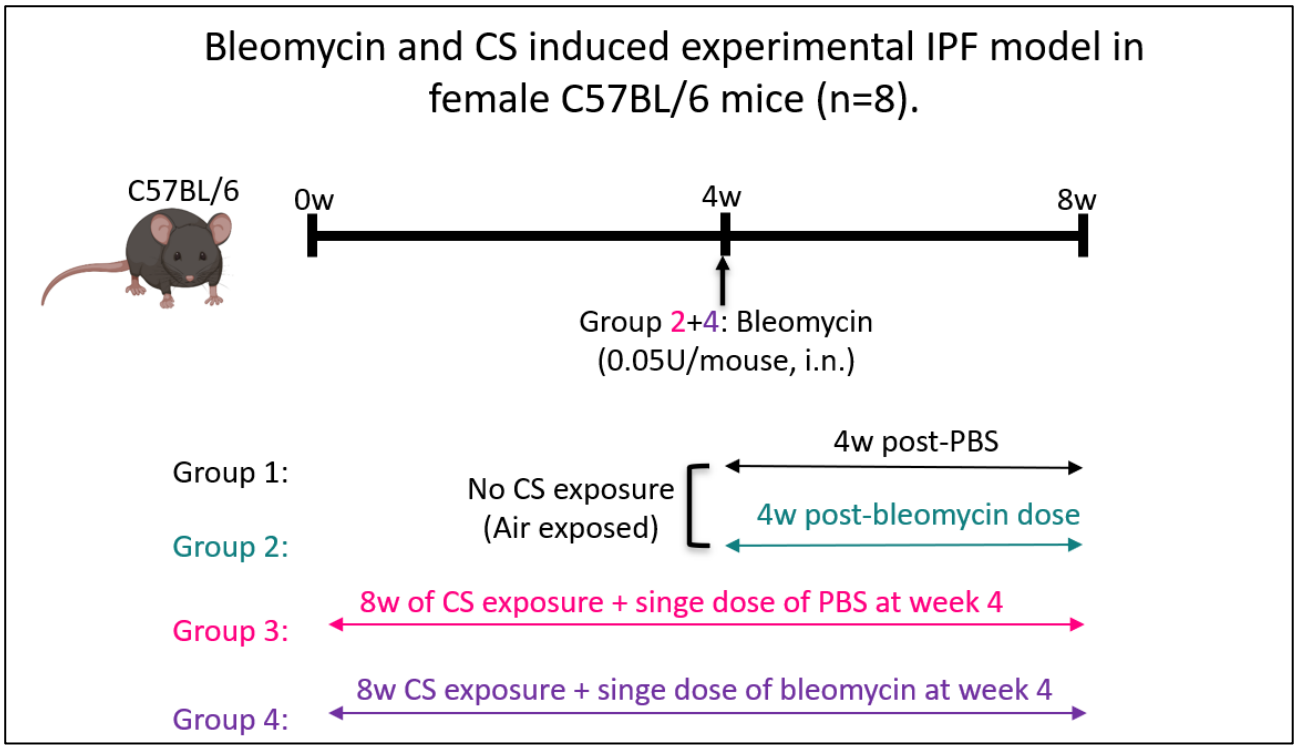

Figure 2.4 Overview of an 8w single dose i.n. bleomycin and CS-induced IPF murine model

Four groups of C57BL/6 mice (n=8) were exposed to CS or room air for 8w and administered either a single dose of bleomycin or PBS at the 4w time point. Groups 1 and 2 were not exposed to CS smoke but were challenged with a single dose of PBS or bleomycin respectively 4w into the model. Groups 3 and 4 were exposed to CS for 8w and were challenged with a single dose of PBS or bleomycin, respectively, 4w into the model.

2.4 Mouse model of moderate and severe asthma

Moderate (steroid sensitive) asthma (Figure 2.5): BALB/c mice (n=8) were ovalbumin (Albumin from chicken egg white lyophilized powder ≥ 98%; Sigma-Aldrich, Cat: A5503-10G) sensitised at day 0 and re-challenged with ovalbumin day 12&13 and day 33 and 34 (Figure 2.5). Ovalbumin sensitisation (or immunisation) of mice was done with a 200µL i.p. injection of a solution of ovalbumin (5µL of 10mg/mL stock) and Aluminium hydroxide gel (aka Alum) (26µL of Alhydrogel® adjuvant 2%; InVivogen, Cat: Vac-Alu-250) made up in PBS (169µL). The total dose of i.p. administered ovalbumin was therefore 50µg. I.n. Ovalbumin challenge was carried out twice over

two days (days 13-14 and 33-34) with a 20µg i.n. dose of ovalbumin made up in PBS. Non-ovalbumin immunised mice were still given an i.p. injection of Alum solution (26uL of Alhydrogel® adjuvant 2% in 174µL of PBS) and given i.n. saline on days 13-14 and 33-34. Details relating to these experimental models of asthma have been published by my lab [128, 148, 262, 302].

Severe (steroid insensitive) asthma (Figure 2.5): BALB/c mice (n=8) underwent the same protocols as for the moderate asthma model. However, the severe asthma, received an i.n. *chlamydia muridarum* (CMU; ATCCVR-123 strain) induced respiratory infection with 100 inclusion-forming units (IFU) was carried out at day 14 to induce severe asthma in the severe asthma model. Sham infected mice were given i.n. sucrose phosphate glutamate (SPG). Steroid sensitivity was determined by lung function analysis. Titration with increasing doses (0.3, 1, 1.5, 3, 5, 10mg/mL in PBS) of methacholine (Acetyl-β-methylcholine chloride; Sigma-Aldrich) induces AHR, which is increased in ovalbumin sensitised mice.

Dexamethasone (Dexamethasone water soluble; Sigma-Aldrich CatD2915-100MG) treatment reduces AHR in steroid sensitive asthma but not in steroid insensitive asthma. A 2mg/kg i.n. dose of dexamethasone was used in combination with the final ovalbumin i.n. to remove the need for two i.n. procedures [128, 148, 262, 302].

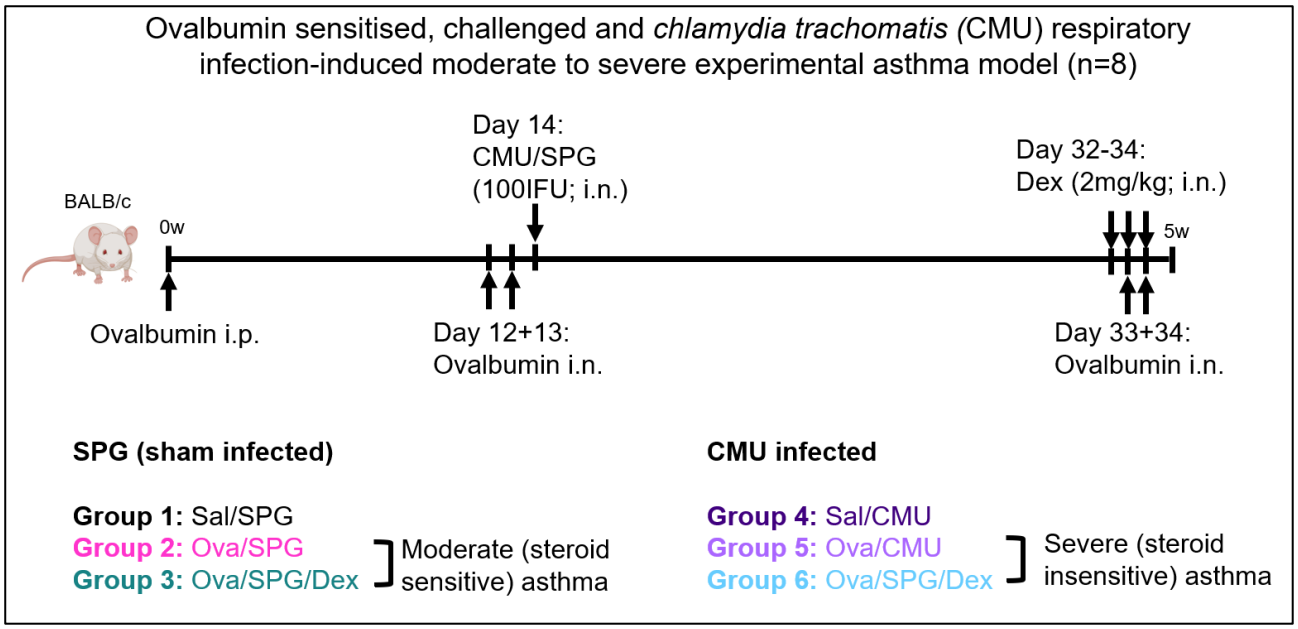

Figure 2.5 Overview of a model of moderate (steroid sensitive) and severe (steroid insensitive) asthma

Six groups of BALB/c mice (n=8) were used in an experimental model of moderate and severe asthma. **Moderate (steroid sensitive) asthma:** Groups 1-3 were sham infected with sucrose phosphate glutamate (SPG) on day 14. Group 1 was given a single i.p. of saline. Groups 2 and 3 were sensitised (Day 0) and challenged with ovalbumin (Day 12+13; Day 33+34). **Severe (steroid insensitive) asthma:** Groups 4-6 were given a *chlamydia muridarum* (CMU) respiratory infection. Group 4 was given a single i.p. of saline. Groups 5 and 6 were sensitised (Day 0) and challenged with ovalbumin (Day 12+13; Day 33+34). Group 3 and 6 were treated with dexamethasone (Dex) to assess steroid sensitivity during lung function assessment.

2.5 Lung Function Assessment by Invasive Plethysmography

Mice were weighed and given three separate doses of an anaesthetic ketamine (Ilium Ketamil; TROY Laboratories Pty Ltd) and xylazine (Ilium Xylazil-20; TROY Laboratories Pty Ltd) via intraperitoneal (I.P.) injection based on their weight. The first anaesthetic mix (ketamine 13mg/ml; xylazine 1.6mg/ml) was given immediately after weighing the mouse and was proportional to the weight (e.g. a standard 20g mouse receives 200ul). Once the mouse was anesthetised, the N-A (nose-to-anus) length was measured with a 30cm ruler, and the mouse on its back. The second anaesthetic

mix (ketamine 40mg/ml; xylazine 2mg/ml), typically half the volume of the first, was given once the mouse was stationary. This was to ensure the mouse was completely anaesthetized for the procedure and unable to feel anything. Loss of feeling was confirmed by pedal reflex, whisker movement (to touch) and palpebral reflex (to touch). Following this, a tracheostomy was performed and a custom blunted canula was inserted into the trachea. This was tied into place to ensure a tight seal for plethysmography assessments, and the canula was attached to the FlexiVent system adapter module. A third anaesthetic mix (xylazine 2mg/ml) was given to prevent the use of the ventilatory muscles of the mouse which may operate automatically while the mouse is unconscious. *in vivo* measurement of respiratory mechanics was carried out using a Scireq Flexivent system (Scireq, QC, Canada). This device contains a piston that breathes on behalf of the mouse (at a rate of 450 breaths/minute, 8ml/kg tidal volume) and conducts several manually prompted tests that give structural and functional data on the mouse lungs. The doses of anaesthetic are lethal within approximately 20 minutes after the second anaesthetic mix and the degassing step of the total lung capacity (TLC) test includes 5 minutes without oxygen, resulting in the death of the mouse at this stage.

Anaesthetic mix	Dosage (made up in PBS)	Volume of dose/20g mouse
1	ketamine 13mg/ml; xylazine 1.6mg/ml	200µL
2	ketamine 40mg/ml; xylazine 2mg/ml	100µL
3	xylazine 2mg/ml	50µL

Table 2.1 Lung function - Anaesthetic mixes and concentrations of ketamine and xylazine (in PBS)

Lung function	Measurement name	Description of output
Inspiratory capacity (IC)	Deep inflation-35	The amount of air inhaled after a normal exhalation
Hysteresis	PVs-P-35 (Area). Area enclosed by the pressure-volume loop	Indicates work done to inflate and deflate the lungs i.e. to overcome surface tension and compliance dynamics.
Forced vital capacity (FVC); forced expiratory volumes (FEVx).	Negative pressure forced expiration (NPFE)	The total volume of air forcibly exhaled over a period of time.
Resistance of the central airways	QuickPrime-3 (Rn)	Bronchoconstriction
Resistance of the whole respiratory system (central & peripheral airways)	Snapshot-150 (Rrs)	Whole Lung constriction
Total lung capacity (TLC)	TLC	Largest possible volume of air the lungs can take in.
Elastic properties without airflow	Static compliance (Cst)	Distensibility of the main elastic components of the lungs and chest walls.
Elastic properties during airflow	Dynamic compliance (Crs)	Distensibility of the entire respiratory system (lungs, chest walls and airways)

Table 2.2: Lung function - Description of the output of lung function measurements/techniques using a SCIREQ Flexivent.

Source: https://www.scireq.com/flexivent/techniques-measurements/

2.6 Tissue Collection

Following lung function testing, the diaphragm and rib cage were removed. Blood was collected from the left ventricle of the heart and centrifuged in EDTA coated tubes to isolate plasma. Prior to BALF collection the right lung was tied off to prevent flushing of the buffer into these lobes during BALF collection procedure, retaining the immune cell infiltrate. BALF was collected by flushing the left lung 10 times gently with a total of 1mL of Hank's Balanced Salt Solution (HBSS; ThermoFisher). The superior, middle, inferior and post-caval lobe of the right lung were removed individually and snap frozen in liquid nitrogen (LN). The left lung was then perfused by flushing 0.9% saline solution through the left heart ventricle using a 19G needle attached to a 5ml syringe. The perfused lung was then inflated with 0.4ml of neutral buffered formalin (12.5%) and collected in a 5ml tube filled with formalin. The quadriceps, gastrocnemius, soleus, and extensor digitorum longus (EDL) were collected from the hind legs and weighed separately, approximately 10-20m *post-mortem*. Muscles were gathered from both legs; half were snap frozen in LN and the other prepared for histology. Muscles collected for embedding in O.C.T. for this model were pinned to a piece of cork and slow frozen in isopentane that was precipitating in LN, then transferred into LN. Other muscles were fixed in neutral buffered formalin (12.5%). The tibia and femur length were also measured.

2.7 Histology

Muscle tissues fixed in formalin were transferred to 30% sucrose solution after at least 2 days and stored at 4^{o}C. After the muscles had sunk in solution they were embedded in Tissue-Tek® Optimal Cutting Temperature (O.C.T.) compound. Muscles were individually embedded in a Tissue-Tek® Cryomold using Tissue-Tek® O.C.T. compound on dry ice. Muscles that were not cryo-sectioned were not transferred into 30% sucrose solution but into 70% ethanol and later embedded in

paraffin. Muscles were orientated upright to get trans-sections for muscle fibre area (MFA) analysis. Cryo-sectioning was done using a Leica CM1950 at -20^{o}C. Hematoxylin and Eosin (H&E) staining of muscle tissue was carried out using a Leica ST5010 Autostainer XL. A Zeiss Axio Imager.M2 microscope was used to image muscle slices at 20X magnification. Using (Fiji Is Just) ImageJ 1.54f, ≥100 fibres/sample were outlined with the drawing tool, with the scale at 4.3478pixels/µm.

2.8 RNA extraction from muscle tissue

Large muscle tissues (gastrocnemius, quadriceps) were crushed into a fine powder using a Cellcrusher or a Cellcrusher-mini for smaller muscle tissues (soleus, EDL) over dry ice. An aliquot of fine powdered muscle was transferred to a Safe-Lock Eppendorf tube containing a 5mm stainless steel bead (Qiagen). 1ml of TRIzol (Invitrogen) was added to the tube and the tube was placed in a TissueLyser LT (Qiagen) at 50Hz for 3 minutes. A standard phase separation protocol was then followed, and RNA was precipitated. RNA was resuspended in 60µL of water and concentration was calculated using a NanoDrop One Microvolume UV-Vis Spectrophotometer (ThermoFisher). RNA concentrations were normalized to the lowest RNA concentration of the samples and stored at -80^{o}C.

2.9 Reverse transcription (RT) and real time-qPCR

RNA samples were prepared for reverse transcription using the High-Capacity cDNA Reverse Transcription Kit (Applied Biosystems™). Samples were added to a T100 Thermal Cycler (Bio-Rad) which followed the program in Table 1. After the RT program ends, the cDNA was removed from the thermal cycler and 80µL of dH2O was added to each sample. A master mix was made containing nuclease-free dH2O, the forward and reverse primer for the gene of interest, and KAPA SYBR® FAST

(Table 2). This was added to the wells of a hard shell 384-well PCR plate along with cDNA. The plate was then sealed using a Microseal® 'B' seal (Bio-Rad), centrifuged using a PlateFuge (Benchmark Scientific) and placed in a CFX384™ Real-time system. The program for RT-qPCR is shown in Table 3. The target genes investigated by RT-qPCR and their respective forward and reverse primer sequences are listed in Table 4

	Stage 1	Stage 2	Stage 3	Stage 4
Temperature	25°C	37°C	85°C	4°C
Time	10 minutes	2 hours	5 minutes	∞

Table 2.3 T100 Thermal cycler program for reverse transcription.

Reagent	Volume per sample (µL)
Kapa SYBR	6.25
Forward Primer (5uM)	0.5
Reverse Primer (5uM)	0.5
Nuclease-free dH2O	3.25
cDNA	2
Total Volume per well	12.5

Table 2.4 384-well plate volumes of reagents used per well for RT-qPCR.

	Holding stage		Cycling stage (45X)		Melt-Curve stage			
Temperature (°C)	50	95	95	60	95	60	92	60
Time (seconds)	2	2	3	30	15	60-95	15	15

Table 2.5 CFX384TM Real-time system program for RT-qPCR.

Target Gene	Forward Sequence	Reverse Sequence
HPRT	AGGCCAGACTTTGTTGGATTTGAA	CAACTTGCGCTCATCTTAGGCTTT
ACTB	GGAGAAAATCTGGCACCACA	AGAGGCGTACAGGGATAGCA
IL6	AGAAAACAATCTGAAACTTCCAGAGAT	GAAGACCAGAGGAAATTTTCAATAGG
IFNG	TCTTGAAAGACAATCAGGCCATCA	GAATCAGCAGCGACTCCTTTTCC
IL1B	TGGGATCCTCTCCAGCCAAGC	AGCCCTTCATCTTTTGGGGTCCG
KC	GCTGGGATTCACCTCAAGAA	CTTGGGGACACCTTTTAGCA
TNF	TCTGTCTACTGAACTTCGGGGTGA	TTGTCTTTGAGATCCATGCCGTT
FBXO32 (MAFbx/Atrogin-1)	CTTTCAACAGACTGGACTTCTCGA	CAGCTCCAACAGCCTTACTACGT
TRIM63 (MuRF1)	GCTGGTGGAAAACATCATTGACAT	CATCGGGTGGCTGCCTTT
HDAC4	GTCTTGGGAATGTACGACGC	GTTGCCAGAGCTGCTATTTG
GADD45	AGTCAGCGCACCATTACG	TGAGGGTGAAATGGATCTGC
CHRNA1	CCAACCTCATCTCCCTGAATG	CAAGTTGATCTCACTGGTGCTG

Table 2.6 List of RT-qPCR primers with their forward and reverse sequences.

2.10 Immunoblotting (Western Blotting)

2.10.1 Tissue preparation

Quadriceps were powdered using a Cellcrusher over dry ice, and ~20mg was aliquoted into Axygen® 2.0mL Conical Screw Cap microcentrifuge tubes complete DAP lysis buffer (cOmplete™ protease inhibitor cocktail (PIC) + cOmplete™ protease inhibitor tablet). Tissue was homogenised using a Precellys® Evolution Touch tissue homogenizer (Speed: 7600RPM; Cycle 2x30s; Pause 15s). Tissue homogenate was then centrifuged at 14,800RPM for 20m at 4°C and the supernatant

aliquoted into fresh tubes. Protein quantification was carried out using a BIO-RAD DC™ protein assay kit, using a BSA standard curve (2mg/ml; 1:2 serial diluted). and absorbance values (750nm) were read using a BMG FLUOstar Omega microplate reader. Samples were then normalised in DAP lysis buffer and 4X Laemlli buffer (BIO-RAD) supplemented with dimethyl sulphoxide (DMSO). Samples were stored at -80°C.

2.10.2 Protein separation by electrophoresis and membrane transfer.

For protein separation by gel electrophoresis, a 15 lane, BIO-RAD mini-PROTEAN TGX Stain Free-Precast gel was inserted into a BIO-RAD Mini-PROTEAN Tetra Vertical Electrophoresis Cell, and the cell was filled with 1X Running Buffer. 12.5 µg of protein in loading buffer was loaded/well, with a BIO-RAD Precision Plus Protein Dual Colour Standard and A549 cell line derived loading control in separate wells. The gel was run at a constant 110V for ~1h using a PowerPac™ High-Current Power Supply.

A transfer sandwich was prepared during the electrophoresis step, with filter paper and nitrocellulose membrane soaking in 1X transfer buffer (4°C). Once the sandwich was prepared and the run finished, the gel was placed on filter paper in the sandwich and the membrane laid over it with filter paper on top. Bubbles were removed using a small roller. The sandwich was closed tight and placed in a BIO-RAD Criterion™ Blotter, being careful to line up the blot with the cathode and the gel on the anode side. The transfer was then run at 100V for 1h10m (wet transfer).

2.10.3 Ponceau imaging and antibody incubation.

After transferring, the blot is removed and kept in MilliQ water until ready. Ponceau S stain was added to the blot and imaged using a BIO-RAD ChemiDoc MP Imaging System (white light/colourimetric image. Ponceau S stain images were later used for densitometry protein normalisation. Membranes were then cut at specific bands if needed, and the membrane was

washed 3X with Tris-buffered saline-Tween20 (TBS-T). Blocking with 3% BSA (for phosphorylated protein blots) or 3% milk made up in TBS-T 1h was then carried out for 1h at room temperature. Blots were then washed 3X with TBS-T and incubated with primary antibody in TBS-T overnight at 4^{o}C. The next day, the primary antibody was removed (and stored at -20^{o}C) and the membrane was washed 3X with TBS-T. The membrane was incubated with HRP-conjugated (primary specific) secondary antibody for 1h at room temperature, after which it was washed 3X with TBS-T.

2.10.4 Imaging and densitometry

Chemiluminescent Substrate was added to the membrane and immediately placed in the BIO-RAD ChemiDoc MP Imaging System for imaging. A colourimetric image was taken and then band intensity was captured using rapid-acquisition mode. Custom acquisition settings were used based on the rapid-acquisition result. Images were downloaded as Image Lab Image Document files and band intensity relative to total protein was calculated in BIO-RAD Image Lab software (V6.1) and Microsoft Excel.

2.10.5 Immunoblot Buffers

Buffer	Final concentration	1L buffer	
10X (Tris-buffered saline) TBS pH7.6	Tris Base (0.2M)	24g	Make up to volume with MilliQ water
	NaCl (1.5M)	88g	
1X TBS-T	Tween-20 (0.05%)	100mL TBS + 0.5mL Tween-20	
10X Running Buffer	Tris Base (0.25 Molar; 121.14 mw)	30.29g	
	Glycine (1.92M; 75.07mw)	144g	
	1% SDS (20% SDS stock)	50mL	
10X Transfer Buffer	Tris Base (0.25 Molar; 121.14 mw)	30.29g	
	Glycine (1.92M; 75.07mw)	144g	
1X Transfer Buffer	Methanol	100mL TBS + 200ml methanol	

Table 2.7 Buffers used in western blotting (immunoblotting)

2.10.6 Primary Antibodies

Signalling Pathway	Antibody name	Dilution factor	Mw (kDa)	Species origin	Company	Category #
mTOR signalling	mTOR Antibody #2972	1000	289	Rabbit	Cell Signalling	2972
	Akt Antibody #9272	1000	60	Rabbit	Cell Signalling	9272
	Phospho-Akt (Ser473) Antibody #9271	1000	60	Rabbit	Cell Signalling	9271
	Phospho-Akt (Thr308) Antibody #9275	1000	60	Rabbit	Cell Signalling	9275
	4E-BP1 (53H11) Rabbit mAb #9644	1000	15-20	Rabbit	Cell Signalling	9644
	Phospho-4E-BP1 (Thr37/46) (236B4) Rabbit mAb #2855	1000	15-20	Rabbit	Cell Signalling	2855
	p70 S6 Kinase Antibody #9202	1000	70, 85	Rabbit	Cell Signalling	9202
	Phospho-p70 S6 Kinase (Thr389) Antibody #9205	1000	70, 85	Rabbit	Cell Signalling	9205
	S6 Ribosomal Protein (5G10) Rabbit mAb #2217	1000	32	Rabbit	Cell Signalling	2217
	Phospho-S6 Ribosomal Protein (Ser240/244) Antibody #2215	1000	32	Rabbit	Cell Signalling	2215
cGAS-STING signalling	cGAS (D3O8O) Rabbit mAb #31659	1000	62	Rabbit	Cell Signalling	31659
	STING (D1V5L) Rabbit mAb #50494	1000	33, 35	Rabbit	Cell Signalling	50494
Atrophy	MuRF1 Polyclonal Antibody (TRIM63)	1000	40	Rabbit	Thermo Fisher	PA5-76695
	MAFbx Polyclonal Antibody (FBXO32)/Atrogin-1	1000	42	Rabbit	Thermo Fisher	PA5-91959
	GADD45 alpha (D17E8) Rabbit mAb #4632	1000	22	Rabbit	Cell Signalling	4632
ETC	Total OXPHOS Rodent WB Antibody Cocktail (CI subunit NDUFB8 (ab110242), CII-30kDa (ab14714), CIII-Core protein 2 (ab14745), CIV subunit I (ab14705) and CV alpha subunit (ab14748)). + Positive control	500	15-55	Mouse	Abcam	ab110413

Table 2.8 Primary antibodies used in western blotting with dilution factor (DIF), species origin, company name and category number.

Expected molecular weight (Mw; kDa) on blotting membrane as outlined by the manufacturer website with link to the manufacturer website.

2.10.7 Secondary antibodies

Secondary antibody	Isotype	Conjugate	DIF	Company name	Category#
Goat anti-rabbit #ab205718	IgG	HRP	10000	Abcam	ab205719
Goat anti-rabbit #ab205719	IgG	HRP	10000	Abcam	ab205718

Table 2.9 Secondary antibodies used in western blotting with dilution factor (DIF), isotype and conjugate, company name and category number.

2.11 Skeletal muscle mitochondrial respiration – Oroboros Oxygraph-2k

A fresh segment of gastrocnemius tissue (~20mg) was prepped and stored in BIOPS buffer (5.77 mM Na2ATP, 2.77 mM CaK2EGTA, 7.23 mM K2EGTA, 15 mM Na2Phosphocreatine, 6.56 mM MgCl2-6H2O, 20 mM taurine, 20 mM imidazole, 0.5 mM dithiothreitol, 50 mM MES hydrate, pH= 7.1) at 4^{o}C (on ice). This sample was broken up using a tweezers and approximately 5mg of tissue was added to 2 mL of BIOPS buffer with 50 µg/µL of saponin. Saponin permeabilises the sarcolemma (myofiber cell membrane) and allows mitochondrial to access substrates. an Oroborus Oxygraph-2k chamber. After equilibrating by rocking gently for 15 minutes at 4^{o}C, fibres were then placed in 2 mL of MiRO5 buffer (0.5 mM EGTA, 3 mM MgCl2-6H2O, 60 mM lactobionic acid, 20 mM taurine, 10 mM KH2PO4, 20 mM HEPES, 110 mM D-sucrose, 1 g/l BSA, pH=7.1) and rocked for a further 15 minutes at 4^{o}C. Afterwards, tissues were placed in 1mL of MiRO5 to prevent further saponin activity. Muscle fibres were placed on filter paper to remove excess liquid, weighed (~2.5mg-5mg is needed for skeletal muscle) and then put back in MiRO5 buffer before respirometry.

2mL of MiRO5 buffer (25µM Blebistatin) was aliquoted into each chamber in an Oroboros oxygraph-2k high resolution respirometer (Oroboros instruments, Austria). Blebistatin prevents

muscle contraction during ADP titration The chambers were heated up to 37^{o}C and oxygen concentration was kept between 150-220 µM throughout the tests. Muscle fibres were then added, and the system was allowed to stabilise before any addition of substrates.

Pyruvate (10mM) and malate (2mM) was added in the absence of adenosine diphosphate (ADP) to induce complex I mediated proton leak (CI-Leak) and was measured through baseline oxygen consumption rate (pmol.sec^{-1}.mg^{-1}) at 37^{o}C. ADP (2.5mM) was then added to couple Complex I respiration to ATP production (CI-P). The oxygen flux was allowed to stabilise before beginning the ADP titration which measures ADP sensitivity. 0.1M, 0.175M, 0.5M and 6M, followed by the addition of 10 mM glutamate. Succinate (10mM) was then added to assess the combined complex I&II driven ADP phosphorylation (ATP production; CI&II). As a way of restoring/measuring outer mitochondrial membrane (OMM) integrity 10 µM of cytochrome C was added and respiration measured. Respiration levels within 10% of those seen after the addition of succinate was seen as acceptable for further analysis, as an intact OMM is required for accurate measurement of the maximally uncoupled oxygen consumption rate. Carbonyl cyanide m-chlorophenyl hydrazone (CCCP; 0.5µM) titration up to 0.5µM was used to induce maximally uncoupled respiration, and antimycin A (2.5µM) was added to stop respiration and measure base respiration.

2.12 Pathway enrichment analysis of a publicly available microarray data.

Pathway enrichment analysis was performed using the clusterProfiler package (V4.10.0) in R studio (V 2023.12.1 Build 402) on microarray data deposited in the NCBI GEO repository with Accession Number GSE100281 [303]. Differentially expressed genes were grouped into pathways based on the Reactome GMT dataset and visualised using the ggplot2 (V3.4.4) package.

Acknowledgements for chapter 3

I acknowledge the members of my lab who ran the murine models that facilitated the collection of skeletal muscle samples, reducing the need for unnecessary model repetitions. I specifically thank A'qilah Banu Clarke for conducting the bleomycin-induced pulmonary fibrosis models and providing spirometry and total leukocyte count data; Dr. Ridhima Wadhwa and Dr. Gesa Albers for running the moderate and severe asthma models and supplying lung function and leukocyte count data; and Mounika Guntipally for conducting the male and female COPD model comparison models and providing lung function and weigh sheet data.

Chapter 3 Investigating the prevalence and mechanisms of muscle atrophy in murine models of pulmonary disease

3.1 Introduction

Patients with IPF, asthma or COPD frequently develop cachexia which is often associated with a worse prognosis than non-cachectic patients [20, 304]. The aims of this chapter were to elucidate the impact of experimental murine models of IPF, asthma and COPD on skeletal muscle, establish parallels between the murine disease model and human pathology, and identify the most suitable model for future therapeutic studies targeting cachexia. The experimental pulmonary disease model was required to exhibit relevant lung function alterations, skeletal muscle atrophy, and comparable effects on skeletal muscle between the model and human patients.

This chapter examines 5 models of pulmonary diseases with different experimental conditions: Two single dose i.n. bleomycin-induced IPF models (with and without CS-exposure), a model of moderate (steroid sensitive) to severe (steroid resistant) asthma, and two models of CS-induced COPD. One COPD model was carried out in female mice of different ages at 5 time points and the other in both male and female mice of the same age at 3 time points. C57BL/6 mice were used in the COPD and IPF models, and BALB/c mice were used in the moderate to severe asthma model.

Lung function and total BALF leukocytes were used to validate lung function changes and lung inflammation associated with the pulmonary disease the model is aiming to emulate. Significant weight changes due to disease compared to control conditions over time were used to validate pathology-induced disruption to skeletal muscle heath and atrophy. Muscles from the hind legs (gastrocnemius, quadriceps, soleus and EDL) were weighed to investigate the impact of pulmonary disease on skeletal muscle mass.

A comprehensive muscle focused analysis of these models was used to elucidate the prevalence of cachexia in murine models of pulmonary disease and potential mechanisms of how muscle atrophy may occur. Risk factors associated with cachexia, including skeletal muscle inflammatory gene and atrogene expression were measured. Proteins associated with protein synthesis, degradation, and their phosphorylation states were quantified. The abundance of mitochondrial electron transport chain (ETC) complex proteins was also measured to gain an understanding of changes to mitochondrial health and function. Lastly, a pathway enrichment analysis was performed on publicly available microarray data, which used biopsies from the quadriceps of COPD and healthy patients.

These data were used to select an appropriate model of pulmonary disease-induced cachexia and to inform the therapeutic targets of follow up studies.

3.2 Lung function analysis of IPF, asthma and COPD mouse models of respiratory disease

3.2.1 Mice from a single dose bleomycin-induced experimental IPF model exhibited lung function decline after 4w but not 10w.

A single dose of i.n. bleomycin or PBS was given to C57BL/6 mice, which were then assessed for lung function changes and BALF total leukocyte induction after 4 and 10w. The mice from both time points were the same age at endpoint i.e. age matched.

There was a clear increase in total leukocytes in the BALF of mice challenged with bleomycin vs PBS after 4w but not at 10w (Figure 3.1: A). No lung function measurements were significantly augmented 10w post bleomycin challenge (Figure 3.1: B-G). IC, Crs, Cst and FVC lung function measurements were significantly decreased 4w post bleomycin exposure (Figure 3.1: B-E), but no change was observed for FEV0.05 or FEV0.1 (Figure 3.1 F+G). These data validate that our Bleo-induced pulmonary fibrosis model did induce the intended lung function changes, and the characteristic immune cell induction associated with this murine model. The 10w model showed reduced changes compared to the 4w model which may indicate that recovery occurs between 4w and 10w.

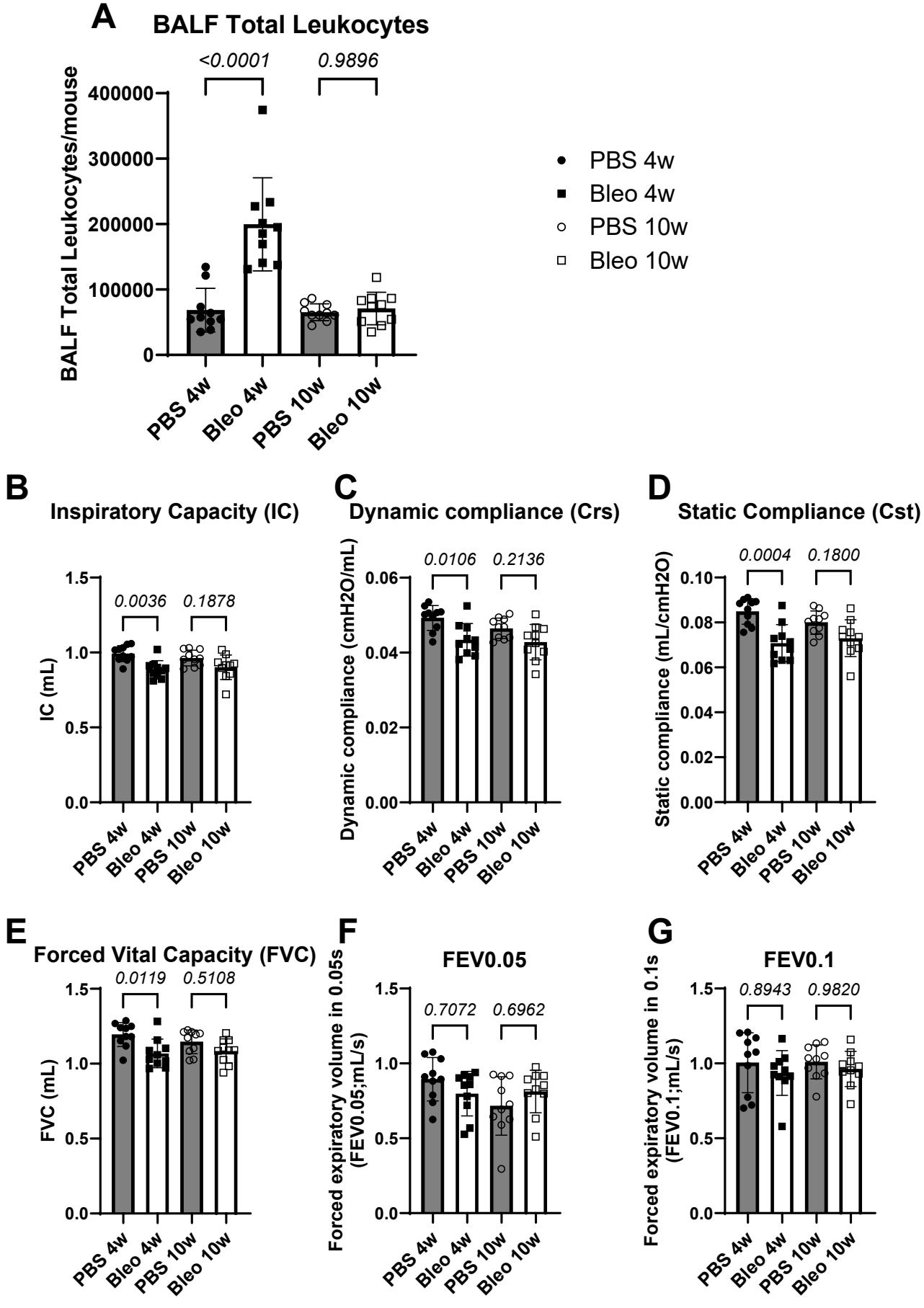
A
BALF Total Leukocytes
<0.0001
0.9896
BALF Total Leukocytes/mouse
400000
300000
200000
100000
0
PBS 4w
Bleo 4w
PBS 10w
Bleo 10w
PBS 4w
Bleo 4w
PBS 10w
Bleo 10w
B
Inspiratory Capacity (IC)
0.0036
0.1878
IC (mL)
1.5
1.0
0.5
0.0
C
Dynamic compliance (Crs)
0.0106
0.2136
Dynamic compliance (cmH2O/mL)
0.06
0.04
0.02
0.00
D
Static Compliance (Cst)
0.0004
0.1800
Static compliance (mL/cmH2O)
0.10
0.08
0.06
0.04
0.02
0.00
E
Forced Vital Capacity (FVC)
0.0119
0.5108
FVC (mL)
F
FEV0.05
0.7072
0.6962
Forced expiratory volume in 0.05s (FEV0.05;mL/s)
G
FEV0.1
0.8943
0.9820
Forced expiratory volume in 0.1s (FEV0.1;mL/s)

Figure 3.1 Mice from a single dose bleomycin-induced experimental IPF model exhibited lung function decline and lung inflammation after 4w but not 10w.

Lung function of C57BL/6 mice (n=8) was assessed under anaesthetic at endpoint using a SCIREQ Flexivent. Bronchoalveolar lavage fluid (BALF) was collected directly after lung function assessment **A** BALF total leukocytes/ml was calculated using a haemocytometer on day of endpoint. **B** Inspiratory capacity (IC) is a measure of the amount of air that can be inhaled after normal exhalation. **C** Crs (dynamic compliance) describes the elasticity of the entire respiratory system. **D** Cst (quasi-static compliance) describes the elasticity of the main elastic components of the lungs. **E** Forced vital capacity (FVC) is the total volume of air exhaled during a forced expiration, whereas **F** FEV0.05 and **G** FEV0.1 are a measure of the forced exhaled volume (FEV) in 0.05 or 0.1 seconds respectively. BALF and Lung function data provided by model lead A'qilah Banu Clarke. Ordinary one-way ANOVA with Tukey's multiple comparisons test was performed on each data set. Individual values were graphed with mean ± SD displayed. Results with a P-value≤0.05 were considered significant.

3.2.2 Mice from a single dose bleomycin and CS-induced experimental IPF model exhibited lung inflammation and lung function changes.

C57BL/6 mice were exposed to CS or room air for 8w. After 4 weeks, mice were challenged with a single i.n. dose of bleomycin or PBS. Mice were sacrificed after 8w total CS exposure i.e. 4w post-bleomycin challenge.

There was a significant increase in total leukocyte count in the BALF of air mice challenged with bleomycin compared to the PBS control (Figure 3.2: A) which reflected what was observed in the previous experimental IPF model at 4 weeks (Figure 3.1: A). Mice exposed to CS had significantly higher BALF total leukocytes compared to air exposed mice, which was not significantly changed by bleomycin challenge (Figure 3.2: A).

There was a significant decrease in IC (Figure 3.2: B) and Cst (Figure 3.2: D), but not for Crs (Figure 3.2: C) in Air + bleomycin challenged mice compared to Air + PBS mice. Crs was significantly decreased by bleomycin challenge in CS exposed mice (Figure 3.2: C), however, there was no significant overall effect of CS exposure on IC, Crs or Cst compared to air exposed mice (Figure 3.2: B-D). FVC, FEV.05 and FEV.1 were not significantly affected by either bleomycin challenge alone or CS exposure (Figure 3.2: E-G).

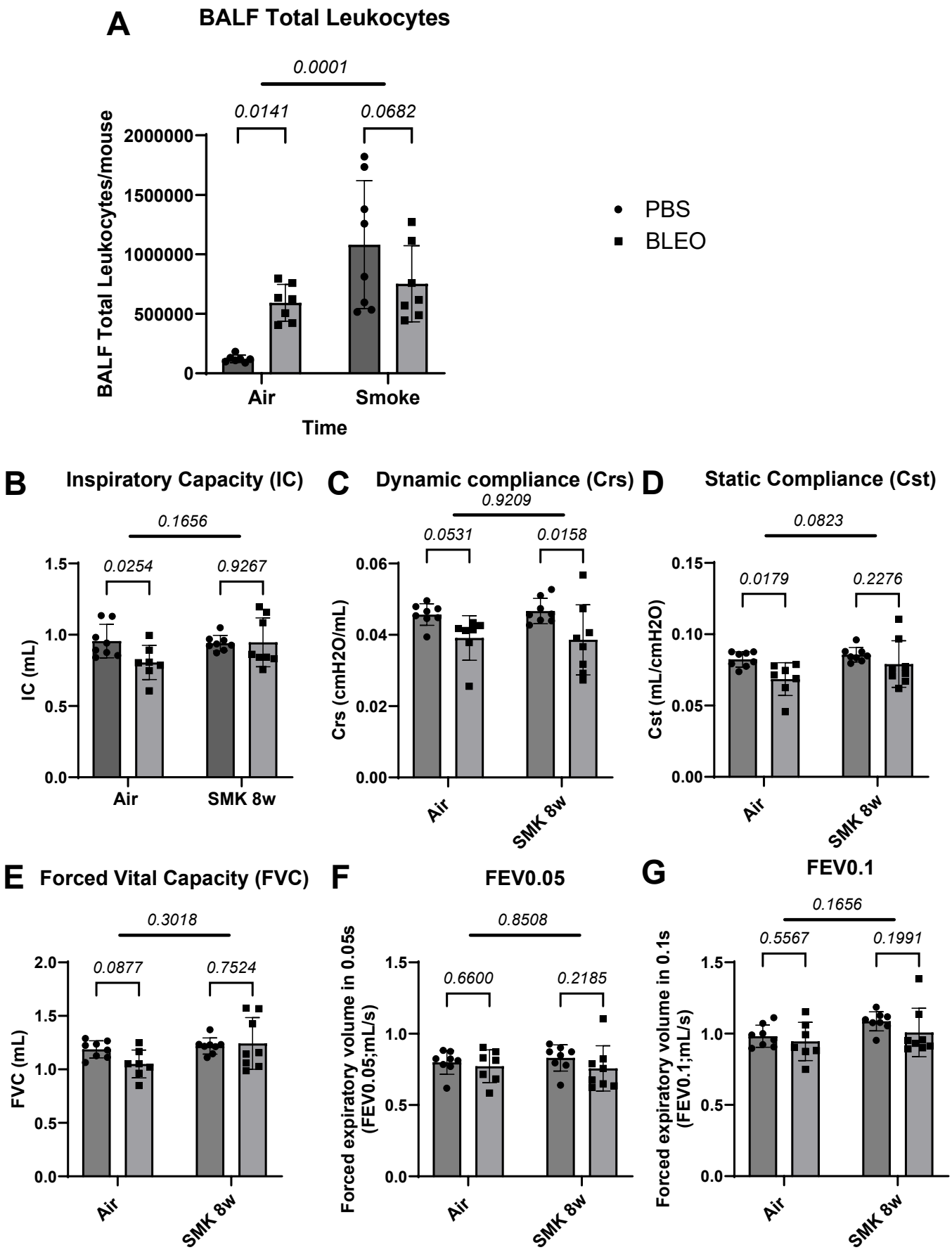
A
BALF Total Leukocytes
0.0001
0.0141
0.0682
BALF Total Leukocytes/mouse
2000000
1500000
1000000
500000
0
Air
Smoke
Time
PBS
BLEO
B
Inspiratory Capacity (IC)
0.1656
0.0254
0.9267
IC (mL)
1.5
1.0
0.5
0.0
Air
SMK 8w
C
Dynamic compliance (Crs)
0.9209
0.0531
0.0158
Crs (cmH2O/mL)
0.06
0.04
0.02
0.00
Air
SMK 8w
D
Static Compliance (Cst)
0.0823
0.0179
0.2276
Cst (mL/cmH2O)
0.15
0.10
0.05
0.00
Air
SMK 8w
E
Forced Vital Capacity (FVC)
0.3018
0.0877
0.7524
FVC (mL)
2.0
1.5
1.0
0.5
0.0
Air
SMK 8w
F
FEV0.05
0.8508
0.6600
0.2185
Forced expiratory volume in 0.05s (FEV0.05;mL/s)
1.5
1.0
0.5
0.0
Air
SMK 8w
G
FEV0.1
0.1656
0.5567
0.1991
Forced expiratory volume in 0.1s (FEV0.1;mL/s)
1.5
1.0
0.5
0.0
Air
SMK 8w

Figure 3.2 Mice from a single dose bleomycin and CS-induced experimental IPF model exhibited lung inflammation and lung function changes

Lung function of C57BL/6 mice (n=8) was assessed under anaesthetic at endpoint using a SCIREQ Flexivent. Bronchoalveolar lavage fluid (BALF) was collected directly after lung function assessment **A** Bronchoalveolar lavage fluid (BALF) was collected, and leukocytes/ml were calculated using a haemocytometer. **B** Inspiratory capacity (IC) is a measure of the amount of air that can be inhaled after normal exhalation. **C** Crs (dynamic compliance) describes the elasticity of the entire respiratory system. **D** Cst (static compliance) describes the elasticity of the main elastic components of the lungs. **E** Forced vital capacity (FVC) is the total volume of air exhaled during a forced expiration, whereas **F** FEV0.05 and **G** FEV0.1 are a measure of the forced exhaled volume (FEV) in 0.05 or 0.1 seconds respectively. BALF and lung function data provided by model lead A'qilah Banu Clarke. Two-way ANOVA with Šídák's multiple comparisons test was performed and mean ± SD displayed. Individual values were graphed with mean ± SD displayed. Results with a P-value≤0.05 were considered significant.

3.2.3 Mice from an experimental moderate and severe asthma model experienced increased lung inflammation methacholine-induced AHR.

This study used female BALB/c mice for an experimental model of moderate (steroid sensitive) and severe (steroid insensitive) asthma. Moderate asthma was induced through ovalbumin sensitisation (i.p.) and challenge (i.n.). Severe asthma was induced through a combination of ovalbumin sensitisation and challenge and CMU respiratory infection. To assess steroid resistance, two groups (Ova/SPG/Dex and Ova/CMU/Dex) were given daily i.n. dexamethasone treatment for the final 3 days of the model. Lung function assessment was conducted and AHR was measured after increasing doses of methacholine exposure via a nebuliser and BALF was attained immediately post lung function.

Mice with moderate asthma (Ova/SPG) had a significant increase in total leukocytes in the BALF compared to Sal/SPG treated mice, which was not significantly decreased in the dexamethasone treated moderate asthma mice (Ova/SPG/Dex). However, total leukocytes were not significantly higher compared to saline treated mice, which suggests some inhibition of immune cell induction with dexamethasone treatment in moderate asthma (Figure 3.3: A).

Mice with severe asthma (Ova/CMU) exhibited a significant increase in total leukocytes compared to mice infected with CMU only. Dexamethasone treatment did not decrease total leukocytes in severe asthma mice (Ova/CMU/Dex) and was still significantly higher than Sal/CMU mice. Methacholine induced significantly higher AHR in moderate asthma and severe asthma compared to controls (Figure 3.3: C). AHR was decreased by dexamethasone treatment in moderate asthma (Ova/SPG/Dex) but not severe asthma (Ova/CMU/Dex) (Figure 3.3: B+C).

These results reflect the steroid sensitivity, and insensitivity typically observed in human cases of moderate and severe asthma respectively.

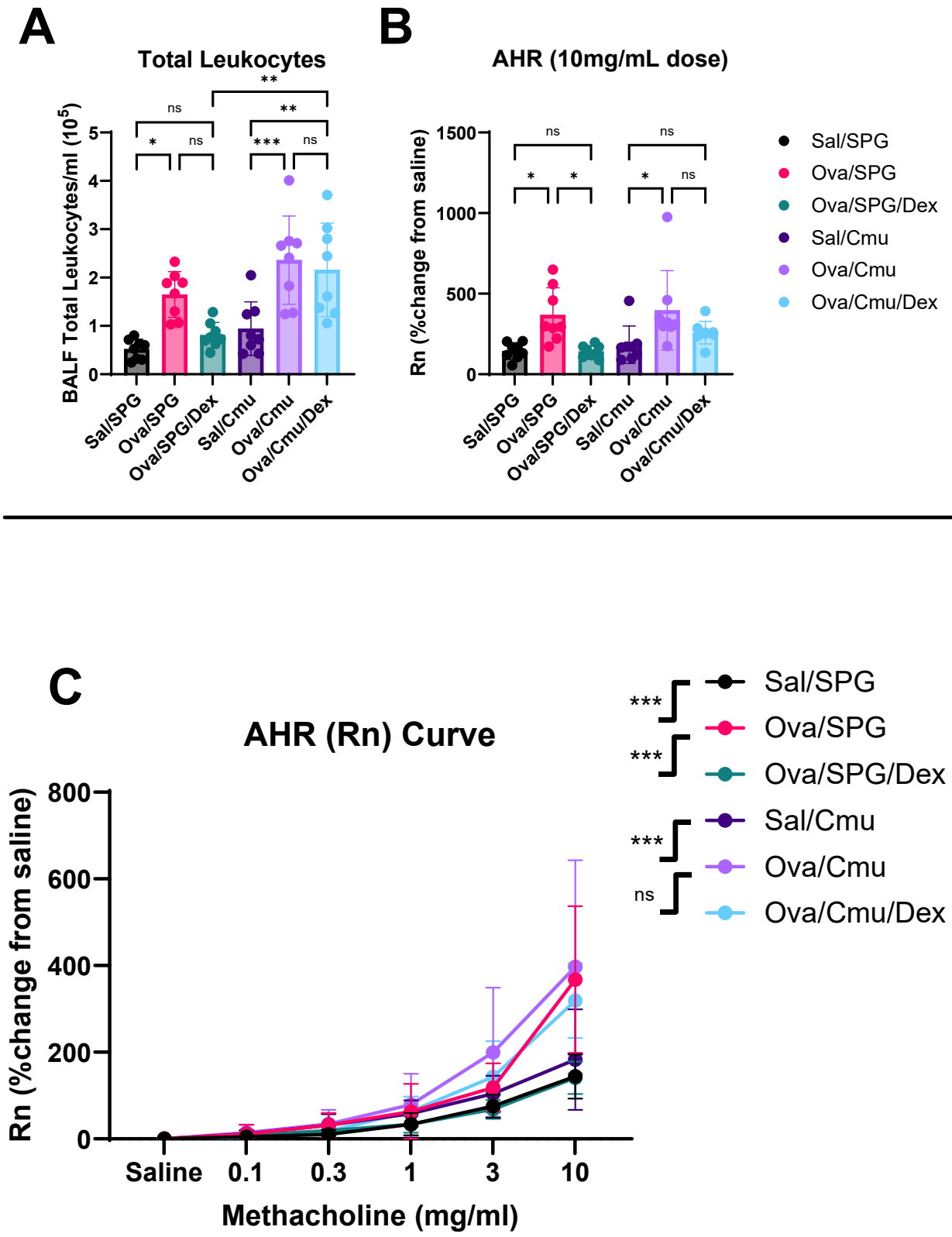
A
Total Leukocytes
BALF Total Leukocytes/ml (10^5)
B
AHR (10mg/mL dose)
Rn (%change from saline)
Sal/SPG
Ova/SPG
Ova/SPG/Dex
Sal/Cmu
Ova/Cmu
Ova/Cmu/Dex
C
AHR (Rn) Curve
Rn (%change from saline)
Saline
0.1
0.3
1
3
10
Methacholine (mg/ml)
***
***
***
ns

Figure 3.3 Mice from an experimental moderate and severe asthma model experienced increased methacholine-induced AHR and lung inflammation

Bronchoalveolar lavage fluid (BALF) was collected from BALB/c mice (n=8) after lung function analysis, and leukocytes/ml were calculated using a haemocytometer. AHR was measured with increasing doses of methacholine (0, 0.1, 0.3, 1.0, 3.0, 10mg/ml) **A+B** Ordinary one-way ANOVA with Tukey's multiple comparisons test was performed on each data set. Individual values were graphed with mean ± SD displayed. **C** Rn (central airway resistance) with increasing doses of methacholine as a percentage change from a saline baseline control. All lung function parameters were measured under anaesthetic on day of endpoint. BALF and Lung function data was provided by model leads Dr. Ridhima Radhwa and Dr. Gesa Albers. Two-way ANOVA with Šídák's multiple comparisons test was performed and mean ± SD displayed. Results with a P-value≤0.05 were considered significant (*P≤0.05; **P≤0.01; ***P≤0.001).

3.2.4 Increased BALF total leukocytes at 8 and 12w, and lung function decline was observed in mice from a CS-induced experimental COPD model time course model.

Female C57BL/6 mice were exposed to smoke from 12 cigarettes twice daily, 5d/week for time points of 2, 4, 6, 8 and 12w. Lung function from the mice of the 12w timepoint was assessed, but not from any other timepoint as that was not feasible. BALF total leukocytes were increased at all time points however these data are not shown in this report.

BALF total leukocytes were increased at 8w and 12w in CS exposed mice compared to air exposed mice (Figure 3.4: A+B), demonstrating CS induced immune cell induction to the lung. There was a significant increase in IC, FVC, TLC and hysteresis in the CS exposed mice when compared to the air control (Figure 3.4: C-F). There was no significant change to measures of either Crs or Cst (Figure 3.4: G+H).

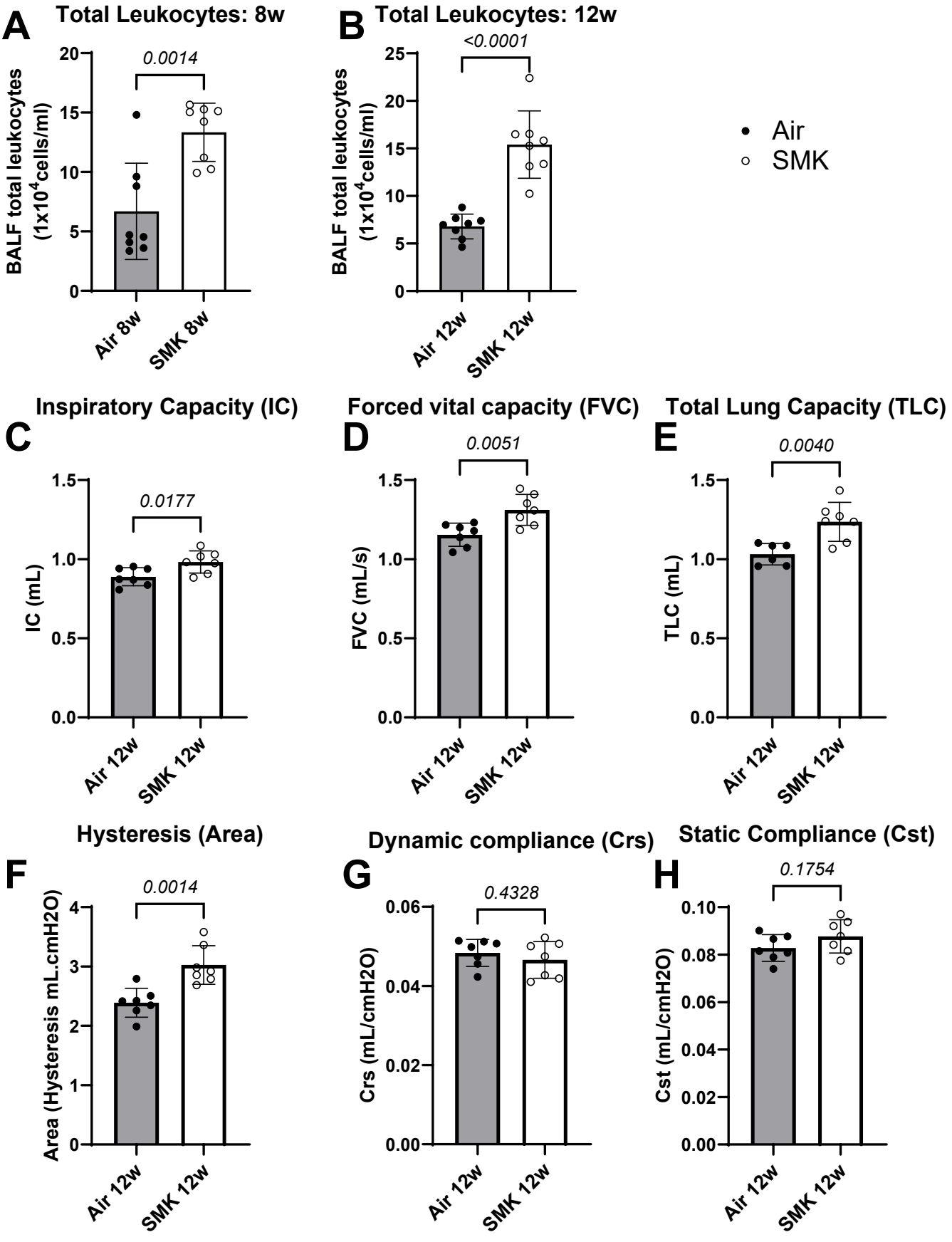
A
Total Leukocytes: 8w
BALF total leukocytes (1x10^4cells/ml)
0.0014
Air 8w
SMK 8w
B
Total Leukocytes: 12w
<0.0001
BALF total leukocytes (1x10^4cells/ml)
Air 12w
SMK 12w
Air
SMK
C
Inspiratory Capacity (IC)
0.0177
IC (mL)
D
Forced vital capacity (FVC)
0.0051
FVC (mL/s)
E
Total Lung Capacity (TLC)
0.0040
TLC (mL)
F
Hysteresis (Area)
0.0014
Area (Hysteresis mL.cmH2O)
G
Dynamic compliance (Crs)
0.4328
Crs (mL/cmH2O)
H
Static Compliance (Cst)
0.1754
Cst (mL/cmH2O)

Figure 3.4 Increased BALF total leukocytes at 8 and 12w, and lung function decline was observed in mice from a CS-induced experimental COPD model time course model.

Lung function of C57BL/6 mice (n=8) was assessed under anaesthetic at endpoint using a SCIREQ Flexivent, after 12w of cigarette smoke and room air exposure. Bronchoalveolar lavage fluid (BALF) was collected directly after lung function assessment for the 8 and 12w timepoint models. **A+B** BALF total leukocyte count at 8 and 12w respectively **C** Inspiratory capacity (IC) is a measure of the amount of air that can be inhaled after normal exhalation. **D** Forced vital capacity (FVC) is the total volume of air exhaled during a forced expiration. **E** Total lung capacity (TLC) is the maximum possible lung volume. **F** Hysteresis is a measure of recoil and surface tension of the lungs. **G** Crs (dynamic compliance) describes the elasticity of the entire respiratory system. **H** Cst (quasi-static compliance) describes the elasticity of the main elastic components of the lungs. Lung function data was provided by model leads Dr. Elinor Hortle and Dr. Matt Johansen. An unpaired t test statistical analysis was performed on each data set. Individual values were graphed with mean ± SD displayed. Results with a P-value≤0.05 were considered significant.

3.2.5 Male and female mice from a CS-induced experimental COPD model showed similar proportions of lung function decline at an 8w time point.

Lung function of male and female C57BL/6 mice was assessed under anaesthetic at endpoint after 3, 8 and 12 weeks of cigarette smoke or room air exposure (controls). Unfortunately, only lung function data from the 8-week timepoint was available for analysis, and BALF data was unavailable from the model.

Lung volume parameters including IC, FVC, TLC were significantly increased by CS exposure in both male and female mice compared to room air controls (Figure 3.5: A-C). Hysteresis and Cst (Figure 3.5: D+F), but not Crs (Figure 3.5: E), were also significantly increased in male and female mice with CS exposure versus air exposed mice. This demonstrated similarities in the direction and proportion of lung function changes due to CS exposure in both male and female mice.

IC and Crs were significantly lower in female mice compared to male mice, regardless of CS or air exposure (Figure 3.5: A+ E), and FVC was significantly lower in female mice but only with CS exposure (Figure 3.5: B). Hysteresis was significantly lower in female air control mice compared to male air control mice (Figure 3.5: D).

These results demonstrated that the 8-week CS exposure timepoint in male and female mice sufficiently altered lung function changes to emulate what is observed in COPD patients. Although there were some lung function differences between male and female mice, these seem likely to be due to size differences between male and female mice. Male mice have larger lungs and therefore higher lung volume parameters.

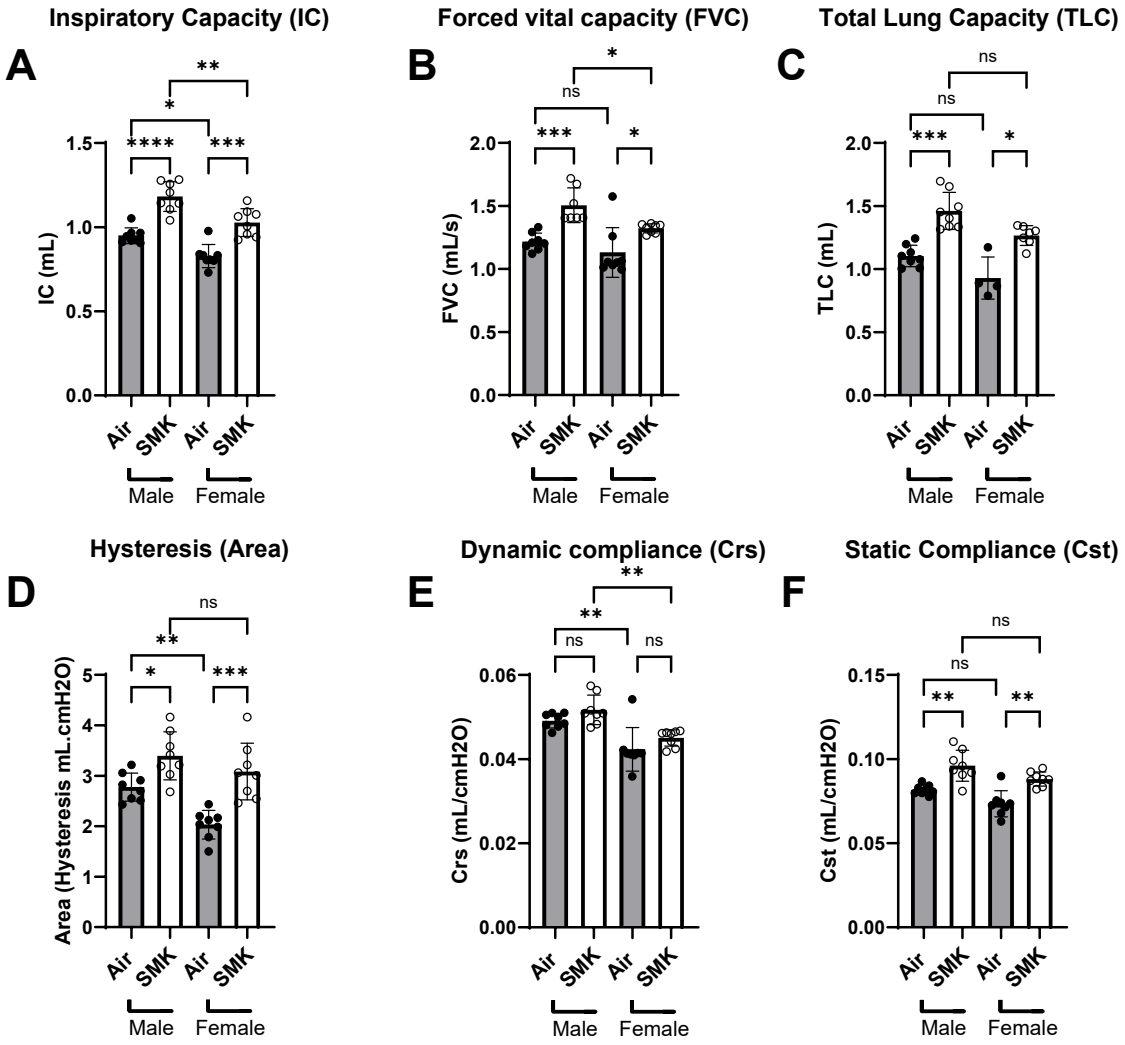

Figure 3.5 Male and female mice from a CS-induced experimental COPD model showed similar proportions of lung function decline at an 8w time point.

Lung function of C57BL/6 mice (n=8) was assessed under anaesthetic at endpoint using a SCIREQ Flexivent, after 8 weeks of cigarette smoke or room air exposure. **A** Inspiratory capacity (IC) is a measure of the amount of air that can be inhaled after normal exhalation. B Forced vital capacity (FVC) is the total volume of air exhaled during a forced expiration. **C** Total lung capacity (TLC) is the maximum possible lung volume. **D** Hysteresis is a measure of recoil and surface tension of the lungs. **E** Crs (dynamic compliance) describes the elasticity of the entire respiratory system. **F** Cst (quasi-static compliance) describes the elasticity of the main elastic components of the lungs. Lung function data provided by model lead Mounika Guntipally. Two-way ANOVA with Šídák's multiple comparisons test was performed and mean ± SD displayed. Results with a P-value≤0.05 were considered significant (*P≤0.05; **P≤0.01; ***P≤0.001, ****=P≤0.0001).

3.3 Mouse models of IPF, asthma and COPD: impact on whole body and skeletal muscle weight changes.

3.3.1 Mice from a single dose bleomycin-induced IPF model exhibited no change in total body weight or skeletal muscle mass after 4 or 10w.

A single dose of i.n. bleomycin or PBS was given to C57BL/6 mice. The 4 and 10w bleomycin challenge mice were age matched and sacrificed on the day of endpoint. Mice were weighed 3 times/week from the date of the bleomycin challenge. Individual skeletal muscles were collected and weighed on the day of endpoint.

There was no significant change in body weight in mice 4 or 10w after a single dose bleomycin challenge compared to control groups. (Figure 3.6: A+B). The gastrocnemius, quadriceps, soleus, and EDL weights were not altered 4 or 10w after single i.n. dose bleomycin or PBS challenge (Figure 3.6: C-F). There was also no significant difference in N-A length 4 or 10w post bleomycin challenge (Figure 3.6: G).

These results indicated that the bleomycin-induced model of pulmonary fibrosis did not cause changes to total body or skeletal muscle weight, or mouse length after 4 or 10w.

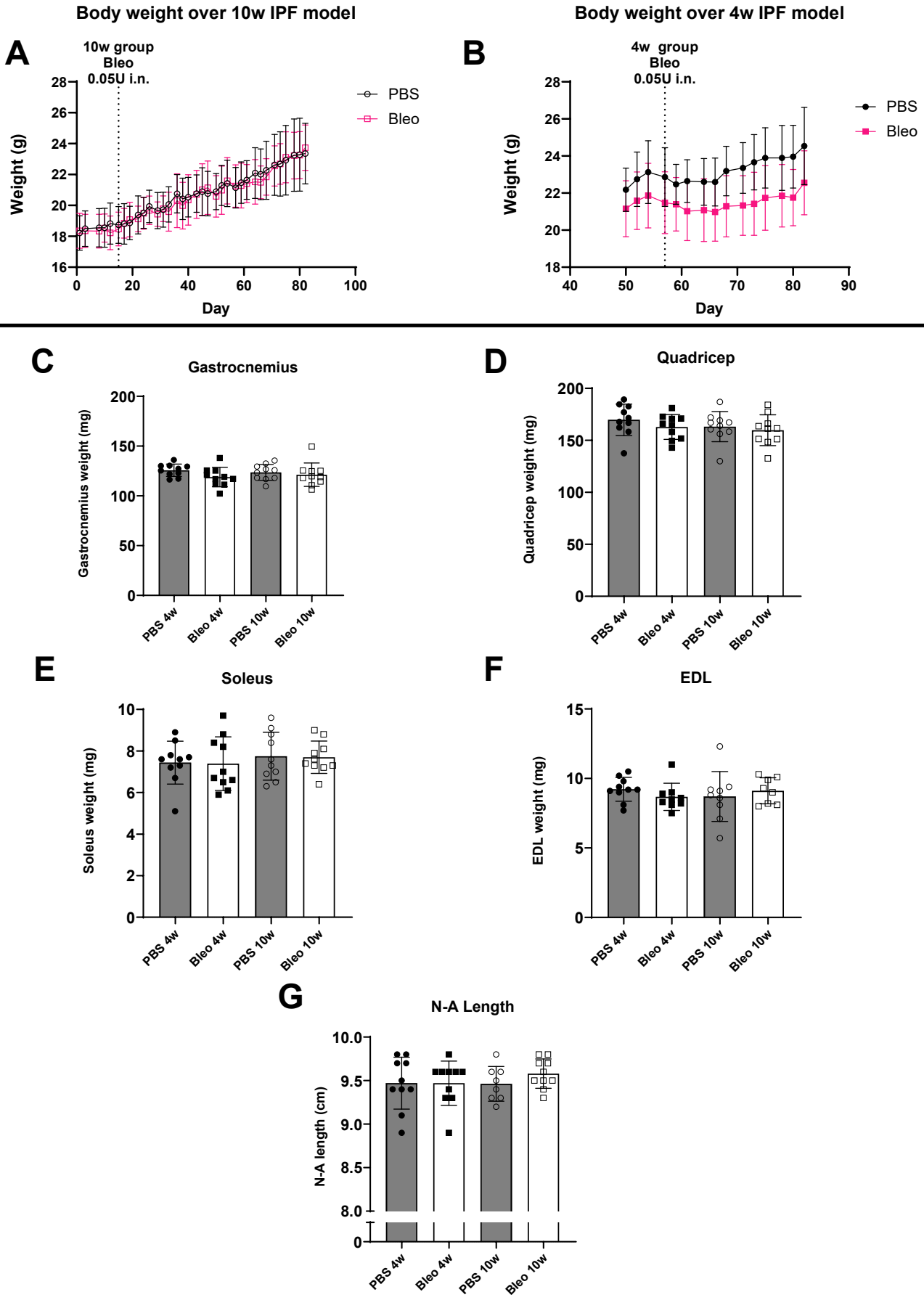
A
Body weight over 10w IPF model
10w group
Bleo
0.05U i.n.
Weight (g)
Day
PBS
Bleo
B
Body weight over 4w IPF model
4w group
Bleo
0.05U i.n.
Weight (g)
Day
PBS
Bleo
C
Gastrocnemius
Gastrocnemius weight (mg)
D
Quadricep
Quadricep weight (mg)
E
Soleus
Soleus weight (mg)
F
EDL
EDL weight (mg)
G
N-A Length
N-A length (cm)
PBS 4w
Bleo 4w
PBS 10w
Bleo 10w

Figure 3.6 Mice from a single dose bleomycin-induced IPF model exhibited no change in total body weight or skeletal muscle mass after 4 or 10w.

C57BL/6 mice (n=10) were weighed 5 times per week from day 0 up until the endpoint. Body length was measured while the mouse was under anaesthetic and skeletal muscles were collected and immediately weighed after lung function assessment **A** 10-week bleomycin challenge model body weight (g) over days 0-82 (bleomycin i.n. day 15). **B** 4-week bleomycin challenge model body weight (g) over days 50-82 (bleomycin i.n. day 57). **C-F** Gastrocnemius, Quadricep muscles, soleus and extensor digitorum longus (EDL) weight (mg) respectively at endpoint. **G** Nose-anus (N-A) length (cm) at endpoint. A mixed-effect analysis (REML) statistical analysis was performed for analysis of mouse body weight over time. Ordinary one-way Anova with Tukey's multiple comparison statistical analysis was performed on each data set. Individual values were graphed with mean **±** SD displayed. Results with a P-value≤0.05 were considered significant. Bleo = Bleomycin.

3.3.2 Mice from a single dose bleomycin and CS-induced experimental IPF model exhibited changes to body weight and skeletal muscle mass

C57BL/6 mice were exposed to CS or room air for 8w. After 4 weeks, mice were challenged with a single i.n. dose of bleomycin or PBS. Mice were sacrificed after 8w total CS exposure i.e. 4w post-bleomycin challenge. CS exposed mice (SMK 8w groups) were weighed daily (Monday-Friday), and room air exposed mice (Air groups) were weighed 3 times per week. (Monday, Wednesday, Friday). Individual skeletal muscle weights were measured on the day of endpoint.

There was no significant change to body weight over time because of bleomycin or PBS challenge alone. However, CS exposed mice gained significantly less weight over time compared to room air exposed mice, regardless of bleomycin or PBS challenge (Figure 3.7: A).

There was no significant change in skeletal muscle mass of the gastrocnemius, quadriceps, soleus or EDL muscles between groups challenged with bleomycin compared to PBS groups, regardless of CS exposure when they were weighed at endpoint. CS exposed mice had significantly lighter gastrocnemius, quadriceps and soleus muscles compared to and air control groups, regardless of bleomycin or PBS challenge. (Figure 3.7: B-D). CS exposed mice also had significantly shorter N-A lengths than the air control group, which was unaffected by bleomycin challenge (Figure 3.7: F). These results demonstrated an effect of CS exposure, but not bleomycin challenge, on mouse development. CS exposure reduced weight gain, skeletal muscle mass, and N-A length in young female C57BL/6 mice over time.

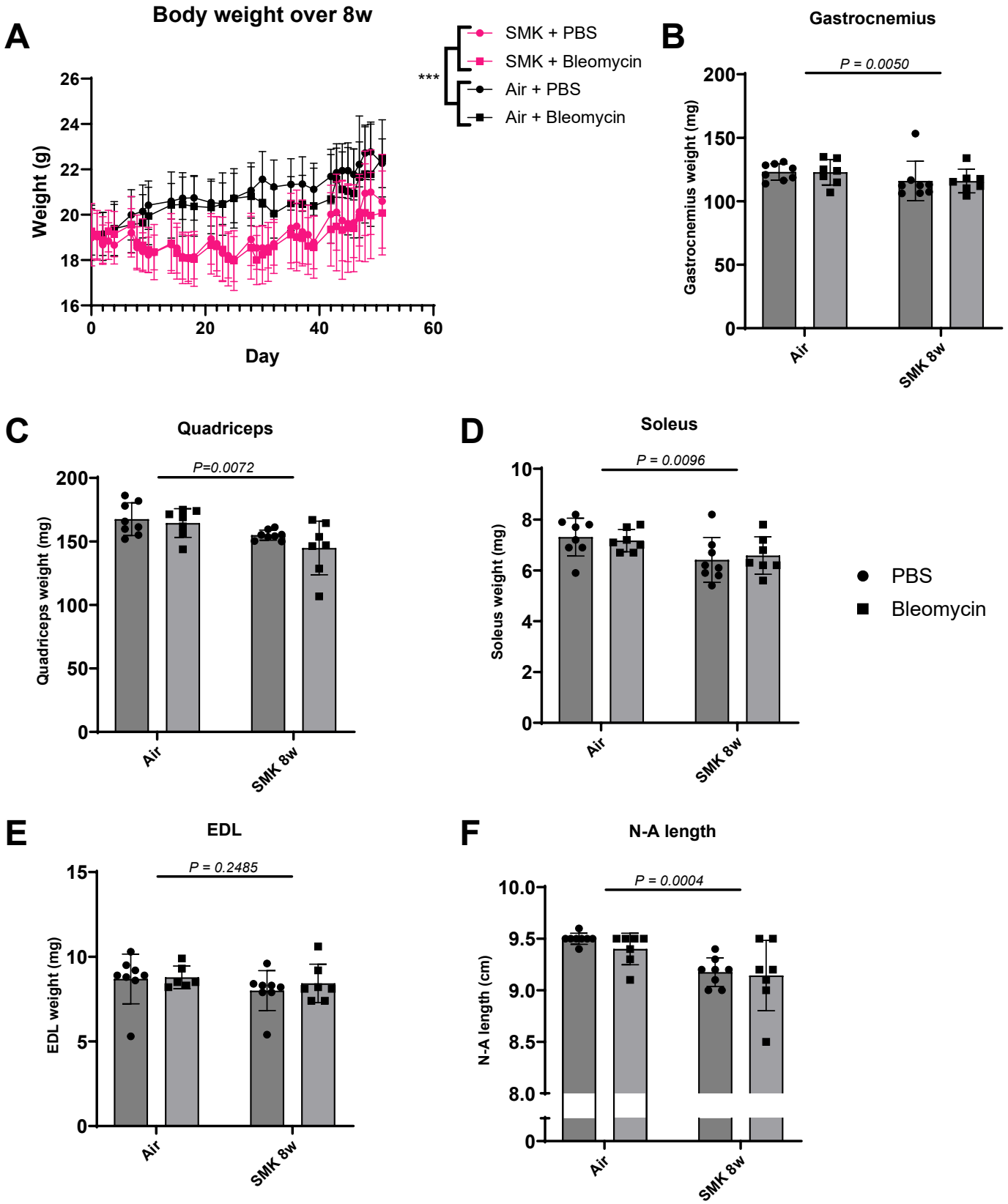
A
Body weight over 8w
Weight (g)
Day
***
SMK + PBS
SMK + Bleomycin
Air + PBS
Air + Bleomycin
B
Gastrocnemius
P = 0.0050
Gastrocnemius weight (mg)
Air
SMK 8w
C
Quadriceps
P=0.0072
Quadriceps weight (mg)
D
Soleus
P = 0.0096
Soleus weight (mg)
PBS
Bleomycin
E
EDL
P = 0.2485
EDL weight (mg)
F
N-A length
P = 0.0004
N-A length (cm)

Figure 3.7 Mice from a single dose bleomycin and CS-induced experimental IPF model exhibited changes to body weight and skeletal muscle mass.

C57BL/6 mice (n=8) were weighed 5 times per week from day 0 up until the endpoint. Body length was measured while the mouse was under anaesthetic and skeletal muscles were collected and immediately weighed after lung function assessment. **A** Body weight (g) over time (day 0-51). SMK 8w mice were weighed daily, air exposed mice were weighed 3 times/week (n=12). **B-E** Gastrocnemius, Quadriceps, soleus and extensor digitorum longus (EDL) weight (mg) respectively (n=8). **F** Nose-anus (N-A) length (cm; n=8). A Mixed-effect analysis (REML) statistical analysis was performed for analysis of mouse body weight over time. Two-way Anova with Šídák's multiple comparisons test statistical analysis was performed on each muscle weight data set. Individual values were graphed with mean **±** SD displayed. Results with a P-value≤0.05 were considered significant (*** P≤0.001).

3.3.3 Mice from an experimental moderate and severe asthma model did no exhibit whole body weight or length changes, or changes to skeletal muscle mass

This study used female BALB/c mice for an experimental model of moderate (steroid sensitive) and severe (steroid insensitive) asthma. Moderate asthma was induced through ovalbumin sensitisation (i.p.) and challenge (i.n.). Severe asthma was induced through a combination of ovalbumin sensitisation and challenge and CMU respiratory infection. To assess steroid resistance, two groups (Ova/SPG/Dex and Ova/CMU/Dex) were given daily i.n. dexamethasone treatment for the final 3 days of the model. Mice were weighed 3 days per week over the course of the model (5w). Gastrocnemius, quadriceps, soleus and EDL muscles were weighed on the day of endpoint. The N-A length was also measured along with the tibia and femur length from the hind legs.

There was no significant change in weight over time for any group (Figure 3.8: A) and no significant weight differences were observed for gastrocnemius, quadriceps, soleus or extensor digitorum longus (EDL) muscles as a result of any challenge or treatment (Figure 3.8: B-E). Severe asthma mice that were treated with dexamethasone (Ova/CMU/Dex) had a significantly shorter nose-anus length compared to saline group (Figure 3.8: F). There was no significant difference in tibia or femur length between any of the groups (Figure 3.8: G+H).

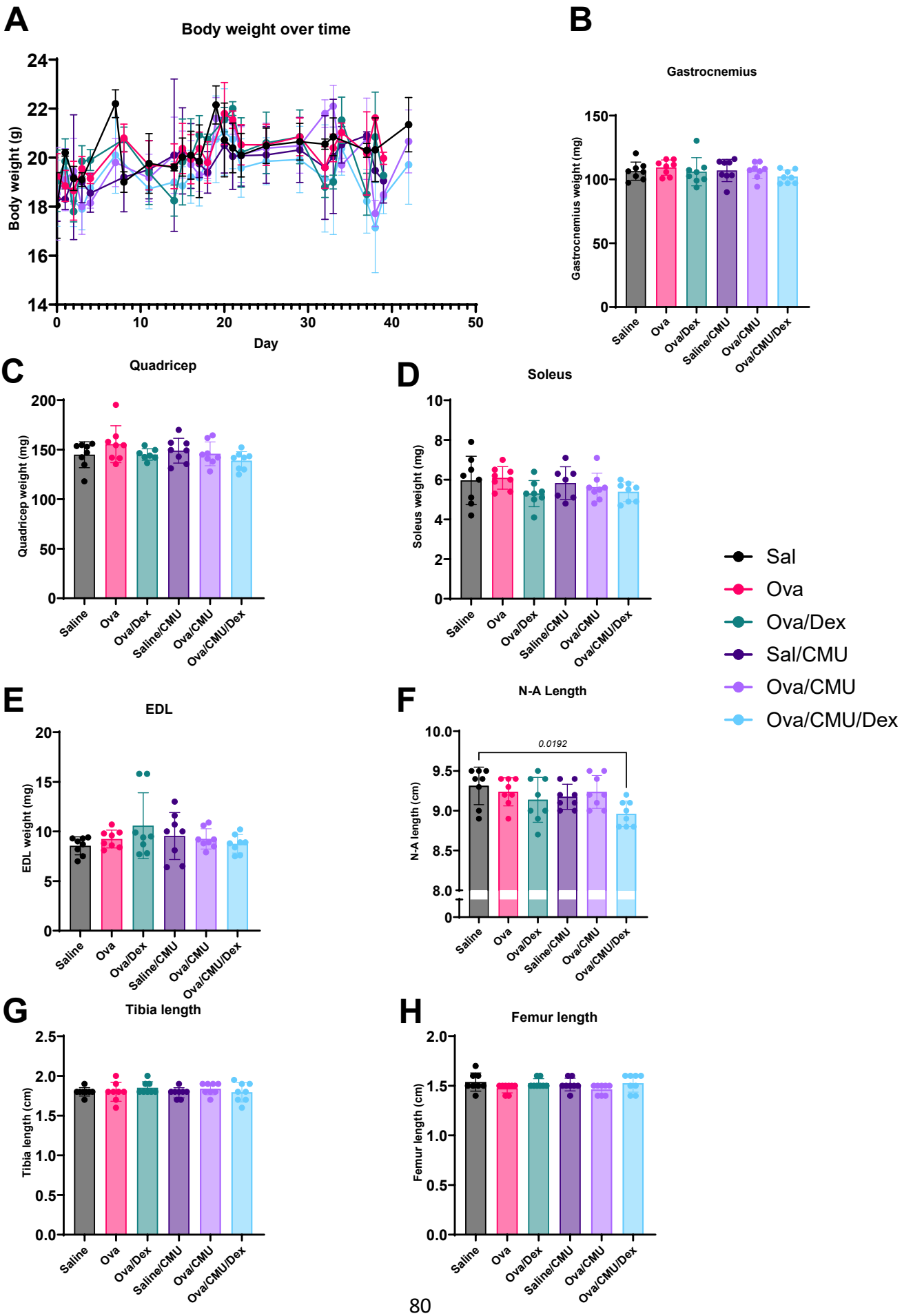
A
Body weight over time
Body weight (g)
Day
B
Gastrocnemius
Gastrocnemius weight (mg)
C
Quadricep
Quadricep weight (mg)
D
Soleus
Soleus weight (mg)
E
EDL
EDL weight (mg)
F
N-A Length
N-A length (cm)
0.0192
G
Tibia length
Tibia length (cm)
H
Femur length
Femur length (cm)
Saline
Ova
Ova/Dex
Saline/CMU
Ova/CMU
Ova/CMU/Dex
Sal
Ova
Ova/Dex
Sal/CMU
Ova/CMU
Ova/CMU/Dex

Figure 3.8 Mice from an experimental moderate and severe asthma model did no exhibit whole body weight or length changes, or changes to skeletal muscle mass.

BALB/c mice (n=8) were weighed 3 times per week until the endpoint. Body length was measured while the mouse was under anaesthetic and skeletal muscles were collected and immediately weighed after lung function assessment. **A** Average mouse weight (g) over time for each group. **B-E** Gastrocnemius, Quadricep muscles, soleus and EDL weight (mg) measured at endpoint. **F-H** nose-anus (N-A) length (cm), tibia and femur length (cm) measured at endpoint respectively. Groups represent non-disease control (Sal), moderate asthma (Sal/Ova), control to demonstrate steroid responsiveness of moderate asthma (Ova/Dex), non-asthma infection control (Sal/CMU), severe asthma (Ova/CMU), and control to demonstrate steroid resistance of severe asthma (Ova/CMU/Dex). A mixed-effect analysis (REML) statistical analysis was performed for analysis of mouse body weight over time. Ordinary one-way Anova with Tukey's multiple comparison statistical analysis was performed on each data set. Individual values were graphed with mean **±** SD displayed. Results with a P-value≤0.05 were considered significant. Ova = Ovalbumin, Dex = Dexamethasone

3.3.4 Female C57BL/6 mice from a CS-induced experimental COPD model time course model exhibited impaired development after 4, 6, 8 and 12 weeks of CS exposure.

For a cigarette smoke (CS)-induced mouse model of COPD, C57BL/6 female mice were exposed to smoke from 12 cigarettes, twice daily, 5days/week (w) for time points of 2, 4, 6, 8 and 12w. CS exposed mice were weighed daily (Monday -Friday) and room air exposed mice were weighed 3 times per week (Monday, Wednesday, Friday) until the endpoint.

Mice exposed to CS for 4, 6 and 12w had significantly lower body weight than their respective room air exposed controls (Figure 3.9: B, C+E). No significant difference was observed in body weight over time for mice exposed to CS for 2 or 8w vs air controls (Figure 3.9: A+D). Body weight over time was also displayed as a percentage change from starting weight to account for groups with higher average starting weights. This is especially evident in the 8w group where the CS exposed mice had a higher average starting weight than the air controls. Mice exposed to CS for 4, 6, 8w, and 12w had significantly lower body weight over time compared to their respective air controls (Figure 3.9: G-J), but not at 2w (Figure 3.9: F). These results demonstrate that young mice exposed to CS do not gain total body weight over time, indicating impaired development.

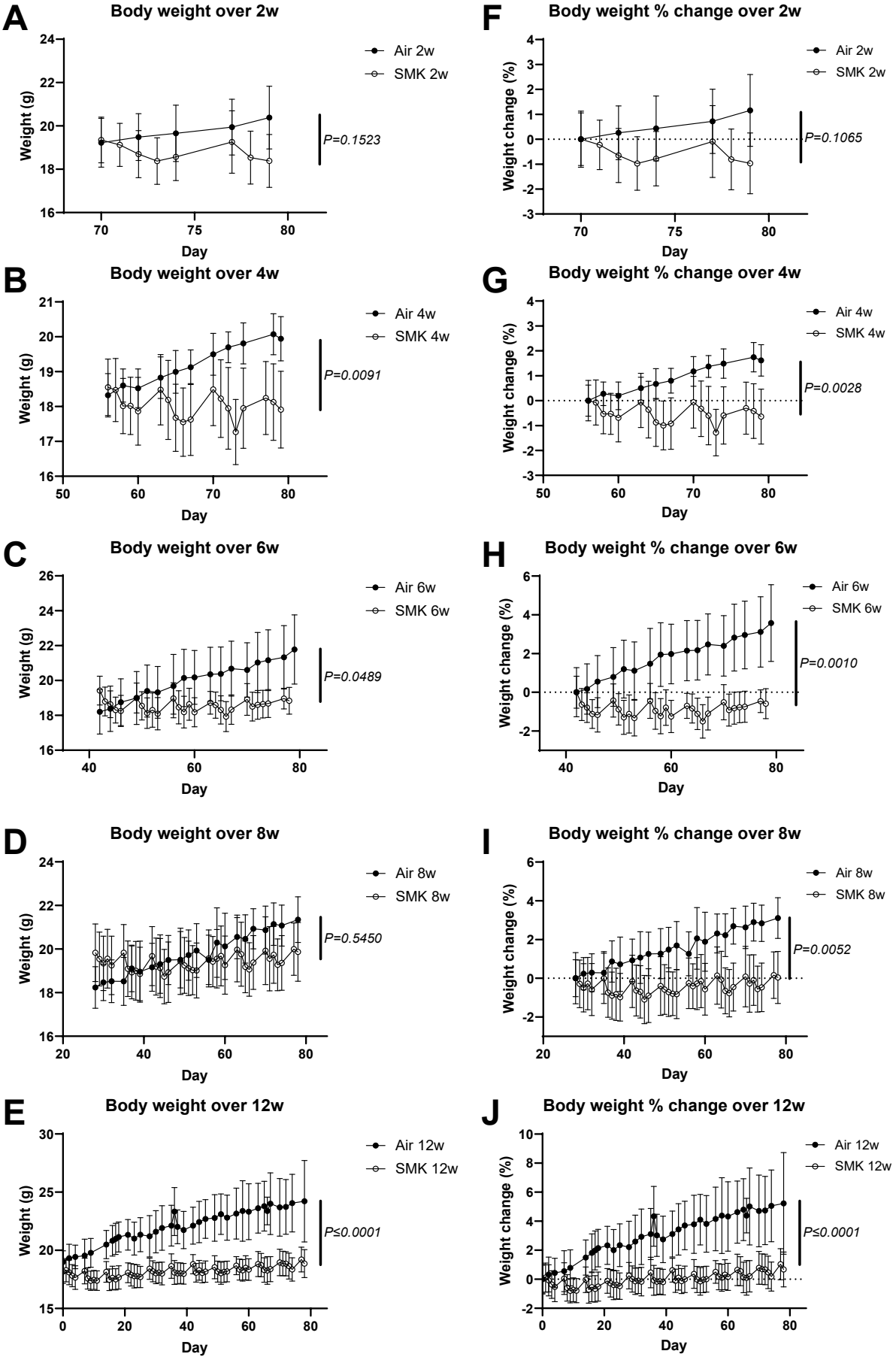
A
Body weight over 2w
Weight (g)
Day
Air 2w
SMK 2w
P=0.1523
B
Body weight over 4w
Weight (g)
Day
Air 4w
SMK 4w
P=0.0091
C
Body weight over 6w
Weight (g)
Day
Air 6w
SMK 6w
P=0.0489
D
Body weight over 8w
Weight (g)
Day
Air 8w
SMK 8w
P=0.5450
E
Body weight over 12w
Weight (g)
Day
Air 12w
SMK 12w
P≤0.0001
F
Body weight % change over 2w
Weight change (%)
Day
Air 2w
SMK 2w
P=0.1065
G
Body weight % change over 4w
Weight change (%)
Day
Air 4w
SMK 4w
P=0.0028
H
Body weight % change over 6w
Weight change (%)
Day
Air 6w
SMK 6w
P=0.0010
I
Body weight % change over 8w
Weight change (%)
Day
Air 8w
SMK 8w
P=0.0052
J
Body weight % change over 12w
Weight change (%)
Day
Air 12w
SMK 12w
P≤0.0001

Figure 3.9 Female C57BL/6 mice from a CS-induced experimental COPD model time course model exhibited impaired development after 4, 6, 8 and 12 weeks of CS exposure.

C57BL/6 mice (n=8) were weighed 5 times per week until the endpoint. CS-exposure for all groups began at age 8w; therefore, at endpoint mice were age-matched to their own air controls, but mice with longer smoke exposure were older than mice with shorter smoke exposure i.e. mice from the 2w time point were 10w old and mice from the 12w time point were 20w old. **A-E** Mouse total body weight (g) over time (12w group n =16; 2, 4, 6, and 8w groups n=8). **F-J** Mouse total body weight change % change over time (12w group n =16; 2, 4, 6 and 8w groups n=8). A mixed-effect analysis (REML) statistical analysis was performed on data sets. Individual values, i.e. individual mouse body weight (g) for each time point (Day) are displayed as mean **±** SD. Results with a P-value≤0.05 were considered significant.

3.3.5 Female C57BL/6 mice from a CS-induced experimental COPD model time course model had decreased muscle weights due to CS exposure

C57BL/6 female mice were exposed to the smoke of 12 cigarettes twice daily, 5d/week for time points of 2, 4, 6, 8 and 12w. Skeletal muscle was collected and weighed on the day of endpoint.

A decrease in gastrocnemius weight was observed for mice exposed to CS for 6w and 12w vs room air exposed mice, but no significant decrease was observed for 2, 4 or 8w exposures (Figure 3.10: A). Comparing the overall grouped effect (the combined effect across all five time points) of CS exposure vs air control there was an overall decrease in gastrocnemius weight for CS exposed mice. ($P<0.0001$; Figure 3.10: A).

A decrease in quadriceps weight was observed in CS exposed mice at 2 and 6w compared to the room air exposed mice, but no significant decrease was observed at 4, 8 or 12w exposures (Figure 3.10: B). Comparing the grouped effect of CS exposure vs air exposure there was an overall decrease in quadricep weight for CS exposed mice. ($P<0.0001$; Figure 3.10: B).

No statistically significant change was observed between CS and room air exposed mice in soleus weight at individual time points. However, the effect CS exposure vs air control was an overall decrease in soleus weight for mice exposed to CS ($P=0.0398$; Figure 3.10: C).

No significant weight differences were observed for the EDL at any time point and there was no grouped effect of CS on EDL weight compared to room air exposure ($P<0.2241$; Figure 3.10: D).

These results indicate that CS exposure does decrease skeletal muscle weight for the gastrocnemius, quadricep and soleus, and demonstrates the ability for CS to decrease the weights of gastrocnemius and quadriceps muscles as early as 6w after the commencement of CS exposure.

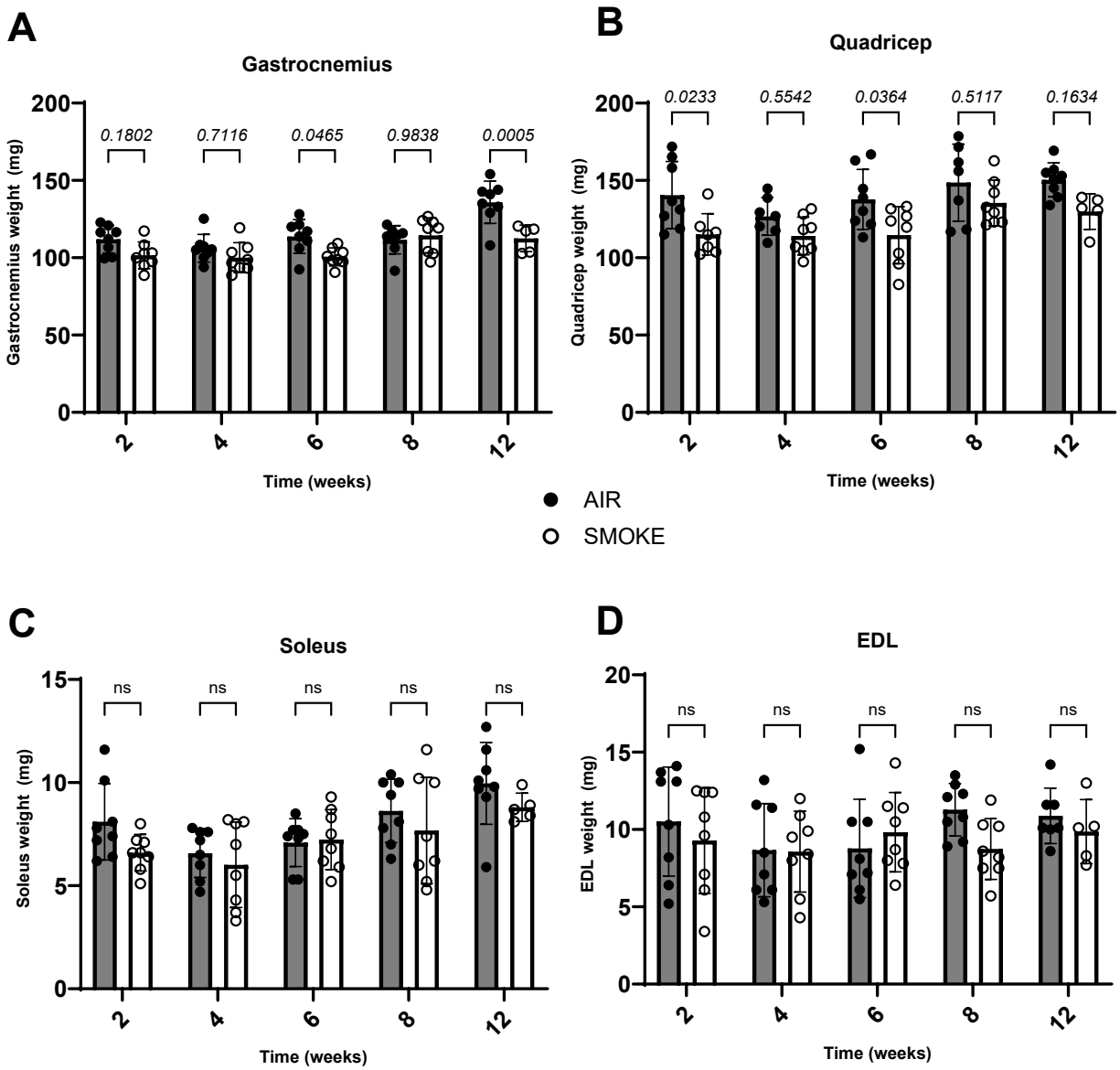

Figure 3.10 Female C57BL/6 mice from a CS-induced experimental COPD model time course model had decreased muscle weights due to CS exposure.

Skeletal muscles from female C57BL/6 mice (n=8) were collected on the day of endpoint and immediately weighed. **A-D** Gastrocnemius, Quadricep, Soleus and EDL weights (mg). Grouped effect analysis was done using an ordinary two-way Anova with a Šídák's multiple comparisons test used to compare CS vs air exposed mice at each time point. Individual values were graphed with mean ± SD displayed. Results with a P-value≤0.05 were considered significant.

3.3.6 Male and female mice from a CS-induced experimental COPD model showed similar proportions of impaired development due to CS exposure after 3, 8 and 12 weeks.

Male and female C57BL/6 mice were exposed to smoke from 12 cigarettes twice daily, 5d/week for time points of 3, 8 and 12w. CS exposed mice were weighed daily (Monday -Friday) and room air exposed mice were weighed 3 times per week (Monday, Wednesday, Friday) until the endpoint. N-A, femur and tibia length were measured on the day of endpoint.

Male mice started the models heavier than female mice and this difference was maintained throughout the time course. CS exposed female and male mice exhibited significantly impaired weight gain compared to air control mice across all time points (Figure 3.11: A-C).

Male mice had longer N-A (Figure 3.11: C+D), tibia (Figure 3.11: E) and femur (Figure 3.11: F) lengths than female mice. There was a decrease in N-A length for male mice exposed to CS vs the air control at 12w, but not at the 3 or 8w time points. (Figure 3.11: C), and female CS exposed mice had reduced N-A length compared to room air exposed mice at 8 and 12w, but not at 3w (Figure 3.11: D). No significant difference was observed in tibia (Figure 3.11: E) or femur (Figure 3.11: F) length in mice under any condition at 12w. Femur and tibia length were not measured at the 3 or 8w time point.

This demonstrated that CS exposure impaired development to similar extents in young male and female mice by decreasing N-A length and total body weight.

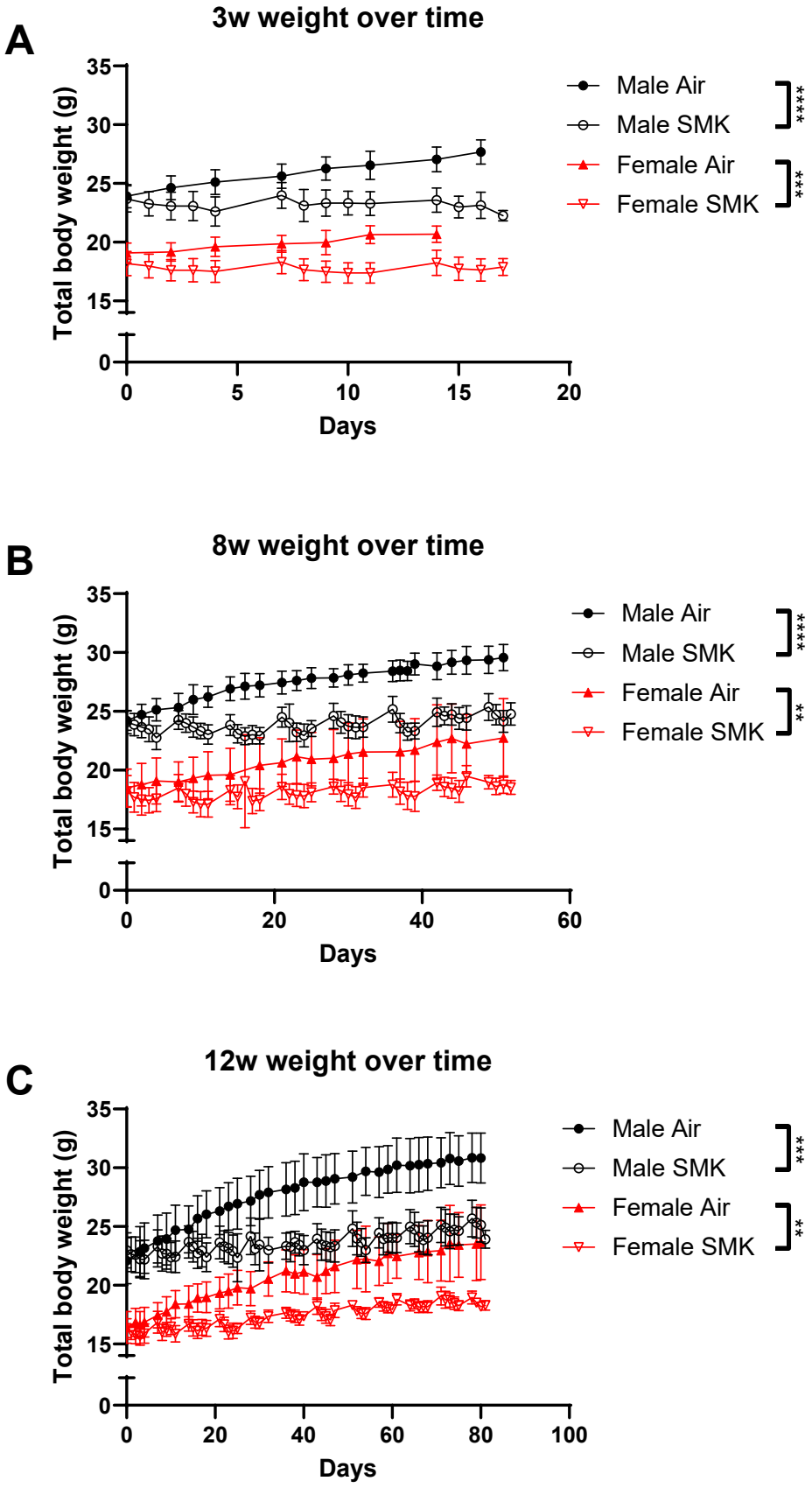
A
3w weight over time
Total body weight (g)
Days
Male Air
Male SMK
Female Air
Female SMK
****
***
B
8w weight over time
Total body weight (g)
Days
Male Air
Male SMK
Female Air
Female SMK
****
**
C
12w weight over time
Total body weight (g)
Days
Male Air
Male SMK
Female Air
Female SMK
***
**

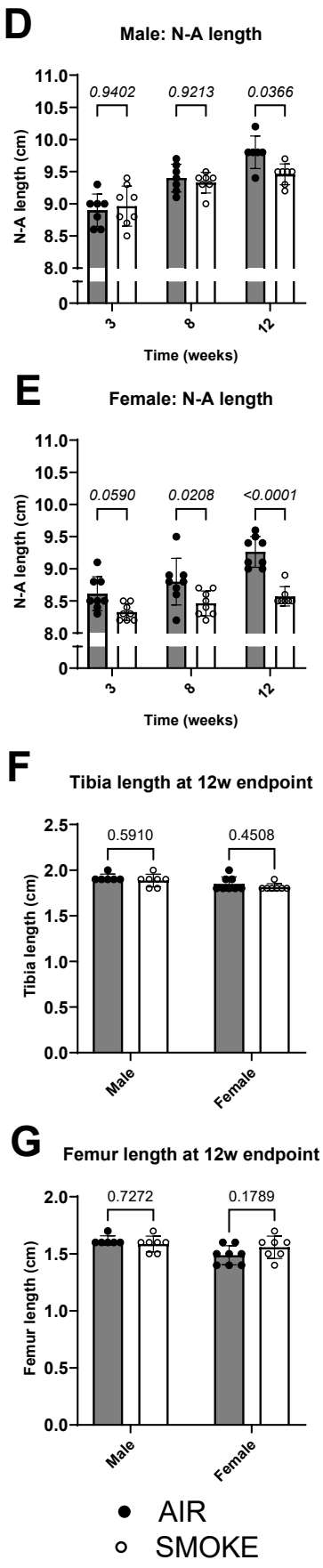
D
Male: N-A length
N-A length (cm)
0.9402
0.9213
0.0366
Time (weeks)
E
Female: N-A length
N-A length (cm)
0.0590
0.0208
<0.0001
Time (weeks)
F
Tibia length at 12w endpoint
Tibia length (cm)
0.5910
0.4508
Male
Female
G
Femur length at 12w endpoint
Femur length (cm)
0.7272
0.1789
Male
Female
AIR
SMOKE

Figure 3.11 Male and female mice from a CS-induced experimental COPD model showed similar levels of impaired development due to CS exposure after 3, 8 and 12 weeks.

CS exposed male and female C57BL/6 mice (n=8) were weighed 5 times per week until the endpoint. N-A was measured on the day of endpoint while the mouse was under anaesthetic. The femur and tibia length were measured on the day of endpoint after lung function. **A-C** Male and female body weight (g) over 3, 8 and 12 weeks (n=8). CS exposed and air control mice were weighed 5 and times per week respectively. **D+E** Male and female N-A length (cm) at endpoint respectively (n=8). **F** Male and female tibia length (cm) at endpoint respectively (n=8). **G** Male and female femur length (cm) at endpoint respectively (n=8). For weight change measurements over time (A-C), A mixed-effect analysis (REML) statistical analysis was performed on data sets. Raw data for the weights over time was provided by the model lead Mounika Guntipally. For length measurements (D-G), ordinary two-way Anova with Šídák's multiple comparisons test statistical analysis was performed on each data set. Individual values were graphed with mean **±** SD displayed. Results with a P-value≤0.05 were considered significant (**P≤0.01; ***P≤0.001, ****=P≤0.0001).

3.3.7 Male and female mice from a CS-induced experimental COPD model showed similar decreases in skeletal muscle mass due to CS exposure after 3, 8 and 12 weeks.

Male and female C57BL/6 female mice were exposed to smoke from 12 cigarettes twice daily, 5d/week for time points of 3, 8 and 12w. Skeletal muscle from male and female mice was collected and weighed on the day of endpoint.

There was a decrease in gastrocnemius weight across all time points for male and female mice exposed to CS vs air control groups (Figure 3.12: A+B). The grouped effect (combined effect across all time points) of CS vs air exposure was an overall CS exposure-induced decrease in female and male gastrocnemius weight ($P<0.0001$ and $P<0.0001$ respectively; Figure 3.12: A+B)

CS exposure did significantly decrease quadriceps weight for male mice at every time point compared to air control groups (Figure 3.12: C). Conversely, there was no significant decrease in quadriceps weight in female mice at any individual time point (Figure 3.12: D), however the grouped effect (combined effect across all time points) of CS vs air exposure was an overall CS exposure-induced decrease in male and female quadricep weight ($P<0.0001$ and $P=0.0024$ respectively; Figure 3.12:C+D).

There was a significant decrease in male and female soleus weight after 8w CS-exposure vs air control, but not at 3 or 12w (Figure 3.12: E+F). The grouped effect of CS exposure for male and female mice across all time points was a significant decrease in soleus weight compared to air exposed mice ($P=0.0026$. and $P=0.0043$ respectively; Figure 3.12: E+F).

There was a significant difference in male EDL weight after 8w CS exposure compared to air exposure, but not at 3 or 12w (Figure 3.12: G). There was no significant difference in female EDL weight at any time point (Figure 3.12: H). However, the grouped effect of CS exposure for male

mice, but not female mice, across all time points was a significant decrease in EDL weight compared to air exposed mice (P=0.0026 and P=0.4873 respectively; Figure 3.12: G+H).

Male mice had higher average gastrocnemius, quadricep, soleus and EDL muscle weights (Figure 3.12: A, C, E + G) at all time points regardless of exposure vs females (Figure 3.12: B, D, F + H). Thus, CS-exposure across all timepoints can negatively impact skeletal muscle growth in both male and female mice.

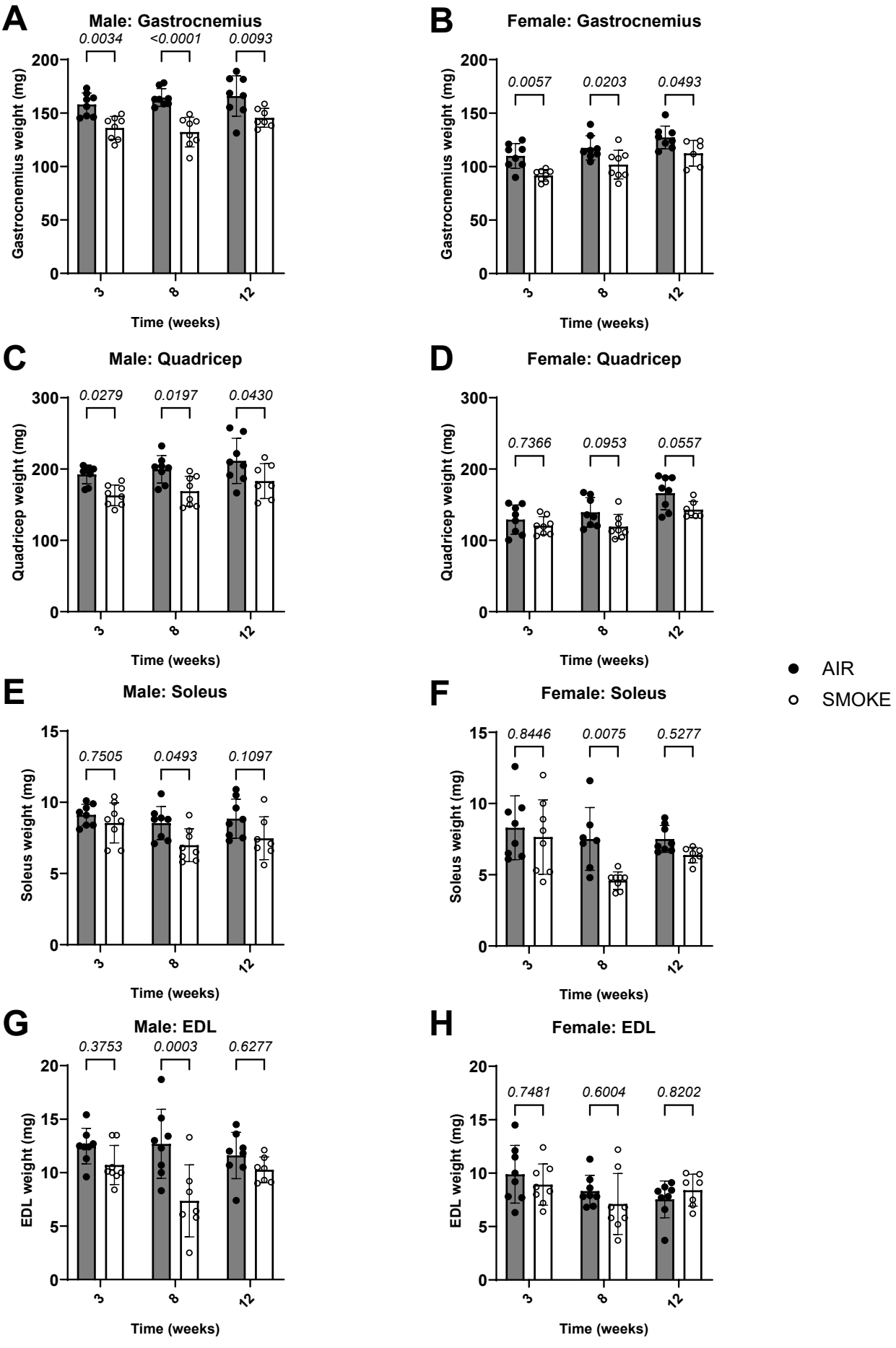
A
Male: Gastrocnemius
0.0034
<0.0001
0.0093
Gastrocnemius weight (mg)
Time (weeks)
B
Female: Gastrocnemius
0.0057
0.0203
0.0493
Gastrocnemius weight (mg)
Time (weeks)
C
Male: Quadricep
0.0279
0.0197
0.0430
Quadricep weight (mg)
Time (weeks)
D
Female: Quadricep
0.7366
0.0953
0.0557
Quadricep weight (mg)
Time (weeks)
E
Male: Soleus
0.7505
0.0493
0.1097
Soleus weight (mg)
Time (weeks)
F
Female: Soleus
0.8446
0.0075
0.5277
Soleus weight (mg)
Time (weeks)
G
Male: EDL
0.3753
0.0003
0.6277
EDL weight (mg)
Time (weeks)
H
Female: EDL
0.7481
0.6004
0.8202
EDL weight (mg)
Time (weeks)
AIR
SMOKE

Figure 3.12 Male and female mice from a CS-induced experimental COPD model showed similar decreases in skeletal muscle mass due to CS exposure after 3, 8 and 12 weeks.

Skeletal muscles from male and female C57BL/6 mice (n=8) were collected on the day of endpoint and immediately weighed **A+B** Male and female gastrocnemius weight (mg) at endpoint respectively **C+D** Male and female quadricep weight (mg) at endpoint respectively **E+F** Male and female soleus weight (mg) at endpoint respectively. **G+H** Male and female extensor digitorum longus (EDL) weight (mg) at endpoint respectively. Ordinary two-way Anova was performed to get the grouped effect of CS vs air exposure and Šídák's multiple comparisons test statistical analysis was performed on each time point. Individual values were graphed with mean **±** SD displayed. Results with a P-value≤0.05 were considered significant.

3.4 Mouse models of IPF, asthma and COPD: Protein analysis of the quadriceps.

Quadriceps were picked for protein analysis as they are commonly chosen as sites for biopsies from patients with sarcopenia and cachexia and provide the most tissue so follow up experiments could be conducted.

3.4.1 There were no changes to protein degradation-associated protein levels in quadriceps of mice from a single dose bleomycin experimental IPF model after 4w

C57BL/6 mice were challenged with a single i.n. dose of bleomycin or. PBS and the quadriceps were collected 4w later. Quadriceps from the 4w, rather than the 10w, model were chosen for protein analysis as there was no significant skeletal muscle weight difference between the 4 and 10w models. Furthermore, short time points (2-4w) for murine models of IPF are more commonly used, as there is less resolution of fibrosis [170].

There were no observed changes to MuRF1 (Figure 3.13: A), Atrogin-1 (Figure 3.13: B), or GADD45α (Figure 3.13: C) protein expression with any condition. All densitometric data were based on the membrane images shown (Figure 3.13: D).

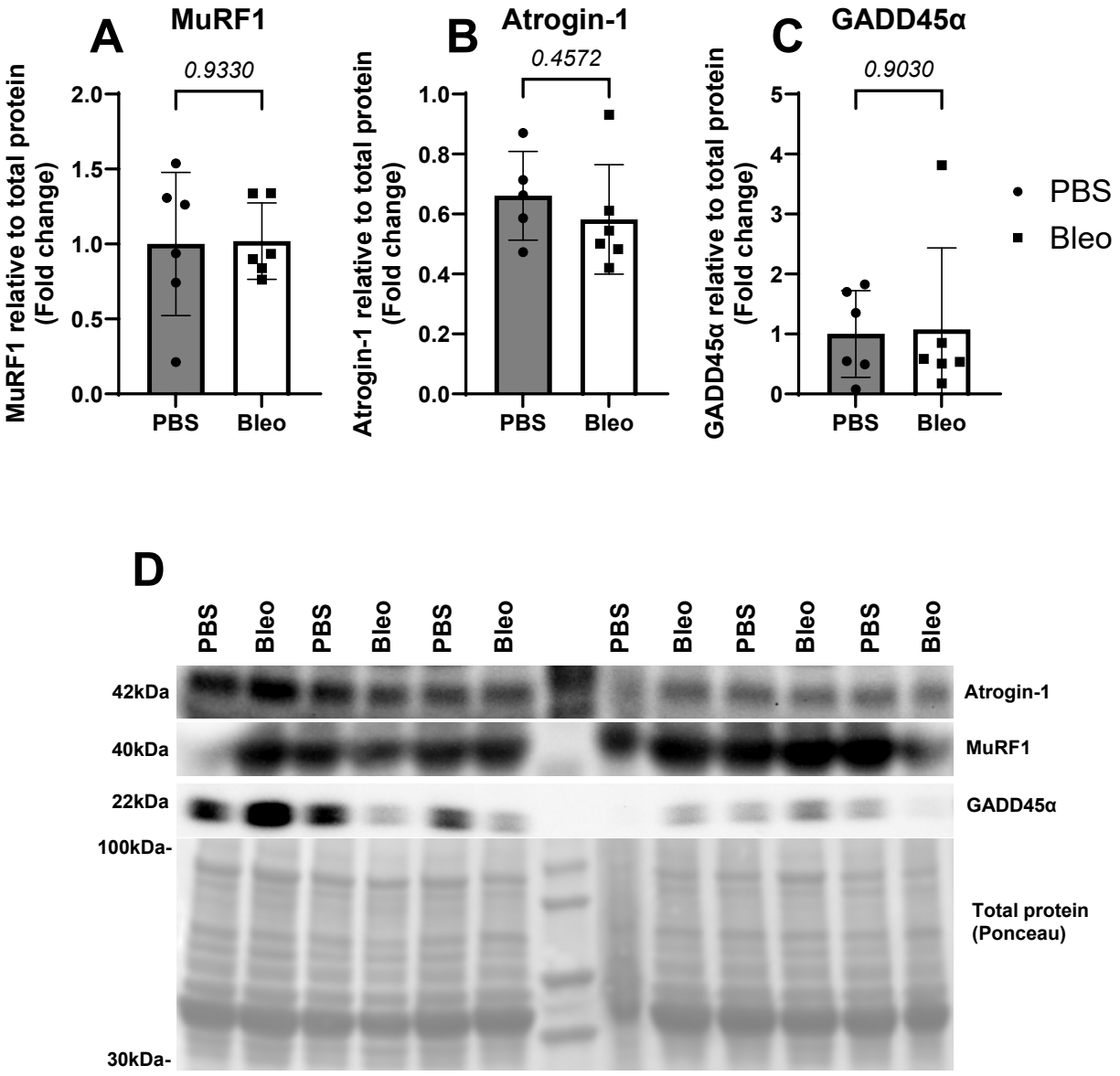

Figure 3.13 There were no changes to protein degradation-associated protein levels in quadriceps of mice from a single dose bleomycin experimental IPF model after 4w.

Immunoblot analysis was used to assess the abundance of protein degradation associated proteins in the quadriceps from female C57BL/6 mice (n=6). Densitometric analysis was performed on membranes for **A** MuRF1. **B** Atrogin-1 and **C** GADD45α relative to total protein. **D** Membrane images of MuRF1 (40kDa), Atrogin-1 (42kDa) and GADD45α (22kDa) with their respective total protein stain (Ponceau) used to normalise band intensity for densitometric analysis. An unpaired t test statistical analysis was performed on each data set. Individual values were graphed with mean ± SD displayed. Results with a P-value≤0.05 were considered significant.

3.4.2 STING protein abundance was reduced in the quadriceps of mice from a single dose bleomycin experimental IPF model after 4w compared.

C57BL/6 mice were challenged with a single i.n. dose of bleomycin or. PBS and the quadriceps were collected 4w later. There was no significant change in cGAS protein expression between the bleomycin and PBS (control) groups (Figure 3.14: A), however, there was a significant decrease in STING protein levels in the quadriceps of bleomycin challenged mice compared to the PBS control (Figure 3.14: B). All densitometric data were based on the membrane images shown (Figure 3.14: C).

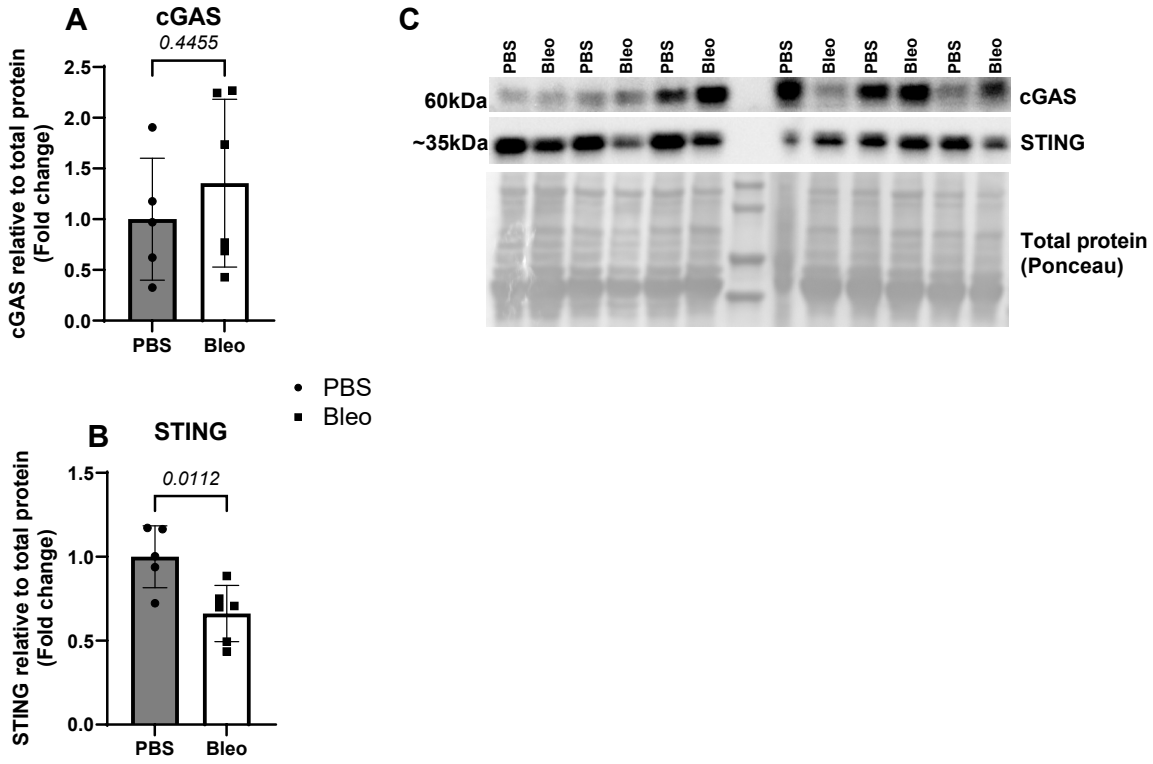

Figure 3.14 STING protein abundance was reduced in the quadriceps of mice from a single dose bleomycin experimental IPF model after 4w compared.

Immunoblot analysis was used to assess the abundance of cGAS and STING proteins in the quadriceps from female C57BL/6 mice (n=6). Densitometric analysis was performed on membranes for **A** cGAS and **B** STING relative to total protein. **C** Membrane images of cGAS (60kDa)

and STING (42kDa) with their respective total protein stain (Ponceau) used to normalise band intensity for densitometric analysis. An unpaired t test statistical analysis was performed on each data set. Individual values were graphed with mean ± SD displayed. Results with a P-value≤0.05 were considered significant.

3.4.3 mTOR, Akt and phosphorylated p-Akt protein levels were unchanged in quadriceps of mice from a single dose bleomycin experimental IPF model after 4w.

C57BL/6 mice were challenged with a single i.n. dose of bleomycin or. PBS and the quadriceps were collected 4w later. There was no significant change in total Akt protein, or Akt activation, as measured by Thr308Akt and Ser473Akt abundance (Figure 3.15: B+E) and their relative expression to total Akt protein (Figure 3.15: C+F). There was also no change in mTOR protein expression (Figure 3.15: D). All densitometric data were based on the membrane images shown (Figure 3.15: G). These results suggest no change in upstream activation of Akt or modulation of total mTOR protein 4w post-bleomycin challenge.

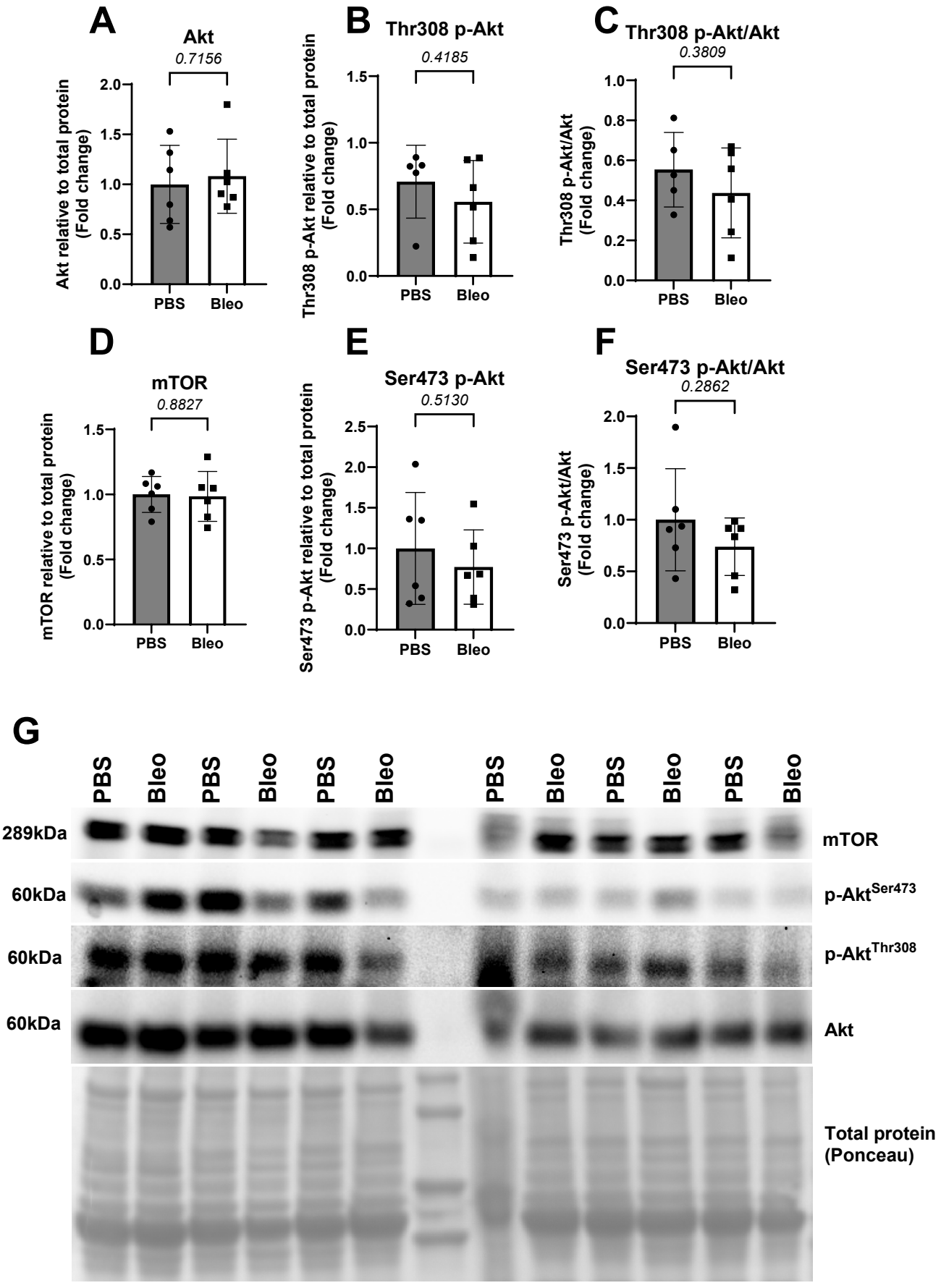
A
Akt
0.7156
Akt relative to total protein (Fold change)
PBS
Bleo
B
Thr308 p-Akt
0.4185
Thr308 p-Akt relative to total protein (Fold change)
C
Thr308 p-Akt/Akt
0.3809
Thr308 p-Akt/Akt (Fold change)
D
mTOR
0.8827
mTOR relative to total protein (Fold change)
E
Ser473 p-Akt
0.5130
Ser473 p-Akt relative to total protein (Fold change)
F
Ser473 p-Akt/Akt
0.2862
Ser473 p-Akt/Akt (Fold change)
G
289kDa
mTOR
60kDa
p-Akt^Ser473
60kDa
p-Akt^Thr308
60kDa
Akt
Total protein (Ponceau)

Figure 3.15 mTOR, Akt and phosphorylated p-Akt protein levels were unchanged in quadriceps of mice from a single dose bleomycin experimental IPF model after 4w.

Immunoblot analysis was used to assess the abundance of mTOR and Akt and p-Akt protein abundance in the quadriceps from female C57BL/6 mice (n=6). Densitometric analysis was performed on membranes for **A** Akt, **B** p-Akt^{Thr308} **C** p-Akt^{Thr308}/Akt **D** p-AKT^{Ser473} **E** p-Akt^{Ser473}/Akt and **F** mTOR relative to total protein. **G** Western blot membrane images with their respective total protein stain (ponceau) used to normalise band intensity for densitometric analysis. An unpaired t test statistical analysis was performed on each data set. Individual values were graphed with mean ± SD displayed. Results with a P-value≤0.05 were considered significant.

3.4.4 Abundance and activation of downstream effector proteins of mTORC1 were unchanged in quadriceps of mice from a single dose bleomycin experimental IPF model after 4w.

C57BL/6 mice were challenged with a single i.n. dose of bleomycin or. PBS and the quadriceps were collected 4w later. mTORC1 activates S6K by phosphorylation of Thr389, however there were no significant changes to total S6K protein or its activation (Figure 3.16: A-C). Activated S6K can phosphorylate rpS6 at Ser235/236, resulting in increased protein synthesis. As there was no change to S6K activation it would not be expected for rpS6 to be activated either, and indeed there was no significant change in rpS6 total protein abundance or it's activation (Figure 3.16: D-F). 4E-BP1, which binds and negatively regulates eIF-4E, can be phosphorylated at Thr37/46 by mTORC1. This results in 4E-BP1 decoupling from eIF-4E, allowing eIF-4E to participate in protein translation. However, there was no observed change in 4E-BP1 total protein abundance or its activation (Figure 3.16: G-I). Together these results indicate that 4w post bleomycin challenge there is no change to mTORC1 activity, and that downstream protein synthesis is not modulated in the quadriceps of these mice.

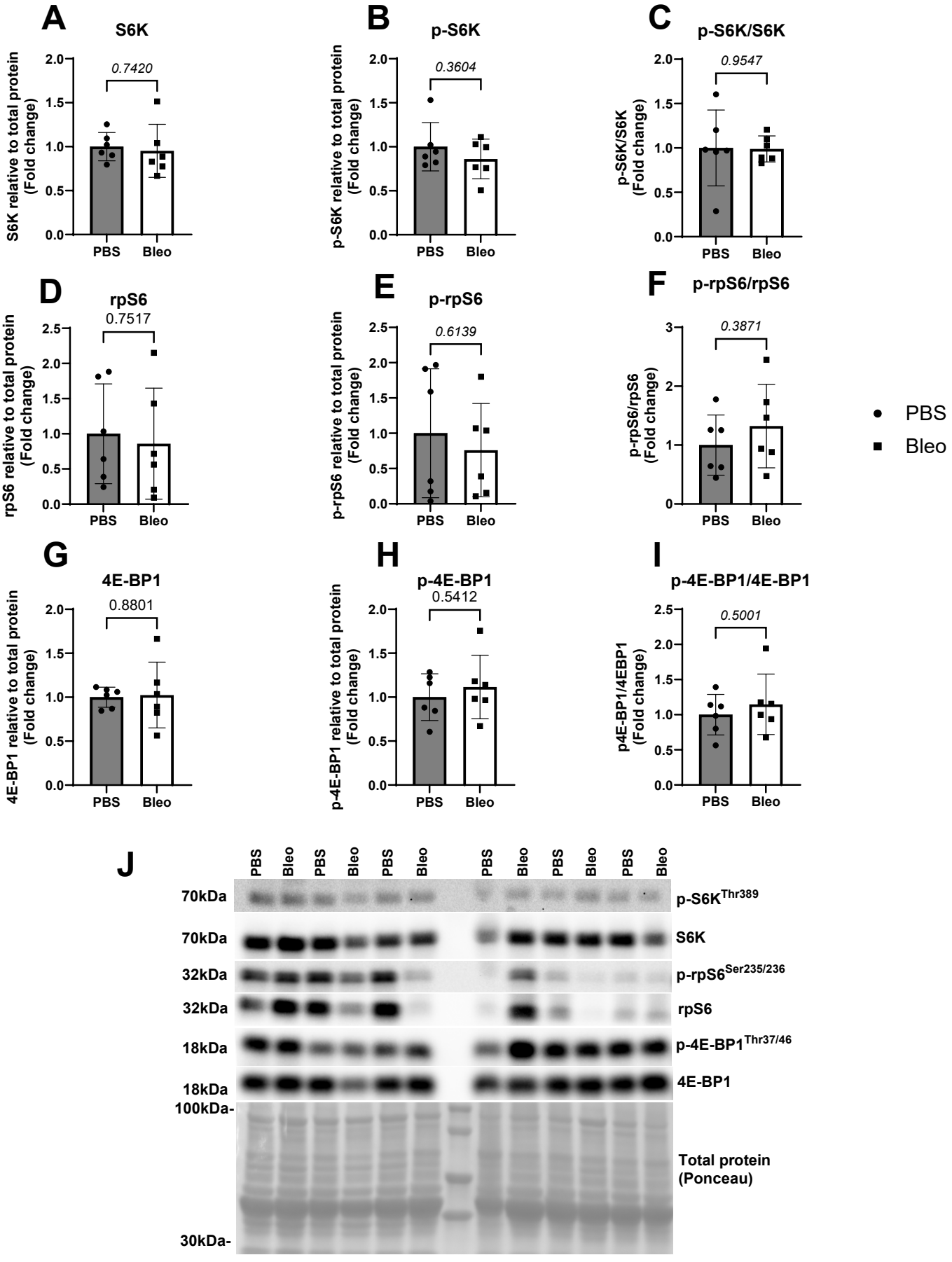
A
S6K
S6K relative to total protein (Fold change)
0.7420
PBS
Bleo
B
p-S6K
p-S6K relative to total protein (Fold change)
0.3604
C
p-S6K/S6K
p-S6K/S6K (Fold change)
0.9547
D
rpS6
0.7517
rpS6 relative to total protein (Fold change)
E
p-rpS6
p-rpS6 relative to total protein (Fold change)
0.6139
F
p-rpS6/rpS6
p-rpS6/rpS6 (Fold change)
0.3871
G
4E-BP1
0.8801
4E-BP1 relative to total protein (Fold change)
H
p-4E-BP1
0.5412
p-4E-BP1 relative to total protein (Fold change)
I
p-4E-BP1/4E-BP1
p4E-BP1/4EBP1 (Fold change)
0.5001
PBS
Bleo
J
70kDa
p-S6K Thr389
S6K
32kDa
p-rpS6 Ser235/236
rpS6
18kDa
p-4E-BP1 Thr37/46
4E-BP1
100kDa-
30kDa-
Total protein (Ponceau)

Figure 3.16 Abundance and phosphorylation of downstream effector proteins of mTORC1 were unchanged in quadriceps of mice from a single dose bleomycin experimental IPF model after 4w.

Immunoblot analysis was used to assess the abundance and activation of downstream effectors of mTORC1 in the quadriceps from female C57BL/6 mice (n=6). Densitometric analysis was performed on membranes for **A** S6K **B** p-S6K^{Thr389}**C** p-S6K^{Thr389}/ S6K **D** rpS6 **E** p-rpS6$^{Ser235/236}$ **F** p-rpS6$^{Ser235/236}$/rpS6 **G** 4E-BP1 **H** p-4E-BP1$^{Thr37/46}$ and **I** p-4E-BP1$^{Thr37/46}$/4E-BP1 abundance relative to total protein **J**. Western blot membrane images with their respective total protein stain (ponceau) used to normalise band intensity for densitometry. An unpaired t test statistical analysis was performed on each data set. Individual values were graphed with mean ± SD displayed. Results with a P-value≤0.05 were considered significant.

3.4.5 There were no changes to protein degradation-associated protein levels in quadriceps of mice from an experimental moderate and severe asthma model

Moderate (steroid sensitive) and severe (steroid insensitive) asthma was induced in BALB/c mice and quadriceps were collected for the protein analysis. by western blot analysis. There were no observed changes to MuRF1, Atrogin-1, or GADD45α protein expression (Figure 3.17: A-C).

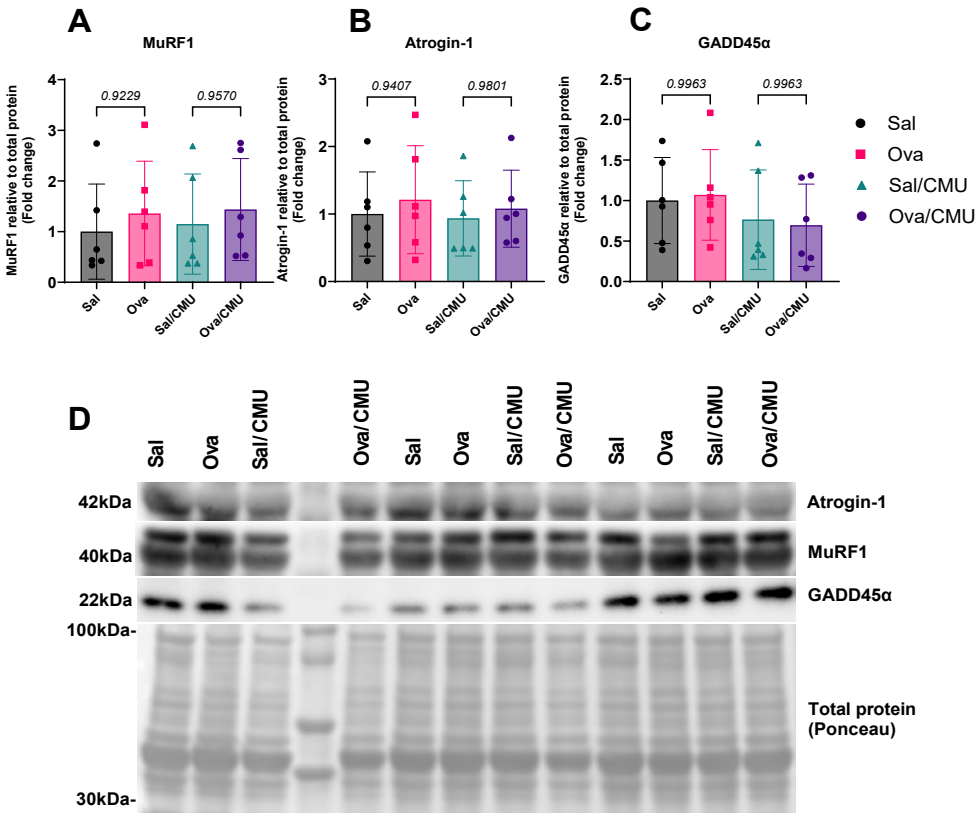

Figure 3.17 There were no changes to protein degradation-associated protein levels in quadriceps of mice from an experimental moderate and severe asthma model.

Immunoblot analysis was used to assess the abundance of protein degradation associated proteins in the quadriceps of female BALB/c mice (n=6) with moderate and severe asthma. Densitometric analysis was performed on membranes for **A** MuRF1 **B** Atrogin-1 and **C** GADD45α relative to total protein. **D** Membrane images of MuRF1 (40kDa), Atrogin-1 (42kDa) and GADD45α (22kDa) with their respective total protein stain (ponceau) used to normalise band intensity for densitometric analysis. An unpaired t test statistical analysis was performed on each data set. Individual values were graphed with mean ± SD displayed. Results with a P-value≤0.05 were considered significant.

3.4.6 There were no changes to cGAS or STING protein levels in quadriceps of mice from an experimental moderate and severe asthma model.

Quadriceps were assessed for the abundance of cGAS and STING protein by western blot analysis. There was no change in protein abundance of cGAS or STING with the induction of moderate or severe asthma compared to their respective controls (Figure 3.18: A-C)).

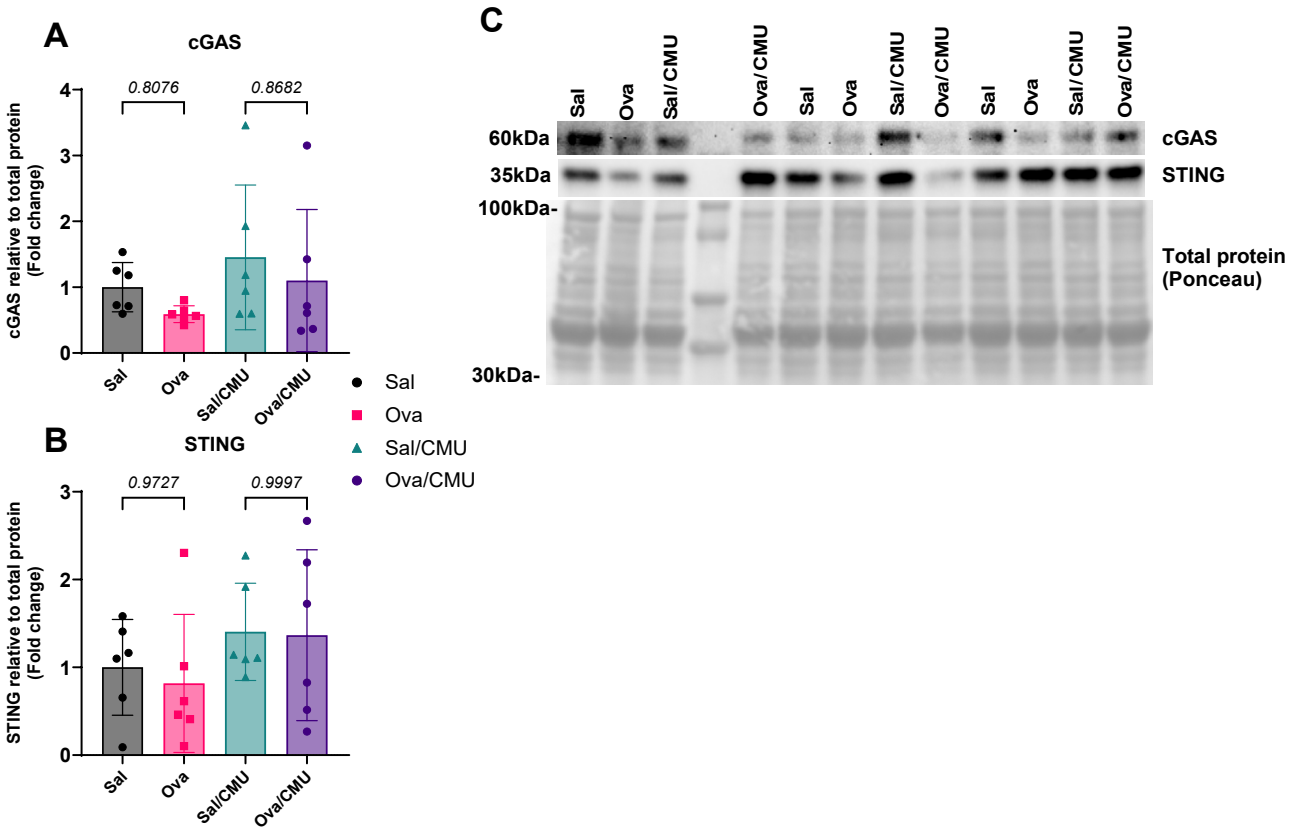

Figure 3.18 There were no changes to cGAS or STING protein levels in quadriceps of mice from an experimental moderate and severe asthma model

Immunoblot analysis was used to assess the abundance of cGAS and STING proteins in the quadriceps of female BALB/c mice (n=6) with moderate and severe asthma. Densitometric analysis was performed on membranes for **A** cGAS and **B** STING relative to total protein. **C** Membrane images of cGAS (60kDa) and STING (42kDa) with their respective total protein stain (ponceau) used to normalise band intensity for densitometric analysis. An unpaired t test statistical analysis was performed on each data set. Individual values were graphed with mean ± SD displayed. Results with a P-value≤0.05 were considered significant.

3.4.7 mTOR, Akt and phosphorylated p-Akt protein levels were unchanged in quadriceps of mice from an experimental moderate and severe asthma model.

Both a moderate and severe asthma model were conducted using BALB/c mice. Moderate asthma was induced through ovalbumin sensitisation (i.p.) and challenge (i.n.). Severe asthma was induced through a combination of ovalbumin sensitisation and challenge and CMU respiratory infection. There was no significant change in total Akt protein (Figure 3.19: A) or it's activation through phosphorylation of Thr308 (Figure 3.19: B) or Ser473 (Figure 3.19: D) amino acid sites, or the ratio of phosphorylated Akt to Akt (Figure 3.19: C+E). Increased phosphorylation of sites results in increased Akt activity and subsequent activation of mTOR, especially mTORC1. No change in total mTOR protein was observed, and so further downstream effector molecules of the Akt-mTOR pathway were investigated (Figure 3.19).

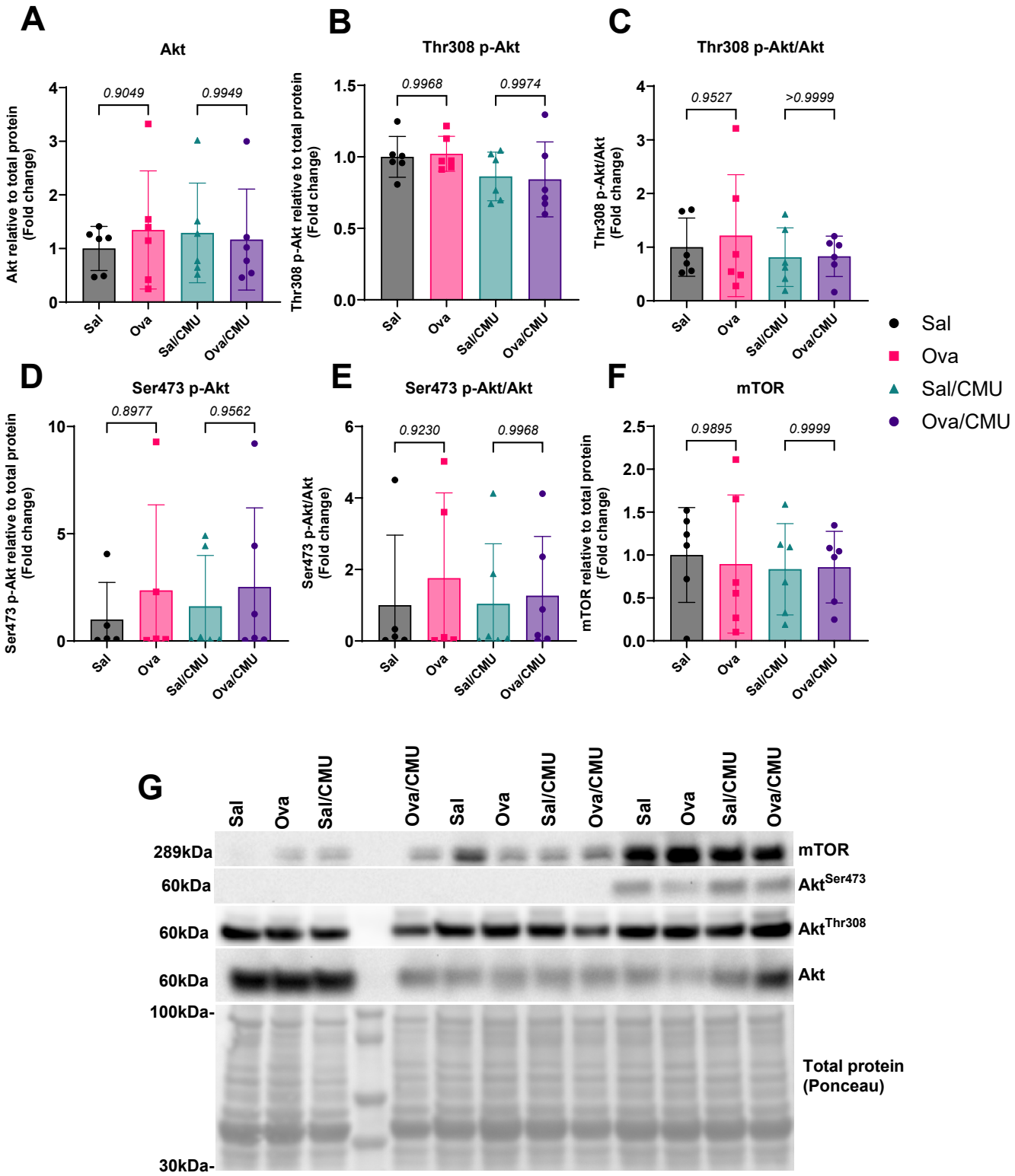
A
Akt
Akt relative to total protein (Fold change)
0.9049
0.9949
B
Thr308 p-Akt
Thr308 p-Akt relative to total protein (Fold change)
0.9968
0.9974
C
Thr308 p-Akt/Akt
Thr308 p-Akt/Akt (Fold change)
0.9527
>0.9999
D
Ser473 p-Akt
Ser473 p-Akt relative to total protein (Fold change)
0.8977
0.9562
E
Ser473 p-Akt/Akt
Ser473 p-Akt/Akt (Fold change)
0.9230
0.9968
F
mTOR
mTOR relative to total protein (Fold change)
0.9895
0.9999
Sal
Ova
Sal/CMU
Ova/CMU
G
289kDa
60kDa
60kDa
60kDa
100kDa-
30kDa-
mTOR
Akt^Ser473
Akt^Thr308
Akt
Total protein (Ponceau)

Figure 3.19 mTOR, Akt and phosphorylated p-Akt protein levels were unchanged in quadriceps of mice from an experimental moderate and severe asthma model.

Immunoblot analysis was used to assess mTOR and Akt and p-Akt protein abundance in the quadriceps of female BALB/c mice (n=6) with moderate and severe asthma. Densitometric analysis was performed on membranes for **A** Akt, **B** p-Akt^{Thr308} **C** p-Akt^{Thr308}/Akt **D** p-AKT^{Ser473} **E** p-Akt^{Ser473}/Akt and **F** mTOR relative to total protein. **G** Western blot membrane images with their respective total protein stain (ponceau) used to normalise band intensity for densitometric analysis. An unpaired t test statistical analysis was performed on each data set. Individual values were graphed with mean ± SD displayed. Results with a P-value≤0.05 were considered significant.

3.4.8 Abundance and activation of downstream effector proteins of mTORC1 were unchanged in quadriceps of mice from an experimental moderate and severe asthma model

Both a moderate and severe asthma model were conducted using BALB/c mice. Moderate asthma was induced through ovalbumin sensitisation (i.p.) and challenge (i.n.). Severe asthma was induced by ovalbumin sensitisation, challenge and CMU respiratory infection. mTORC1 activates S6K by phosphorylation of Thr389, however there were no significant changes to total S6K protein or its activation in moderate or severe asthma (Figure 3.20: A-C). Activated S6K can phosphorylate rpS6 at Ser235/236, resulting in increased protein synthesis. As there was no change to S6K activation it would not be expected for rpS6 to be activated either, and indeed there was no significant change in rpS6 total protein abundance or it's activation in moderate or severe asthma (Figure 3.20: D-F). 4E-BP1, which binds and negatively regulates eIF-4E, can be phosphorylated at Thr37/46 by mTORC1. This results in 4E-BP1 decoupling from eIF-4E, allowing eIF-4E to participate in protein translation. However, there was no observed change in 4E-BP1 total protein abundance or its activation in moderate or severe asthma (Figure 3.20: G-I). Altogether, these results indicate that these murine models of asthma do not change mTORC1 activity in the quadriceps, and that there was no observed modulation of protein synthesis.

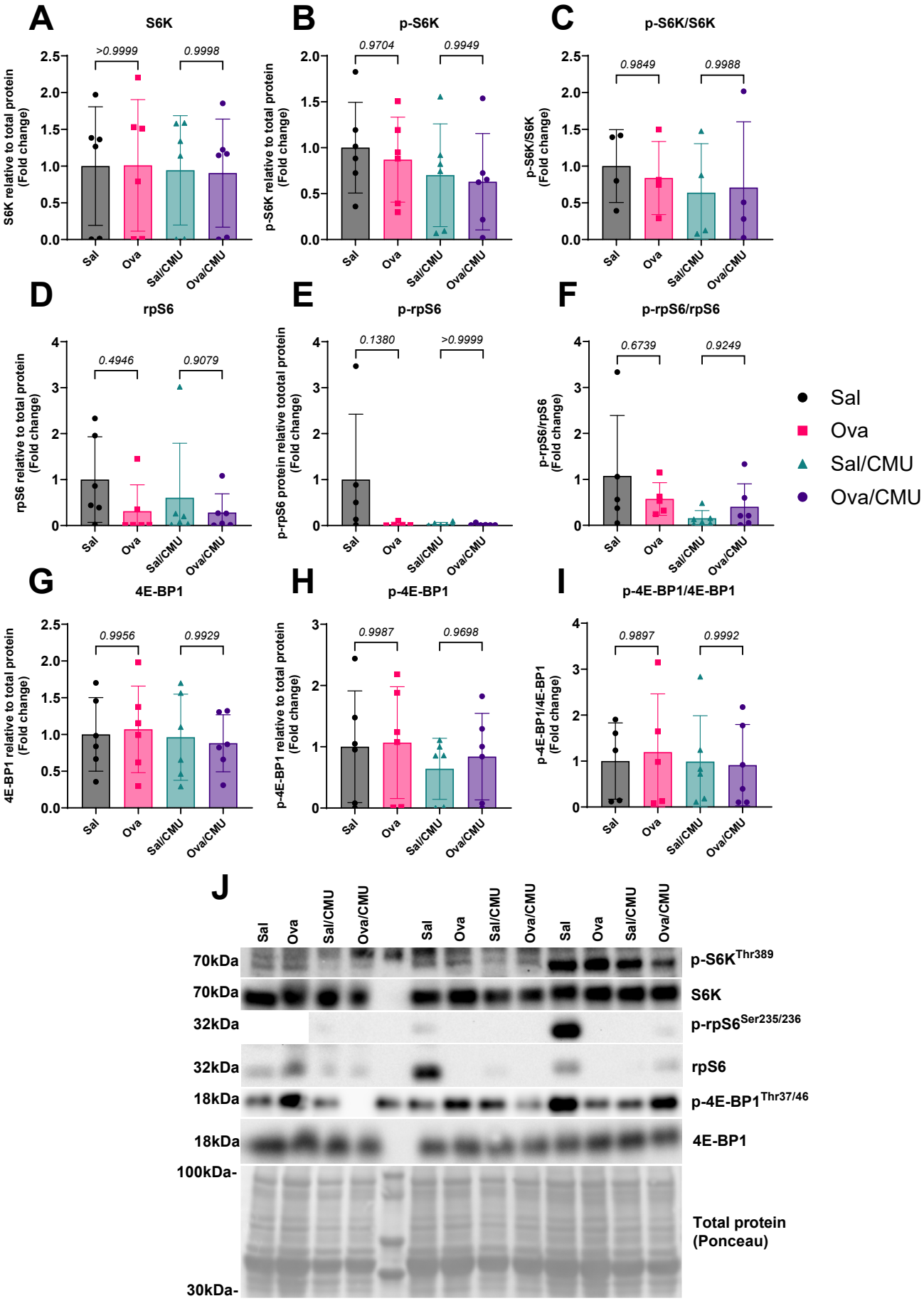
A
S6K
S6K relative to total protein (Fold change)
>0.9999
0.9998
B
p-S6K
p-S6K relative to total protein (Fold change)
0.9704
0.9949
C
p-S6K/S6K
p-S6K/S6K (Fold change)
0.9849
0.9988
D
rpS6
rpS6 relative to total protein (Fold change)
0.4946
0.9079
E
p-rpS6
p-rpS6 protein relative tototal protein (Fold change)
0.1380
>0.9999
F
p-rpS6/rpS6
p-rpS6/rpS6 (Fold change)
0.6739
0.9249
G
4E-BP1
4E-BP1 relative to total protein (Fold change)
0.9956
0.9929
H
p-4E-BP1
p-4E-BP1 relative to total protein (Fold change)
0.9987
0.9698
I
p-4E-BP1/4E-BP1
p-4E-BP1/4E-BP1 (Fold change)
0.9897
0.9992
Sal
Ova
Sal/CMU
Ova/CMU
J
70kDa
p-S6K Thr389
70kDa
S6K
32kDa
p-rpS6 Ser235/236
32kDa
rpS6
18kDa
p-4E-BP1 Thr37/46
18kDa
4E-BP1
100kDa-
30kDa-
Total protein (Ponceau)

Figure 3.20 Abundance and activation of downstream effector proteins of mTORC1 were unchanged in quadriceps of mice from an experimental moderate and severe asthma model.

Immunoblot analysis was used to assess the the abundance and activation of downstream effectors of mTORC1 in the quadriceps of female BALB/c mice (n=6) with moderate and severe asthma. Densitometric analysis was performed on membranes for **A** S6K **B** p-S6K^{Thr389}**C** p-S6K^{Thr389}/ S6K **D** rpS6 **E** p-rpS6$^{Ser235/236}$ **F** p-rpS6$^{Ser235/236}$/rpS6 **G** 4E-BP1 **H** p-4E-BP1$^{Thr37/46}$ and **I** p-4E-BP1$^{Thr37/46}$/4E-BP1 abundance relative to total protein **J**. Western blot membrane images with their respective total protein stain (ponceau) used to normalise band intensity for densitometric analysis. An unpaired t test statistical analysis was performed on each data set. Individual values were graphed with mean ± SD displayed. Results with a P-value≤0.05 were considered significant.

3.4.9 There were no changes to protein degradation-associated protein levels in quadriceps of female C57BL/6 mice from the 8w time point of the CS-induced experimental COPD time course (3, 8 and 12w) model.

8-weeks of CS exposure in male and female mice resulted in COPD-associated changes in lung function, and impaired whole body and skeletal muscle growth. The male, female experimental CS-induced COPD time course demonstrated similar physiological changes in both sexes and female mice were selected for subsequent experiments. This decision aligned with previous and planned studies in the lab, which primarily used female C57BL/6 mice in COPD models. Utilizing female mice ensured sample availability, minimized the need for redundant experimental repeats, and reduced unnecessary use of animals.

Quadriceps from female C57BL/6 mice exposed to smoke from 12 cigarettes, twice daily for 8 weeks were collected on the day of the endpoint and prepared for western blot analysis. No significant change to MuRF1, Atrogin-1 and GADD45α protein expression was observed (Figure 3.21: A-C).

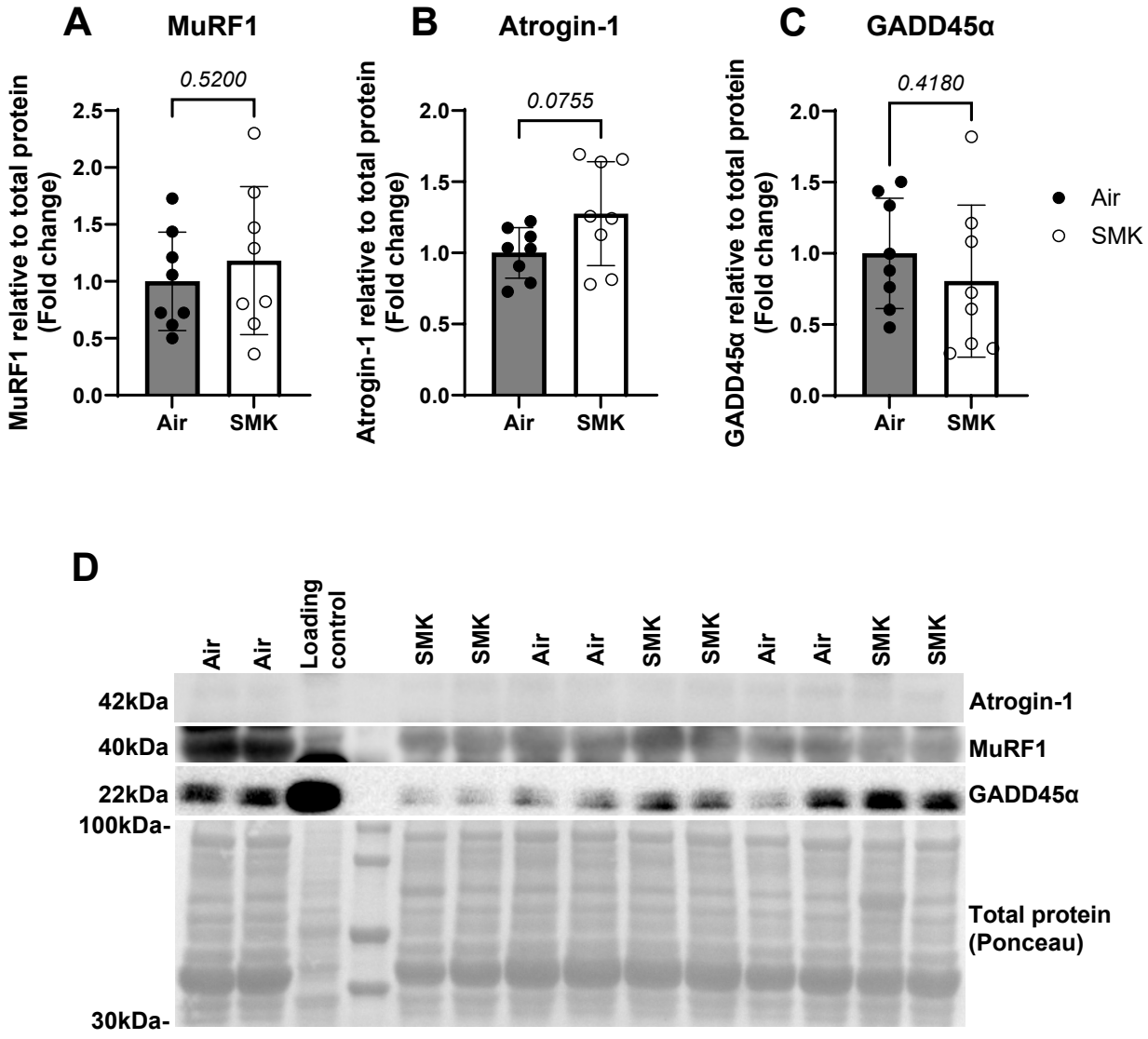

Figure 3.21 There were no changes to protein degradation-associated protein levels in quadriceps of female C57BL/6 mice from the 8w time point of the CS-induced experimental COPD time course (3, 8 and 12w) model.

Immunoblot analysis was used to assess the abundance of protein degradation-associated proteins in the quadriceps from female C57BL/6 mice (n=8) after 8w CS or room air exposure. Densitometric analysis was performed on membranes for **A** MuRF1 **B** Atrogin-1 and **C** GADD45α relative to total protein. **D** Membrane images of Atrogin-1 (42kDa), MuRF1 (40kDa) and GADD45α (22kDa) with their respective total protein stain (ponceau) used to normalise band intensity for densitometric analysis. An unpaired t test statistical analysis was performed on each data set. Individual values were graphed with mean ± SD displayed. Results with a P-value≤0.05 were considered significant.

3.4.10 There were no changes to cGAS or STING protein levels in quadriceps of female C57BL/6 mice from the 8w time point of the CS-induced experimental COPD time course (3, 8 and 12w) model

Quadriceps from female C57BL/6 mice exposed to smoke from 12 cigarettes, twice daily for 8 weeks were collected on the day of the endpoint and prepared for western blot analysis. There were no significant changes in cGAS or STING protein expression (Figure 3.22: A+B), however, two of the CS exposed mice had a significant increase in cGAS and STING protein expression, compared to other mice (Figure3-22: C).

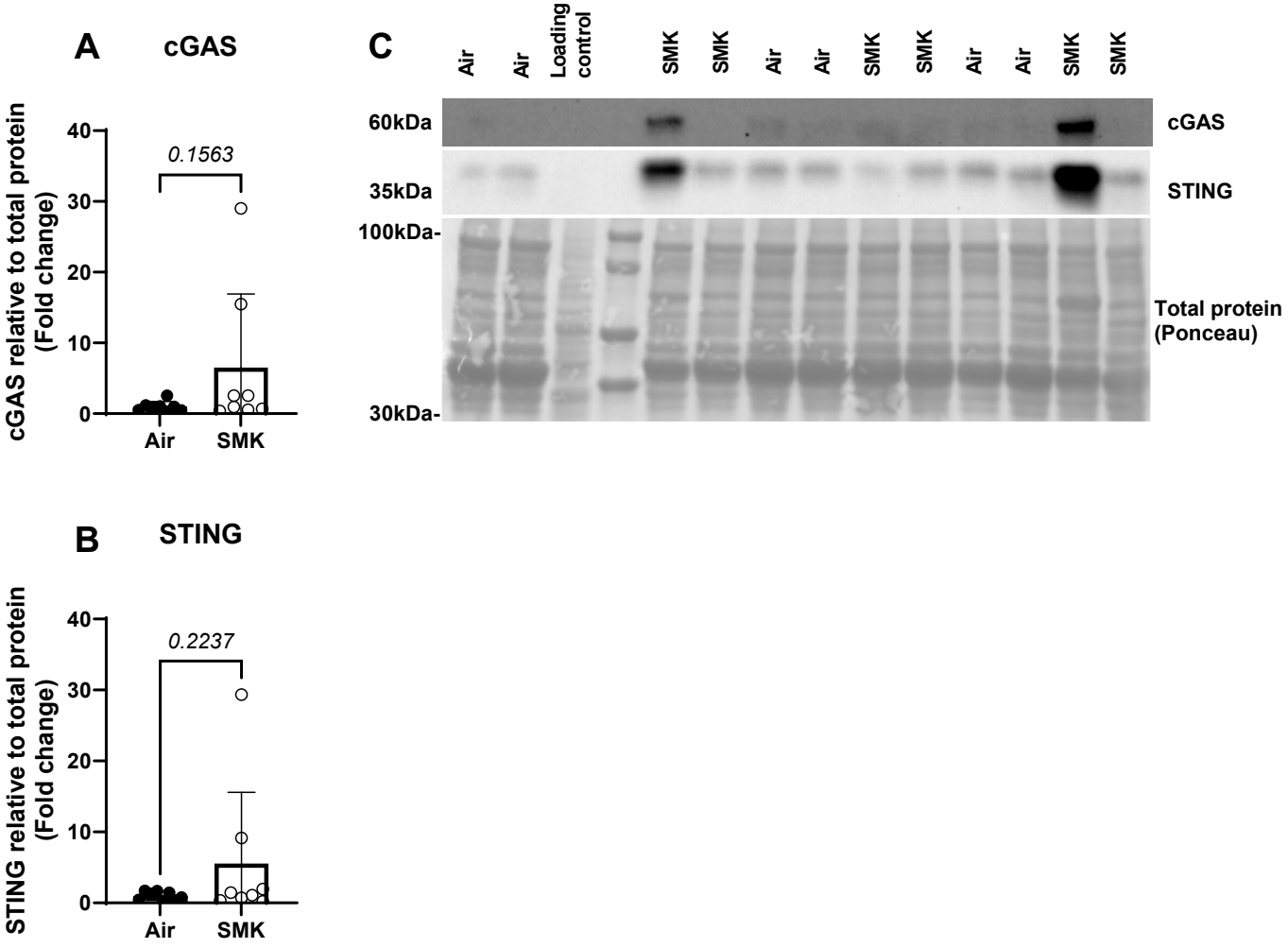

Figure 3.22 There were no changes to cGAS or STING protein levels in quadriceps of female C57BL/6 mice from the 8w time point of the CS-induced experimental COPD time course (3, 8 and 12w) model.

Immunoblot analysis was used to assess the abundance of cGAS and STING proteins in the quadriceps from female C57BL/6 mice (n=8) after 8w CS or room air exposure. Densitometric analysis was performed on membranes for **A** cGAS and **B** STING relative to total protein. **C** Membrane images of cGAS (60kDa) and STING (42kDa) with their respective total protein stain (ponceau) used to normalise band intensity for densitometric analysis. An unpaired t test statistical analysis was performed on each data set. Individual values were graphed with mean ± SD displayed. Results with a P-value≤0.05 were considered significant.

3.4.11 mTOR, Akt and phosphorylated p-Akt protein levels were unchanged in the quadriceps of female C57BL/6 mice from the 8w time point of the CS-induced experimental COPD time course (3, 8 and 12w) model

Quadriceps from female C57BL/6 mice exposed to smoke from 12 cigarettes, twice daily for 8 weeks were collected on the day of the endpoint and prepared for western blot analysis. There was no significant change in total Akt protein (Figure 3.23: A) or it's activation as measured by phosphorylation of Thr308 (Figure 3.23: B) or Ser473 (Figure 3.23: E), or their ratio to total Akt protein (Figure 3.23: C+F). No significant change in total mTOR protein was observed, and so further downstream effector molecules of the Akt-mTOR pathway were investigated (Figure 3.23). These results indicate no changes to the activation of Akt or a modulation of mTOR protein, suggesting no impact of CS exposure on protein synthesis.

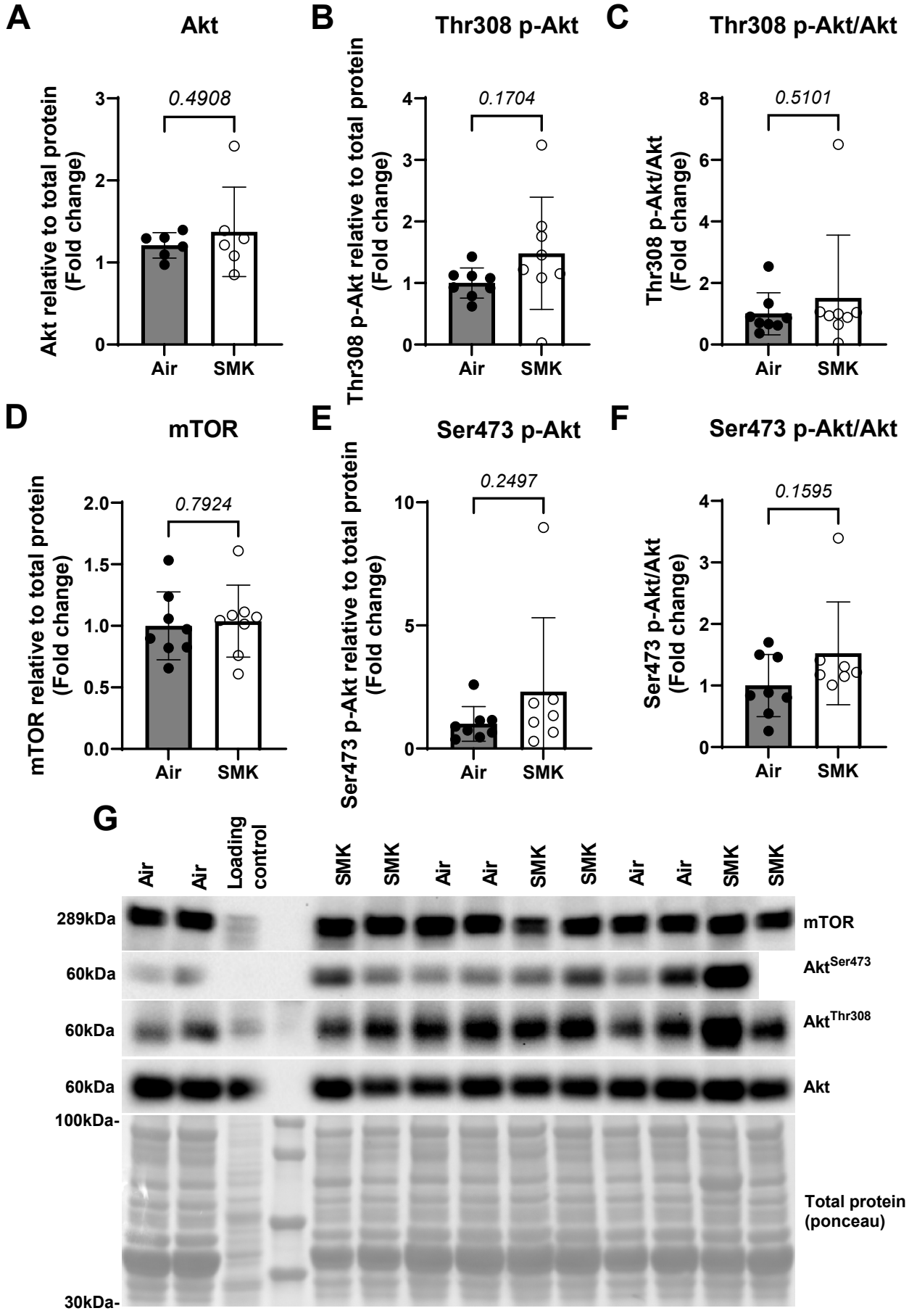
A
Akt
Akt relative to total protein (Fold change)
0.4908
Air
SMK
B
Thr308 p-Akt
Thr308 p-Akt relative to total protein (Fold change)
0.1704
C
Thr308 p-Akt/Akt
Thr308 p-Akt/Akt (Fold change)
0.5101
D
mTOR
mTOR relative to total protein (Fold change)
0.7924
E
Ser473 p-Akt
Ser473 p-Akt relative to total protein (Fold change)
0.2497
F
Ser473 p-Akt/Akt
Ser473 p-Akt/Akt (Fold change)
0.1595
G
Air
Air
Loading control
SMK
SMK
Air
Air
SMK
SMK
Air
Air
SMK
SMK
289kDa
60kDa
60kDa
60kDa
100kDa-
30kDa-
mTOR
Akt^Ser473
Akt^Thr308
Akt
Total protein (ponceau)

Figure 3.23 mTOR, Akt and phosphorylated p-Akt protein levels were unchanged in the quadriceps of female C57BL/6 mice from the 8w time point of the CS-induced experimental COPD time course (3, 8 and 12w) model.

Immunoblot analysis was used to assess mTOR and Akt and p-Akt protein abundance in the quadriceps from female C57BL/6 mice (n=8) after 8w CS or room air exposure. Densitometric analysis was performed on membranes for **A** Akt, **B** p-Akt^{Thr308} **C** p-Akt^{Thr308}/Akt **D** p-AKT^{Ser473} **E** p-Akt^{Ser473}/Akt and **F** mTOR relative to total protein. **G** Western blot membrane images and representative total protein stain (ponceau) used to normalise band intensity for densitometric analysis. An unpaired t test statistical analysis was performed on each data set. Individual values were graphed with mean ± SD displayed. Results with a P-value≤0.05 were considered significant.

3.4.12 Abundance and activation of downstream effector proteins of mTORC1 were not significantly altered in the quadriceps of female C57BL/6 mice from the 8w time point of the CS-induced experimental COPD time course (3, 8 and 12w) model

Quadriceps from female C57BL/6 mice exposed to smoke from 12 cigarettes, twice daily for 8 weeks were collected on the day of the endpoint and prepared for western blot analysis. There was no significant change in total s6 kinase protein (Figure 3.24: A) or its activation (Figure 3.24: B+C). S6 kinase mediates the phosphorylation of rps6 at Ser235/236 but no change in total rps6 (Figure 3.24: D) or its activation (Figure 3.24: E+F) was observed. 4E-BP1 is phosphorylated by activated mTORC1 at Thr37/46 which causes its 4E-BP1 to decouple from eIF4E, allowing for the transcription of more proteins (protein synthesis). No significant change was observed in total 4E-BP1 protein (Figure 3.24: G), p-4E-BP1 (Figure 3.24: H), or the ratio of p-4E-BP1/4E-BP1 (Figure 3.24: I). This would indicate that there was no effect of CS-exposure after 8w on mTORC1 mediated protein synthesis.

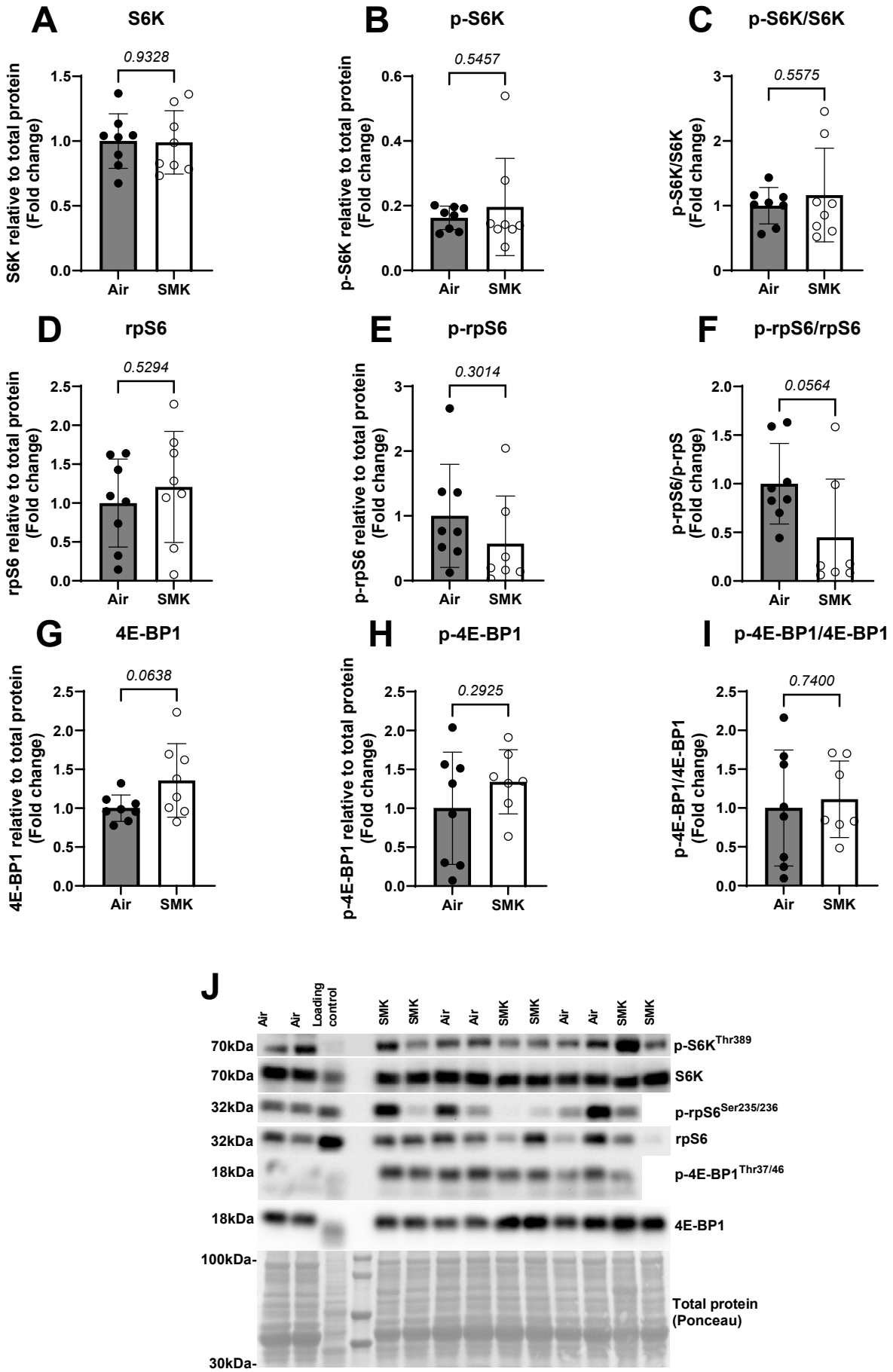
A
S6K
0.9328
S6K relative to total protein (Fold change)
Air
SMK
B
p-S6K
0.5457
p-S6K relative to total protein (Fold change)
C
p-S6K/S6K
0.5575
p-S6K/S6K (Fold change)
D
rpS6
0.5294
rpS6 relative to total protein (Fold change)
E
p-rpS6
0.3014
p-rpS6 relative to total protein (Fold change)
F
p-rpS6/rpS6
0.0564
p-rpS6/p-rpS (Fold change)
G
4E-BP1
0.0638
4E-BP1 relative to total protein (Fold change)
H
p-4E-BP1
0.2925
p-4E-BP1 relative to total protein (Fold change)
I
p-4E-BP1/4E-BP1
0.7400
p-4E-BP1/4E-BP1 (Fold change)
J
Air
Air
Loading control
SMK
SMK
Air
Air
SMK
SMK
Air
Air
SMK
SMK
70kDa
p-S6K Thr389
70kDa
S6K
32kDa
p-rpS6 Ser235/236
32kDa
rpS6
18kDa
p-4E-BP1 Thr37/46
18kDa
4E-BP1
100kDa-
30kDa-
Total protein (Ponceau)

Figure 3.24 Abundance and activation of downstream effector proteins of mTORC1 were not significantly altered in the quadriceps of female C57BL/6 mice from the 8w time point of the CS-induced experimental COPD time course (3, 8 and 12w) model.

Immunoblot analysis was used to assess the abundance and activation of downstream effectors of mTORC1 quadriceps from female C57BL/6 mice (n=8) after 8w CS or room air exposure. Densitometric analysis was performed on membranes for **A** S6K **B** p-S6K^{Thr389}**C** p-S6K^{Thr389}/ S6K **D** rpS6 **E** p-rpS6$^{Ser235/236}$ **F** p-rpS6$^{Ser235/236}$/rpS6 **G** 4E-BP1 **H** p-4E-BP1$^{Thr37/46}$ and **I** p-4E-BP1$^{Thr37/46}$/4E-BP1 abundance relative to total protein. Western blot membrane images with a representative total protein stain (ponceau) used to normalise band intensity for densitometric analysis. An unpaired t test statistical analysis was performed on each data set. Individual values were graphed with mean ± SD displayed. Results with a P-value≤0.05 were considered significant.

3.4.13 Electron transport chain complex V (ATP5A) levels were increased in the quadriceps of female C57BL/6 mice from the 8w time point of the CS-induced experimental COPD time course (3, 8 and 12w) model

Quadriceps from female C57BL/6 mice exposed to smoke from 12 cigarettes, twice daily for 8 weeks were collected on the day of the endpoint and prepared for western blot analysis. There was no significant change in complex I (NDUFB8), complex II (SDHB), complex III (UQRC2), complex IV (MTCO1; Figure 3.25 A-D). However, there was a significant increase in complex V (ATP5A) protein (Figure 3.25: E).

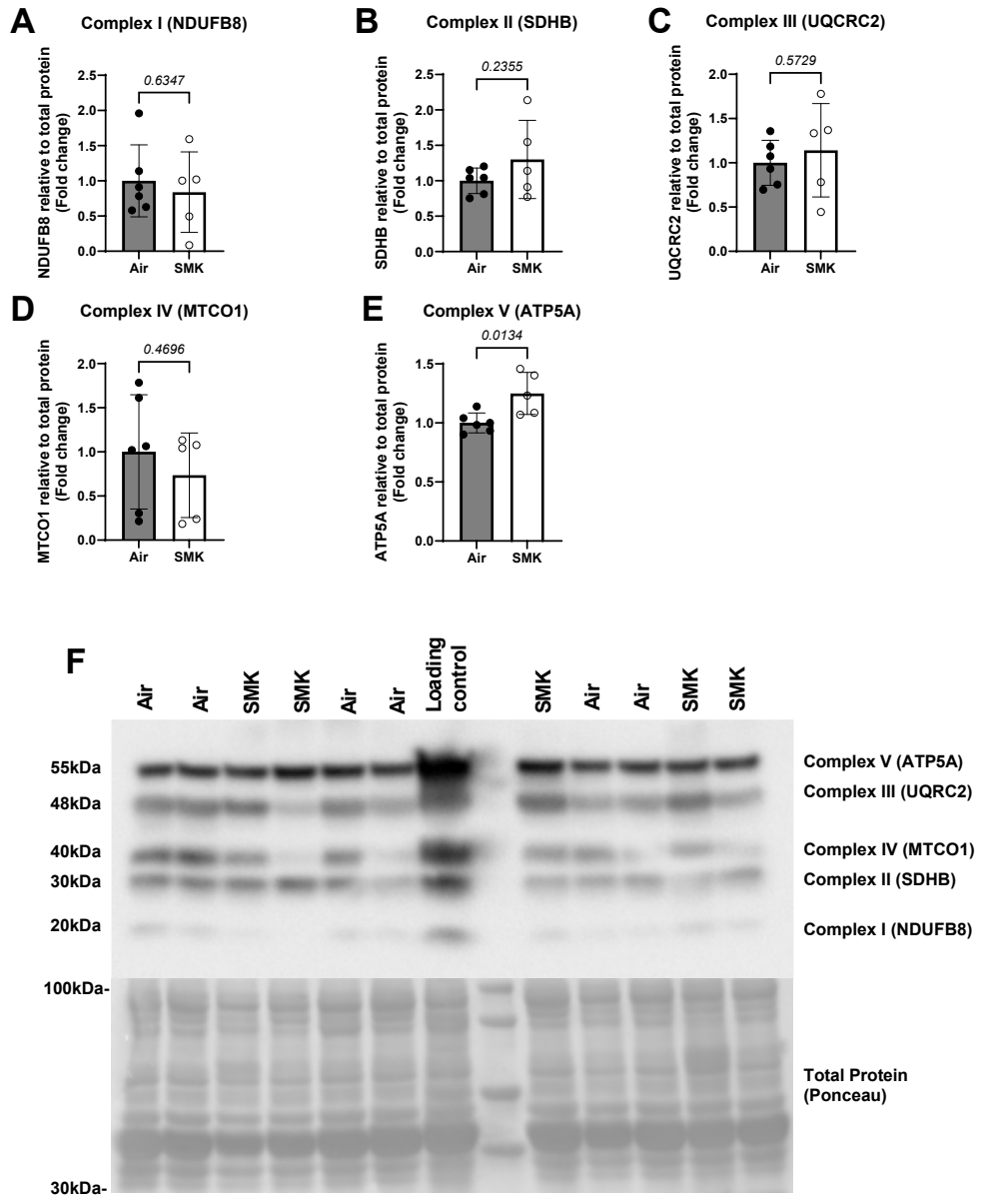

Figure 3.25 Electron transport chain complex V (ATP5A) levels were increased in the quadriceps of female C57BL/6 mice from the 8w time point of the CS-induced experimental COPD time course (3, 8 and 12w) model.

Immunoblot analysis was used to assess the abundance electron transport chain (ETC) complex proteins from female C57BL/6 mice (n=8) after 8w CS or room air exposure. Densitometric analysis was performed on membranes for **A** Complex I (NDUFB8) **B** Complex II (SDHB) **C** Complex III (UQRC2) **D** Complex IV (MTCO1) **E** Complex V (ATP5A). **J** Western blot membrane images with their respective total protein stain (ponceau) used to normalise band intensity for densitometric analysis. An unpaired t test statistical analysis was performed on each data set. Individual values were graphed with mean ± SD displayed. Results with a P-value≤0.05 were considered significant.

3.5 CS-induced experimental COPD time course (3, 8 and 12w) model in male and female mice – RT-qPCR analysis of inflammation and proteolysis related genes in the gastrocnemius and quadriceps

The gastrocnemius and quadriceps were chosen for RT-qPCR analysis because they were consistently lost muscle mass at most time points in both CS-induced experimental COPD time course models. It was decided to also compare female and male mice gene expression to investigate any potential sex differences in the response to CS exposure.

3.5.1 There were no major changes local expression of inflammatory genes in the gastrocnemius and quadriceps of male and female mice of a CS-induced experimental COPD time course model

Male and female C57BL/6 mice were exposed to CS or air (control) for 3w, 8w or 12w. RNA was isolated from gastrocnemius and quadriceps samples from male and female mice exposed to CS vs air control for 3w, 8w and 12w, and reverse transcribed for analysis by qPCR. When comparing the effect of CS exposure vs air exposure in male and female mice quadriceps, the RT-qPCR data revealed few significant changes at 3w, 8w or 12w (Figure 3.26). However, at 12w time point there was significantly higher IL-1β expression in the gastrocnemius of male mice vs female mice exposed to CS (Figure 3.26: C). There was a decrease IL-10 expression in male mice in CS exposed mice vs air control at 3w (Figure 3.26: J). Furthermore, a significant difference in IL-10 expression was also observed between male and female air control mice (Figure 3.26: J).

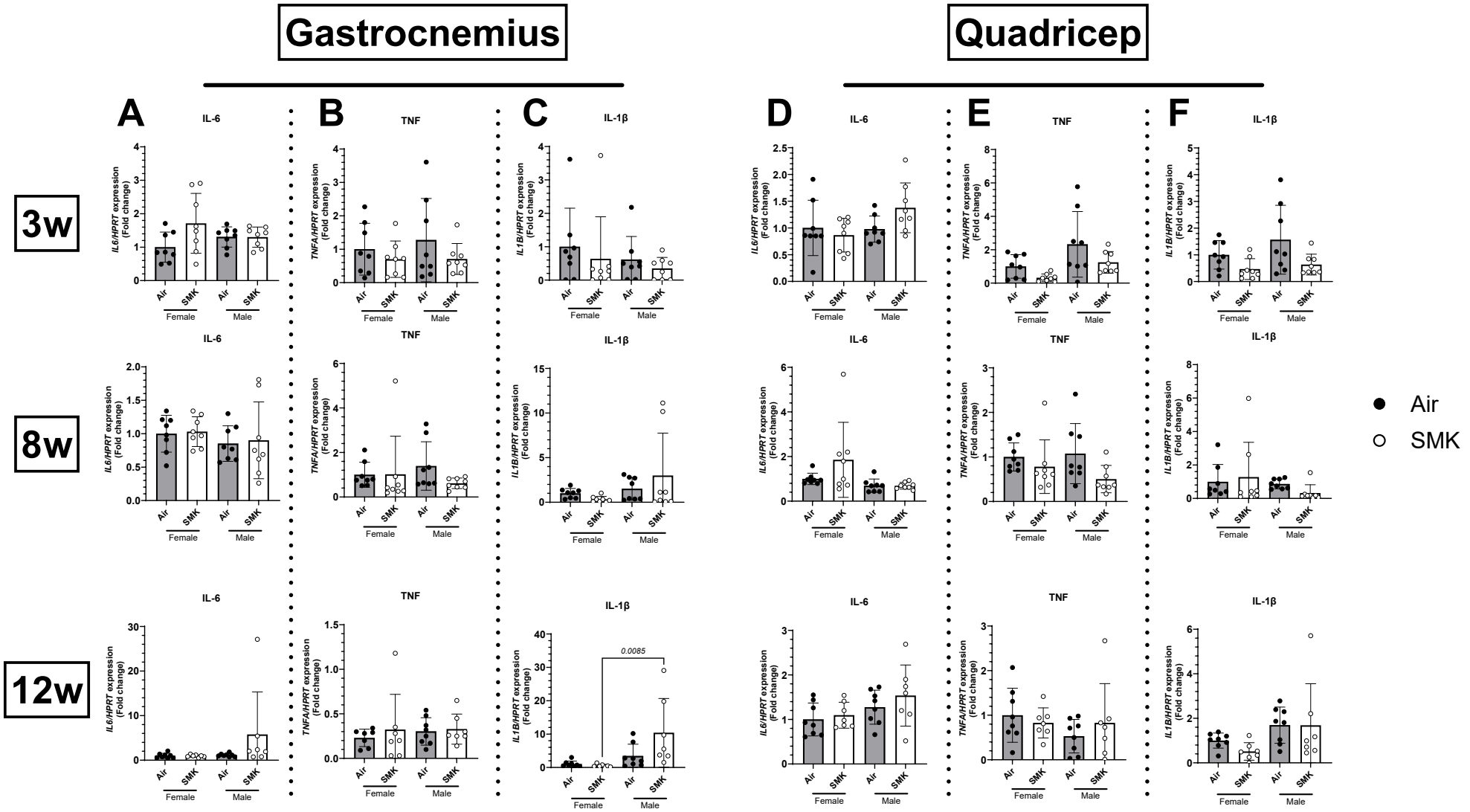
Gastrocnemius
Quadricep
A
B
C
D
E
F
IL-6
TNF
IL-1β
3w
8w
12w
IL6/HPRT expression (Fold change)
TNFA/HPRT expression (Fold change)
IL1B/HPRT expression (Fold change)
Air
SMK
Female
Male
0.0085
Air
SMK

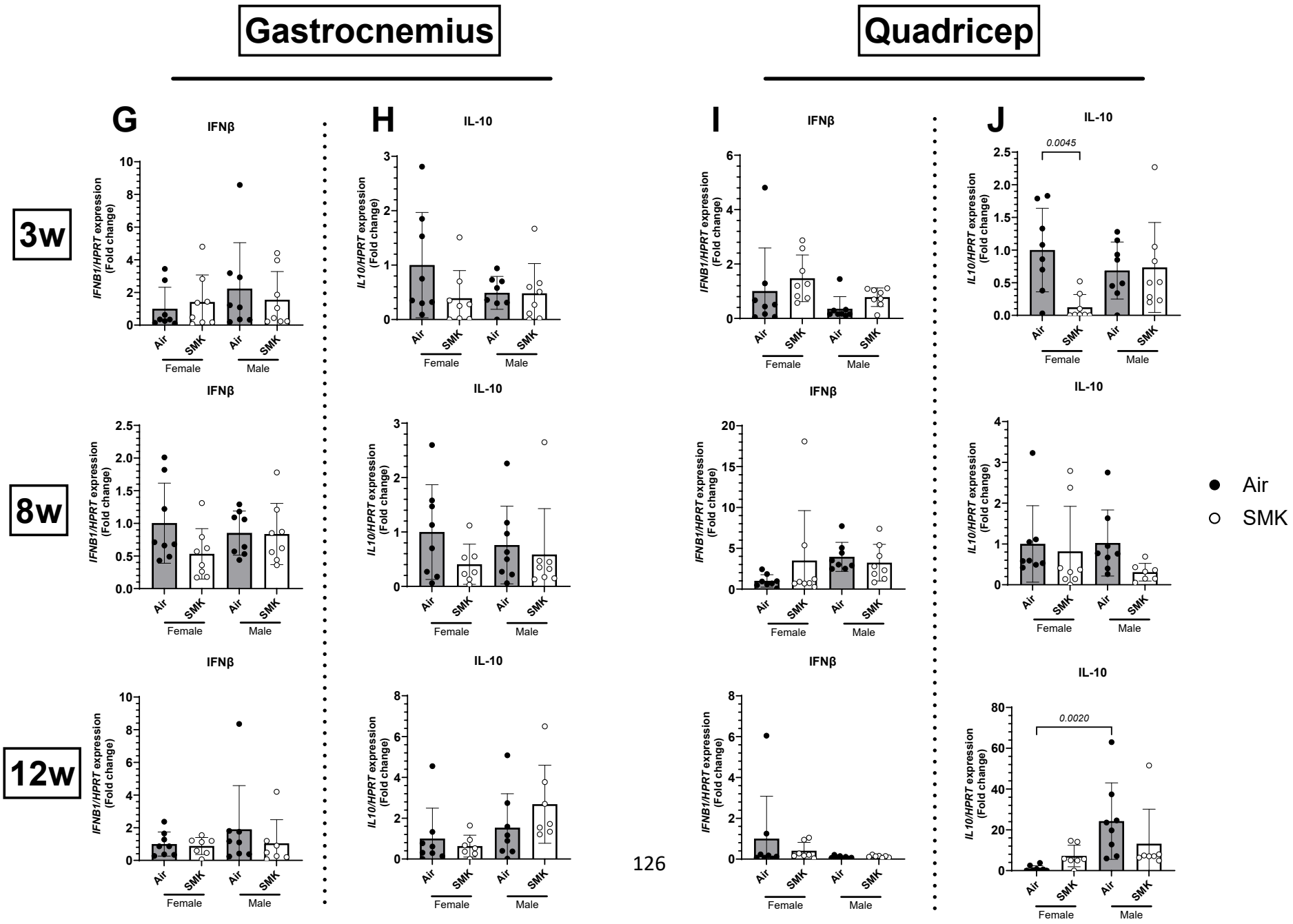
Gastrocnemius
Quadricep
G
H
I
J
IFNβ
IL-10
3w
8w
12w
IFNB1/HPRT expression (Fold change)
IL10/HPRT expression (Fold change)
0.0045
0.0020
Air
SMK
Female
Male
Air
SMK

Figure 3.26 There were no major changes local expression of inflammatory genes in the gastrocnemius and quadriceps of male and female mice of a CS-induced experimental COPD time course model.

Male and female mice gastrocnemius and quadriceps gene expression fold change of **A+D** IL-6 **B+E** TNF **C+F** IL-1β **G+I** IFNβ **H+J** IL-10 relative to HPRT at 3, 8 and 12w time points, respectively. Ordinary two-way Anova with Šídák's multiple comparisons test statistical analysis was performed on each data set. Individual values were graphed with mean **±** SD displayed. Results with a P-value≤0.05 were considered significant.

3.5.2 Atrogene expression was modulated in the gastrocnemius and quadriceps of male and female mice of a CS-induced experimental COPD time course model

Male and female C57BL/6 mice were exposed to CS or air (control) for 3w, 8w or 12w. RNA was isolated from Gastrocnemius and Quadriceps samples from male and female mice exposed to CS vs air control for 3w, 8w and 12w, and reverse transcribed for analysis by qPCR. MuRF1 expression in the gastrocnemius of male and female mice exposed CS was significantly lower than the air control, however, no significant changes were observed at 3w or 12w (Figure 3.27: A). In the quadriceps of male mice exposed to CS there was also a significant decrease in MAFbx expression vs air control at 8w and 12w (Figure 3.27: B). GADD45 expression was also significantly lower at 8w between male and female CS exposed groups (Figure.3-27: E). The quadriceps from the 3w and 8w time point showed a significant decrease in MuRF1 expression at 3w and 8w in male mice exposed to CS vs air control, as well as a significantly higher baseline expression in air control male mice vs female mice (Figure 3.27: C). Only male mice exposed to CS for 8w showed a significant decrease in MAFbx expression in the quadriceps (Figure 3.27: D) and only female mice exposed to CS for 12 showed a significant decrease in GADD45 expression. No other significant changes in MAFbx or GADD45 expression were observed. Lastly, there were no significant changes to HDAC4 expression observed for either the gastrocnemius or quadricep at 3w, 8w or 12w (Figure 3.27: F).

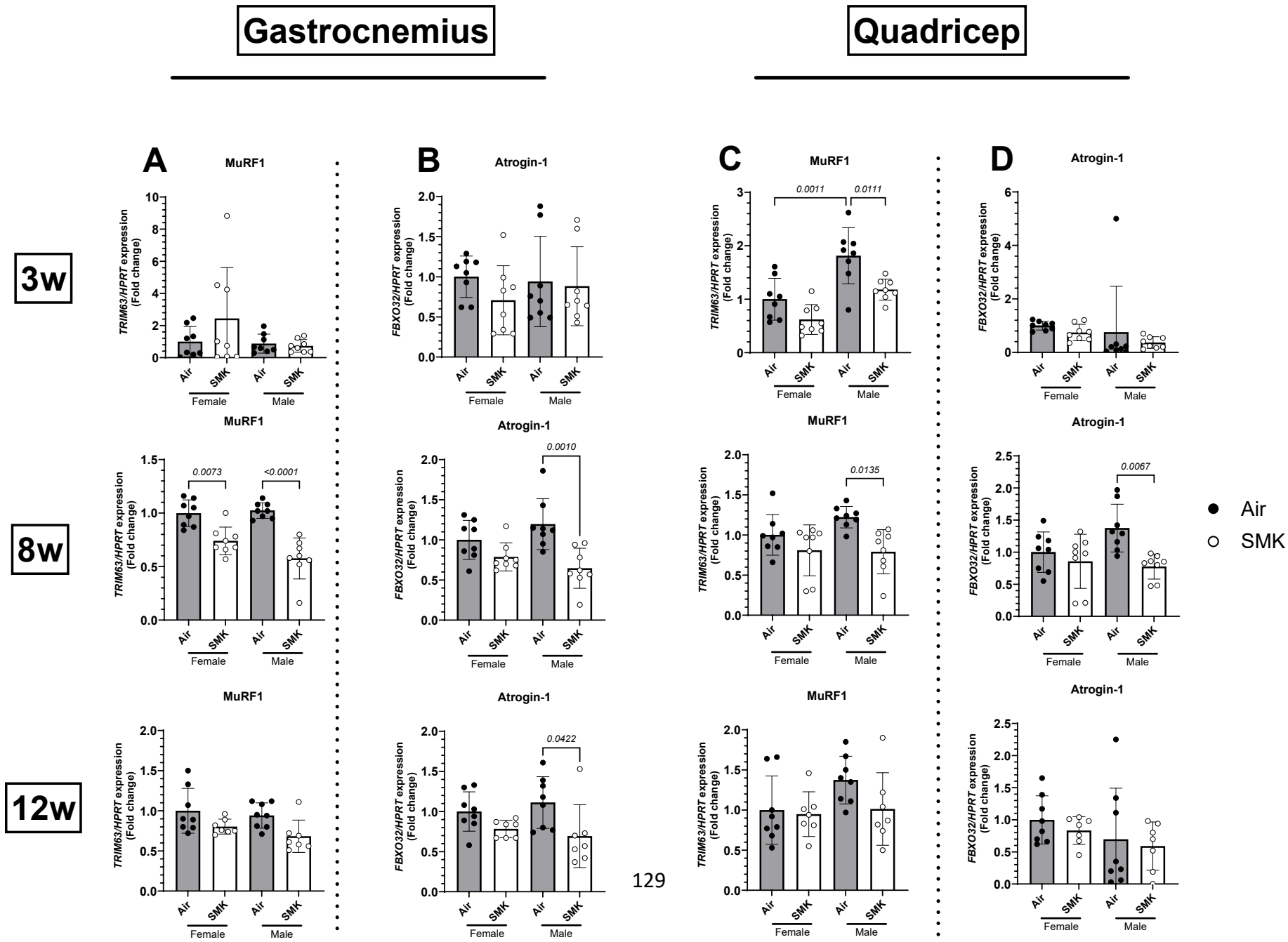
Gastrocnemius
Quadricep
A
MuRF1
B
Atrogin-1
C
MuRF1
D
Atrogin-1
3w
8w
12w
TRIM63/HPRT expression (Fold change)
FBXO32/HPRT expression (Fold change)
0.0011
0.0111
0.0073
<0.0001
0.0010
0.0135
0.0067
0.0422
Air
SMK
Female
Male
Air
SMK

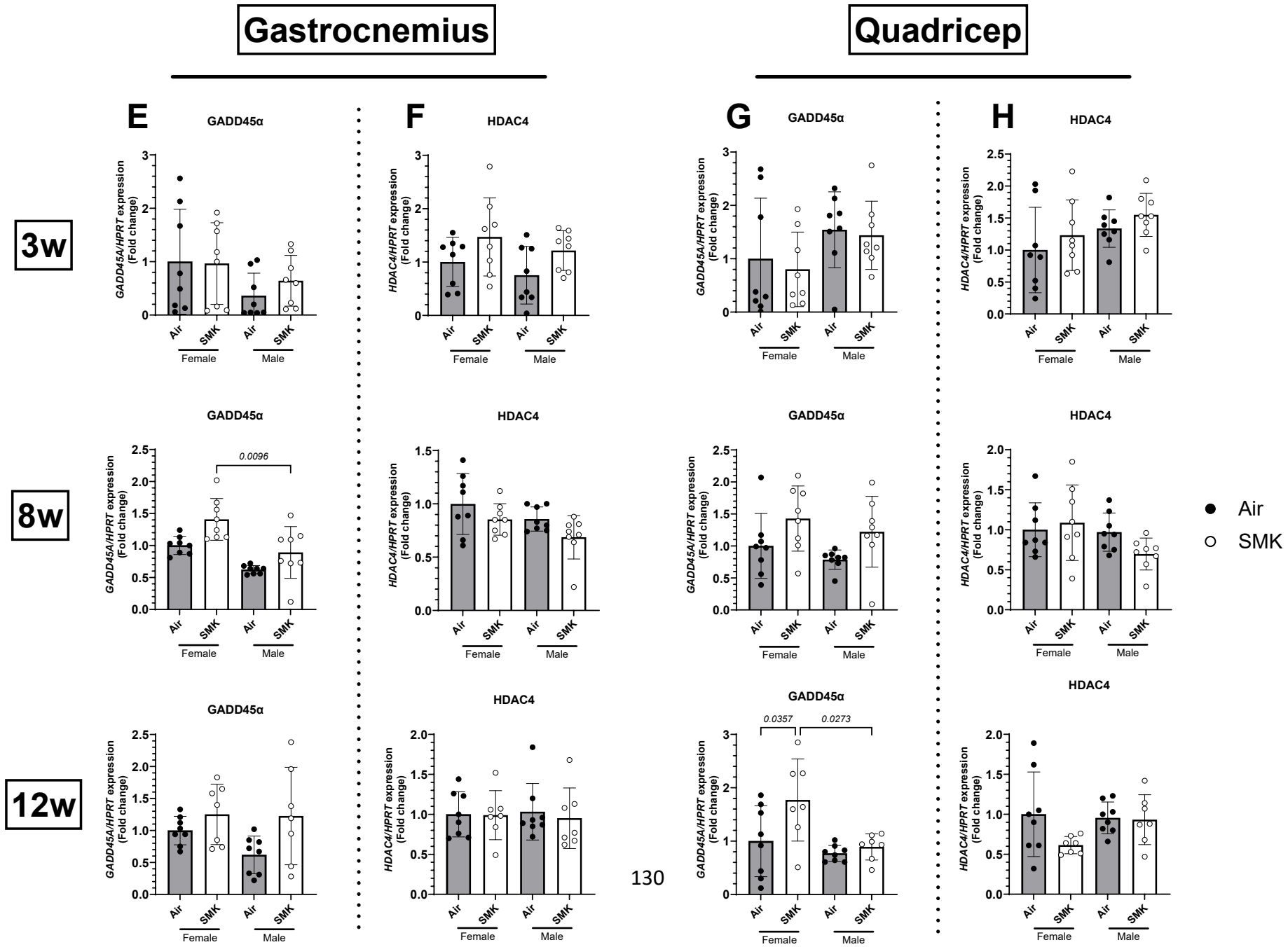
Gastrocnemius
Quadricep
E
F
G
H
GADD45α
HDAC4
3w
8w
12w
GADD45A/HPRT expression (Fold change)
HDAC4/HPRT expression (Fold change)
Air
SMK
Female
Male
0.0096
0.0357
0.0273
Air
SMK

Figure 3.27 Atrogene expression was modulated in the gastrocnemius and quadriceps of male and female mice of a CS-induced experimental COPD time course model.

Male and female mice gastrocnemius and quadriceps gene expression fold change of **A+C** MuRF1 **B+D** MAFbx **E+G** GADD45 **F+H** HDAC4 relative to HPRT at 3, 8 and 12w time points. Ordinary two-way Anova with Šídák's multiple comparisons test statistical analysis was performed on each data set. Individual values were graphed with mean **±** SD displayed. Results with a P-value≤0.05 were considered significant.

3.6 Pathway Enrichment analysis of human COPD vs healthy donor quadriceps transcriptome.

3.6.1 Pathway enrichment analysis of human COPD vs healthy patient quadriceps revealed upregulated pathways associated with inflammation and atrophy.

A study by Willis-Owens et al. highlighted specific transcripts with a greater than 2-fold change in COPD vs healthy human quadriceps samples, and they highlighted some genes relating to the mitochondrial antioxidant pathway and ECM features. I wanted to identify more pathways that were changed and using their publicly available dataset [303] I enriched for biological pathways that were upregulated in the quadricep muscles of COPD patients and compared to healthy controls. This identified unique pathways that were not identified in the original paper. There were 74 significantly upregulated genes associated with post-translational protein modification pathways in the COPD patient quadriceps. The post translational protein modification pathways also had the highest gene ratio in COPD quadriceps of any pathway investigated (0.16; Figure 3.28). Of these genes, some were associated with higher proteasome function and protein degradation, like the E3 ubiquitin-protein ligase mouse double minute 2 homolog *(MDM2)*, ubiquitin-conjugating enzyme E2 Q2 *(UBE2Q2)*, cullin 1 *(CUL1),* Proteasome subunit alpha type-2 *(PSMA2)* and 26S proteasome non-ATPase regulatory subunit 1 and 8 *(PSMD-1/-8)*, which indicated cellular stress. *RICTOR*, a component of the mTORC2 complex was also upregulated. mTORC2 activation of Akt via Ser473 phosphorylation increases cell survival responses and could be involved in managing cellular stress.

Innate and adaptive immune genes, neutrophil degranulation and genes associated with cellular responses to infectious diseases and viral infections were all also upregulated, indicating a comprehensive increased local immune response that is possibly driven by tissue damage, as

indicated by the cellular stress) (Figure 3.28). Increased gene expression of *NFKB2*, a subunit of the NF-κB complex, could indicate increased priming for signalling via NF-κB, which can increase pro-inflammatory signalling and transcription of atrogenes.

These data demonstrate increased cellular stress, which may be causing increased local inflammation in the quadriceps of COPD patients with increased protein degradation and proteasome function (Figure 3.28).

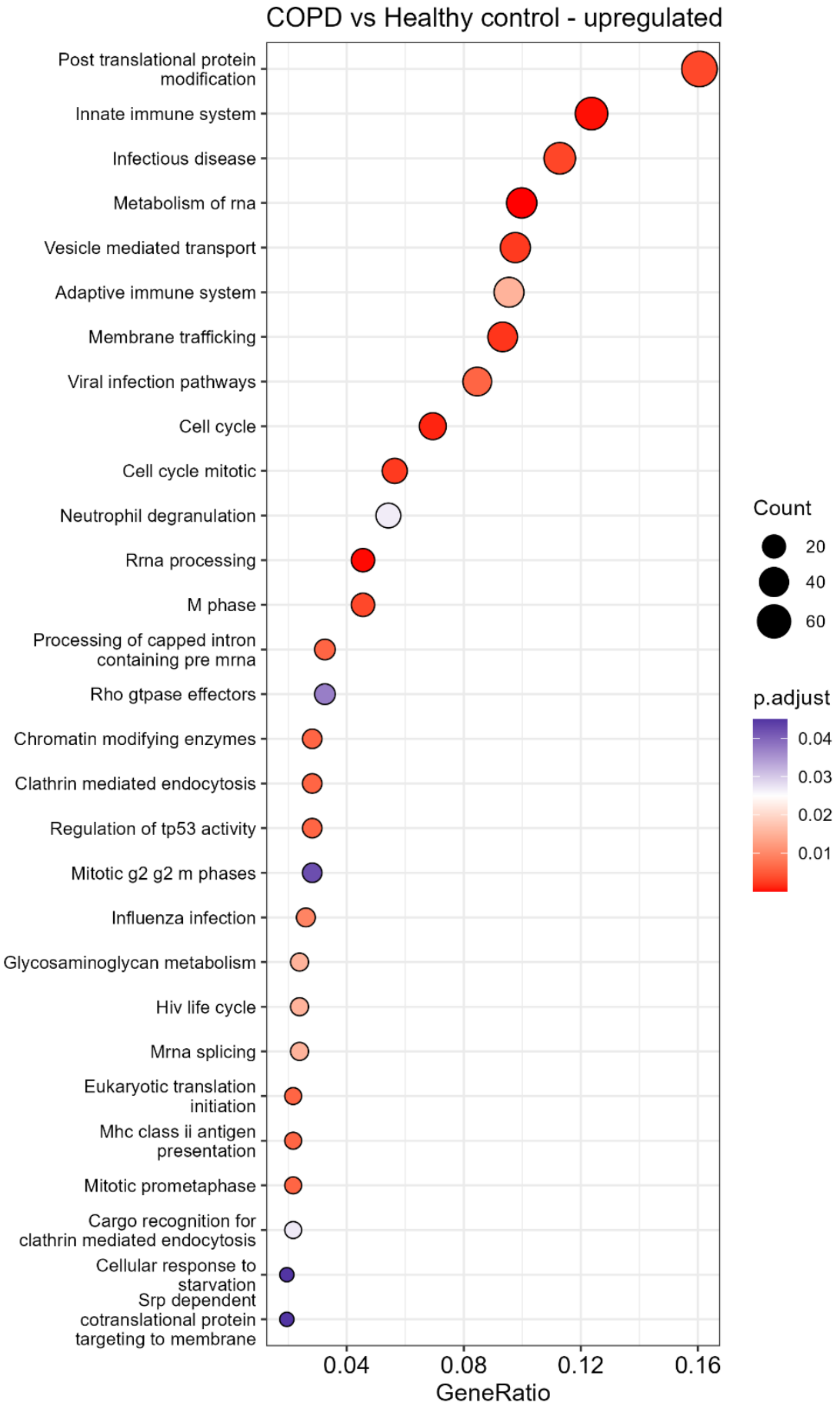
COPD vs Healthy control - upregulated
Post translational protein modification
Innate immune system
Infectious disease
Metabolism of rna
Vesicle mediated transport
Adaptive immune system
Membrane trafficking
Viral infection pathways
Cell cycle
Cell cycle mitotic
Neutrophil degranulation
Rrna processing
M phase
Processing of capped intron containing pre mrna
Rho gtpase effectors
Chromatin modifying enzymes
Clathrin mediated endocytosis
Regulation of tp53 activity
Mitotic g2 g2 m phases
Influenza infection
Glycosaminoglycan metabolism
Hiv life cycle
Mrna splicing
Eukaryotic translation initiation
Mhc class ii antigen presentation
Mitotic prometaphase
Cargo recognition for clathrin mediated endocytosis
Cellular response to starvation
Srp dependent cotranslational protein targeting to membrane
0.04
0.08
0.12
0.16
GeneRatio
Count
20
40
60
p.adjust
0.04
0.03
0.02
0.01

Figure 3.28 Pathway enrichment analysis of human COPD vs healthy patient quadriceps revealed upregulated pathways associated with inflammation and atrophy.

Pathway enrichment analysis was performed on microarray data deposited in the NCBI GEO repository with Accession Number GSE100281 with R studio using the Reactome GMT. This identified enriched biological pathways associated with significantly differentially expressed genes between COPD and healthy control samples. Only pathways with more than 6 significantly increased genes were included. There were 16 healthy age and sex matched controls compared to 79 COPD patients (GOLD grading: 4 GOLD I; 24 GOLD II; 32 GOLD III; 19 GOLD IV). These data were analysed for differential gene expression as previously described [94]. The gene ratio describes the proportion of genes associated with a particular pathway that were significantly upregulated in COPD samples, and the count describes the number of individual genes significantly changed within that pathway.

3.6.2 Pathway enrichment analysis of human COPD vs healthy patient quadriceps revealed pathways relating to mitochondrial function were suppressed.

A publicly available dataset [303] was enriched for biological pathways that were suppressed in the quadricep muscles of COPD patients and compared to healthy controls. Pathways with suppressed genes included the TCA cycle, respiration, fatty acid and amino acid metabolism, indicating impaired mitochondrial function. (Figure 3.29) and a shift away from oxidative phosphorylation. Genes encoding subunits of the ETC were significantly downregulated, compromising metabolic flexibility within the cells and limiting the ability of the cells to use alternative fuel sources like fatty acids and amino acids for energy production.

These data indicate a mitochondrial dysfunction and a complete metabolic shift in the quadriceps of COPD patients from oxidative phosphorylation towards glycolysis, potentially increasing oxidative stress and lactic acid build-up.

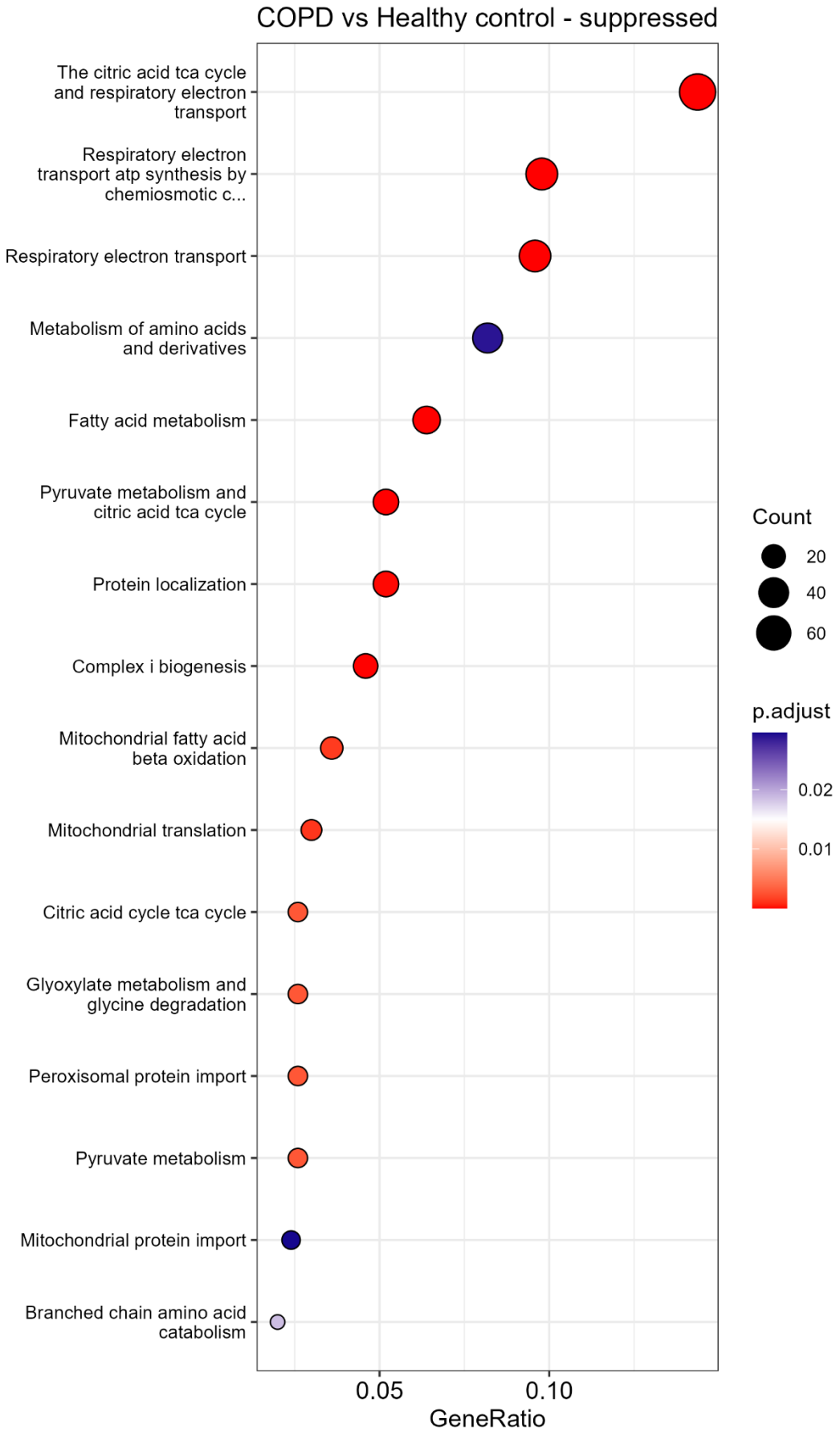
COPD vs Healthy control - suppressed
The citric acid tca cycle and respiratory electron transport
Respiratory electron transport atp synthesis by chemiosmotic c...
Respiratory electron transport
Metabolism of amino acids and derivatives
Fatty acid metabolism
Pyruvate metabolism and citric acid tca cycle
Protein localization
Complex i biogenesis
Mitochondrial fatty acid beta oxidation
Mitochondrial translation
Citric acid cycle tca cycle
Glyoxylate metabolism and glycine degradation
Peroxisomal protein import
Pyruvate metabolism
Mitochondrial protein import
Branched chain amino acid catabolism
0.05
0.10
GeneRatio
Count
20
40
60
p.adjust
0.02
0.01

Figure 3.29 Pathway enrichment analysis of human COPD vs healthy patient quadriceps revealed pathways relating to mitochondrial function were suppressed.

Pathway enrichment analysis was performed on microarray data deposited in the NCBI GEO repository with Accession Number GSE100281 with R studio using the Reactome GMT. This identified enriched biological pathways associated with significantly differentially expressed genes between COPD and healthy control samples. Only pathways with more than 6 significantly increased genes were included. There were 16 healthy age and sex matched controls compared to 79 COPD patients (GOLD grading: 4 GOLD I; 24 GOLD II; 32 GOLD III; 19 GOLD IV). These data were analysed for differential gene expression as previously described [94]. The gene ratio describes the proportion of genes associated with a particular pathway that were significantly upregulated in COPD samples and the count describes the number of individual genes significantly changed within that pathway.

Chapter 3 - Discussion

The aim of this first study was to assess the prevalence of muscle atrophy across different experimental murine models of IPF, asthma, and COPD, and to identify the most suitable model for therapeutic studies targeting cachexia in a pulmonary disease, as well as to observe the effect of these models on mediators of protein degradation and synthesis that are associated with cachexia were also measured.

The standard 4-week bleomycin-induced model of experimental pulmonary fibrosis in C57Bl/6 mice demonstrated the expected changes to lung function whilst the 10-week model and the CS + bleomycin models did not. When considering why the 10-week model did not have the intended decrease in FVC, it is worth noting that most studies report bleomycin-induced lung fibrosis in mice eventually resolves, and that lung function parameters also return to baseline over time. Bleomycin models of pulmonary fibrosis also typically have decreased lung volume parameters, whereas CS-induced lung changes typically increase them. This is because fibrosis increases scarring in the lung [305], creating a stiffer less elastic environment, decreasing lung volume [306]. In contrast, CS induces emphysema and the breakdown of the alveolar space creating more volume. Due to these contrasting phenomena, it is likely that lung health was still compromised in this model as the negative impacts of both models may have cancelled out each other's effects on lung function. Also, there was still significant leukocyte induction in the BALF with both bleomycin and CS-challenge, compared to the PBS + Air control, suggesting an inflammatory response to lung damage.

Histological analysis of the combined bleomycin + CS-exposure model lungs would improve the analysis of the impact on lung architecture and validate the development of pulmonary fibrosis, or other changes. Moreover, despite limited changes to lung function in the bleomycin + CS induced

IPF model, it was the only model of IPF that had any significant total body weight, or skeletal muscle weight loss, though CS-exposure was required for this effect. Therefore, with confirmation of the development of pulmonary fibrosis via histological analysis, like a Sirius Red stain for collagen deposition, this model may be more reflective of IPF in humans with cachexia co-morbidity than the current standard 4w Bleo-induced IPF model. However, this histological analysis is currently beyond the scope of my study.

Quadriceps were selected from the 4w model for immunoblot analysis for three reasons. 1. Short term bleomycin-induced murine IPF models (2-4w) are currently considered the gold standard model for emulating IPF [173] and for trialling preventative and therapeutic interventions in mice [307]. This is because fibrosis can resolve over time, but also too early a time point will still be during the inflammatory phase of the model, during which there is an induction of neutrophils and inflammatory cytokine production which is not associated with human IPF [307] and may confound results. Thus, it was clear that the 4w time point would be more appropriate than the 10-week time point, as it is just after the inflammatory phase of bleomycin induced IPF and before the resolution of fibrosis. 2. The lung function changes in the 4-week bleomycin model, particularly in relation to IC, FVC and compliance, reflected the changes seen in humans with IPF, whereas the 10-week timepoint did not. 3. Despite not demonstrating a significant change in total body or skeletal muscle weight, it was still possible that skeletal muscle dysfunction was occurring at 4w. This is because, unless caused by acute exacerbation of symptoms, cachexia occurs over years in IPF, and a 4w model may be too early to see significant weight changes. Therefore, there may be changes to protein synthesis and degradation pathways which can impact skeletal muscle health.

There was no observed changes to proteins associated with protein degradation (Atrogin-1, MuRF1 or GADD45α) or the protein synthesis pathway (Akt, mTOR, 4E-BP1, S6K or rpS6), or their activation via phosphorylation (p-Akt^{Thr308}, p-Akt^{Ser473}, p-4E-BP1$^{Thr37/47}$, p-S6K^{Thr389}, p-rpS6$^{Ser235/236}$)

in the quadriceps of mice in the 4w model of Bleo-induced IPF. This suggested that this model of IPF did not alter protein synthesis or degradation in any of the ways measured.

However, there was a decrease in total STING, but not cGAS protein levels. This may limit signalling via TBK1 and decrease inflammation in the muscles, limiting inflammation dependent protein degradation. Unlike COPD or asthma, IPF is not characterised by chronic inflammation or a particular inflammatory phenotype, so this observed decrease in STING expression in the skeletal muscle may indicate an immunosuppressive aspect of IPF that has not been described previously. Interestingly, cGAS-STING inhibition has been suggested as a potential therapeutic avenue in pulmonary fibrosis [308], particularly in silica induced fibrosis, where STING signalling is important for alveolar macrophage and fibroblast fibrotic effects [309]. However, whilst targeting the cGAS-STING pathway may be a promising route of treatment for pulmonary fibrosis, it is important to consider the role that cGAS-STING pathway has in cancer detection. Decreased cGAS-STING protein/signalling has been linked to increased prevalence of gastric cancer [310], non-small cell lung carcinoma [311] and high cGAS and STING gene expression is linked to improved outcome in lung adenocarcinoma [312]. The importance of cGAS-STING in lung cancers should therefore provide reason for cautious inhibition of this pathway.

BALB/c are the preferred choice for murine experimental asthma models, as they have a proportionally larger Type-2 immune response compared to C57BL/6 mice [313]. There is also evidence to suggest that BALB/c mice can have a higher airway neutrophilic response to allergen (cockroach) than C57BL/6 mice [314], making them an ideal candidate strain for studying moderate and severe asthma, which are eosinophilic and neutrophilic respectively [128]. The mice with moderate and severe experimental asthma demonstrated a dose-dependent increase in central airway resistance (Rn) in response to escalating doses of methacholine. This increase in Rn was inhibited by dexamethasone treatment in moderate but not severe asthma. These lung

function findings mirror the bronchoconstriction observed in asthma patients. The differential response to dexamethasone, with inhibition in moderate but not severe asthma, reflects the steroid-resistant phenotype characteristic of severe asthma. Similarly, BALF total leukocytes were elevated in both experimental models of moderate and severe asthma. While dexamethasone attenuated this leukocyte induction in moderate asthma, it failed to do so in severe asthma, further illustrating the steroid resistance associated with the severe asthma phenotype.

There were no changes to total body or skeletal muscle weights in either moderate or severe asthma. However, whether the skeletal muscles exhibited any changes to protein synthesis or degradation pathways was still assessed. This is because exacerbations likely contribute to muscle weakness and atrophy [27, 106, 315], and thus exacerbations, through methacholine induced AHR, could induce acute changes to these pathways in the skeletal muscle. Nevertheless, immunoblot analysis of the quadriceps showed no changes to the expression of proteins associated with protein degradation, protein synthesis or the cGAS-STING pathway.

The experimental COPD time point models showed significant changes to total body weight and skeletal muscle mass, even at early timepoints. Lung function measurements at 8 and 12w demonstrated increases in lung volume parameters IC, FVC, TLC and hysteresis, but no changes in compliance. As previously mentioned, increased lung volume parameters in experimental COPD models are consistent with the development of emphysema. Therefore, from these initial findings we can conclude that our experimental models emulated human COPD lung function changes, and that CS-induced COPD negatively impacted skeletal muscle mass. These effects were consistent across male and female C57BL/6 mice.

Gene expression analysis of gastrocnemius and quadriceps muscles showed no significant changes to local expression of inflammatory markers at 3, 8 or 12w of CS-exposure in males or females.

However, there were notable changes in atrogene expression, particularly in male mice at 8w, though female mice had similar trends. These inflammatory gene observations do not necessarily mean that there is no role for inflammation in mediating atrophy. It is possible that inflammation contributes to muscle atrophy in a non-IL-6, TNF, IL-1β, IFNβ or IL-10 mediated mechanism as there are many inflammatory factors implicated in muscle atrophy [53, 316], and inflammatory changes may occur earlier than the time points examined. Moreover, factors of inflammation may not be expressed locally in the muscle but instead at other sites, like the lung, which would contribute to systemic inflammation mediated atrophy [317-319]. There is therefore a need for future experiments need to investigate key inflammatory factors in the muscle and blood on the protein level.

Interestingly, results showing downregulated *TRIM63* and *FBXO32*, and upregulation of *GADD45α* gene expression at 8w may infer time-dependent induction of the UPS. Indeed, this has been demonstrated in previous studies [205, 320, 321]. *TRIM63* and *FBXO32* gene expression was shown to peak after 3d in multiple models of muscle atrophy, including immobilisation, hind-limb suspension, IL-1-mediated cachexia, denervation and glucocorticoid-induced atrophy, and is downregulated afterwards [205, 320, 321]. Despite downregulation of these genes after 3d, muscle mass still decreases over time, highlighting the role of these atrogenes as both markers and triggers of atrophy. *GADD45A* was also upregulated early in skeletal muscle after denervation but had sustained expression up to 90d, in contrast to other UPS proteins [222]. Since the data I have gathered reflect previous studies that examined atrogene expression at different timepoints, it is possible that the key signalling that induces the UPS and autophagy pathways that regulate cachexia in COPD occurs earlier than the timepoints I have investigated. This may also explain the lack of local inflammatory signalling in the gastrocnemius and quadriceps as inflammation is a likely trigger for muscle atrophy and may only be the initial signal, but local inflammatory gene

expression is suppressed over time (e.g. *TRIM63* and *FBXO32*). Despite these changes in mRNA expression, no change in protein levels for atrophy markers was observed, which may indicate that mRNA does not reflect protein levels. However, the antibody quality for both MuRF1 and Atrogin-1 were both poor and showed non-specific binding across the membrane.

There were no significant changes in signalling for protein synthesis. However, there was a trend in changes for the ratio of p-rpS6 and total 4E-BP1 (P=0.0564 & P=0.0638 respectively) protein levels, which would indicate decreased mTORC1/S6K signalling, and increased atrogene expression, as 4E-BP1 is also considered an atrophy associated protein. Increased 4E-BP1 reduces protein synthesis through inhibition of eIF-4E, that is needed for mRNA translation and reduced phosphorylation of rpS6 also decreases protein synthesis [322-324].

Overall, these data from the experimental COPD studies demonstrated that our model accurately reflects lung function and skeletal muscle weight changes associated with COPD-induced cachexia. Changes were also observed to protein synthesis and degradation pathways that reflect previous findings with other models of atrophy. An increase in ATP5A protein in the quadriceps also demonstrated a potential accumulation of mitochondria in the skeletal muscle and thus, metabolic dysregulation.

The final aim of this chapter was to compare skeletal muscle atrophy observed in experimental COPD models with that in human COPD and appropriately target overlapping mechanisms of disease. The pathway enrichment analysis of microarray data from human COPD quadriceps samples demonstrated increased inflammatory signalling and decreased expression of mitochondrial-related metabolic pathways and mitochondria specific genes. These data indicate inflammation in the skeletal muscle and a potential increase in glycolysis dependent energy

production, as well as a potential decrease in mitochondrial biogenesis and mitochondrial dysfunction.

Thus, it was hypothesised that mitochondrial dysfunction, and subsequent mtDNA into the cytosol, activates cGAS-STING signalling in the skeletal muscle of both experimental and human COPD, and this was targeted therapeutically in chapter 4 with the small molecule STING inhibitor H-151.

Chapter 4 Targeting cGAS-STING mediated inflammation using H-151 single molecule inhibitor as a novel treatment against COPD-induced cachexia.

4.1 Introduction

As a result of the data from my first chapter, I decided to continue investigating cachexia in the context of the experimental COPD model, and to use therapeutics aimed at improving mitochondrial health and reducing inflammation.C57BL/6 mice from the CS-induced COPD model had exhibited lung function changes analogous to those observed in COPD patients, alongside inhibited muscle growth in young mice compared to air-exposed controls. Furthermore, lung function changes and muscle mass loss were consistent across both sexes. These findings, combined with alterations in gene and protein expression in pathways regulating protein synthesis and degradation, informed the decision to adopt a female 8-week experimental COPD murine model to investigate cachexia/muscle atrophy-targeted therapies.

Preliminary findings from these COPD-induced cachexia models, along with quadriceps muscle data from COPD patients, suggest compromised mitochondrial function and health in skeletal muscle. Indeed, mitochondrial dysfunction is increasingly recognized as a driver of cachexia. As a result, it was decided to measure mitochondrial function in the muscles of this model.

One of the main functions of the mitochondrion is to produce energy (or ATP) for the cell through a process called oxidative phosphorylation (OXPHOS) [325]. This involves the transport of electrons through the electron transport chain (ETC), which is made up of complex I, complex II, complex III and complex IV [326]. This creates a H^+ gradient across the inner mitochondrial membrane which is then coupled to ATP and H_2O production by complex V [326]. The oxygen consumed during this process can be measured to provide insight into real-time OXPHOS capacity,

ADP sensitivity and proton leakage [327]. These were measured using the Oroboros Oxygraph-2k for high-resolution respirometry to further investigate mitochondrial dysfunction in the skeletal muscle of this model. This method was favoured over another form of high-resolution respirometry, Agilent's Seahorse XF analysis, as the Oroboros allowed measurements of mitochondrial function in permeabilised skeletal muscle tissue [328].

Complex I and II proton leakage are measures of proton leak back across the inner membrane of the mitochondria and uncoupling of proton flux from ATP production [327]. Proton leak occurs in healthy mitochondria; however, excessive proton leak can indicate reduced membrane integrity, ROS production and energy inefficiency [329, 330]. High ADP sensitivity is typically considered an indication of healthy mitochondria as it can infer close coupling to respiration [331] however, exercise studies have also shown chronic training can lower ADP sensitivity [332]. Low ADP sensitivity in skeletal muscle has been linked to increased ROS production in experimental mouse models of ageing and oxidative stress [333] as well as in humans [331]. High ADP sensitivity could also demonstrate cell stress, as the cell quickly converts ADP to ATP to cope with higher energy demands, though this requires further investigation. High ADP sensitivity/low ADP availability could also indicate hyperpolarisation of the inner membrane, which can lead to increased ROS production and inflammation driven by reverse electron transport at complex I [334-336].

Dysfunctional mitochondria can lead to diverse pathological effects, including the production of mitochondrial reactive oxygen species (mtROS), which activate the atrogene regulator nuclear factor erythroid 2-related factor 2 (NRF2) [337]. Additionally, mitochondrial dysfunction can drive inflammation through NLRP3 inflammasome activation, mediated by cardiolipin externalization, mtROS production, or leakage of oxidized mitochondrial DNA (mtDNA) into the cytosol [338]. In contrast, non-oxidized mtDNA preferentially activates the absent in melanoma 2 (AIM2) inflammasome [339]. Activation of either inflammasome pathway results in IL-1β secretion into

the circulatory system [340] and IL-1β induction is implicated, particularly for cancer-associated cachexia, in atrophy [341-343]. Thus, targeting mitochondrial health or downstream pathways activated by mitochondrial dysfunction, such as innate immune sensing of mtDNA, represents a promising therapeutic strategy for preventing cachexia.

The cGAS-STING pathway has recently emerged as a potential mediator of muscle atrophy [60, 344]. Mitochondrial dysfunction results in mtDNA leak into the cytosol, triggering activation of the cGAS-STING pathway [345] promoting inflammation-driven protein degradation through JAK-STAT and NF-κB signalling pathways.

H-151, a small-molecule STING inhibitor, prevents palmitoylations and STING clustering, which is essential for TBK1 activation [346]. Activated TBK1 drives IRF3 and NF-κB translocation to the nucleus [279], where they upregulate ISGs, atrogenes, and inflammatory gene expression. The aim of this study was to evaluate H-151 as a therapeutic intervention to block STING signalling and thus mitigate inflammation and mitochondrial dysfunction-mediated muscle atrophy.

4.2 Methodology and Experimental design

4.2.1 Overview of an H-151 intervention in experimental COPD.

C57BL/6 female mice (8w.o.) were subjected to an experimental COPD model where mice were exposed to CS from 12 cigarettes, twice/d, 5d/w for 8w. Mice were treated with H-151, a small molecule inhibitor of STING protein function. H-151 was prepared in 4%DMSO/96%PBS solution (vehicle) to a concentration of 10mg/kg. Under isoflurane anaesthetic, mice were given daily i.n. administration of H-151 or vehicle and weighed daily (Monday-Friday).

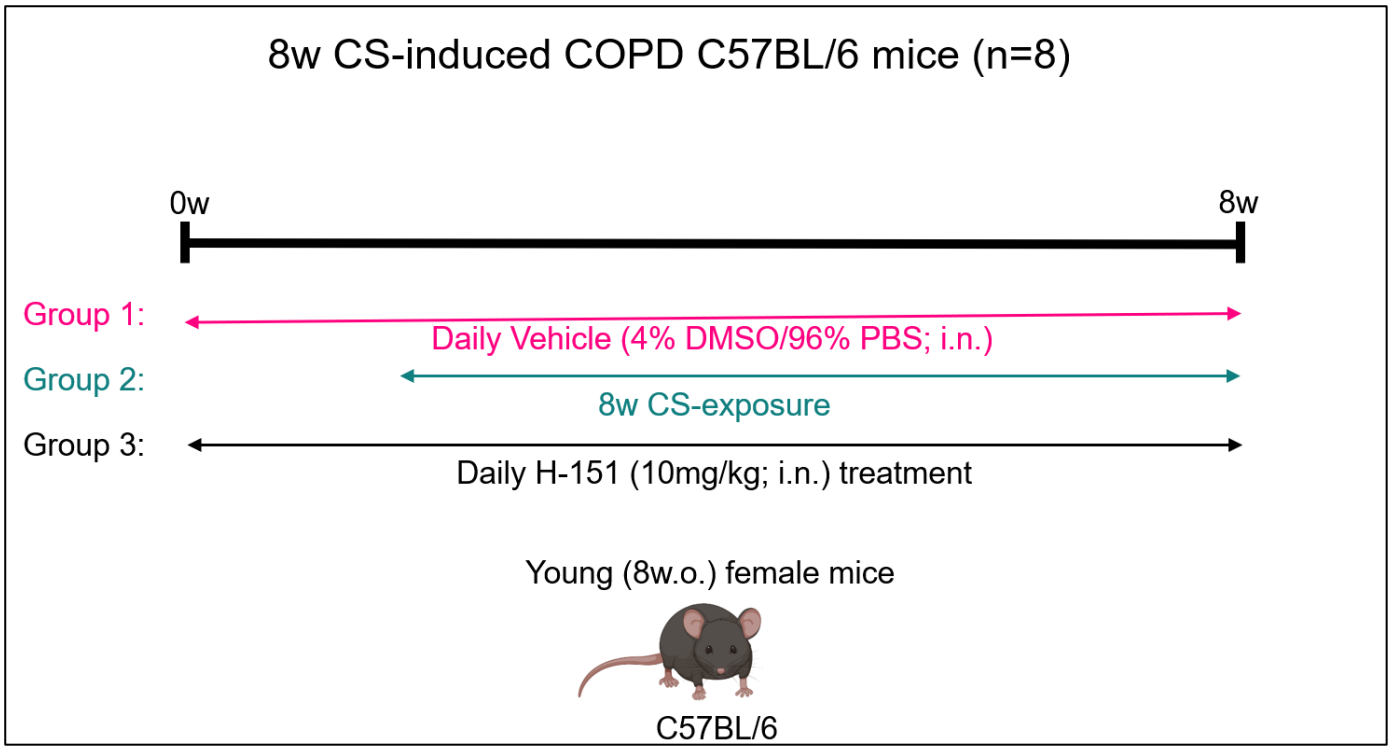

Figure 4.1 H-151 intervention in experimental COPD.

C57BL/6 mice (n=8) were exposed CS or air for 8w. 30µL of i.n. H-151 (10mg/kg) was administered 5d/w (Monday-Friday) for 2w prior to the beginning of CS exposure until the endpoint. Mice were 8w.o. at the commencement of H-151 treatment.

Acknowledgements for chapter 4

I acknowledge Dr. Matt Johansen and Dr. Shatarupa Das for their contributions in running the model, enabling the collection of skeletal muscle samples without the need for a repeat study targeting the same pathway. Their provision of mouse weight data and lung function results was instrumental in validating the model and its association with body weight loss during disease onset. I also acknowledge Dr. Ashleigh Philp for conducting the Oroboros analysis of the gastrocnemius muscle.

4.3 Whole body phenotype from experimental COPD with H-151 intervention model

4.3.1 Lung function decline in an experimental COPD model was not recovered with H-151 treatment

C57BL/6 mice underwent an experimental CS-induced COPD model for 8w. Treated and untreated mice were given H-151 or vehicle, respectively, 5d/w for 10w. Lung function was measured under anaesthetic on the day of endpoint and BALF was collected immediately after.

Lung function measurements related to lung volume including IC, FVC, and TLC were increased with CS-exposure, but were not decreased with H-151 treatment (Figure 4.2: B-D). Hysteresis was also increased with CS exposure but were also unchanged with H-151 treatment (Figure 4.2: E). Rrs was unchanged with CS-exposure and H-151 (Figure 4.2: F). However, Rn (Central airway resistance) was decreased with CS-exposure regardless of treatment (Figure 4.2: G).

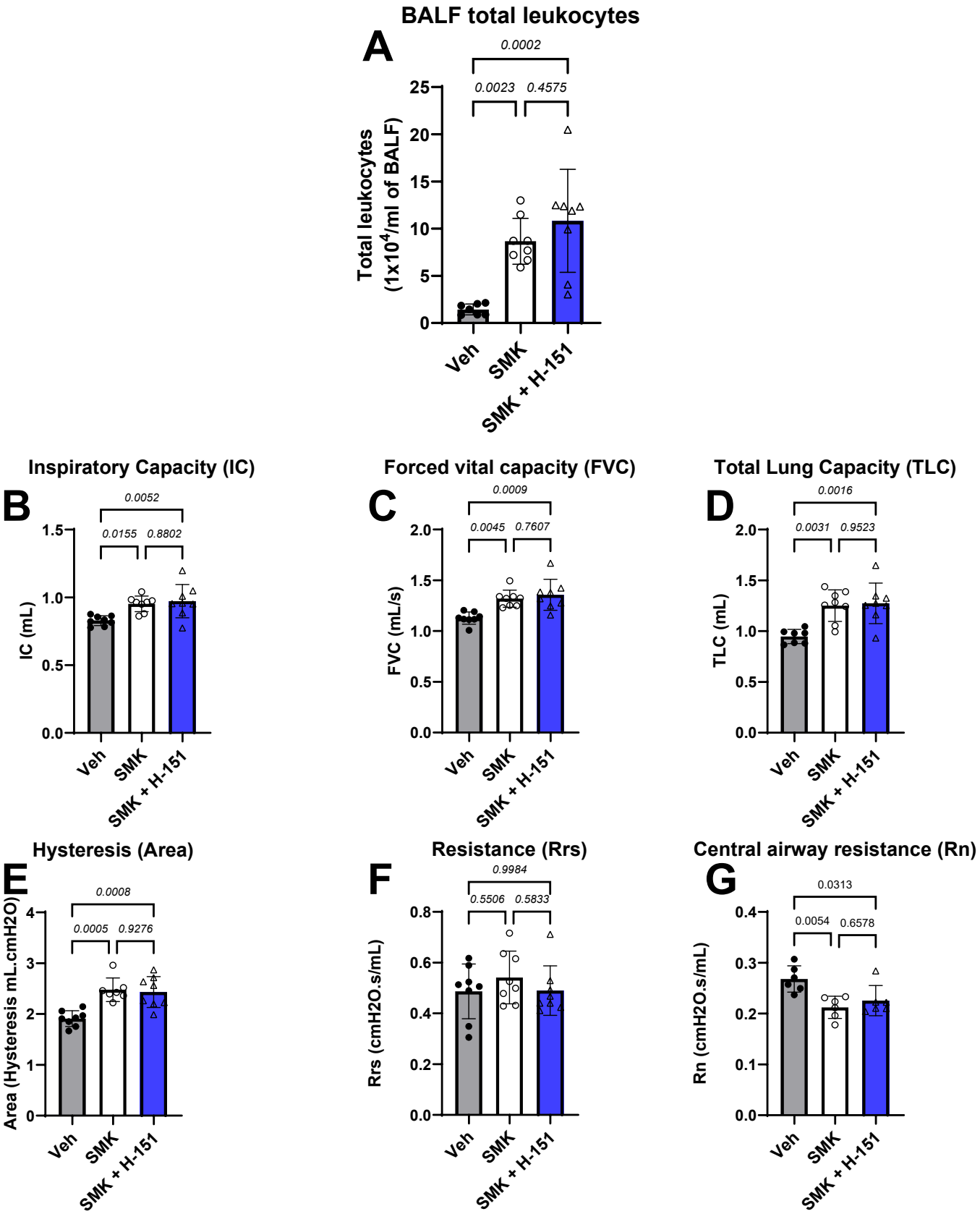
BALF total leukocytes
A
0.0002
0.0023
0.4575
Total leukocytes (1x10^4/ml of BALF)
25
20
15
10
5
0
Veh
SMK
SMK + H-151
Inspiratory Capacity (IC)
B
0.0052
0.0155
0.8802
IC (mL)
1.5
1.0
0.5
0.0
Veh
SMK
SMK + H-151
Forced vital capacity (FVC)
C
0.0009
0.0045
0.7607
FVC (mL/s)
2.0
1.5
1.0
0.5
0.0
Veh
SMK
SMK + H-151
Total Lung Capacity (TLC)
D
0.0016
0.0031
0.9523
TLC (mL)
2.0
1.5
1.0
0.5
0.0
Veh
SMK
SMK + H-151
Hysteresis (Area)
E
0.0008
0.0005
0.9276
Area (Hysteresis mL.cmH2O)
4
3
2
1
0
Veh
SMK
SMK + H-151
Resistance (Rrs)
F
0.9984
0.5506
0.5833
Rrs (cmH2O.s/mL)
0.8
0.6
0.4
0.2
0.0
Veh
SMK
SMK + H-151
Central airway resistance (Rn)
G
0.0313
0.0054
0.6578
Rn (cmH2O.s/mL)
0.4
0.3
0.2
0.1
0.0
Veh
SMK
SMK + H-151

Figure 4.2 Lung function decline in an experimental COPD model was not recovered with H-151 treatment.

The lung function of H-151 treated C57BL/6 mice (n=8) was assessed under anaesthetic at endpoint using a SCIREQ Flexivent, after 8w of cigarette smoke (CS) or air exposure. Bronchoalveolar lavage fluid (BALF) was collected directly after lung function assessment. **A** Total leukocytes concentration/ml of BALF collected on day of endpoint **B** Inspiratory capacity (IC) is a measure of the amount of air that can be inhaled after normal exhalation. **C** Forced vital capacity (FVC) is the total volume of air exhaled during a forced expiration. **D** Total lung capacity (TLC) is the maximum possible lung volume. **E** Hysteresis. **F** Resistance (Rrs) is a dynamic measure of lung constriction. **G** Central airway resistance (Rn). All lung function parameters were measured under anaesthetic on day of endpoint. Ordinary one-way Anova with Tukey's multiple comparison statistical analysis was performed on each data set. Individual values were graphed with mean ± SD displayed. Results with a P-value≤0.05 were considered significant.

4.3.2 Impaired development in an experimental COPD model was not recovered with H-151 treatment

Body weight of CS and air exposed was measured 5 and 3 times/w, respectively, for 10w. Hind leg muscles from mice were collected and weighed on the day of endpoint within 20m of death.

Room air exposed (control) mice continued to gain weight over time, however CS exposed mice remained approximately the same weight over the 10w, which was unaffected by H-151 treatment (Figure 4.3: A).

CS-exposure over 8w resulted in lighter gastrocnemius (Figure 4.3: B), quadriceps (Figure 4.3: C) and EDL (Figure 4.3: E). H-151 treatment did not affect quadriceps weight compared to Veh or CS exposed only groups (Figure 4.3: C), and decreased soleus weight compared to the vehicle only group but not the Veh + CS group (Figure 4.3: D).

N-A length was decreased in CS exposed mice regardless of treatment (Figure 4.3: F). These data indicate H-151 treatment did not prevent CS-induced weight changes in young female mice. Although, there were differential effects in the soleus and quadriceps that may indicate a role in skeletal muscle of different muscle fibre types and bioenergetic demands.

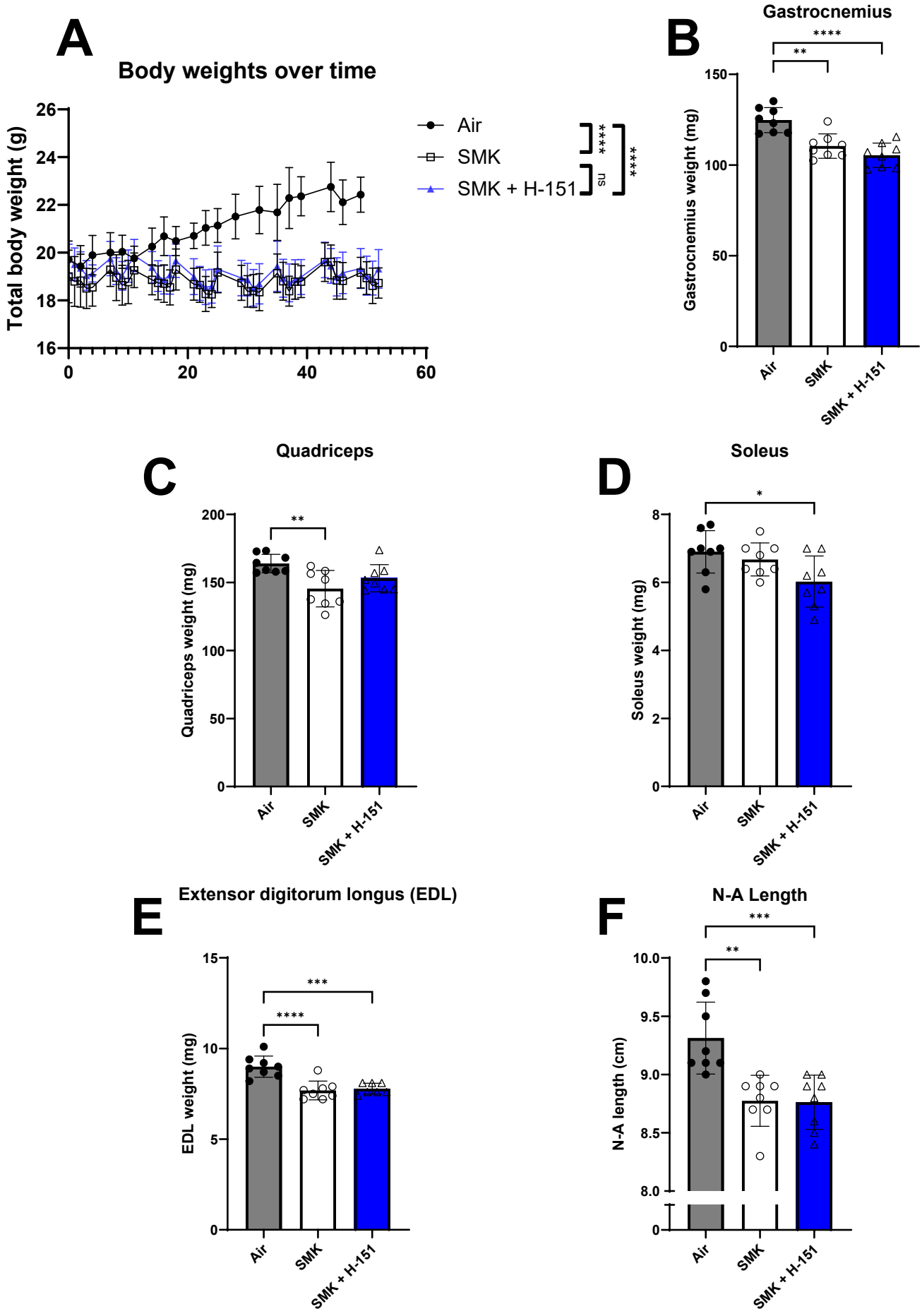
A
Body weights over time
Total body weight (g)
26
24
22
20
18
16
0
20
40
60
Air
SMK
SMK + H-151
****
ns
****
B
Gastrocnemius
Gastrocnemius weight (mg)
150
100
50
0
****
**
Air
SMK
SMK + H-151
C
Quadriceps
Quadriceps weight (mg)
200
150
100
50
0
**
Air
SMK
SMK + H-151
D
Soleus
Soleus weight (mg)
8
6
4
2
0
*
Air
SMK
SMK + H-151
E
Extensor digitorum longus (EDL)
EDL weight (mg)
15
10
5
0
***
****
Air
SMK
SMK + H-151
F
N-A Length
N-A length (cm)
10.0
9.5
9.0
8.5
8.0
0
***
**
Air
SMK
SMK + H-151

Figure 4.3 Impaired development in an experimental COPD model was not recovered with H-151 treatment.

H-151 i.n. treated C57BL/6 mice (n=8) were exposed to cigarette smoke (CS) or air for 8w and weighed 5d/w (Monday-Friday). N-A length was measured while the mice were under anaesthetic and muscles were collected and weighed after lung function assessment. **A** Mouse weight (g) over time. **B-E** Gastrocnemius, quadriceps, soleus and EDL weight (mg) respectively. **F** N-A length (cm). A mixed-effect analysis (REML) statistical analysis was performed for analysis of mouse body weight over time. Ordinary one-way Anova with Tukey's multiple comparison statistical analysis was performed on each data set. Individual values were graphed with mean ± SD displayed. Results with a P-value≤0.05 were considered significant (*P≤0.05; **P≤0.01; ***P≤0.001, ****P≤0.0001).

4.4 Protein analysis of the quadriceps from experimental COPD with H-151 intervention.

4.4.1 Protein degradation-associated protein abundance was unaffected by H-151 treatment or CS in an experimental COPD model

C57BL/6 mice underwent an experimental CS-induced COPD model for 8w. Treated and untreated mice were given H-151 or vehicle, respectively, 5d/w for 10w. Quadriceps were collected on the day of endpoint along with other skeletal tissues from the hind legs. There were no observed changes to GADD45α, atrogin-1 or MuRF1 protein levels regardless of CS-exposure or treatment status (Figure 4.4: A-C).

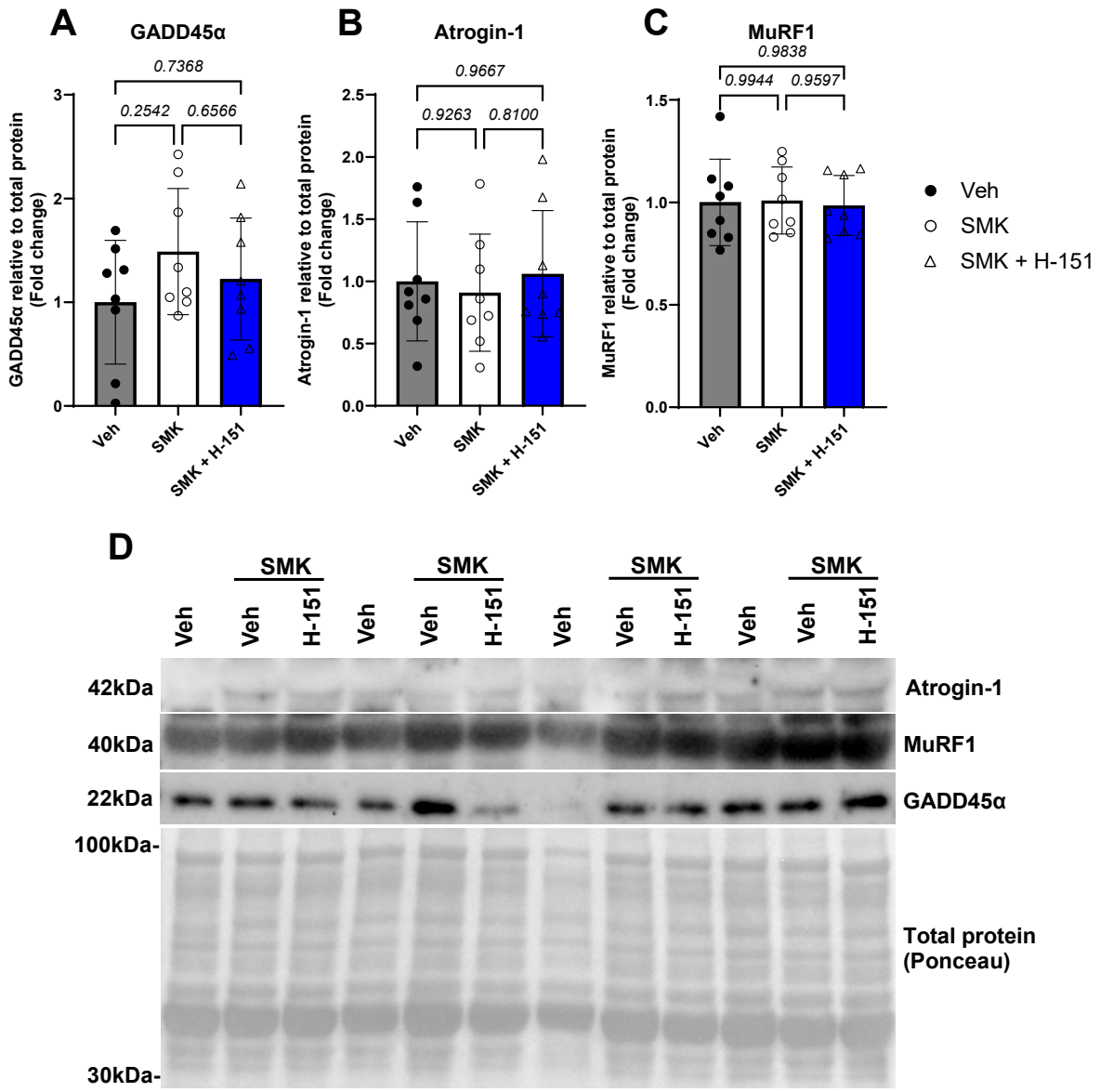

Figure 4.4 Protein degradation-associated protein abundance was unaffected by H-151 treatment or CS in an experimental COPD model.

Immunoblot analysis was used to assess the abundance of protein degradation-associated proteins in the quadriceps from H-151 treated female C57BL/6 mice (n=8) after 8w CS or room air exposure. Densitometric analysis was performed on membranes for **A** MuRF1 **B** Atrogin-1 and **C** GADD45α relative to total protein. **D** Membrane images of MuRF1 (40kDa), Atrogin-1 (42kDa), GADD45α (22kDa) and representative total protein stain (ponceau) used to normalise band intensity for densitometric analysis. Ordinary one-way Anova with Tukey's multiple comparison statistical analysis was performed on each data set. Individual values were graphed with mean ± SD displayed. Results with a P-value≤0.05 were considered significant.

4.4.2 cGAS and STING protein abundance in the quadriceps from mice in an experimental COPD model were unmodulated by CS exposure or H-151 treatment

C57BL/6 mice underwent an experimental CS-induced COPD model for 8w. Treated and untreated mice were given H-151 or vehicle, respectively, 5d/w for 10w. Quadriceps were collected on the day of endpoint along with other skeletal tissues. No change to cGAS or STING protein levels were observed, regardless of CS exposure or treatment status (Figure 4.5: A+B).

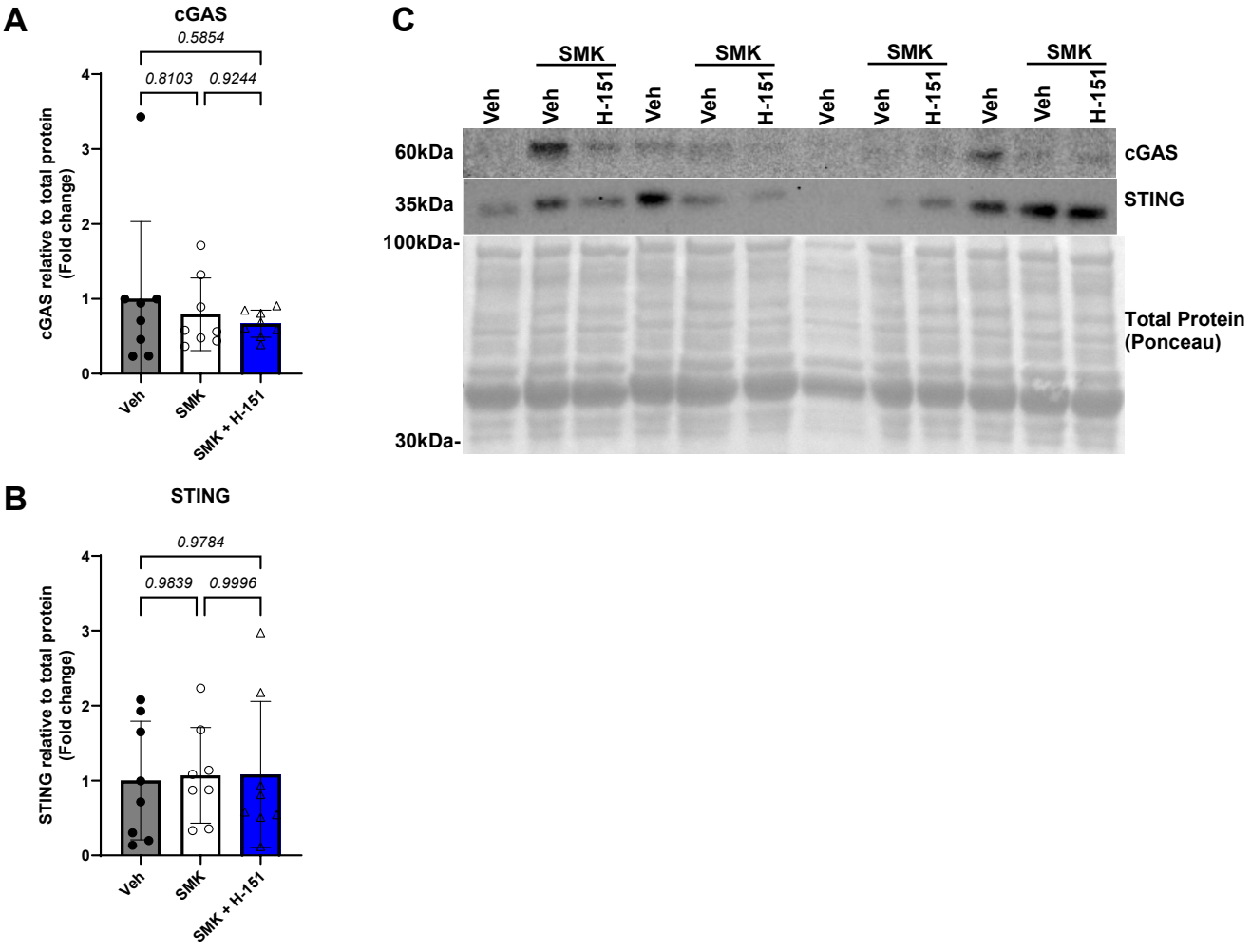

Figure 4.5 cGAS and STING protein abundance in the quadriceps from mice in an experimental COPD model were unmodulated by CS exposure or H-151 treatment.

Immunoblot analysis was used to assess the abundance of cGAS and STING proteins in the quadriceps from H-151 treated female C57BL/6 mice (n=8) after 8w CS or room air exposure.

Densitometric analysis was performed on membranes for **A** cGAS and **B** STING relative to total protein **C** Membrane images of cGAS (60kDa) and STING (42kDa) and representative total protein stain (ponceau) used to normalise band intensity for densitometric analysis. Ordinary one-way Anova with Tukey's multiple comparison statistical analysis was performed on each data set. Individual values were graphed with mean ± SD displayed. Results with a P-value≤0.05 were considered significant.

4.4.3 H-151 treatment had no effect on mTOR, Akt and p-Akt protein levels in the quadriceps of mice from an experimental COPD model.

C57BL/6 mice underwent an experimental CS-induced COPD model for 8w. Treated and untreated mice were given H-151 or vehicle, respectively, 5d/w for 10w. Quadriceps were collected on the day of endpoint along with other skeletal tissues. Regardless of CS exposure or treatment there were no changes to total mTOR or Akt protein expression (Figure 4.6: A+D). There were also no changes to Akt activation as indicated by phosphorylation at Thr308 Akt (Figure 4.6: B+C) and Ser473 Akt (Figure 4.6: E+F).

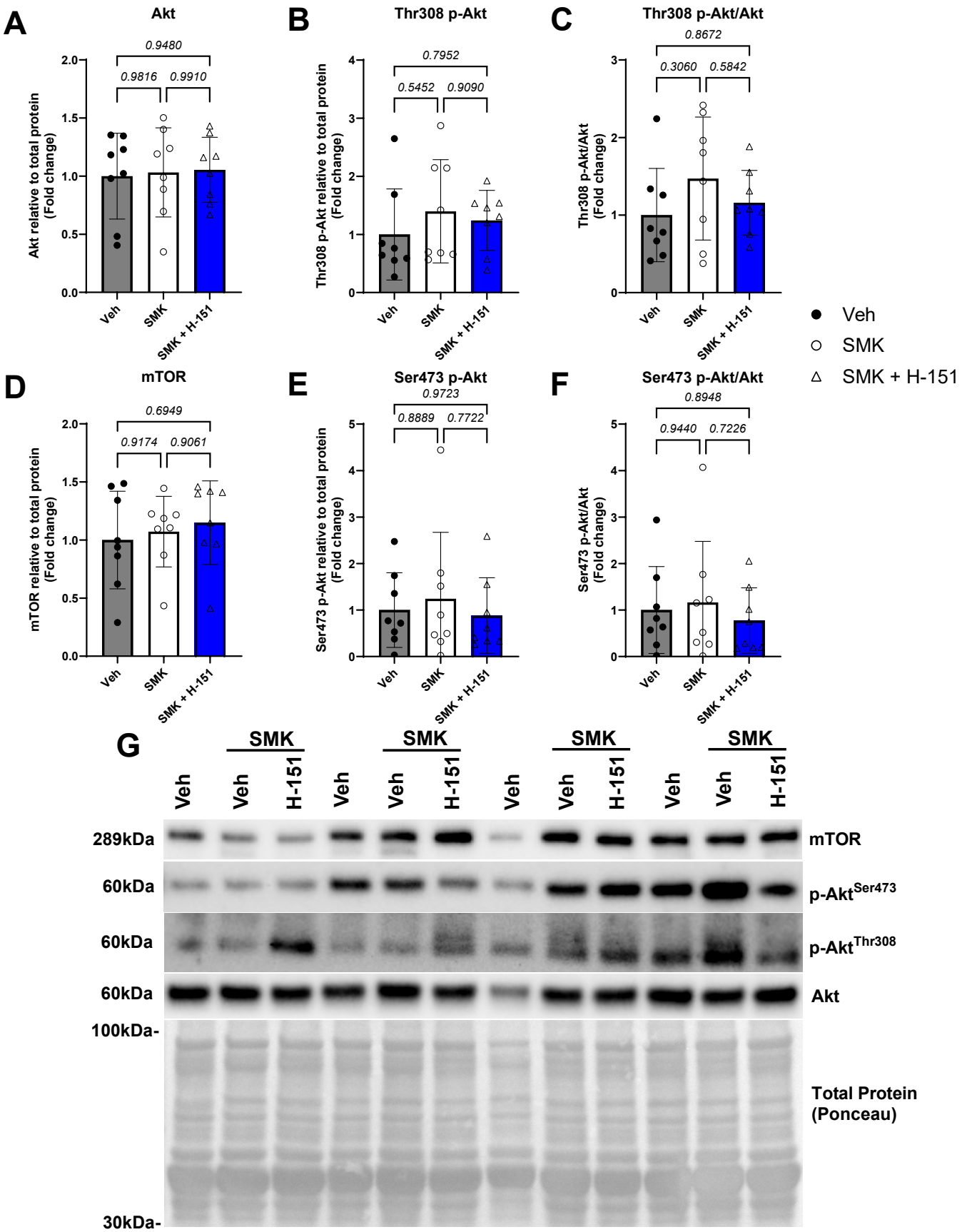
A
Akt
Akt relative to total protein (Fold change)
0.9480
0.9816
0.9910
B
Thr308 p-Akt
Thr308 p-Akt relative to total protein (Fold change)
0.7952
0.5452
0.9090
C
Thr308 p-Akt/Akt
Thr308 p-Akt/Akt (Fold change)
0.8672
0.3060
0.5842
D
mTOR
mTOR relative to total protein (Fold change)
0.6949
0.9174
0.9061
E
Ser473 p-Akt
Ser473 p-Akt relative to total protein (Fold change)
0.9723
0.8889
0.7722
F
Ser473 p-Akt/Akt
Ser473 p-Akt/Akt (Fold change)
0.8948
0.9440
0.7226
Veh
SMK
SMK + H-151
G
SMK
Veh
Veh
H-151
289kDa
60kDa
60kDa
60kDa
100kDa-
30kDa-
mTOR
p-Akt Ser473
p-Akt Thr308
Akt
Total Protein (Ponceau)

Figure 4.6 H-151 treatment had no effect on mTOR, Akt and p-Akt protein levels in the quadriceps of mice from an experimental COPD model.

Immunoblot analysis was used to assess mTOR and Akt and p-Akt protein abundance in the quadriceps from H-151 treated female C57BL/6 mice (n=8) after 8w CS or room air exposure. Densitometric analysis was performed on membranes for **A** Akt, **B** p-Akt^{Thr308} **C** p-Akt^{Thr308}/Akt **D** p-Akt^{Ser473} **E** p-Akt^{Ser473}/Akt and **F** mTOR relative to total protein in the quadriceps of female C57BL/6 mice exposed to CS for 8w and treated daily with H-151 (i.n.). **G** Western blot membrane images and representative total protein stain (ponceau) used to normalise band intensity for densitometric analysis. Ordinary one-way Anova with Tukey's multiple comparison statistical analysis was performed on each data set. Individual values were graphed with mean ± SD displayed. Results with a P-value≤0.05 were considered significant.

4.4.4 4E-BP1 protein levels were increased in the quadriceps of mice from an experimental COPD model and was not reduced by H-151 treatment.

C57BL/6 mice underwent an experimental CS-induced COPD model for 8w. Treated and untreated mice were given H-151 or vehicle, respectively, 5d/w for 10w. Quadriceps were collected on the day of endpoint along with other skeletal tissues. There were no changes to total S6K, or its activation via Thr389 phosphorylation (Figure: 4.7: A-C). There was also no observed change to total rpS6 or it's activation at via S6K phosphorylation of Ser235/236 (Figure 4.7: D-F).

However, there was a significant increase in 4E-BP1 protein in CS exposed mice with and without treatment (Figure 4.7: G), but no change to its phosphorylation state (Figure 4.7: H+I) which is controlled by mTORC1. This would suggest 4E-BP1 protein expression is upregulated by CS exposure and since it's ratio of p-4E-BP1/4E-BP1 does not change (Figure 4.7: I) it is likely free to bind eI-F4E, preventing protein synthesis.

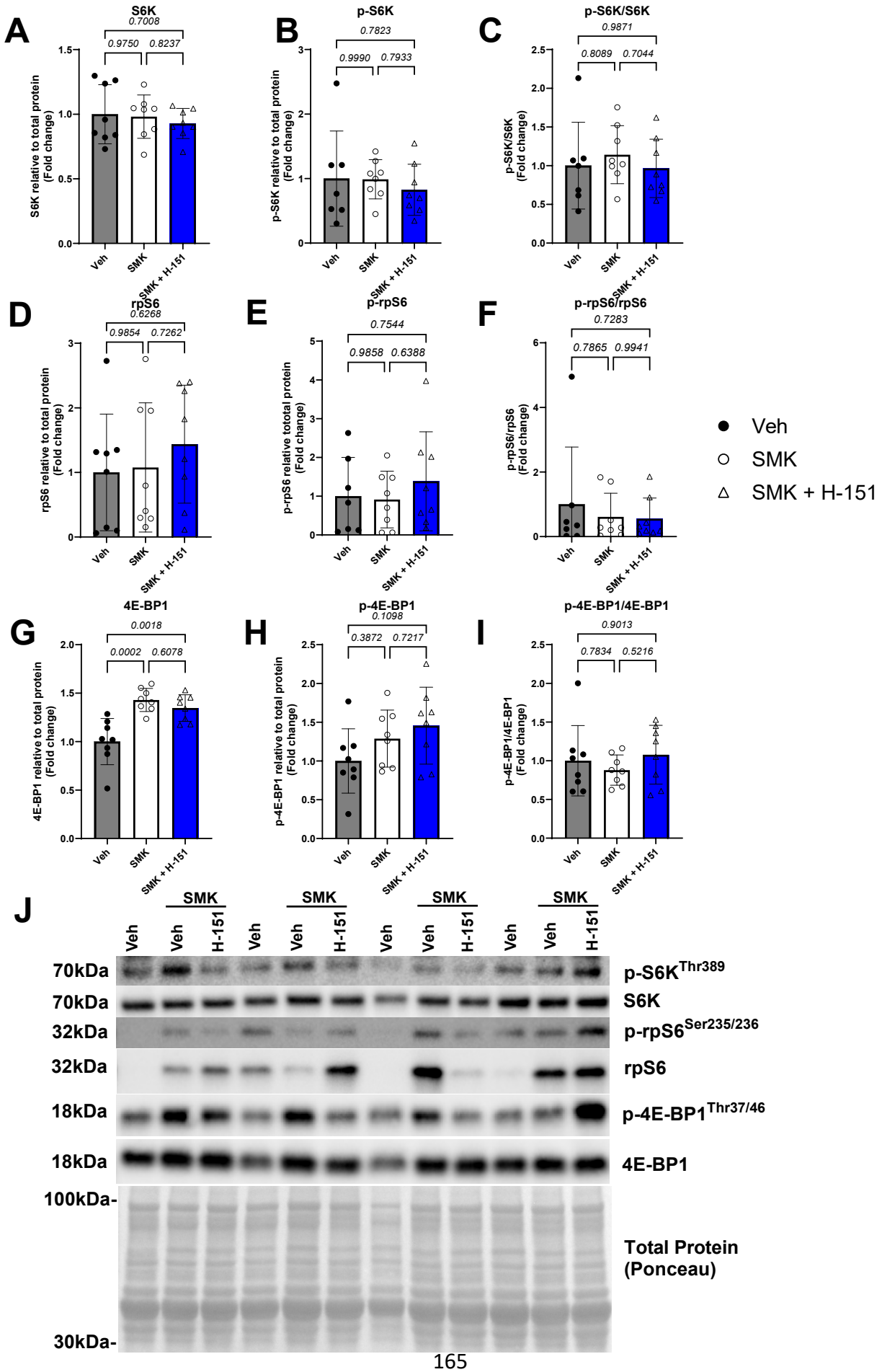
A
S6K
0.7008
0.9750
0.8237
S6K relative to total protein (Fold change)
B
p-S6K
0.7823
0.9990
0.7933
p-S6K relative to total protein (Fold change)
C
p-S6K/S6K
0.9871
0.8089
0.7044
p-S6K/S6K (Fold change)
D
rpS6
0.6268
0.9854
0.7262
rpS6 relative to total protein (Fold change)
E
p-rpS6
0.7544
0.9858
0.6388
p-rpS6 relative tototal protein (Fold change)
F
p-rpS6/rpS6
0.7283
0.7865
0.9941
p-rpS6/rpS6 (Fold change)
G
4E-BP1
0.0018
0.0002
0.6078
4E-BP1 relative to total protein (Fold change)
H
p-4E-BP1
0.1098
0.3872
0.7217
p-4E-BP1 relative to total protein (Fold change)
I
p-4E-BP1/4E-BP1
0.9013
0.7834
0.5216
p-4E-BP1/4E-BP1 (Fold change)
Veh
SMK
SMK + H-151
J
Veh
SMK
Veh
H-151
70kDa
p-S6K^Thr389
70kDa
S6K
32kDa
p-rpS6^Ser235/236
32kDa
rpS6
18kDa
p-4E-BP1^Thr37/46
18kDa
4E-BP1
100kDa-
30kDa-
Total Protein (Ponceau)

Figure 4.7 4E-BP1 protein levels were increased in the quadriceps of mice from an experimental COPD model and was not reduced by H-151 treatment.

Immunoblot analysis was used to assess the abundance of downstream effectors of mTORC1 in the quadriceps from H-151 treated female C57BL/6 mice (n=8) after 8w CS or room air exposure. Densitometric analysis was performed on membranes for **A** S6K **B** p-S6K^{Thr389}**C** p-S6K^{Thr389}/ S6K **D** rpS6 **E** p-rpS6$^{Ser235/236}$ **F** p-rpS6$^{Ser235/236}$/rpS6 **G** 4E-BP1 **H** p-4E-BP1$^{Thr37/46}$ and **I** p-4E-BP1$^{Thr37/46}$/4E-BP1 abundance relative to total protein **J** Western blot membrane images with a representative total protein stain (ponceau) used to normalise band intensity for densitometric analysis. Ordinary one-way Anova with Tukey's multiple comparison statistical analysis was performed on each data set. Individual values were graphed with mean ± SD displayed. Results with a P-value≤0.05 were considered significant.

4.4.5 The abundance of ETC complex proteins was unaltered in the quadriceps of mice from an experimental COPD model and was not affected by H-151 treatment.

C57BL/6 mice underwent an experimental CS-induced COPD model for 8w. Treated and untreated mice were given H-151 or vehicle, respectively, 5d/w for 10w. Quadriceps were collected on the day of endpoint along with other skeletal tissues. In contrast to the first 8w COPD model (Figure 3.28: E), there were no observed changes in complex V subunit protein expression in this model, regardless of CS exposure or treatment status (Figure 4.8: E). There was also no observed change to other complex subunit proteins (Figure 4.8: A-D).

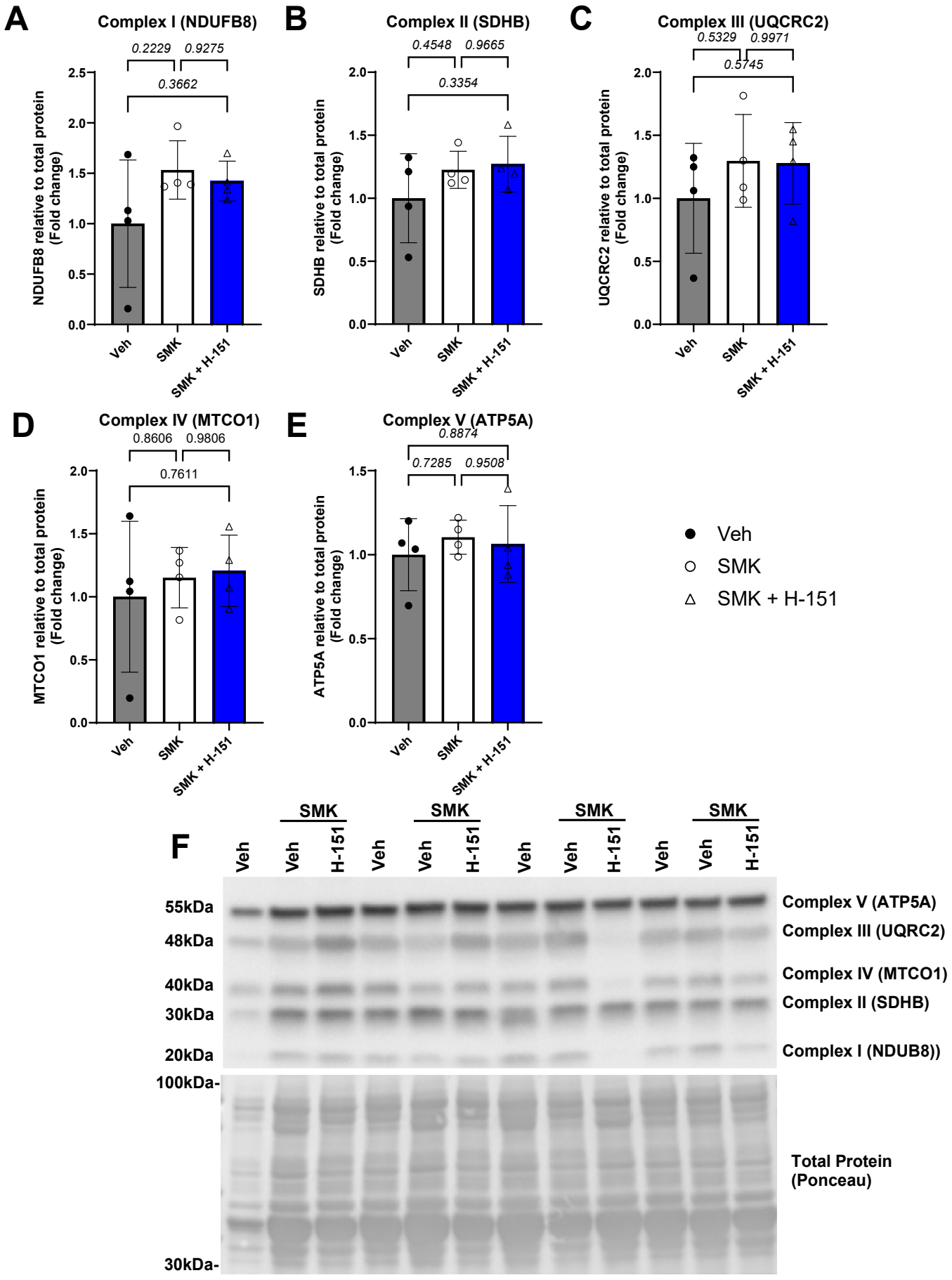
A
Complex I (NDUFB8)
0.2229
0.9275
0.3662
NDUFB8 relative to total protein (Fold change)
Veh
SMK
SMK + H-151
B
Complex II (SDHB)
0.4548
0.9665
0.3354
SDHB relative to total protein (Fold change)
C
Complex III (UQCRC2)
0.5329
0.9971
0.5745
UQCRC2 relative to total protein (Fold change)
D
Complex IV (MTCO1)
0.8606
0.9806
0.7611
MTCO1 relative to total protein (Fold change)
E
Complex V (ATP5A)
0.8874
0.7285
0.9508
ATP5A relative to total protein (Fold change)
Veh
SMK
SMK + H-151
F
SMK
SMK
SMK
SMK
Veh
Veh
H-151
55kDa
48kDa
40kDa
30kDa
20kDa
100kDa-
30kDa-
Complex V (ATP5A)
Complex III (UQRC2)
Complex IV (MTCO1)
Complex II (SDHB)
Complex I (NDUB8))
Total Protein (Ponceau)

Figure 4.8 The abundance of ETC complex proteins was unaltered in the quadriceps of mice from an experimental COPD model and was not affected by H-151 treatment.

Immunoblot analysis was used to assess the abundance electron transport chain (ETC) complex proteins in the quadriceps from H-151 treated female C57BL/6 mice (n=8) after 8w CS or room air exposure. Densitometric analysis was performed on membranes for **A** Complex I (NDUFB8) **B** Complex II (SDHB) **C** Complex III (UQRC2) **D** Complex IV (MTCO1) **E** Complex V (ATP5A). **J**. Western blot membrane images and total protein stain (ponceau) used to normalise band intensity for densitometric analysis. Ordinary one-way Anova with Tukey's multiple comparison statistical analysis was performed on each data set. Individual values were graphed with mean ± SD displayed. Results with a P-value≤0.05 were considered significant.

4.5 Complex I respiration and ADP sensitivity were altered in the gastrocnemius of mice from an experimental COPD model and returned to baseline with H-151 treatment

The gastrocnemius muscle was collected at the endpoint and 15-25mg of fresh tissue was excised from the hip-end of the muscle and placed in BIOPS buffer at 4^{o}C for later use in Oroborus measurements of mitochondrial respiration.

There was a significant increase in complex I proton leakage due to CS-exposure compared to the vehicle control (Figure 4.9: A). However, this significant increase in complex I leak was not observed in H-151 treated mice (Figure 4.9: A) which suggests H-151 prevents CS-induced complex I leak. There was no observed change to complex I only linked OXPHOS capacity (Figure 4.9: B), complex I & II linked OXPHOS capacity (Figure 4.9: C), or maximally uncoupled OXPHOS capacity (Figure 4.9: D). A significant increase in ADP sensitivity was observed in CS exposed mice, which was significantly decreased with H-151 treatment (Figure 4.9: E).

These data suggest CS exposure induces changes to mitochondrial respiration and that H-151 can inhibit some of these changes.

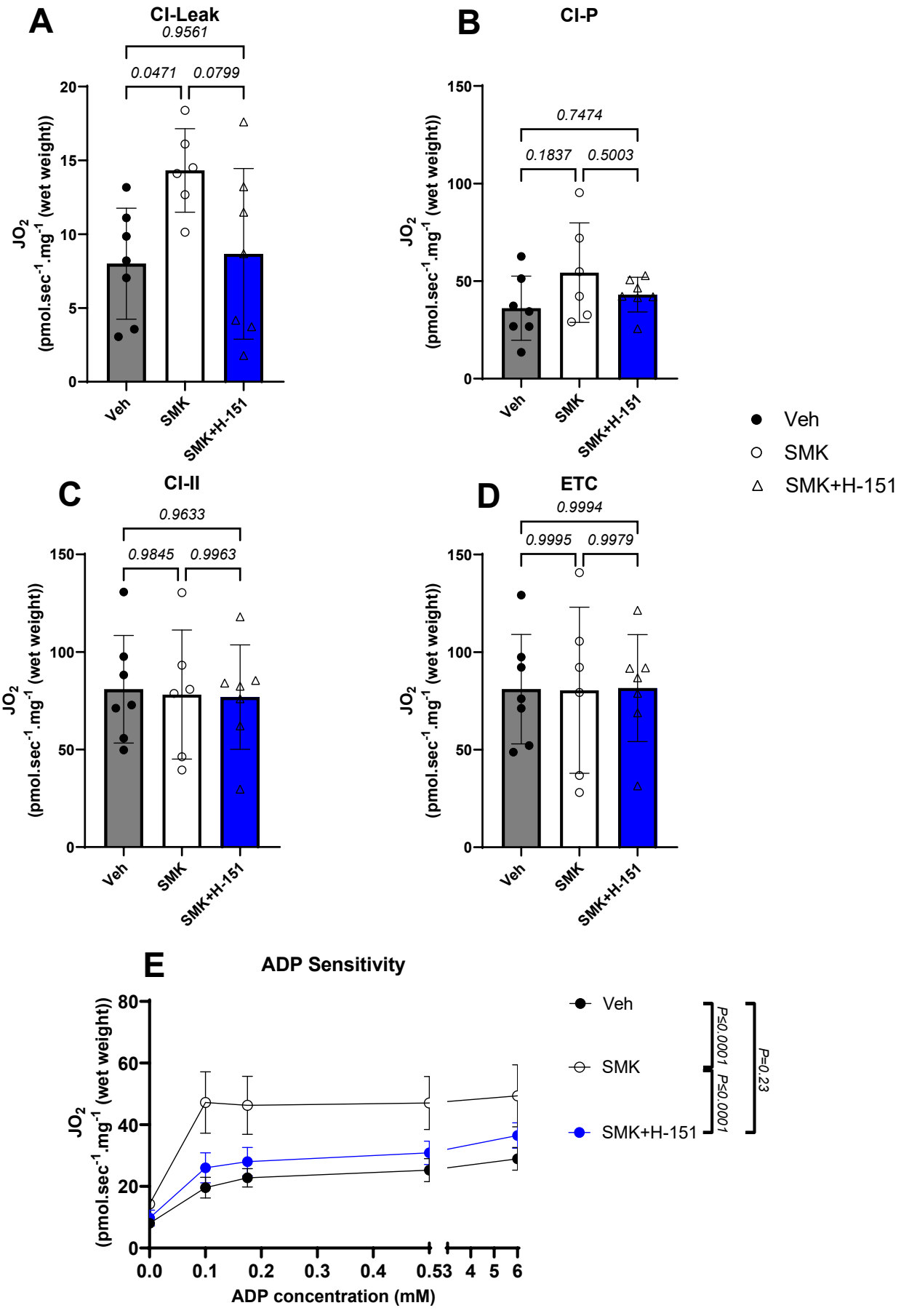
A
CI-Leak
0.9561
0.0471
0.0799
JO2 (pmol.sec-1.mg-1 (wet weight))
Veh
SMK
SMK+H-151
B
CI-P
0.7474
0.1837
0.5003
C
CI-II
0.9633
0.9845
0.9963
D
ETC
0.9994
0.9995
0.9979
Veh
SMK
SMK+H-151
E
ADP Sensitivity
ADP concentration (mM)
P≤0.0001
P≤0.0001
P=0.23

Figure 4.9 Complex I dynamics and ADP sensitivity were altered in the gastrocnemius of mice from an experimental COPD model and returned to near baseline with H-151 treatment

Oroboros Oxygraph-2k analysis of gastrocnemius' mitochondrial respiration from a H-151 treatment model of COPD. **A** Oxygen consumption rate attributed to complex I linked proton flux across the inner mitochondrial membrane that bypasses ATP synthase ($pmol.sec^{-1}.mg^{-1}$). **B** Oxygen consumption rate attributed to Complex I linked OXPHOS capacity ($pmol.sec^{-1}.mg^{-1}$). **C** Oxygen consumption rate attributed to OXPHOS capacity of complex I and II ($pmol.sec^{-1}.mg^{-1}$). **D** Maximal oxygen consumption rate with oligomycin induced decoupling of proton flux across the inner mitochondrial membrane. **E+F** Oxygen consumption rate with increasing doses of ADP ($pmol.sec^{-1}.mg^{-1}$). Ordinary one-way Anova with Tukey's multiple comparison statistical analysis was performed on each data set (A-D) and individual values were graphed with mean ± SD displayed. Two-way Anova Tukey's multiple comparison statistical analysis was performed on the ADP sensitivity data (E) and replicate values were graphed as mean ± SD. Results with a P-value≤0.05 were considered significant.

4.6 MFA was unchanged with CS exposure or H-151 treatment in the quadriceps of mice from an experimental COPD model.

Quadriceps were collected at endpoint and stored in formalin for histological processing. There was a significant decrease in quadriceps weight with CS exposure, and no significant change with CS exposure + H-151 treatment (Figure 4.3: C). However, there was no significant change to MFA of the quadriceps under any condition (Figure 4.10).

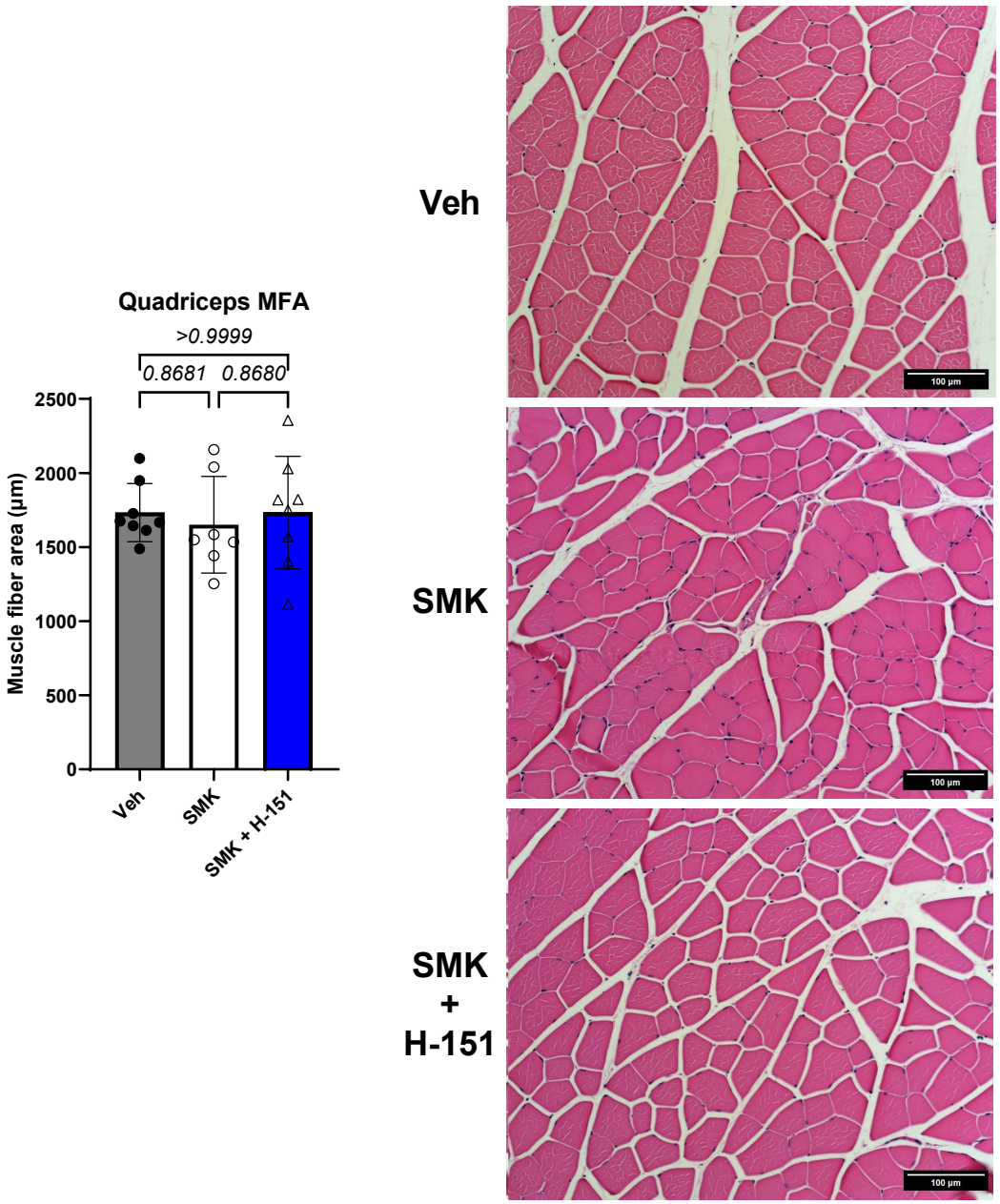

Figure 4.10 MFA was unchanged with CS exposure or H-151 treatment in the quadriceps of mice from an experimental COPD model.

Cross sectional areas (CSA) were taken of the quadriceps mid-belly from an 8w H-151 intervention murine model of CS-induced COPD. CSAs then haematoxylin and eosin stained. Sections of quadriceps were imaged at 20X magnification with brightfield microscopy. Images were imported into ImageJ and muscle fibre areas were measured manually by drawing around each fibre for at least 100 technical replicates per biological sample. Ordinary one-way Anova with Tukey's multiple comparison statistical analysis was performed on each data set and individual values were graphed with mean ± SD displayed. Results with a P-value≤0.05 were considered significant.

Discussion - Chapter 4

The aim of this study was to prevent mitochondrial dysfunction-mediated muscle atrophy in an experimental model of COPD. H-151, which was used to prevent mtDNA induced inflammation through inhibition of STING signalling, did not prevent COPD induced skeletal muscle atrophy in young female mice. As anticipated, lung volumes increased in the CS exposed murine model. However, this effect was not reversed by H-151 treatment. Body weight plateaued over time and N-A length was decreased in CS exposed mice, with no improvement observed following H-151 treatment, indicating that H-151 did not provide a beneficial effect in restoring normal lung function or development in young mice. Loss in Skeletal muscle mass was also observed in the gastrocnemius, quadriceps, EDL and soleus muscles with CS exposure, and this was not significantly improved with H-151 treatment.

Despite significant decreases in muscle mass, there was no change in muscle fibre area with CS exposure with H-151 treatment. Hyperplasia, the increase in the number of myofibers, may be negatively impacted by CS exposure during mouse development and could explain the decrease in muscle mass without a loss of MFA. However, studies that have investigated postnatal muscle fibre growth in murine EDL muscle showed that there is no increase in total myofibers between the ages of 1-8 weeks, and rather an increase in myofiber size (hypertrophy) is responsible for a gain in skeletal muscle mass [347]. Therefore, fluid loss and subsequent dehydration, or a decrease in glycogen, may be responsible for the observed decrease in skeletal muscle weight without a loss of myofiber area due to CS exposure.

An increase in total 4E-BP1 protein was observed in CS exposed mice, however, this was not changed with H-151 treatment. This highlights 4E-BP1, an mRNA translation inhibitor, as a

potential mediator of COPD associated muscle atrophy, since this was the second model where this effect was observed.

Complex I linked proton leak was also observed in the gastrocnemius of CS exposed, but not H-151 treated mice. This indicates that mitochondrial dysfunction occurs in the gastrocnemius in experimental COPD. It is possible that the increased proton leak is a protective mechanism employed by the mitochondria to reduce mtROS production [329], however, this decouples the proton gradient from ATP production, resulting in inefficient ATP production [330]. Increased proton leak can also indicate disruption to inner mitochondrial membrane integrity due to cellular/mitochondrial stress [330]. ADP sensitivity was also increased in CS exposed, but not in H-151 treated mice, suggesting that mitochondria respond to cellular stress to try to meet energy demands.

H-151 prevented increases in proton leak and ADP sensitivity, suggesting a potential role for STING in regulating bioenergetics in skeletal muscle. For instance, a shift towards aerobic glycolysis may be accounted for by the observed increase in ADP sensitivity, as ADP is required for glycolysis and is rate limiting [348]. This metabolic shift is characterized by rapid ATP production, which is essential for supporting inflammatory responses but comes at the cost of reduced energy efficiency and mitochondrial dysfunction [349]. As a result, there was increased cellular sensitivity to ADP concentration.

STING activation can promote a glycolytic switch through TBK1 activation [350] and the subsequent induction of inflammatory cytokines such as IL-6 [351]. However, activation of the cGAS-STING pathway also results in type I IFN production, which negatively regulates glycolysis [352]. The role of cGAS-STING in regulating autophagy and mitophagy are more elucidated. STING activation is known to induce autophagy and mitophagy through TBK1 mediated inhibition of

mTORC1 [353] However, these mechanisms require further investigation in the context of skeletal muscle.

In conclusion, H-151 may confer protective effects on mitochondrial health in skeletal muscle by preventing proton leak and ADP sensitivity in the skeletal muscle of an experimental COPD model. Mechanistically, this may be achieved through inhibiting a STING-dependent metabolic switch, that is possibly mediated by TBK1 activation by STING. Targeting this switch may result in improved skeletal muscle health and mitochondrial function, without a change to overall skeletal muscle mass. Although no improvement in skeletal muscle mass was observed in this COPD model, inhibition of STING mediated TBK1 activity may also promote protein synthesis by inhibiting TBK1 mediated inhibition of mTORC1. However, the metabolic pathways induced by STING activation, and the effect of STING inhibition on those pathways require further investigation.

The mitochondrial respiratory changes observed with CS exposure in this model indicated disruption to mitochondrial functions. This provided the basis for a follow up study aimed at improving mitochondrial function by inducing mitophagy with a dietary UA intervention.

Chapter 5 Urolithin A (UA) as a novel treatment against COPD induced cachexia.

5.1 Introduction

The results described in my previous chapters on muscle atrophy in various murine models of pulmonary disease revealed that experimental COPD exhibited a significant reduction in both total body weight and skeletal muscle mass, particularly in the gastrocnemius and quadriceps muscles. This reduction was consistent across both male and female C57BL/6 mice. Additionally, CS exposure in this model led to a marked decrease in N-A length, indicating impaired overall development in these mice.

The previously examined murine models of experimental COPD were initiated in 8w old mice, an age at which mice are considered sexually mature, but still juvenile. In these mice, COPD is established by 16w old; however, this does not accurately reflect the typical age at which humans are diagnosed with COPD, which usually occurs from approximately 45 years old, the equivalent of about 1y old mice. Furthermore, young mice (8w old) are still in a developmental stage, continuing to gain weight until around 24 weeks of age at which point weight plateaus [354]. This poses a challenge for researching cachexia, which is characterized by strength and muscle loss over time. In young mice CS prevented weight gain compared to control mice. This plateau made it difficult to observe progressive muscle loss. In this chapter, I sought to further address my first thesis aim of identifying an appropriate model of pulmonary disease-induced COPD by including a cohort of 1y old mice to better mimic the disease's progression in humans and the typical age of COPD diagnosis (~45y old).

In this chapter, I sought to evaluate the impact of Urolithin A treatment on inflammation, skeletal muscle protein degradation, synthesis, and mitochondrial respiration in young and adult mice within the context of experimental COPD. Pathway enrichment analysis of human biopsy data from COPD patients indicated reduced mitochondrial biogenesis, evidenced by reduced expression of genes associated with mitochondrial function in the quadriceps (Figure 3.29). Both systemic inflammation and impaired mitochondrial function are known contributors to cachexia. The therapeutic intervention used here was Urolithin A (UA). Studies on UA have demonstrated significant benefits in skeletal muscle health in numerous *in vivo* models across various species, as well as in human clinical trials. UA improves skeletal muscle function by enhancing mitophagy and overall mitochondrial health, leading to increased muscle endurance, and reduced inflammation and muscle atrophy. Moreover, these beneficial outcomes have been demonstrated in aged mouse and human studies, so the treatment should remain relevant in 1y old mice.

Therefore, a UA intervention in the experimental COPD model was utilised to attempt to enhance mitophagy and reduce the systemic inflammation associated with COPD in both young and old mice. It was hypothesised that UA -induced mitophagy would improve skeletal muscle health and mitigate muscle loss in experimental COPD.

5.2 Methodology and Experimental design

5.2.1 Overview of a Urolithin A dietary intervention, COPD model in young and adult C57BL/6 mice.

8w old (Young) and 1y old (Adult) C57BL/6 female mice were subjected to an 8w experimental COPD model where mice were exposed to CS from 12 cigarettes, twice/d, 5d/w. From 2w prior to the start of the COPD model mice began treatment with UA (25mg/kg), which was given ad libitum

in DietGel® Boost. An average daily serving of ~4.7g of boost gel was provided per cage of 4 mice, into which UA was mixed. The mix was almost always completely eaten by early afternoon. Mice were weighed daily (Monday-Friday).

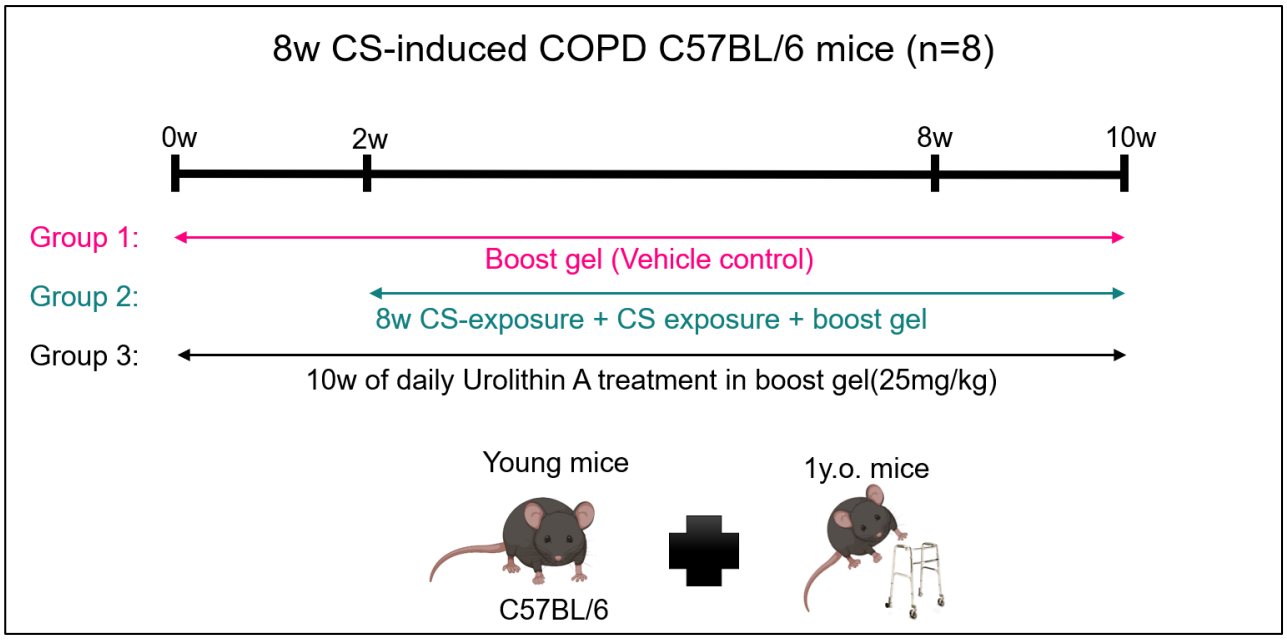

Figure 5.1 Overview of a UA dietary intervention in experimental COPD in young and adult C57BL/6 mice.

C57BL/6 mice (n=8) were exposed CS or air for 8w. UA (25mg/kg) was given *ad libitum* in the diet 5d/w (Monday-Friday) for 2w prior to the beginning of CS exposure until the endpoint (10w). UA was mixed into a calorie boost gel (Vehicle) that was also given to each group. Young and adult mice were 8w and 1y old, respectively, at the commencement of H-151 treatment.

As a standard part of the labs smoke exposure safety operating procedure (SOP), CS exposure is stopped if mouse weight loss exceeds 15% of the starting weight of that mouse. This did occur for some of the mice in the adult mice CS and CS + UA treated groups.

An amendment to the project's animal ethics allowed certain mice that were still deemed healthy but had exceeded 15% weight loss to continue CS exposure. This was done because adult mice had much higher starting weights (25.77g-33.88g) than the young mice cohort (17.9g-19.79g). As a

result, some adult mice did not receive CS exposure for one week of the model despite being considerably heavier than other mice that were still receiving CS exposure. One mouse that temporarily halted CS-exposure was 28.2g (we routinely smoke young mice that weigh as little as 16g). This amendment changed the criteria for the cessation of smoking by adding the need for a second condition besides an arbitrary weight loss figure. This condition was based on category 2 conditions for monitoring infected animals. These conditions are, signs of being ungroomed, reddening and swelling at an injection site (in the context of this COPD model this was the area exposed to CS), coughing and sneezing, aggression, abdominal swelling, hunched posture, awkward gait, lack of defecation when handling and loose stool. These criteria were introduced to maximise the accuracy of our model, without unnecessarily compromising the wellbeing of any mice. CS was well tolerated by all adult mice that had >15% weight loss, and no adverse events were reported during the duration of the model.

5.3 Flow cytometry – Urolithin A intervention in an experimental model of COPD in young and adult mice

5.3.1 Flow Cytometry – Fluorescent antibodies, Live/dead (L/D) stain and compensation beads

Antibody	Fluorophore	DIF	Laser	Clone	Company	Category#	Lot#
CD45	BV 786	400	Violet	30-F11	BD Horizon	564225	3152770
CD4	PerCP	200	Blue	RM4-5	BD Pharmingen	553052	9052677
CD8a	BUV 805	200	UV	53-6.7	BD Horizon	612898	3109401
CD19	APC-Fire 750	200	Red	6D5	BioLegend	115558	B379744
TCR beta	BV 510	200	Violet	H57-597	BioLegend	109233	B397405
CD11b	BUV 395	400	UV	M1/70	BD Horizon	563553	3109427
F4/80	BUV 737	100	UV	T45-2342	BD OptiBuild	749283	4036011
Ly-6G	BV 711	200	Violet	1A8	BD Horizon	563979	1225765
Ly-6C	PE-Cy7	200	Yellow	AL-21	BD Pharmingen	560593	1040494
CD11c	FITC	200	Blue	N418	BioLegend	117306	B370929
CD170 (Siglec-F)	AF 647	200	Red	S17007L	BioLegend	155520	B38699
CD115 (CSF-1R)	PE-Dazzle 594	200	Yellow	AFS98	BioLegend	135528	B374475
MHCII (I-A/I-E)	AF 700	400	Red	M5/114.15.2	Invitrogen	56-5321-82	2608864

Stain/Bead	Fluorophore	DIF	Laser	α-Specificity	Company	Category#	Lot#
Live &Dead (L/D)	BUV450	800	UV	-	ThermoFisher	L23105	267402
UltraComp™ eBeads	-	-	-	Mouse, Rat, Hamster	Invitrogen	01-2222-42	-
BD™ CompBeads	-	-	-	Rat, Hamster Ig,κ	BD Biosciences	552845	-

Table 5.1 Flow Cytometry – Fluorescent antibodies.

Bronchoalveolar lavage fluid (BALF) and blood leukocytes were isolated and incubated with primary antibodies. Antibody concentration, fluorophore, dilution factor (DIF), laser type needed for fluorophore activation, clone, company from which the antibody was bought, category number (#) and lot # are provided.

5.3.2 Flow Cytometry – Sample preparation and fluorescent antibody incubation

Blood was collected by cardiac puncture, injected into a MiniCollect Tube 1ml K3EDTA (InterPath Services) and placed on ice to prevent coagulation. BALF was collected in 1.5mL microcentrifuge tubes, put on ice, and the volume of BALF recovered, out of 1mL, was recorded so that total leukocyte concentration could be calculated. Buffers were prepared as described in Table 5.2.

Blood sample preparation: 300uL of blood was added to a screw cap, 50mL conical centrifuge tube (FALCON). 10mL of (red blood cell) RBC lysis buffer was added to the tube and kept on ice for 7 minutes. 20mL of FACS buffer was added and sample was centrifuged at 350g for 5 minutes. Supernatant was discarded, and the cell pellet resuspended in 420µL of fluorescence-activated cell sorting (FACS) buffer on ice. 200µL of sample was added to the respective V-bottom well based on the plate map (Table 2.10). 200µL of each remaining sample was pooled and the pooled sample

was added to the pooled sample wells (Table 2.10). Pooled blood sample was used instead of BALF as total cells recovered are usually much lower.

BALF sample preparation: BALF samples were centrifuged at 300g for 5m at 4^{o}C and supernatant transferred into fresh 1.5mL microcentrifuge tubes (stored at -80^{o}C). 250µL of RBC lysis buffer was added to the cell pellet for 5m on ice before being neutralised with 1mL HANKS buffer. Cells were centrifuged again at 300g for 5m at 4^{o}C, the supernatant was discarded, and cell pellet resuspended in HANKS buffer. 200µL of sample was added to the respective V-bottom well based on the plate map and 20uL was kept for calculating total leukocytes in each BALF sample. This was done using a 2:1 dilution in trypan blue and counting cells using a light microscope and haemocytometer.

L/D staining: Once all samples, including pooled and unstained samples, were plated the plate was centrifuged at 300g for 5m (SS beads plated before cells). Cells were re-suspended in 50uL of Live dead (L/D) stain (L23105 Thermo Fisher). L/D was made up fresh on the day (made up in PBS not FACS otherwise the serum will inhibit it). L/D stain was not added to the SS or unstained wells. 50µL of FACS buffer was instead added to the unstained and Fc block was added to the single stain. Cells were then incubated for 20m in the dark at 4^{o}C. 150µL of PBS was added and samples were centrifuged at 300g for 5m. Supernatant was discarded.

Incubation with antibodies: Cells were resuspended in 50µL of antibody cocktail and incubated for 30m in the dark at 4^{o}C. 50µL of CytoPERM (fix buffer) was added and the cells were incubated for 20m in the dark at 4^{o}C. 150µL of FACS buffer was then added, and samples were centrifuged at 300g for 5m, and supernatant was discarded. 100uL of FACS buffer was then added to each well. 100uL more FACS buffer was added just before flow cytometric analysis.

5.3.3 Flow Cytometry Buffers

Buffer	Final concentration	For working stock
FACS buffer	1X sterile PBS	1L (filter sterilise working stock)
	1% BSA (minimal to decrease interference)	10g
	EDTA (2mM)	4mL of 0.5M EDTA stock
10X HEPES (4-(2-Hydroxyethyl)piperazine-1-ethane-sulfonic acid)	HEPES (0.1M; pH7.4)	23.83 g
	NaCl (150mM)	87.66g
	KCl (50mM)	3.72g
	$MgCl_2$ (10mM)	2.033g
	$CaCl_2 \bullet H_2O$ (18mM)	2.6g
	MilliQ	Make up to 1L; pH7.4; filter sterilise

Table 5.2 Flow Cytometry – Buffers with stock concentrations of each reagent and working stock concentration.

5.3.4 Flow Cytometry - Gating strategy for a Urolithin A intervention in young and adult mice in an experimental COPD model: FlowJo™ (v10.10) software.

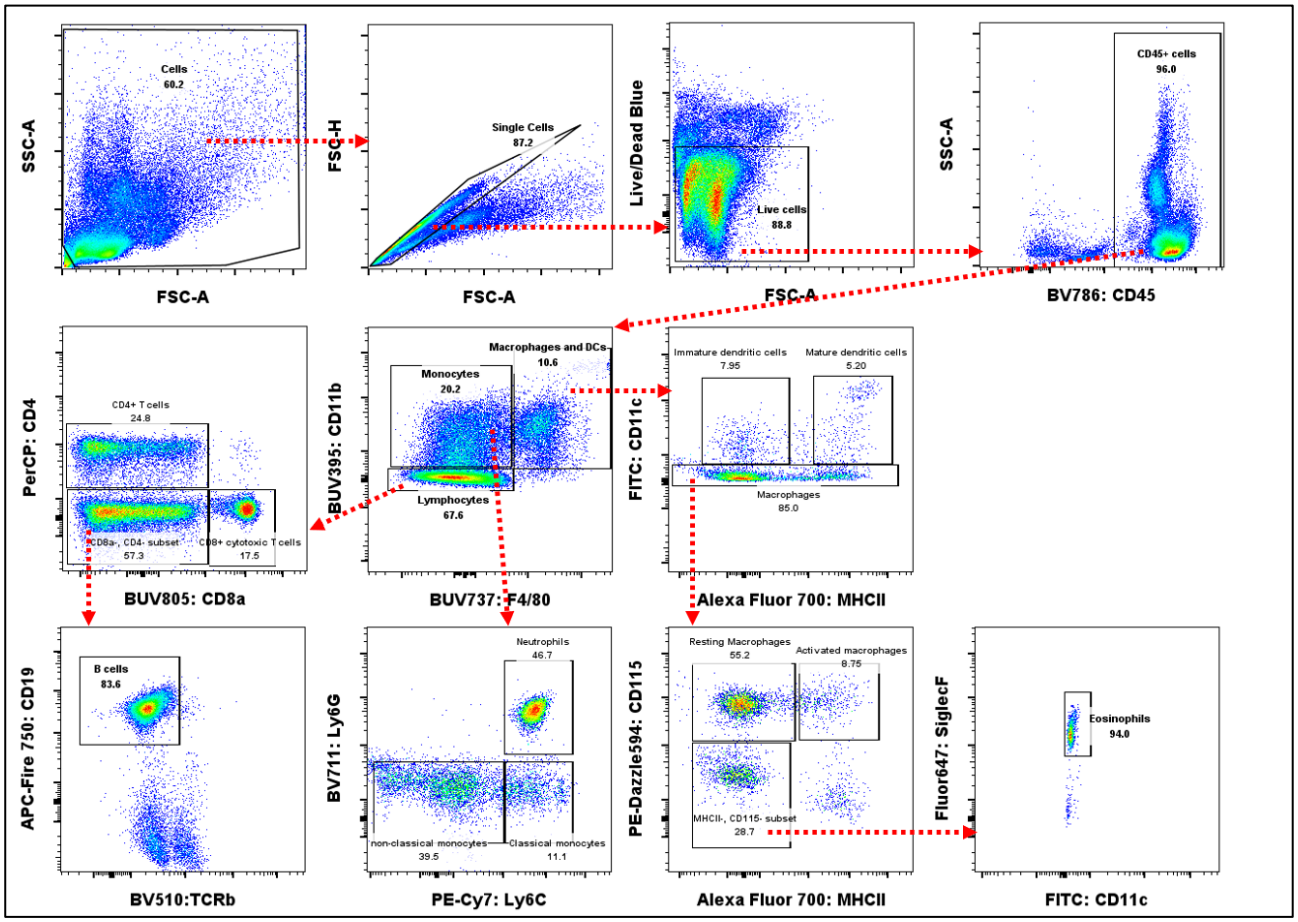

Table 5.3 Flow Cytometry - Gating strategy for a Urolithin A intervention in young and adult mice in an experimental COPD model.

Gating strategy and flow cytometry analysis done using FlowJo™ (v10.10) software.

Acknowledgements for chapter 5

I would like to acknowledge Tsung-yu (Johann) Pai for his integral assistance with the flow cytometry. Tsung-yu helped me plan my flow panel and was there to provide his expertise on the day of endpoint. I also thank Dr. Ashleigh Philp, who conducted the Oroboros analysis of the gastrocnemius muscle in this chapter. Dr. Elinor Hortle, Dr. Matt Johansen, Dr. Ashleigh Philp, Dr. Jacqueline Marshall and Angelica Katsifis provided assistance in the endpoint, helping to collect tissues and measure lung function.

5.4 Lung function, whole body and skeletal muscle weights of young and old mice with experimental COPD treated with UA intervention

5.4.1 Lung function decline was observed in young and old mice in an experimental COPD model and lung volumes were increased with UA treated CS exposed adult mice.

Young (8w old) and adult (1y old) C57BL/6 female mice were exposed to the smoke of 12 cigarettes twice daily, 5d/w for 8w. Some mice were treated with UA (25mg/kg) in the diet ad libitum beginning 2w prior to the start of CS-exposure.

Young mice air, CS and CS+UA group comparison: CS exposed young mice had significantly higher TLC and hysteresis (Figure 5.2: C+D) in comparison to room air exposed mice, but not in comparison to the CS only mice (Figure 5.2: A). CS+UA treatment also increased IC compared to room air exposed mice, but not when compared to CS exposure alone.

Adult mice air, CS and CS+UA comparisons: CS+UA treated adult mice had increased IC, FVC, TLC and hysteresis compared to room air exposed adult mice (Figure 5.2: A-D). However, CS alone only had higher IC and TLC, compared to the room air exposed group (Figure 5.2: A+C).

Young vs adult comparison: In adult CS exposed mice, IC, FVC and TLC (Figure 5.2: A-C) were significantly increased, and Rrs and Rn were decreased (Figure 5.2: E+F) compared to young mice across all groups. Hysteresis was also significantly higher in CS+UA treated adult mice compared to CS+UA treated young mice (Figure 5.2: D).

These data showed significant differences in lung function outcomes between young and adult mice. It also demonstrated the negative impact of smoking on lung function, verifying that our model of COPD worked in this instance. Surprisingly, UA treatment appeared to increase some

lung volume parameters in CS exposed mice, particularly in adult mice.

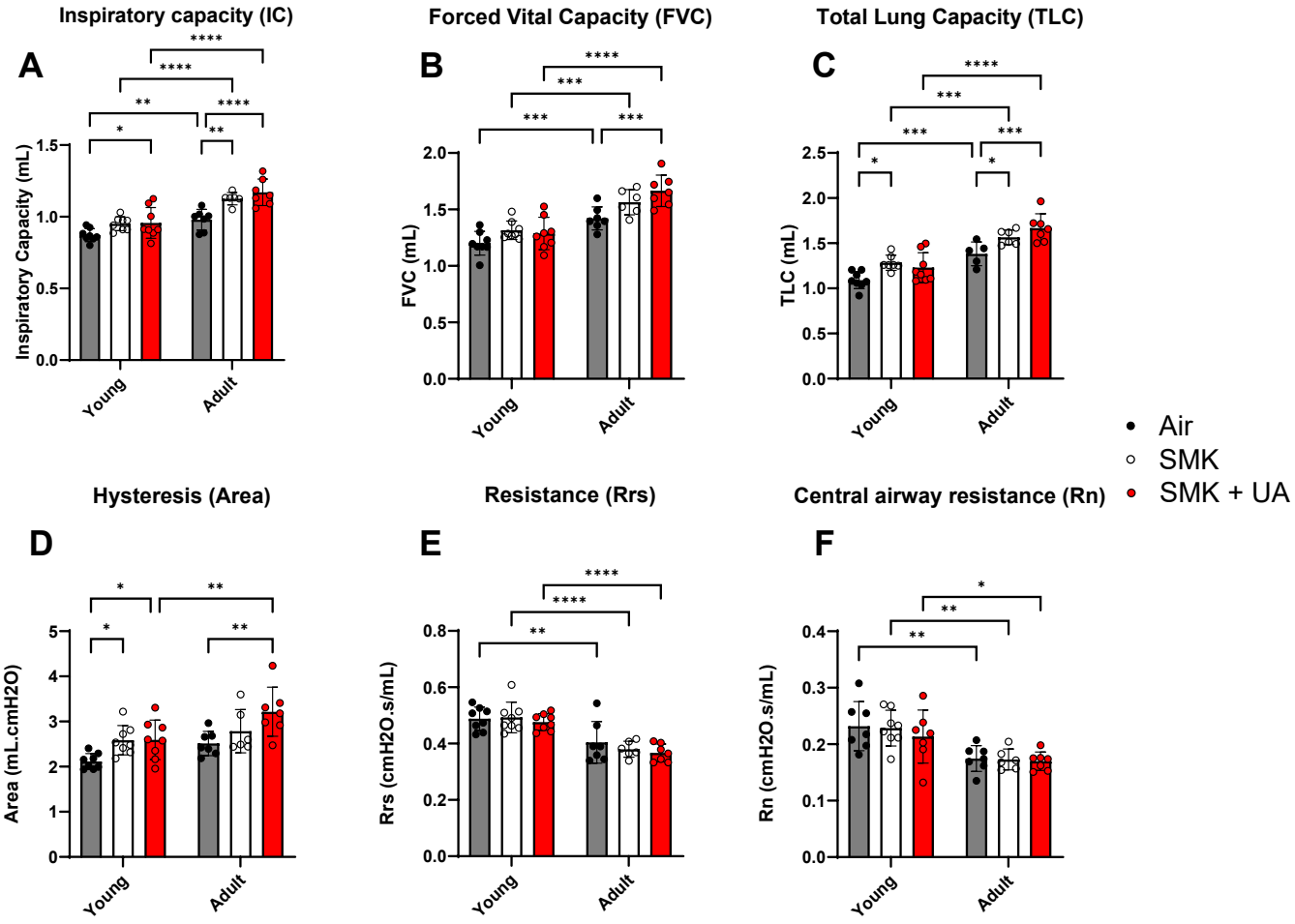

Figure 5.2 Lung function decline was observed in young and adult mice in an experimental COPD model and lung volumes were increased with UA treated CS exposed old mice.

The lung function of UA treated young (8w old), and adult (1y old) C57BL/6 mice (n=8) was assessed under anaesthetic at endpoint using a SCIREQ Flexivent, after 8w of cigarette smoke (CS) or air exposure. **A** Inspiratory capacity (IC) is a measure of the amount of air that can be inhaled after normal exhalation. **B** Forced vital capacity (FVC) is the total volume of air exhaled during a forced expiration. **C** Total lung capacity (TLC) is the maximum possible lung volume. **D** Hysteresis is a measure of recoil and surface tension of the lungs. **E** Resistance (Rrs) is a dynamic measure of lung constriction. **F** Central airway resistance (Rn). Two-way Anova with Dunnett's multiple comparisons test statistical analysis was performed and statistically significant comparisons are shown. Individual values were graphed with mean ± SD displayed. Results with a P-value≤0.05 were considered significant (*P≤0.05; **P≤0.01; ***P≤0.001, ****P≤0.0001).

5.4.2 CS-impaired development in young mice and caused rapid weight loss in adult mice in an experimental model of COPD which was not attenuated by UA treatment.

Young (8w old) and adult (1y old) C57BL/6 female mice were exposed to the smoke of 12 cigarettes twice daily, 5d/w for 8w. Some mice were treated with UA (25mg/kg) in the diet ad libitum beginning 2w prior to the start of CS-exposure.

There was no effect of UA treatment on body weight over time in either young or adult mice exposed to CS (Figure 5.3: A-E) and CS-exposure had a negative impact on weight in both ages compared to room air exposed mice (Figure 5.3: A+B).

In young mice, CS-exposure impaired weight gain and caused weight to plateau from day 18 when CS exposure began. In contrast, young room air exposed mice continued to gain weight over time (Figure 5.3: C+D).

In adult mice, CS-exposure caused rapid weight loss of >15% compared to starting weight (Figure 5.3: E+F), however room air exposed adult mice continued to maintain a steady weight throughout the time-course.

These data demonstrated the negative effect of CS exposure on the weight of young and adult mice. UA treatment did not recover mouse weight in young mice or prevent a decline in weight in adult mice that were CS exposed.

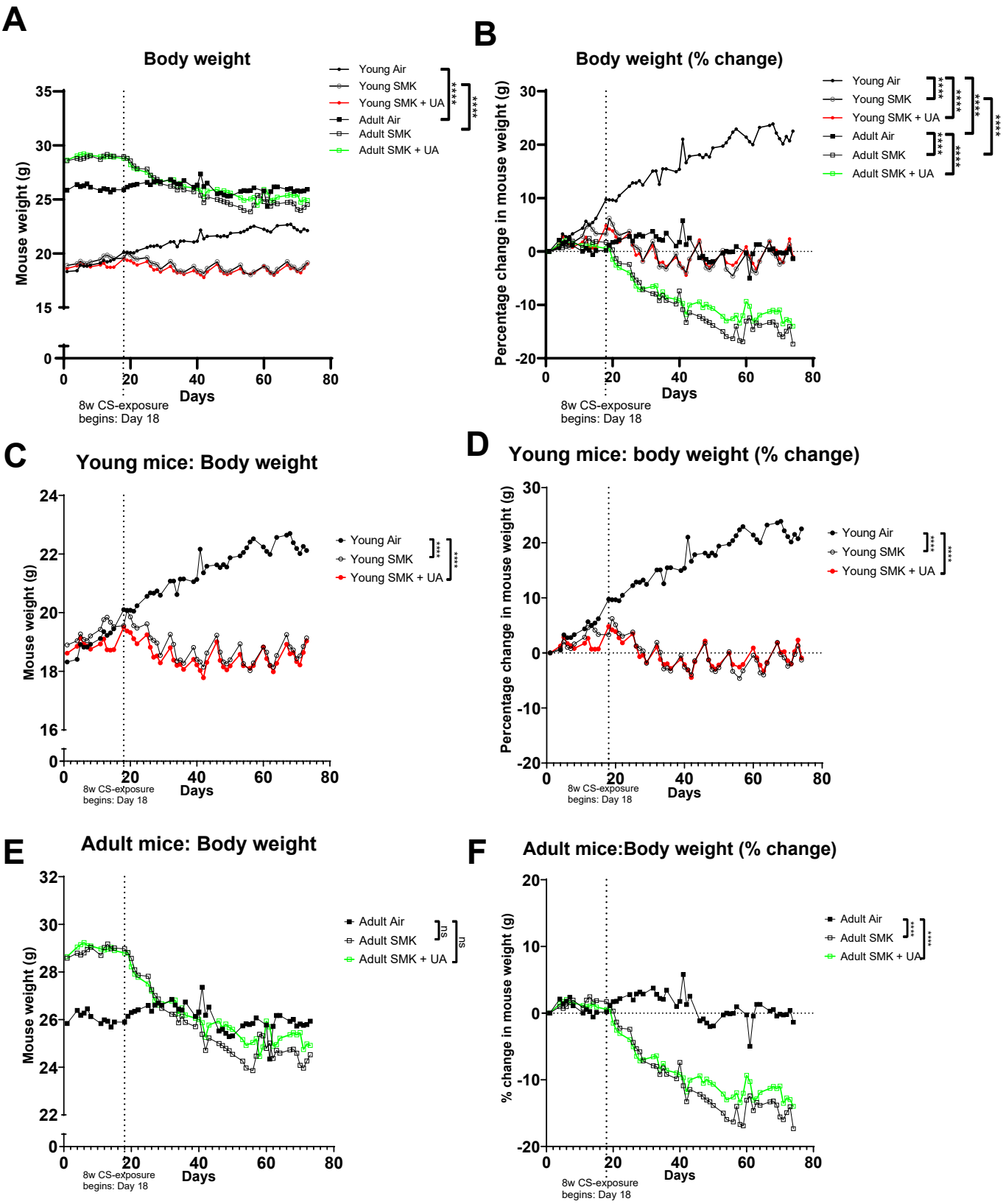
A
Body weight
Mouse weight (g)
Days
8w CS-exposure begins: Day 18
Young Air
Young SMK
Young SMK + UA
Adult Air
Adult SMK
Adult SMK + UA
****
B
Body weight (% change)
Percentage change in mouse weight (g)
Days
8w CS-exposure begins: Day 18
C
Young mice: Body weight
Mouse weight (g)
Days
8w CS-exposure begins: Day 18
D
Young mice: body weight (% change)
Percentage change in mouse weight (g)
Days
8w CS-exposure begins: Day 18
E
Adult mice: Body weight
Mouse weight (g)
Days
8w CS-exposure begins: Day 18
ns
F
Adult mice:Body weight (% change)
% change in mouse weight (g)
Days
8w CS-exposure begins: Day 18

Figure 5.3 CS-impaired development in young mice and caused rapid weight loss in adult mice in an experimental model of COPD which was not attenuated by UA treatment.

UA treated young (8w old), and adult (1y old) C57BL/6 mice (n=8) were exposed to cigarette smoke (CS) or air for 8w and weighed 5d/w (Monday-Friday) up until the endpoint (10w). **A+B** Total body weight over time and percentage change over time for all groups**. C+D** Total body weight over time and percentage change over time for young mice. **E+F** Total body weight over time and percentage change over time for old mice. A mixed-effect analysis (REML) statistical analysis was performed for analysis of mouse body weight over time. Individual values were graphed with mean displayed. Results with a P-value≤0.05 were considered significant (****P≤0.0001).

5.4.3 Skeletal muscle mass was decreased in an experimental model of COPD in young and adult mice treated with UA

Young (8w old) and adult (1y old) C57BL/6 female mice were exposed to the smoke of 12 cigarettes twice daily, 5d/w for 8w. Some mice were treated with UA (25mg/kg) in the diet ad libitum beginning 2w prior to the start of CS-exposure.

Young mice air, CS and CS+UA group comparison: Young, CS exposed mice had lighter gastrocnemius and quadriceps muscles compared to young air controls regardless of treatment (Figure 5.4: A+B), but there was no change to soleus, EDL or N-A length with CS-exposure (Figure 5.4: C-E).

Adult mice air, CS and CS+UA comparisons: CS exposed adult mice had lighter gastrocnemius muscles compared to air exposed adult mice (Figure 5.4: B). UA treatment prevented a significant reduction in gastrocnemius muscles in adult mice, but it was not significantly higher in weight compared to CS exposed mice, suggesting a moderately protective effect of UA treatment against CS-induced cachexia in adult mice (Figure 5.4: B). There were no significant changes to quadriceps, soleus or EDL weights in adult mice, regardless of CS or UA treatment status.

Young vs adult comparison: Adult mice had heavier gastrocnemius muscles compared to young mice across all treatment groups (Figure 5.4: A) and UA treated adult mice also had heavier quadriceps than their young UA treated counterparts (Figure 5.4: B). There were no significant differences in soleus or EDL weights between young or adult mice, regardless of treatment status (Figure 5.4: C+D). Adult mice had higher N-A length compared to young mice, which was not changed with CS-exposure or UA treatment (Figure 5.4: E).

In summary, it was expected that adult mice would have higher skeletal muscle mass than young mice and indeed the gastrocnemius muscles were larger in adult mice than young mice and N-A

length was also higher in adult mice compared to young mice. Surprisingly, the quadriceps of young and adult mice were very similar weights, and there were no significant differences in soleus or EDL weights. UA treatment did prevent a significant decrease in gastrocnemius weight, suggesting a mild protective effect against Cs induced muscle loss in young mice.

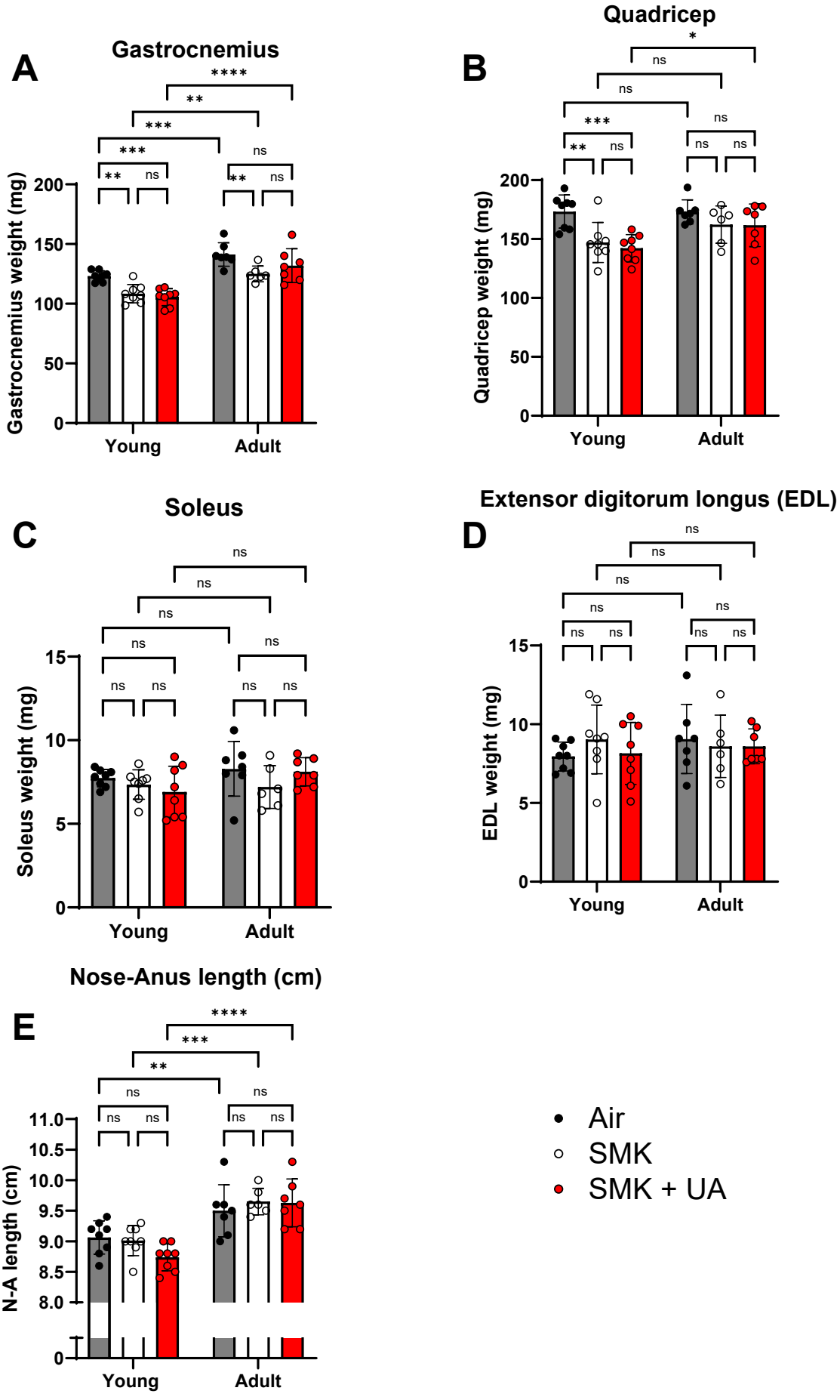
A
Gastrocnemius
Gastrocnemius weight (mg)
Young
Adult
B
Quadricep
Quadricep weight (mg)
C
Soleus
Soleus weight (mg)
D
Extensor digitorum longus (EDL)
EDL weight (mg)
E
Nose-Anus length (cm)
N-A length (cm)
Air
SMK
SMK + UA

Figure 5.4 Skeletal muscle mass was decreased in an experimental model of COPD in young and adult mice treated with UA.

UA treated young (8w old), and adult (1y old) C57BL/6 mice (n=8) were exposed to cigarette smoke (CS) or air for 8w. Skeletal muscles were gathered on day of endpoint and weighed immediately following BALF and blood collection. **A-D** Gastrocnemius, quadricep, soleus and EDL weight (mg) respectively. **E** N-A length (cm). Two-way Anova with Šídák's multiple comparisons test statistical analysis was performed and individual values were graphed with mean ± SD displayed. All comparisons are shown. Results with a P-value≤0.05 were considered significant (*P≤0.05; **P≤0.01; ***P≤0.001, ****P≤0.0001).

5.5 Flow Cytometric analysis of the Blood and BALF

5.5.1 BALF total leukocytes were increased in an experimental model of COPD in young and adult mice treated with UA

Young (8w old) and adult (1y old) C57BL/6 female mice were exposed to the smoke of 12 cigarettes twice daily, 5d/w for 8w. Some mice were treated with UA (25mg/kg) in the diet ad libitum beginning 2w prior to the start of CS-exposure. BALF was collected immediately after lung function analysis and stored on ice before antibody incubation for flow cytometry preparation.

There was a significant increase in BALF leukocyte induction in young and adult mice which was not changed by UA treatment (Figure 5.5: A).

Young mice air, CS and CS+UA group comparison: CS-exposure in young mice resulted in a significant increase in T helper cells, dendritic cells, monocytes and neutrophils than in room air exposed mice (Figure 5.5: B, E, F, H).

Adult mice air, CS and CS+UA comparisons: UA treatment significantly increased T helper cells and B cells compared to the air control in adult mice, but CS-exposure alone did not produce the same effect (Figure 5.5: B+D). However, CS-exposure increased cytotoxic T cells, dendritic cells, monocytes and neutrophils (Figure 5.5: C, E, F H), but decreased macrophages in the BALF (Figure 5.5: G).

Young vs adult comparison: CS-exposure in adult mice resulted in a higher cytotoxic T cells in the BALF compared to young mice (Figure 5.5: C) and more macrophages in room air exposed adult mice compared to young mice (Figure 5.5: G). Adult mice treated with UA also had significantly higher cytotoxic T cells, B cells and monocytes compared to UA treated young mice (Figure 5.5: C, D, F). UA treatment did not significantly alter induction of immune cells into the BALF compared to CS-exposure only groups (Figure A-I). However, UA treatment did prevent a significant increase in

dendritic cell induction compared to the air control in both young and adult mice (Figure 5.5: E), suggesting a potentially dendritic cell specific role for UA in immune cell induction. An increase in dendritic cell numbers is consistent with several studies that have demonstrated an increase in dendritic cell populations in the lungs of COPD patients, and due to CS exposure [355]. As reviewed by Tsoumakidou et al., dendritic cell subsets have many known roles in COPD which can differ based on smoking status. Dendritic cells are professional antigen presenting cells that can migrate to the lymphoid follicles in the lung and activate naïve T cells, causing clonal expansion and Th1/17 and CD8+ T cell mediated inflammation [356]. This was reflected in my results by the increase in both CD4+ and CD+ T cells (Figure 5.5 B+C).

These data demonstrated again the differences between young and adult mice responses to CS-induced COPD, and the differential effects of UA treatment on the induction of dendritic cells into the lung lumen.

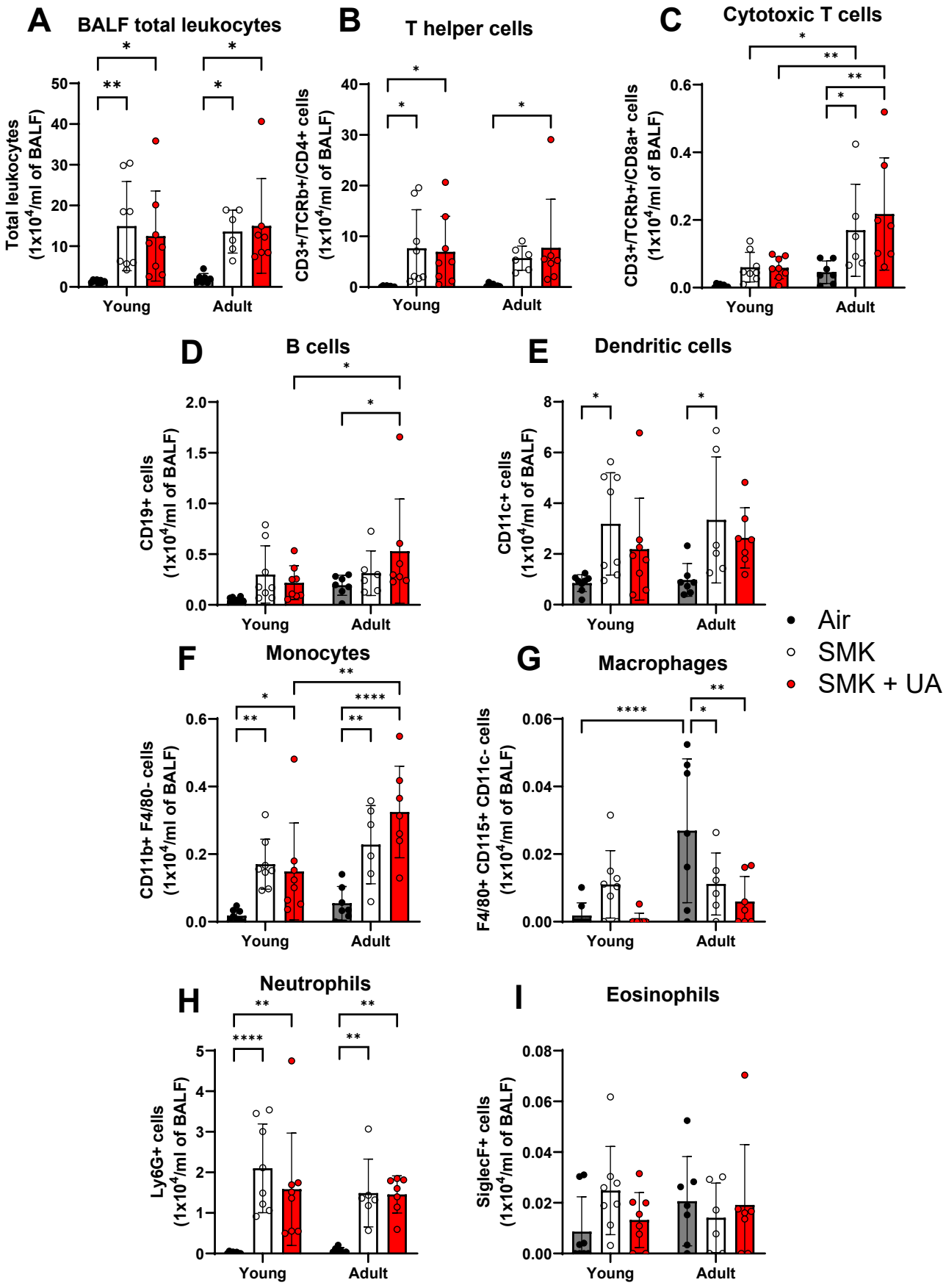
A
BALF total leukocytes
Total leukocytes (1x10^4/ml of BALF)
Young
Adult
B
T helper cells
CD3+/TCRb+/CD4+ cells (1x10^4/ml of BALF)
C
Cytotoxic T cells
CD3+/TCRb+/CD8a+ cells (1x10^4/ml of BALF)
D
B cells
CD19+ cells (1x10^4/ml of BALF)
E
Dendritic cells
CD11c+ cells (1x10^4/ml of BALF)
F
Monocytes
CD11b+ F4/80- cells (1x10^4/ml of BALF)
G
Macrophages
F4/80+ CD115+ CD11c- cells (1x10^4/ml of BALF)
H
Neutrophils
Ly6G+ cells (1x10^4/ml of BALF)
I
Eosinophils
SiglecF+ cells (1x10^4/ml of BALF)
Air
SMK
SMK + UA

Figure 5.5 BALF total leukocytes were increased in an experimental model of COPD in young and adult mice treated with UA.

BALF was collected from the left lung only and cells analysed by flow cytometry for different immune cell populations. **A** T helper cells (CD3+TCRb+CD4+). **B** Cytotoxic T cells (CD3+TCRb+CD8+). **C** B cells (CD19+). **D** Dendritic cells (CD11c+). **E** Monocytes (CD11b+F4/80-). **F** Macrophages (F4/80+ CD115+CD11c-). **G** Neutrophils (Ly6G+). **H** Eosinophils (SiglecF+). Two-way Anova with Dunnett's multiple comparisons test statistical analysis was performed and statistically significant comparisons are shown. Individual values were graphed with mean ± SD displayed. Results with a P-value≤0.05 were considered significant (*P≤0.05; **P≤0.01; ****P≤0.0001).

5.5.2 Immune cell ratios in the blood were different between young and adult mice in an experimental model of COPD with UA treatment

Young (8w old) and adult (1y old) C57BL/6 female mice were exposed to the smoke of 12 cigarettes twice daily, 5d/w for 8w. Some mice were treated with UA (25mg/kg) in the diet ad libitum beginning 2w prior to the start of CS-exposure. Flow cytometric analysis of the blood yielded ratios of individual immune cell types to total circulating leukocytes as defined by the CD45+ cell leukocyte marker.

Young mice air, CS and CS+UA group comparison: Young CS exposed mice had a decreased ratio of circulating T helper cells compared to the room air young mice (Figure 5.6: A) but a higher ratio of dendritic cells with CS-exposure, that was not observed in UA treated young mice (Figure 5.6: D).

Adult mice air, CS and CS+UA comparisons: UA treated adult mice had a decreased proportion of circulating monocytes and macrophages compared to the room air adult mice, but not compared to the CS exposed mice (Figure 5.6: E+F). No other significant changes to the ratio of circulating immune cells was observed in adult mice.

Young vs adult comparison: Adult mice had lower circulating cytotoxic and helper T cells in the blood compared to young mice, regardless of CS-exposure or UA treatment (Figure 5.6: A+B), and adult air control mice also had a higher proportion of circulating monocytes (Figure 5.6: E). Furthermore, UA treatment resulted in a decreased proportion of B cells (Figure 5.6: C), but more neutrophils and eosinophils (Figure 5.6: G+H).

These data demonstrate the differences in the ratios of circulating leukocytes between young and adult mice, as well as the impact of CS-exposure and UA treatment. UA again showed an ability to decrease dendritic cell induction which may warrant further investigation in future models.

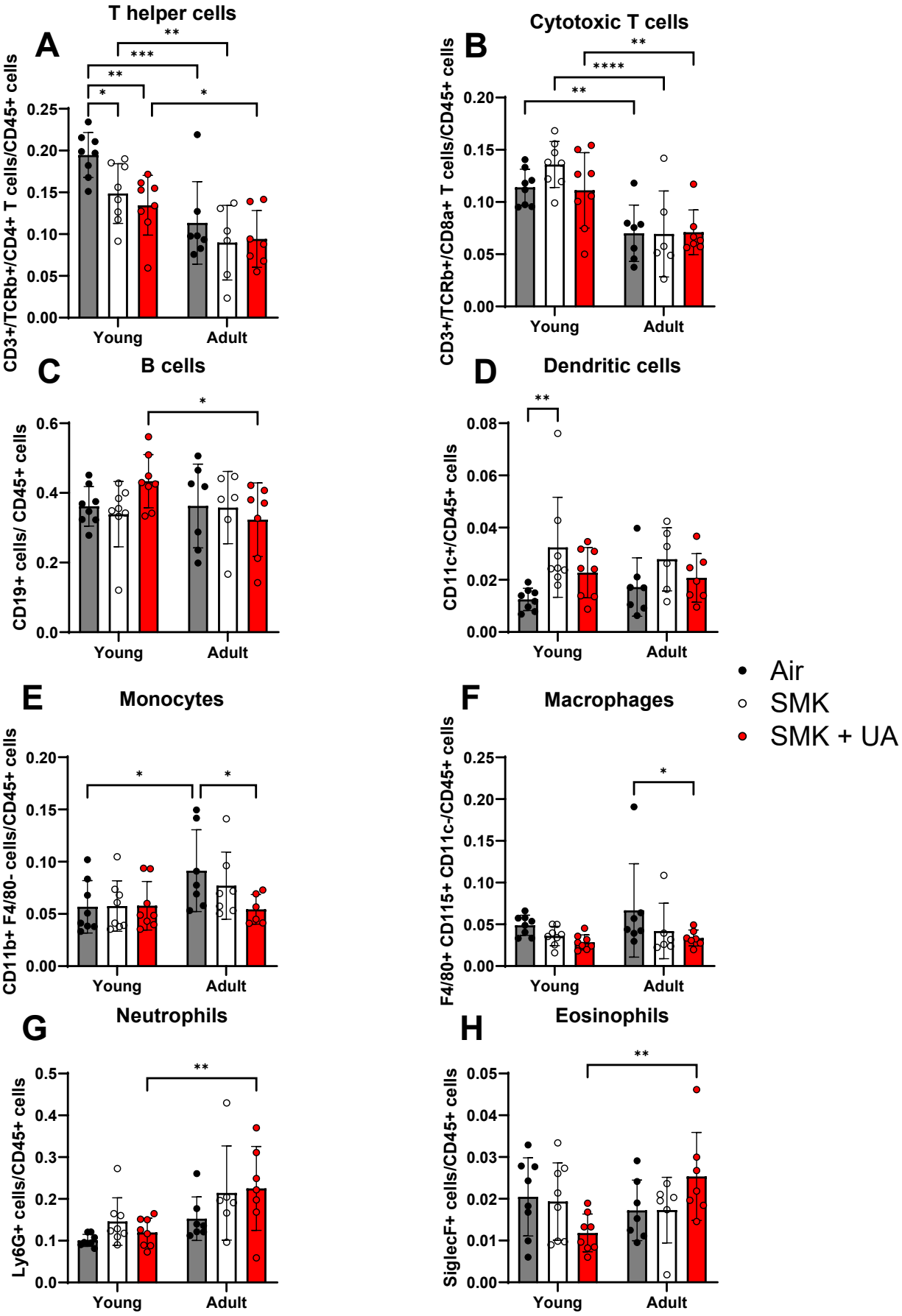
A
T helper cells
CD3+/TCRb+/CD4+ T cells/CD45+ cells
0.25
0.20
0.15
0.10
0.05
0.00
Young
Adult
B
Cytotoxic T cells
CD3+/TCRb+/CD8a+ T cells/CD45+ cells
C
B cells
CD19+ cells/ CD45+ cells
D
Dendritic cells
CD11c+/CD45+ cells
E
Monocytes
CD11b+ F4/80- cells/CD45+ cells
F
Macrophages
F4/80+ CD115+ CD11c-/CD45+ cells
G
Neutrophils
Ly6G+ cells/CD45+ cells
H
Eosinophils
SiglecF+ cells/CD45+ cells
Air
SMK
SMK + UA

Figure 5.6 Immune cell ratios in the blood were different between young and adult mice in an experimental model of COPD with UA treatment.

Blood was collected by cardiac puncture and plasma isolated was analysed by flow cytometry for different immune cell populations. Each cell type is displayed as a ratio to total leukocytes (CD45+). **A** T helper cells (CD3+TCRb+CD4+). **B** Cytotoxic T cells (CD3+TCRb+CD8+). **C** B cells (CD19+). **D** Dendritic cells (CD11c+). **E** Monocytes (CD11b+F4/80-). **F** Macrophages (F4/80+ CD115+CD11c-). **G** Neutrophils (Ly6G+). **H** Eosinophils (SiglecF Two-way Anova with Dunnett's multiple comparisons test statistical analysis was performed and statistically significant comparisons are shown. Individual values were graphed with mean ± SD displayed. Results with a P-value≤0.05 were considered significant (*P≤0.05; **P≤0.01; ***P≤0.001, ****P≤0.0001).

5.6 Immunoblot analysis of the quadriceps from young (8w old) mice in an experimental COPD model with Urolithin A treatment

5.6.1 Protein degradation-associated protein abundance was unaffected by UA treatment or CS in an experimental COPD model

Young (8w old) and adult (1y old) C57BL/6 female mice were exposed to the smoke of 12 cigarettes twice daily, 5d/w for 8w. Some mice were treated with UA (25mg/kg) in the diet ad libitum beginning 2w prior to the start of CS-exposure. There was no significant change to MuRF1, atrogin-1 or GADD45α expression in the quadriceps of young mice after CS-exposure or UA treatment (Figure 5.7: A-C).

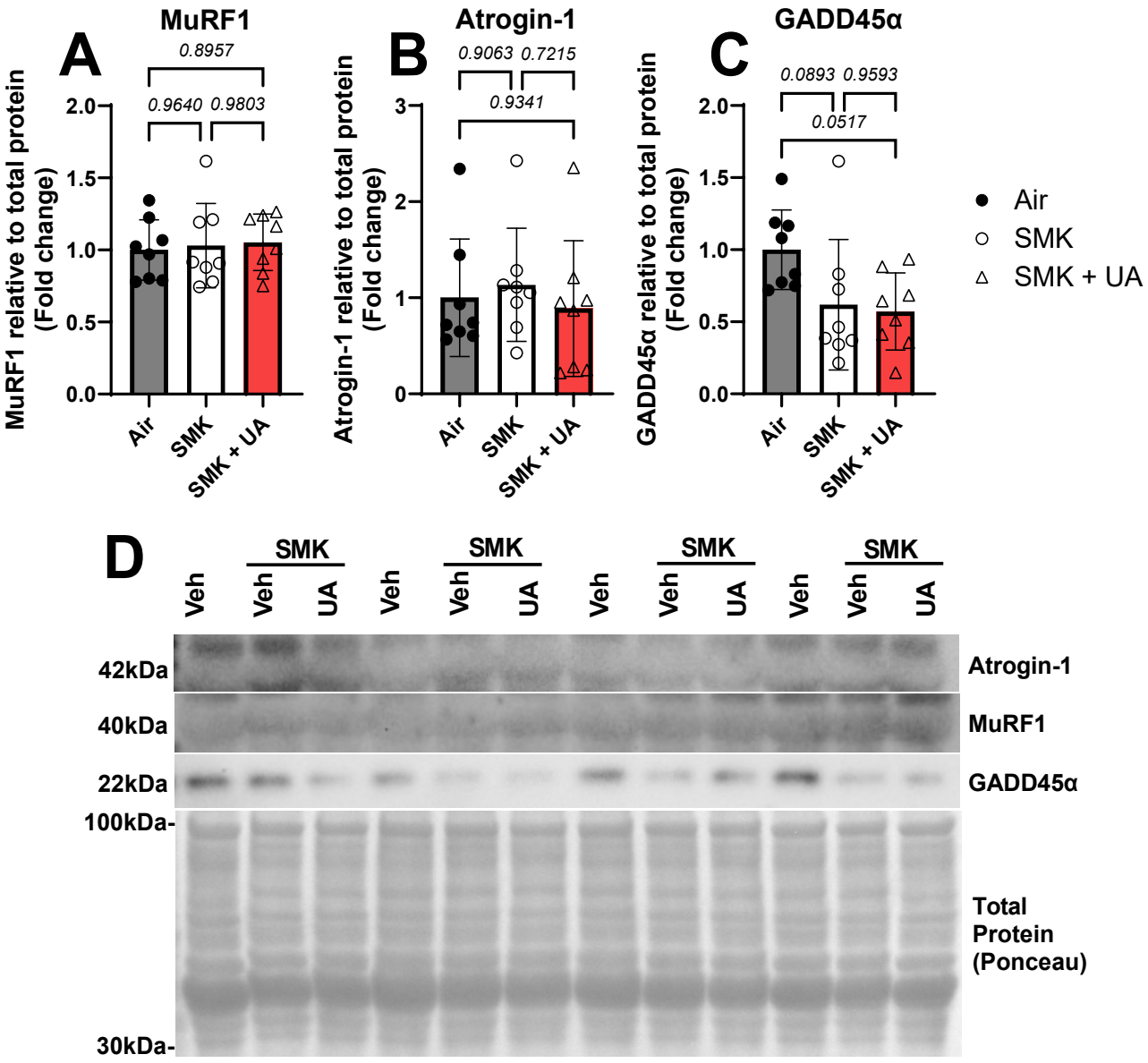

Figure 5.7 Protein degradation-associated protein abundance was unaffected by UA treatment or CS in an experimental COPD model.

Immunoblot analysis was used to assess the abundance of protein degradation-associated proteins in the quadriceps from UA treated young (8w old) C57BL/6 mice (n=8) after 8w CS or room air exposure. Densitometric analysis was performed on membranes for **A** MuRF1 **B** Atrogin-1 and **C** GADD45α relative to total protein. **D** Membrane images of MuRF1 (40kDa), Atrogin-1 (42kDa), GADD45α (22kDa) and representative total protein stain (ponceau) used to normalise band intensity for densitometric analysis. Ordinary one-way Anova with Tukey's multiple

comparison statistical analysis was performed on each data set. Individual values were graphed with mean ± SD displayed. Results with a P-value≤0.05 were considered significant.

5.6.2 cGAS and STING protein abundance in the quadriceps from mice in an experimental COPD model were unmodulated by CS exposure or UA treatment

Young (8w old) and adult (1y old) C57BL/6 female mice were exposed to the smoke of 12 cigarettes twice daily, 5d/w for 8w. Some mice were treated with UA (25mg/kg) in the diet ad libitum beginning 2w prior to the start of CS-exposure. There was no significant change to cGAS or STING expression in the quadriceps of young mice after CS-exposure or UA treatment (Figure 5.8: A-B).

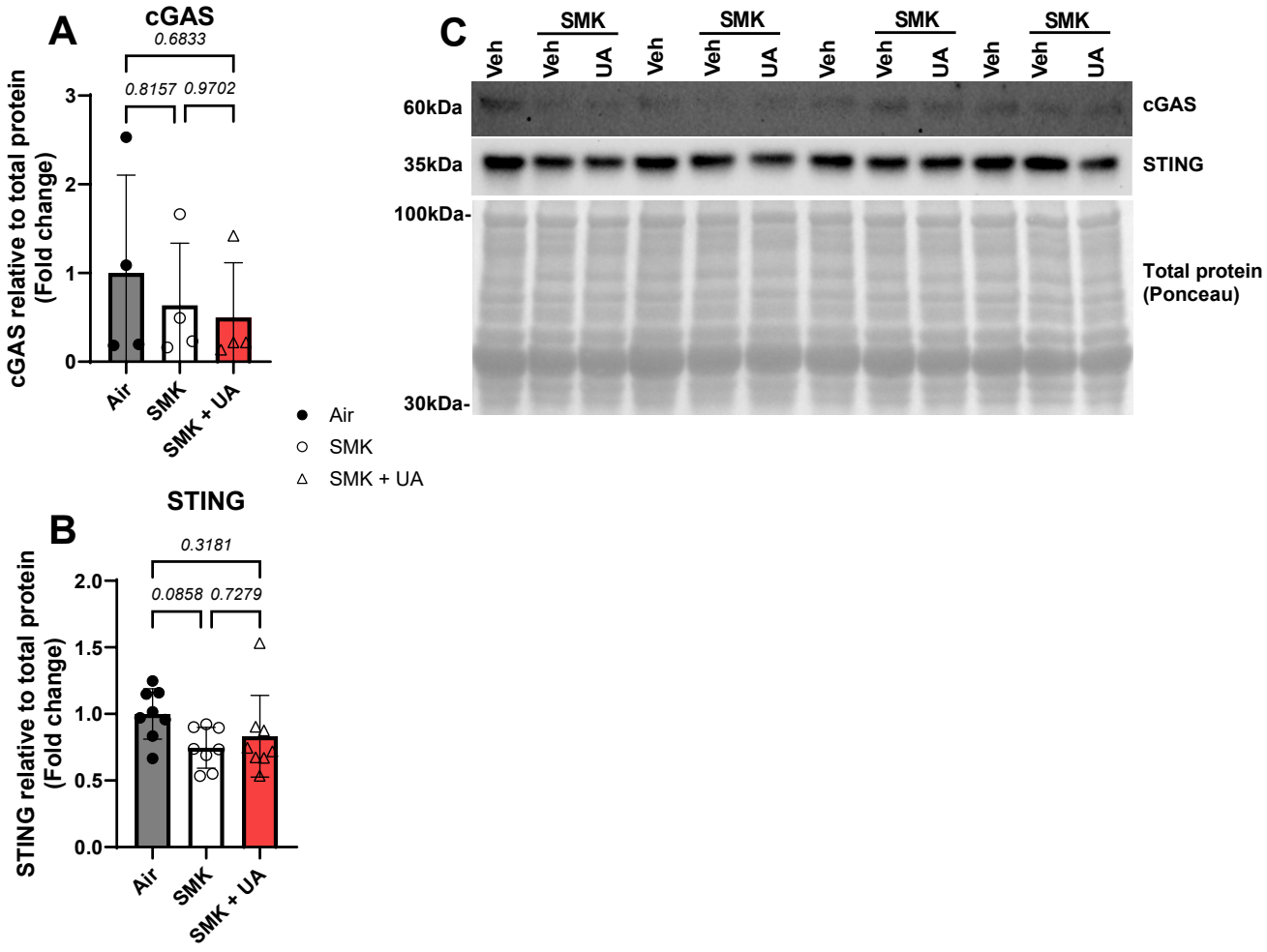

Figure 5.8 cGAS and STING protein abundance in the quadriceps from mice in an experimental COPD model were unmodulated by CS exposure or UA treatment.

Immunoblot analysis was used to assess the abundance of cGAS and STING proteins in the quadriceps from UA treated young (8w old) C57BL/6 mice (n=8) after 8w CS or room air exposure. Densitometric analysis was performed on membranes for **A** cGAS and **B** STING relative to total protein. **C** Membrane images of cGAS (60kDa) and STING (42kDa) and representative total protein stain (ponceau) used to normalise band intensity for densitometric analysis. Ordinary one-way Anova with Tukey's multiple comparison statistical analysis was performed on each data set. Individual values were graphed with mean ± SD displayed. Results with a P-value≤0.05 were considered significant.

5.6.3 Akt activity was decreased by CS exposure +UA treatment in the quadriceps of young mice from an experimental COPD model.

Young (8w old) and adult (1y old) C57BL/6 female mice were exposed to the smoke of 12 cigarettes twice daily, 5d/w for 8w. Some mice were treated with UA (25mg/kg) in the diet ad libitum beginning 2w prior to the start of CS-exposure. There were no changes to CS total mTOR or Akt protein expression (Figure 5.9: A+D), or activation of Akt by Thr308 phosphorylation (Figure 5.9: B-C) in the quadriceps of young mice after CS-exposure or UA treatment. However, there was a significant decrease in the activation of Akt with UA treatment in CS exposed young mice, as measured by Ser473 phosphorylation on Akt (Figure: 5-9: E). As a result, this may infer a role for CS-exposure and UA in decreasing Akt activation, thus limiting mTORC1 mediated protein synthesis.

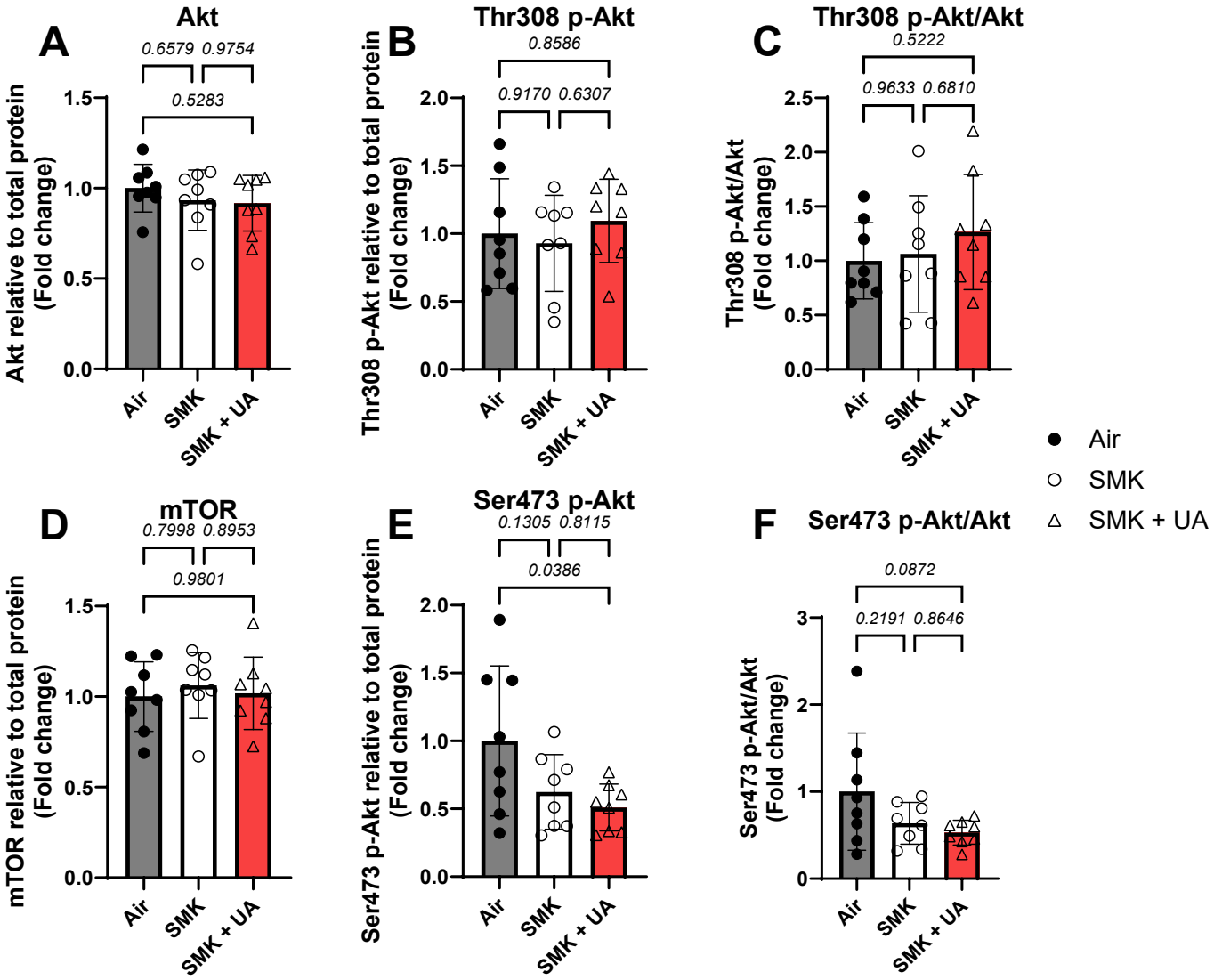
A
Akt
0.6579 0.9754
0.5283
Akt relative to total protein (Fold change)
B
Thr308 p-Akt
0.8586
0.9170 0.6307
Thr308 p-Akt relative to total protein (Fold change)
C
Thr308 p-Akt/Akt
0.5222
0.9633 0.6810
Thr308 p-Akt/Akt (Fold change)
D
mTOR
0.7998 0.8953
0.9801
mTOR relative to total protein (Fold change)
E
Ser473 p-Akt
0.1305 0.8115
0.0386
Ser473 p-Akt relative to total protein (Fold change)
F
Ser473 p-Akt/Akt
0.0872
0.2191 0.8646
Ser473 p-Akt/Akt (Fold change)
Air
SMK
SMK + UA

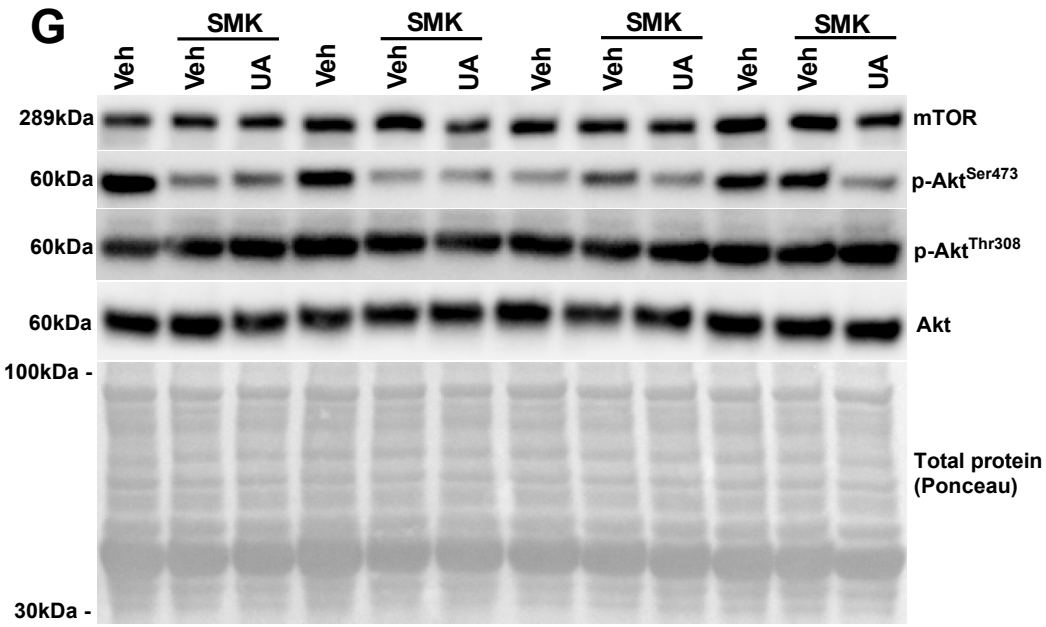
G
SMK
Veh
Veh
UA
289kDa
mTOR
60kDa
p-Akt^Ser473
60kDa
p-Akt^Thr308
60kDa
Akt
100kDa -
30kDa -
Total protein (Ponceau)

Figure 5.9 Akt activity was decreased by CS exposure +UA treatment in the quadriceps of young mice from an experimental COPD model.

Immunoblot analysis was used to assess mTOR and Akt and p-Akt protein abundance in the quadriceps from UA treated young (8w old) C57BL/6 mice (n=8) after 8w CS or room air exposure. Densitometric analysis was performed on membranes for **A** Akt, **B** p-Akt^{Thr308} **C** p-Akt^{Thr308}/Akt **D** p-Akt^{Ser473} **E** p-Akt^{Ser473}/Akt and **F** mTOR relative to total protein in the quadriceps of female C57BL/6 mice exposed to CS for 8w and treated daily with H-151 (i.n.). **G** Western blot membrane images and representative total protein stain (ponceau) used to normalise band intensity for densitometric analysis. Ordinary one-way Anova with Tukey's multiple comparison statistical analysis was performed on each data set. Individual values were graphed with mean ± SD displayed. Results with a P-value≤0.05 were considered significant.

5.6.4 The abundance of p-rpS6 was decreased in the quadriceps of young mice from an experimental COPD model and was not prevented with UA treatment.

Young (8w old) and adult (1y old) C57BL/6 female mice were exposed to the smoke of 12 cigarettes twice daily, 5d/w for 8w. Some mice were treated with UA (25mg/kg) in the diet ad libitum beginning 2w prior to the start of CS-exposure.

There were no changes in total or Thr37/46 phosphorylated 4E-BP1 (Figure 5.10: G-I). However, there was a significant overall decrease in phosphorylated S6K, (Figure: 5-10: A-C) and Ser235/236 p-rpS6 in CS exposed mice with and without treatment (Figure 5.10: E+F), but no significant effect on total protein (Figure 5.10: A+D). Together, these results may indicate reduced mTORC1 activity and reduced protein synthesis, as S6K and 4E-BP1 are both phosphorylated by mTORC1. Also decreased S6K activation may explain a reduction in p-rpS6 in CS exposed mice, since S6K activates rpS6 through Ser235/236 phosphorylation.

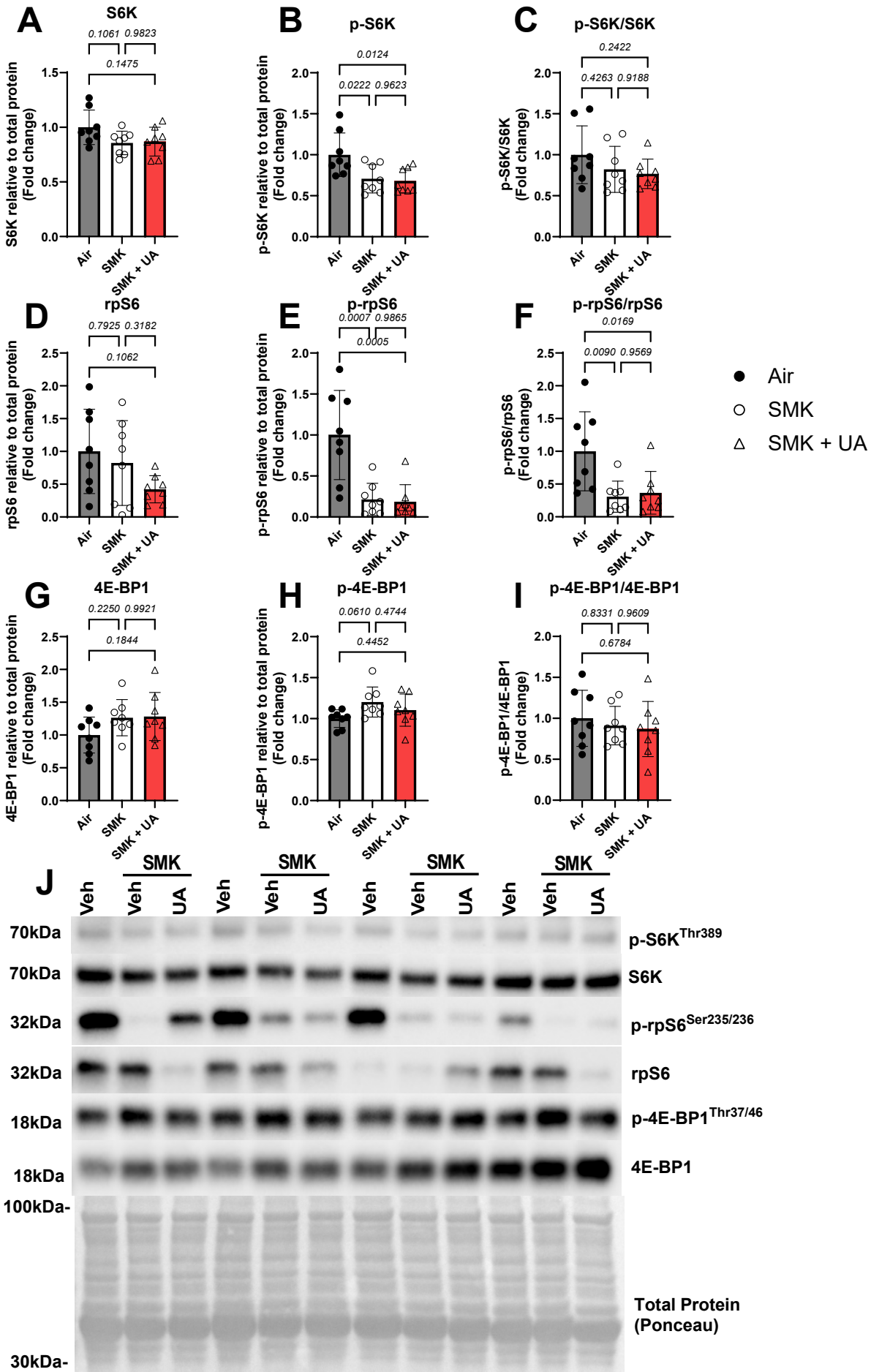
A
S6K
0.1061 0.9823
0.1475
S6K relative to total protein (Fold change)
B
p-S6K
0.0124
0.0222 0.9623
p-S6K relative to total protein (Fold change)
C
p-S6K/S6K
0.2422
0.4263 0.9188
p-S6K/S6K (Fold change)
D
rpS6
0.7925 0.3182
0.1062
rpS6 relative to total protein (Fold change)
E
p-rpS6
0.0007 0.9865
0.0005
p-rpS6 relative to total protein (Fold change)
F
p-rpS6/rpS6
0.0169
0.0090 0.9569
p-rpS6/rpS6 (Fold change)
G
4E-BP1
0.2250 0.9921
0.1844
4E-BP1 relative to total protein (Fold change)
H
p-4E-BP1
0.0610 0.4744
0.4452
p-4E-BP1 relative to total protein (Fold change)
I
p-4E-BP1/4E-BP1
0.8331 0.9609
0.6784
p-4E-BP1/4E-BP1 (Fold change)
Air
SMK
SMK + UA
J
SMK
Veh
Veh
UA
70kDa
p-S6K Thr389
70kDa
S6K
32kDa
p-rpS6 Ser235/236
32kDa
rpS6
18kDa
p-4E-BP1 Thr37/46
18kDa
4E-BP1
100kDa-
30kDa-
Total Protein (Ponceau)

Figure 5.10 The abundance of p-rpS6 was decreased in the quadriceps of young mice from an experimental COPD model and was not prevented by UA treatment.

Immunoblot analysis was used to assess the abundance of downstream effectors of mTORC1 in the quadriceps from UA treated young (8w old) C57BL/6 mice (n=8) after 8w CS or room air exposure. Densitometric analysis was performed on membranes for **A** S6K **B** p-S6K^{Thr389}**C** p-S6K^{Thr389}/ S6K **D** rpS6 **E** p-rpS6$^{Ser235/236}$ **F** p-rpS6$^{Ser235/236}$/rpS6 **G** 4E-BP1 **H** p-4E-BP1$^{Thr37/46}$ and **I** p-4E-BP1$^{Thr37/46}$/4E-BP1 abundance relative to total protein **J** Western blot membrane images with a representative total protein stain (ponceau) used to normalise band intensity for densitometric analysis. Ordinary one-way Anova with Tukey's multiple comparison statistical analysis was performed on each data set. Individual values were graphed with mean ± SD displayed. Results with a P-value≤0.05 were considered significant.

5.6.5 The abundance of ETC complex proteins was unaltered in the quadriceps of young mice from an experimental COPD model and was not affected by UA treatment

Young (8w old) and adult (1y old) C57BL/6 female mice were exposed to the smoke of 12 cigarettes twice daily, 5d/w for 8w. Some mice were treated with UA (25mg/kg) in the diet ad libitum beginning 2w prior to the start of CS exposure.

In contrast to the first 8w COPD model (Figure 3.28: E), but similarly to the H-151 intervention COPD model (Figure 4.8), there were no observed changes in complex V subunit protein expression in this model, regardless of CS exposure or treatment status (Figure 5.11: E). There was also no observed change to other complex subunit proteins (Figure 5.11: A-D).

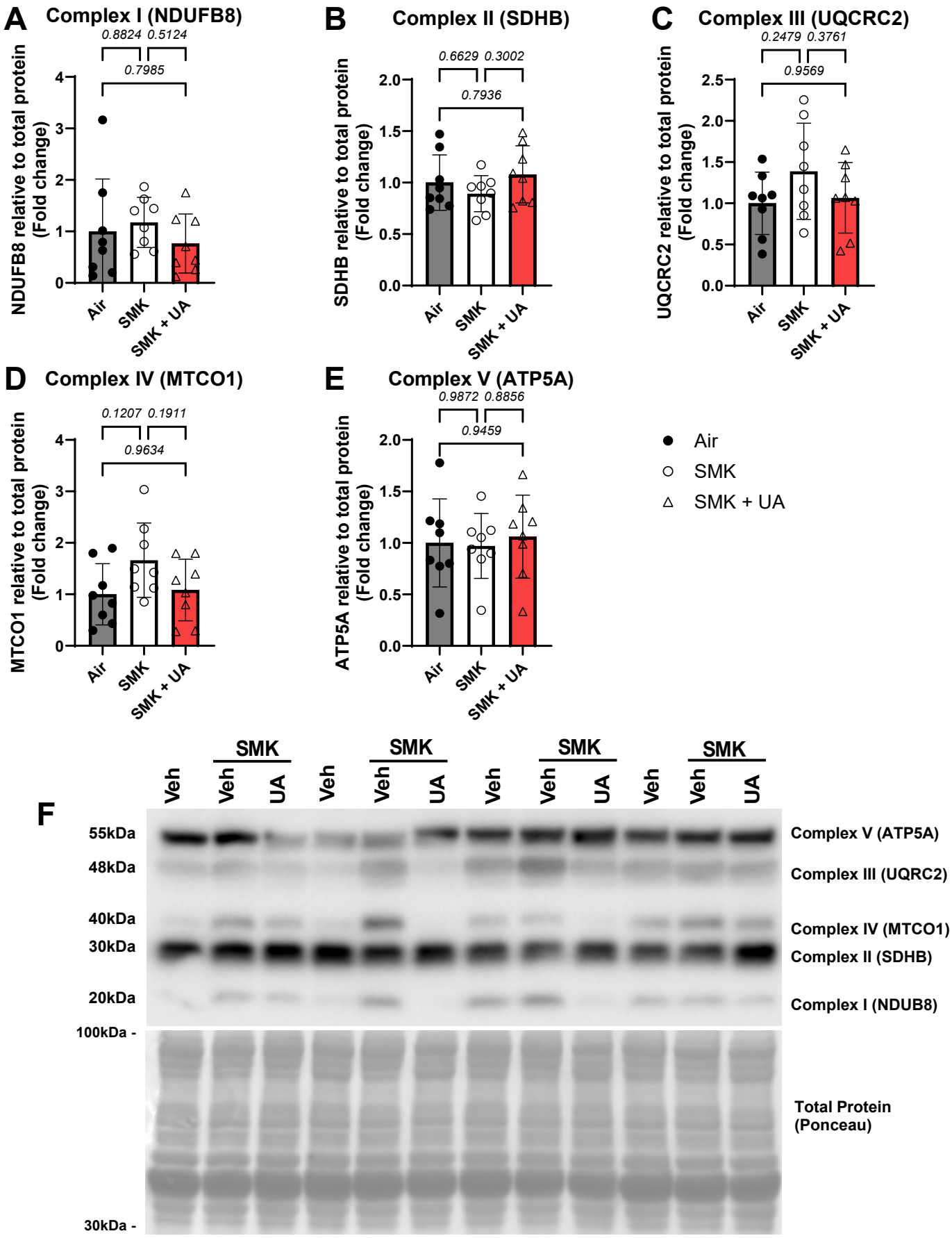
A
Complex I (NDUFB8)
0.8824 0.5124
0.7985
NDUFB8 relative to total protein (Fold change)
Air
SMK
SMK + UA
B
Complex II (SDHB)
0.6629 0.3002
0.7936
SDHB relative to total protein (Fold change)
C
Complex III (UQCRC2)
0.2479 0.3761
0.9569
UQCRC2 relative to total protein (Fold change)
D
Complex IV (MTCO1)
0.1207 0.1911
0.9634
MTCO1 relative to total protein (Fold change)
E
Complex V (ATP5A)
0.9872 0.8856
0.9459
ATP5A relative to total protein (Fold change)
Air
SMK
SMK + UA
F
Veh
SMK
Veh
UA
55kDa
48kDa
40kDa
30kDa
20kDa
100kDa -
30kDa -
Complex V (ATP5A)
Complex III (UQRC2)
Complex IV (MTCO1)
Complex II (SDHB)
Complex I (NDUB8)
Total Protein (Ponceau)

Figure 5.11 The abundance of ETC complex proteins was unaltered in the quadriceps of young mice from an experimental COPD model and was not affected by UA treatment.

Immunoblot analysis was used to assess the abundance of electron transport chain (ETC) complex proteins in the quadriceps from UA treated young (8w old) C57BL/6 mice (n=8) after 8w CS or room air exposure. Densitometric analysis was performed on membranes for **A** Complex I (NDUFB8) **B** Complex II (SDHB) **C** Complex III (UQRC2) **D** Complex IV (MTCO1) **E** Complex V (ATP5A). **F** Western blot membrane images and total protein stain (ponceau) used to normalise band intensity for densitometric analysis. Ordinary one-way Anova with Tukey's multiple comparison statistical analysis was performed on each data set. Individual values were graphed with mean ± SD displayed. Results with a P-value≤0.05 were considered significant.

5.7 Urolithin A decreased ETC complex I respiration and proton leak, and ADP sensitivity in young, but not adult, mice in an experimental model of COPD

The gastrocnemius muscle was collected at the endpoint and 15-25mg of fresh tissue was excised from the hip-end of the muscle and placed in BIOPS buffer at 4oC for later use in Oroborus measurements of mitochondrial respiration.

Complex I linked proton flux (Figure 5.12: A), complex I linked OXPHOS (Figure 5.12: B), combined complex I&II linked OXPHOS (Figure 5.12: C), and maximally uncoupled proton flux (Figure 5.12: D) was higher in young air control and CS exposed mice compared to adult mice but was similar in mice treated with UA (Figure 5.12: A-D).

There was no significant effect of CS-exposure or UA treatment on complex I linked proton flux (Figure 5.12: A), complex I linked OXPHOS (Figure 5.12: B), combined complex I&II linked OXPHOS (Figure 5.12: C) and maximally uncoupled proton flux (Figure 5.12: D).

However, there were changes in young mice with CS-exposure and UA treatment. CS-exposure + UA treatment significantly decreased complex I linked proton flux (Figure 5.12: A) and complex I linked OXPHOS (Figure 5.12: B) compared to air control and CS-exposure only groups. Furthermore, and maximally uncoupled proton flux maximally uncoupled proton flux was decreased by UA treatment compared to air control but not to CS exposed mice (Figure 5.12: D).

These results demonstrate significant differences in mitochondrial dynamics between young and adult mice skeletal muscle, and the potential for UA as a modulator of mitochondrial function.

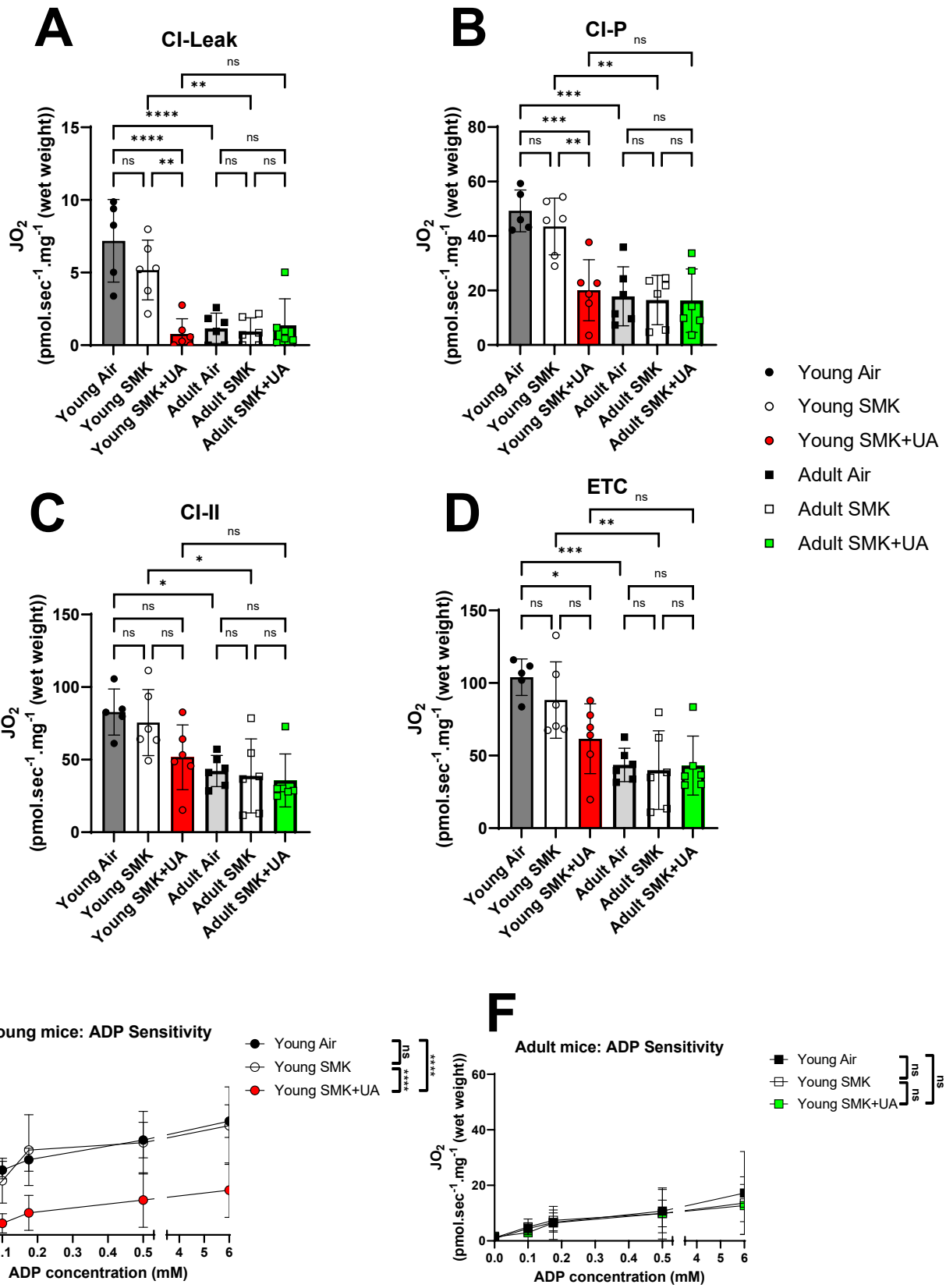
A
CI-Leak
B
CI-P
C
CI-II
D
ETC
JO2 (pmol.sec-1.mg-1 (wet weight))
Young Air
Young SMK
Young SMK+UA
Adult Air
Adult SMK
Adult SMK+UA
E
Young mice: ADP Sensitivity
F
Adult mice: ADP Sensitivity
ADP concentration (mM)

Figure 5.12 Urolithin A decreased ETC complex I respiration and proton leak, and ADP sensitivity in young mice, but not adult mice, in an experimental model of COPD.

Oroboros Oxygraph-2k analysis of gastrocnemius' mitochondrial respiration from a Urolithin A treatment model of COPD in young and adult female C57BL/6 mice. **A** Oxygen consumption rate attributed to complex I linked proton flux across the inner mitochondrial membrane that bypasses ATP synthase (pmol.sec-1.mg-1). **B** Oxygen consumption rate attributed to Complex I linked OXPHOS capacity (pmol.sec-1.mg-1). **C** Oxygen consumption rate attributed to OXPHOS capacity of complex I and II (pmol.sec-1.mg-1). **D** Maximal oxygen consumption rate with oligomycin induced decoupling of proton flux across the inner mitochondrial membrane. **E+F** Oxygen consumption rate with increasing doses of ADP. Ordinary one-way Anova with Tukey's multiple comparison statistical analysis was performed on each data set (A-D) and individual values were graphed with mean ± SD displayed. Two-way Anova Tukey's multiple comparison statistical analysis was performed on the ADP sensitivity data (E+F) and replicate values were graphed as mean ± SD. Results with a P-value≤0.05 were considered significant (*P≤0.05; **P≤0.01; ***P≤0.001, ****=P≤0.0001).

5.8 Muscle Fiber Area was decreased in young, but not adult mice, in an experimental model of COPD, which was prevented with UA treatment

Young (8w old) and adult (1y old) C57BL/6 female mice were exposed to the smoke of 12 cigarettes twice daily, 5d/w for 8w. Some mice were treated with UA (25mg/kg) in the diet ad libitum beginning 2w prior to the start of CS exposure. No significant changes to MFA were observed for the 8w H-151 intervention model (Figure 4.10), which was carried out in 8w old mice. However, the young mice in this model which were of the same age had a significant decrease in MFA with CS exposure, and UA treatment prevented a significant decrease in MFA but was not significantly increased when compared to the CS exposure alone (Figure 5.13).

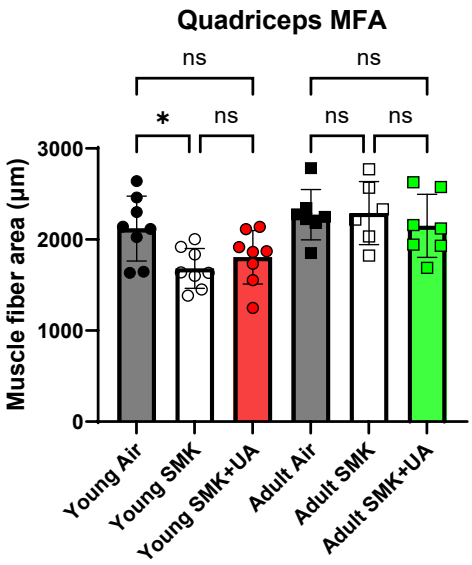
Quadriceps MFA
ns
ns
*
ns
ns
ns
Muscle fiber area (µm)
3000
2000
1000
0
Young Air
Young SMK
Young SMK+UA
Adult Air
Adult SMK
Adult SMK+UA

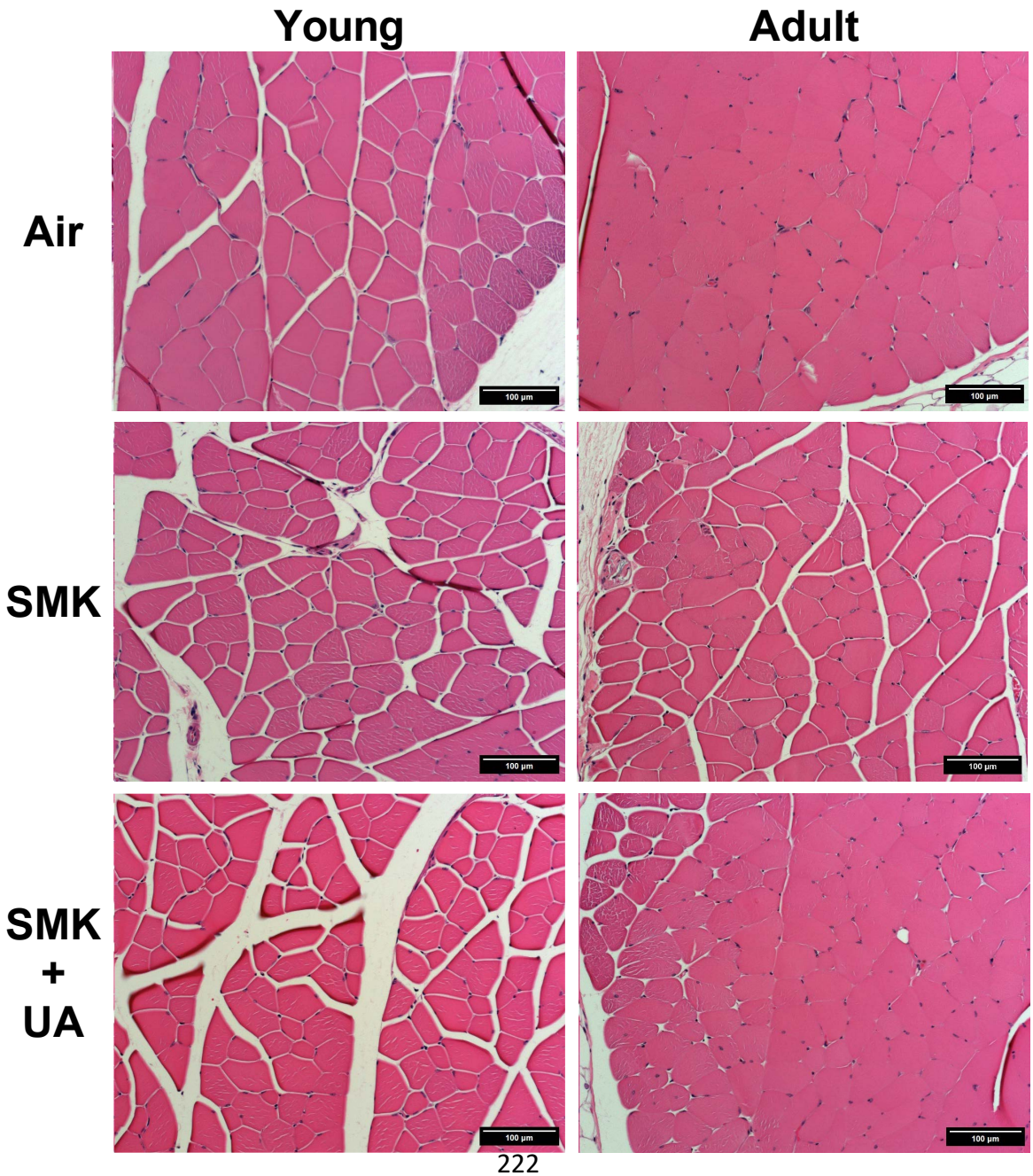
Young
Adult
Air
SMK
SMK
+
UA
100 µm

Figure 5.13 Muscle Fiber Area was decreased in young, but not adult mice, in an experimental model of COPD, which was prevented with UA treatment.

Cross sectional areas (CSA) were taken of the quadriceps mid-belly from an Urolithin A intervention murine model of CS-induced COPD in young and adult mice. CSAs were haematoxylin and eosin (H&E) stained. Brightfield images of quadriceps CSAs were imaged at 20X magnification. Images were imported into ImageJ and muscle fibre areas were measured manually by drawing around each fibre for at least 100 technical replicates per biological sample. Ordinary one-way Anova with Tukey's multiple comparison statistical analysis was performed on each data set and individual values were graphed with mean ± SD displayed. Results with a P-value≤0.05 were considered significant (*P≤0.05; **P≤0.01; ***P≤0.001, ****=P≤0.0001).

Discussion – Chapter 5

The aim of this study was to mitigate CS-induced muscle loss in an 8-week experimental model of COPD, using the dietary supplement/metabolite Urolithin A (UA) in both young and adult mice. UA has demonstrated efficacy in various disease models and clinical settings, where it improved muscle health and endurance, increased lifespan, reduced systemic inflammation, and induced mitophagy in skeletal muscle [285-291, 294]. These properties made UA a potential therapeutic candidate for improving skeletal muscle health while inhibiting inflammation and mitochondrial dysfunction-mediated muscle atrophy. Adult mice were included alongside young mice as they better reflect the age at which humans typically develop COPD. In adult mice, reductions in protein synthesis and increased degradation are more likely to manifest as loss of muscle mass, whereas in young mice, such effects often result in a plateau in growth as they are still growing. This is particularly important when considering the definition of cachexia, which refers to weight loss over time, which does not happen in young mice, making it a less viable model for studying cachexia compared to the same models in adult mice [1].

For both young and adult mice exposed to CS there were lung function changes consistent with what is observed in COPD patients. These changes also were consistent with the three other murine models of COPD that were investigated in my previous chapters. As anticipated, the young mice exposed to CS plateaued in weight, whereas the air control mice continued to gain weight. In contrast, adult mice, which were fully developed, lost weight when exposed to CS but adult air control mice maintained consistent weight . Adult mice better reflected cachexia as seen in COPD patients than young mice, by more closely emulating the age of a typical COPD diagnosis and, since they were fully grown, the mice lost weight as opposed to plateauing in weight like the young mice.

Interestingly, this model revealed a decrease in MFA with CS exposure in young mice, which was not observed in older mice. While UA mitigated this decrease in MFA, it was not significantly improved when compared to CS exposure alone. These findings, for the first time highlight the impact of CS exposure on muscle hypertrophy in an experimental model of COPD.

Notably, the observation that this effect was limited to young mice provides insights into how CS exposure might impair hypertrophy. Supporting this, a study investigating muscle mass in 1.5-, 5-, 12-, and 24-month-old male C57BL/6 mice demonstrated that testosterone depletion significantly reduced muscle mass in the 1.5- and 5-month-old cohorts but had no effect on older mice. Similarly, MFA was reduced only in the younger mice and specifically in the tibialis anterior muscle [357].

These findings suggest that CS exposure may impair muscle mass development and hypertrophy in young mice by reducing testosterone production or interfering with its downstream signalling pathways. However, previous studies have shown that CS increases free circulating testosterone levels in men [358-360], suggesting that the inhibition of downstream targets of testosterone, rather than a reduction in testosterone itself, is more likely to contribute to muscle atrophy and reduced hypertrophy in our model. This idea that smoking has effects downstream of testosterone is further supported by studies that show testosterone is required for early hypertrophy and development in neonatal mice. Therefore, if smoking were to increase testosterone the obvious outcome would be a significant increase in muscle mass and MFA, however the opposite is true in this case and in humans [361, 362].

As previously outlined in humans, cachexia is typically diagnosed on the basis of weight loss (~5-10%) over a given period (~6-12 months) [1]. On average, adult mice exposed to CS lost greater than 10% mass over the course of 8w. This was a rapid weight decrease and may be more

reflective of what is observed during an acute exacerbation in COPD [104, 105, 363]. During acute exacerbations, COPD patients can be hospitalised for extended periods and experience an increased rate of weight loss [364], reduced physical activity and muscle strength [365-367]. In turn, these symptoms are associated with increases in total exacerbations over time. Thus, preventing this positive feedback loop of exacerbation-increased symptom burden, increased exacerbations, may reduce a decline in health in COPD patients [19, 368]. Although the use of adult mice was better able to emulate cachexia in COPD patients, there were unfortunately no improvements to muscle mass with UA during the 8w model.

BALF and plasma immune cell types were investigated for changes due to CS-exposure, the implication of these changes for atrophy and if they would be regulated by UA. An increase in total leukocytes in the BALF, and changes in differential counts were observed in the BALF and blood of both young and adult mice in the experimental COPD model. However, these changes were not significantly influenced by UA treatment. Notably, neutrophils and cytotoxic T cells, which are hallmarks of COPD-associated inflammation, were elevated in the lungs of COPD patients [99] and induced in the lungs of mice with CS-induced experimental COPD [111, 369]. A recent bidirectional two-sample Mendelian randomization (MR) study, using GWAS data from Finland and the United Kingdom, identified correlations between specific immune phenotypes and muscle atrophy. Specifically, cytotoxic T cells and B cell subtypes positively correlated with muscle atrophy, while regulatory T cells were negatively correlated [370]. Although the study did not pinpoint the location of these immune phenotypes, my findings showed a significant increase in cytotoxic T cells in the BALF of adult compared to young mice following CS exposure. Additionally, the ratio of cytotoxic T cells to total leukocytes in plasma was lower in adult compared to young mice, suggesting greater recruitment of cytotoxic T cells from the blood to the lungs in adult mice. Older mice lost weight with CS exposure, and this could be due to increased cytotoxic T cell presence in

the BALF mediating systemic changes through secretion of inflammatory factors[371]. Further investigation is needed to see whether CD8+ T cells infiltration is increased in muscles due to CS exposure, as cytotoxic T cell infiltration has been identified as aetiological in atrophy [372, 373]. In contrast to these findings, cytotoxic T cells have also been shown to aid in muscle regeneration in a murine model of muscle injury, where depletion of CD8+ cells limited macrophage recruitment to the muscles and their subsequent promotion of myoblast proliferation. This effect was rescued with adoptive transfer of CD8+ T cells [374], though the opposite effect was observed in a murine model of colorectal cancer, where adoptive transfer of CD8+ T cells increased muscle wasting [373].

There was no significant effect of CS exposure on B cell induction in the BALF or on the ratio of B cells to total leukocytes in the blood of young or adult mice. Interestingly, UA treatment significantly increased B cells in the BALF of adult CS exposed mice compared to both young mice receiving the same treatment and untreated adult air control mice. Further analysis of these induced B cells may help determine whether their presence contributes to muscle atrophy, similar to the studies of Yu et al [370].

Overall, CS exposure in this experimental COPD model elevated inflammation, particularly innate immune cells like dendritic cells and neutrophils, which likely recruit adaptive lymphocyte cells that drive the disease phenotype. Cytotoxic T cells emerged as a potential mediator of COPD-associated cachexia in our model. Future studies investigating cytotoxic T cell and B cell production of atrophy-linked inflammatory factors, such as IFN-γ, IL-1β, TNF, and IL-6, may provide insights into the mechanisms of inflammation-induced cachexia in COPD.

Immunoblot analysis of proteins and phosphorylated proteins of the protein synthesis pathway indicated a decrease in flux through this pathway with CS exposure alone and with CS exposure +

UA treatment. Total Ser473 p-Akt abundance was reduced with CS exposure and UA treatment, and it was also reduced to a similar degree with CS exposure alone, but this was not statistically significant. Akt is phosphorylated at Ser473 by mTORC2, and a decrease in Ser473 p-Akt indicates decreased interaction between mTORC2 and Akt [196]. It is possible that total levels of mTORC2 complex were reduced, which would account for decreased Ser473 p-Akt, however total mTOR protein was unaffected by CS exposure or UA treatment making this unlikely to be the cause. Instead, it is more likely that decreased mTORC2 recruitment to the cell membrane, which is required for Akt activation, resulted in decreased Ser473 p-Akt. PI3K mediated conversion of PIP2 to PIP3 is required for mTORC2 membrane localisation, as PIP3 anchors mTORC2 via the pleckstrin homology domain of mSin1, a subunit of mTORC2 [375]. PI3K converts PIP2 to PIP3 because of growth factor binding e.g. IGF-1, so a decrease may indicate reduced growth factor signalling in the quadriceps of mice exposed to CS and treated with UA [376].

The decrease in Ser473 Akt does not appear to result from a redirection of mTOR protein toward mTORC1 complex formation, as downstream effectors of mTOR, including Ser389 p-S6K and Ser235/236 p-rpS6, were also reduced. This suggests that CS exposure likely impaired growth factor-mediated PI3K/Akt/mTOR signalling, leading to reduced protein synthesis in the quadriceps. This effect may have been exacerbated by UA treatment, as UA has been shown to decrease flux through the PI3K/Akt/mTORC1 pathway by reducing the phosphorylation of Akt and S6K [293]. This presents a paradox for the use of UA as a treatment for muscle atrophy: while its benefits *in vivo* and in clinical settings are well-documented, it inhibits upstream proteins of the protein synthesis pathway which are required for muscle production. However, as previously outlined in section 1.6.2 of my introduction chapter, mTORC1 can also drive atrophy and myopathy through inhibition of autophagy, which may be overcome with UA treatment

UA treatment was not selected for an ability to directly stimulate protein synthesis but rather based on previous studies that demonstrated its benefits for skeletal muscle health, its anti-inflammatory properties, and its capacity to induce mitophagy [285]. Indeed, mitochondrial dysfunction is known to mediate pathogenesis [258, 260, 377] and skeletal muscle dysfunction in COPD [378]. In the context of COPD-mediated cachexia, the aim of using UA was to mitigate inflammation-driven atrophy, partly by preventing dysfunctional mitochondrial inflammatory signalling and enhancing energy efficiency through mitophagy and the biogenesis of healthy mitochondria.

Surprisingly, there was no change in total expression of ETC complex subunits. In another study that looked at complex protein expression in skeletal muscle (vastus lateralis), COPD patients had lower expression of ETC complex proteins compared to healthy donor patients [379], but this has yet to be repeated in experimental mouse models of COPD. However, confounding factors in that study were that it was carried out in a cohort of only 9 patients and was comparing sedentary COPD patients against similarly sedentary control patients without COPD [260]. In another study that looked at ETC complex proteins in the quadriceps from COPD GOLD grade 2 patients compared to never-smokers found that COPD patients had significantly reduced complex I, II, III and V total protein [380]. It was therefore surprising to see no change to ETC protein expression with CS-exposure in our murine COPD model, even after UA treatment. Future experiments should examine ETC complex activity in vitro to improve the understanding of mitochondrial function in COPD-induced cachexia.

Mitochondrial function in the permeabilised gastrocnemius skeletal muscle was measured using an Oroboros oxygraph-2k. Differences in mitochondrial respiration were observed between young and adult mice. Complex I mediated proton leak, complex I OXPHOS linked oxygen consumption,

combined complex I&II OXPHOS linked oxygen consumption, maximally uncoupled oxygen consumption and ADP sensitivity were reduced in adult mice gastrocnemius compared to air control and CS exposed young mice. Furthermore, UA treatment decreased complex I OXPHOS linked oxygen consumption and proton leak in young mice compared to vehicle treated CS exposed mice and decreased all of these parameters compared to air control mice.

CS exposed young mice had reduced ADP sensitivity (~30JO_2) compared to the mice from the H-151 model of the same age (~47JO_2). Furthermore, there was no significant change to mitochondrial respiration with CS exposure in young mice, which was also in contrast to the H-151 model that showed a significant increase in complex I attributed proton leak and OXPHOS. All parameters were unchanged in adult mice with CS or UA treatment. As a result, it is difficult to know the true impact of CS exposure on skeletal muscle mitochondrial functions in these murine models based purely on these data.

In order to build upon these initial findings, future experiments investigating mitochondrial respiration in the skeletal muscle of CS-induced COPD mice should consider using mitochondrial ETC activity assays to evaluate the activity of individual ETC complexes ex vivo [381]. Transmission electron microscopy (TEM) could be employed to assess mitochondrial morphology, localization, and density within myofibers [382] while measuring autophagic flux would provide valuable insights into protein degradation and mitophagy processes occurring in skeletal muscle [383]. Additionally, examining the abundance and localization of mitochondrial biogenesis-associated proteins, such as PGC1α and TFAM, would be important for understanding the regulation of mitochondrial biogenesis in COPD skeletal muscle. Both proteins are master transcriptional regulators of the mitochondrial genome, and their mitochondrial localisation is associated with increased mitochondrial biogenesis [384, 385].

Overall, the aim of this study was to assess the efficacy of UA in preventing cachexia in an experimental mouse model of COPD and unfortunately UA did not prevent or decrease skeletal muscle atrophy in young or old mice. Furthermore, without further testing, it is also unclear whether UA had a significant impact on mitochondrial health or increased mitophagy in myocytes. Functional assays such as measurements of contractile strength could provide insight into the potential effect of UA on skeletal muscle function in future experiments. Rapid muscle loss occurred in the COPD model that was faster than what occurs in COPD patients (outside of exacerbations) and may have meant any positive effect had by UA on skeletal muscle mass was outweighed by the severe challenge of CS exposure. Thus, an experimental model of recovery from CS exposure, with UA as a supplement, may provide a better idea of the effects of UA on skeletal muscle mass recovery and mitochondrial function.

Chapter 6 General Discussion

When endeavouring to investigate the mechanisms underlying cachexia in pulmonary diseases it was crucial to first establish which murine models of pulmonary disease would be suitable (summarised in figure 6-1). The criteria for suitability included an ability to emulate the human respiratory pathology associated with that pulmonary disease, as well as the presence of muscle atrophy, i.e. significant weight loss/change over time. As the models were predominantly carried out in mice aged 8w old, significantly lower total body weight, coupled with a significant decrease in either quadriceps or gastrocnemius mass was also considered acceptable.

Several murine models for IPF were examined for these criteria: a 4w single dose bleomycin model, a 10w single dose bleomycin model, and an 8w CS-exposure + 4w single dose bleomycin model. Of these models, only the latter demonstrated negative changes to muscle atrophy, but did not emulate human lung function changes in IPF. The muscles of the 4w single dose bleomycin model of IPF were chosen for further analysis as it is a widely used model and demonstrated the appropriate changes to lung function. Despite this, no changes to protein degradation or synthesis pathways were observed. However, there was a significant decrease in total STING protein in the quadriceps which has never been previously described. Further examination of STING protein in the lungs of these mice, as well as acute studies of bleomycin and its effects on STING expression in different cells/tissues may implicate a STING in the pathogenesis of IPF.

Moderate (steroid sensitive) and severe (steroid resistant) models of asthma were also examined for the above criteria: both models demonstrated the desired changes in lung function and were reflective of both phenotypes of asthma, however neither model had any impact on total body weight or skeletal muscle mass. There was also no change in protein expression for proteins associated with protein synthesis or degradation pathways.

The time course models of CS-induced COPD showed negative impacts on whole body and skeletal muscle mass as early as 3w and up until the 12w time point, which was the longest model examined. Lung function was negatively impacted at 8 and 12w and emulated lung function changes seen in COPD. Similar effects of CS-exposure on skeletal muscle mass and lung function were observed in male and female C57BL/6 mice after 8w of CS exposure. Female quadriceps from the 8w timepoint of the sex comparison timepoint model were examined for changes to proteins associated with protein degradation and synthesis, as female mice are abundantly used for models in the lab, so sample availability would be high for follow up experiments and fewer mice would be needed for follow up models. Although there were no significant changes to the proteins examined in association with protein degradation and synthesis. A trend was observed for phosphorylated rpS6 and 4E-BP1, which were significantly downregulated and upregulated respectively in subsequent treatment models. Significant changes to gene expression of atrogenes *FBXO32*, *TRIM63* and *GADD45A*, suggest a role of atrogenes in mediating muscle atrophy in CS-induced COPD models. This role is likely time dependent and warrants further research into different timepoints, but especially in the earlier timepoints of the model, and in direct response to CS. Future experiments should consider the use of *in vitro* culture of myofibers with cigarette smoke extract (CSE), sterile solubilised smoke extract, to see if atrogenes can be directly upregulated by CSE, and if protein synthesis is reduced.

Pathway enrichment analysis of publicly available human COPD quadriceps microarray data revealed increased musculoskeletal inflammation and downregulation of proteins associated with the mitochondria and metabolism. This suggested mitochondrial dysfunction as a possible factor in driving local inflammation in the quadriceps during COPD. Inefficient energy metabolism and inflammation have been reported to drive muscle atrophy. Thus, mitochondrial health and downstream effector molecules of mitochondrial inflammation, cGAS-STING signalling, were

targeted in subsequent therapeutic models. The aim of these therapies was to decrease muscle atrophy and improve muscle health during an 8w CS-induced murine COPD model.

The i.n. H-151 STING inhibitor therapy did not improve CS-induced muscle atrophy after 8w, and did not prevent lung function decline when compared to room air exposed mice. When MFA was examined, there was no observed effect of CS on hypertrophy, which suggested CS decreases muscle mass through some other mechanism such as decreased hydration or loss of glycogen. In the quadriceps, 4E-BP1 protein expression was significantly increased due to CS exposure, indicating the upregulation of certain atrogenes in the quadriceps which was not improved by H-151 therapy. Although muscle mass or lung function was not improved, a significant increase in proton leak and ADP sensitivity due to CS exposure was prevented by H-151 and suggests a previously unreported role of H-151 in modulating mitochondrial function in relation to energy production. Future studies that aim to understand the role of H-151 in cell metabolism could conduct *in vitro* or *ex vivo* studies using STING agonists (e.g. 2'3'-cGAMP [274] or diABZI [386]) and measure metabolic changes using Seahorse real-time cell metabolic analysis. This could provide the basis for future avenues of enquiry when using H-151 (or other interventions) to target CS-induced metabolic changes *in vivo*. Enzyme activity assays, measuring the activity of ETC complex proteins and citrate synthase could also be performed on the cryo-stored powdered tissues from these models to get a better idea of the *in vivo* effect of H-151. H-151 irreversibly covalently binds STING at the transmembrane cysteine residue 91. It is possible that H-151 has its effects on cell metabolism independent of its role as a STING inhibitor molecule and has off target effects through binding cysteine residues of other proteins. Affinity purification-mass spectrometry may be useful in determining whether H-151 does have off target binding sites that could explain its ability to modulate ETC dynamics.

Similarly, UA treatment in an 8w CS-induced COPD model did not prevent muscle atrophy or lung function decline. This model was performed in 1y old adult mice as well as 8w old young mice as adult mice were considered of an equivalent age to that of a typical COPD diagnosis in humans i.e. ~45y old [354, 387]. As a result, instead of impaired body and skeletal muscle growth, as has been seen in the CS-induced COPD models using young mice, adult mice lost weight over time. This presents the first time that one of the pulmonary disease molecules met the criteria for cachexia in a COPD model. However, in contrast to the H-151 intervention model, the young mice from this model exhibited a significant decrease in MFA and thus, hypertrophy. This effect was not observed in adult mice and may suggest a role for CS inhibition of the downstream effectors of testosterone. The effect of CS on MFA was inconsistent between COPD models though so further studies will be needed to fully elucidate the effects of CS on MFA and to understand the role of testosterone in CS induced muscle atrophy.

Young mouse quadricep muscle were examined for changes in expression of proteins associated with protein degradation and synthesis. There was an observed decrease in Thr389 p-rpS6 and Ser473 p-Akt with CS exposure and UA treatment. This suggested a decrease in PI3K/Akt/ mTOR signalling and a decrease in protein synthesis. UA has been previously shown to decrease inhibit this pathway and this was supported by my study, though what impact this had on muscle mass seems too arbitrary as there was no significant difference in muscle mass between UA treated and vehicle treated CS exposed mice. Furthermore, if protein synthesis was already being downregulated by CS exposure, UA inhibition of Akt becomes redundant. Indeed, Thr389 p-rpS6 was significantly downregulated with CS exposure alone, and although Ser473 p-Akt was only significantly reduced with CS exposure and UA treatment compared to the air control. There was no significant difference in expression compared to the CS exposure only group. Therefore, it is

unlikely that Urolithin A had a meaningful negative impact on muscle mass through inhibition of Akt phosphorylation.

UA treatment was chosen for its efficacy in the clinic and across many studies looking to improve skeletal muscle function [290, 291, 388] and also its potential for reducing muscle atrophy [283]. These beneficial effects are thought to be induced predominantly through inhibiting inflammation and improving mitochondrial health by inducing mitophagy and mitochondrial biogenesis. When gastrocnemius muscles were examined by Oroboros analysis, it was shown that UA did influence mitochondrial respiration in young but not adult mice. This was interesting, however, the study was in contrast somewhat to the previous H-151 intervention model that observed a much higher proton leak, complex I associated OXPHOS and ADP sensitivity with CS exposure, than in this model. Furthermore, the adult mice exhibited abnormally low oxygen consumption across all the parameters measured which combined with the contrasting young mouse results, may indicate an issue with the assay on the day. Thus, the data measuring the effect of UA on mitochondrial respiration would be complimented by follow up experiments similar to those suggested for the H-151 model. In addition to those experiments looking at the impact of UA on mitochondrial respiration, it would be important to show whether UA does induce mitophagy in the skeletal muscle of mice in this model. Static measures of autophagy such as LC3 and p62 abundance in tissue samples, as well as TEM of skeletal muscle could give an indication of mitochondrial abundance and morphology. Follow up studies that aim to understand the role of UA in skeletal muscle may consider the use of mito-QC reporter mice, which can be used to quantify mitophagy in tissues.

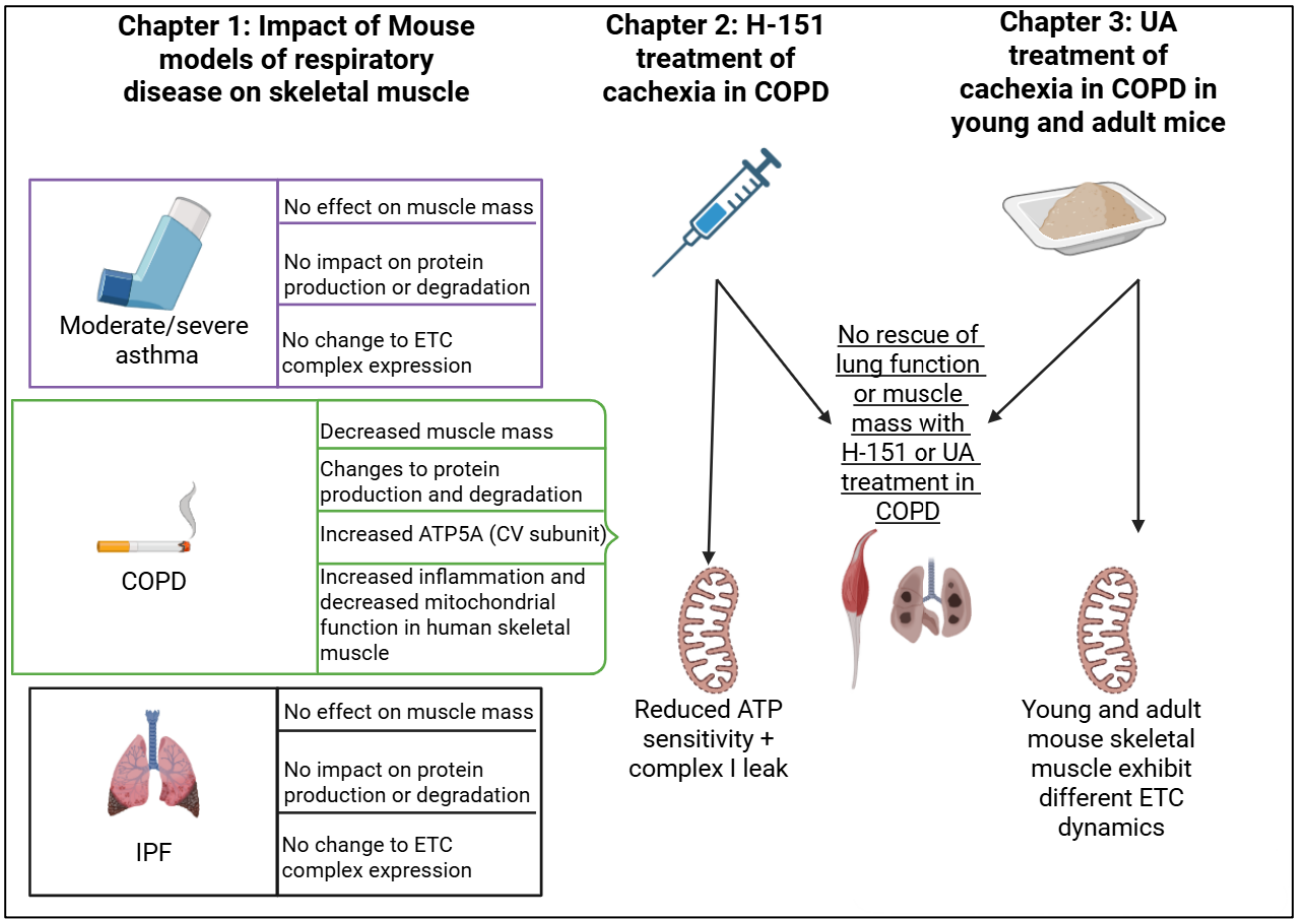

Figure 6.1 Summary of thesis results

Study Limitations

The time elapsed after death is a critical factor when determining levels of protein phosphorylation, as phosphorylated proteins can undergo dephosphorylation postmortem. To preserve phosphorylation states, it is essential to rapidly fix or snap-freeze tissues; however, this was not always feasible during these experiments. A key limitation arose from the invasive lung function manoeuvres required in each model, which necessitated the use of anaesthesia. As a result, mice occasionally died prematurely during lung function assessments, prior to the degassing stage which is a 15m procedure.

Additionally, the protocol's degassing stage, which ensures complete assessment of lung mechanics, invariably results in the death of the mouse but is performed as the final step. Following this, cardiac puncture for blood collection was prioritized, as blood begins to coagulate rapidly postmortem, rendering it unrecoverable. Next, BALF collection and lung tissue collection were often prioritized to maximize the recovery of cells for evaluating lung inflammation. The only exception to this order was in the experimental COPD model involving UA intervention in young and adult mice, where skeletal muscle was collected before BALF and lung tissue collection.

This prioritization led to variation in the time after death before skeletal muscle was collected, which, in some cases, extended up to 20m depending on the mouse and model. This variability represents a confounding factor for analyses such as mitochondrial respiration studies and especially for measuring protein phosphorylation. This may account for the high variability between Immunoblot outcomes for the COPD models when examining PI3K-Akt-mTORC1 signalling, since there was likely high variation in skeletal muscle collection times. However, in the young and adult mice COPD experimental UA intervention model, the time after death before muscle collection was minimized and controlled. In this model, skeletal muscle was processed

immediately for Oroboros analysis, with tissues snap-frozen or formalin-fixed within five minutes of cardiac puncture. BALF and lung tissue collection were conducted only after this step.

Skeletal muscles collected in Chapter 3 that were not snap-frozen were formalin-fixed for histological analysis. Unfortunately, O.C.T. embedding and cryo-sectioning of these tissues for MFA were unsuccessful. This was likely due to the shrinking effect of the 30% sucrose solution, which caused fiber separation and made it difficult for tissue slices to adhere to charged slides during immunohistochemical (IHC) staining.

The decision to use formalin fixation, rather than the more conventional isopentane snap-freezing method for histological analysis, was influenced by challenges encountered during preliminary studies. The high-throughput nature of the *in vivo* experiments and the rapid tissue collection required at their endpoints made it difficult to maintain the isopentane at the correct viscosity, resulting in artifacts in skeletal muscle samples during histological processing. To address these limitations, FFPE processing was adopted for tissue samples analysed in Chapters 4 and 5. This approach ensured consistent skeletal muscle collection at endpoint, preserved muscle architecture, and facilitated reliable IHC staining.

However, there were still some drawbacks to using FFPE tissue instead of isopentane-frozen, O.C.T.-embedded tissue. FFPE tissue required antigen retrieval for muscle fiber type labelling, whereas frozen tissue did not and was better suited for immunofluorescence staining. This led to difficulties in quantifying MFA and made it impossible to assess muscle fiber type distribution. Most freely available software for automatically quantifying MFA (e.g., Myovision [389], ImageJ plugin for quantifying MFA [390]) rely on immunofluorescence staining to define myofiber edges and, therefore, could not be used with my H&E-stained samples, which lack clearly defined edges.

As a result, the MFA quantification process may have been affected by the absence of a streamlined, easy-to-use software solution.

Lastly, the antibodies used for immunoblotting analysis of MuRF1 and Atrogin-1 protein abundance exhibited non-specific binding across most of the nitrocellulose membrane. Efforts to resolve this issue, including the use of various blocking buffers and different concentrations of BSA or skimmed milk powder, were unsuccessful. However, only the bands corresponding to the molecular weight of the target protein, as specified by the manufacturer, were quantified**.**

Future Directions

Follow up histological analysis of experimental pulmonary diseases: For the experimental IPF models, lung histology data are essential to confirm the development of fibrosis, as changes in lung architecture and collagen deposition are critical for model validation. While lung function is a key diagnostic element in IPF, the single i.n. dose bleomycin-, and single i.n. dose bleomycin with CS exposure-induced experimental IPF models required histological confirmation of fibrosis due to inconclusive lung function changes. In particular, the lung function changes in the single i.n. dose bleomycin with CS exposure were not reflective of those typically observed in the standard single-dose bleomycin model, likely because of the effect of CS exposure on lung volumes. Despite these challenges, histological confirmation of pulmonary fibrosis remains necessary.

Moreover, the role of skeletal muscle fibrosis in bleomycin-induced IPF models has not been previously investigated. ECM deposition may explain the lack of muscle mass loss observed in my models, raising important questions about the underlying mechanisms. Simple yet informative techniques, such as Sirius red staining of pulmonary and skeletal muscle tissues, could provide valuable insights into the presence of fibrosis. This analysis would also offer a deeper understanding of skeletal muscle health in IPF patients, contributing to a more comprehensive view of disease pathology. Indeed, skeletal muscle fibrosis has not been described in any of the pulmonary diseases examined in this study and provides an interesting avenue for future enquiry.

Alternative experimental models of pulmonary disease: Although the development of pulmonary diseases such as COPD, asthma, and IPF can accelerate muscle loss in patients, the progression of cachexia typically occurs over years or decades, unless further acceleration is triggered by exacerbations. Cachexia often coincides with sarcopenia, as COPD and IPF are predominantly diagnosed in older populations. To better model these conditions, experimental designs could

involve older (>1y old) mice or be modified to extend the duration of the models. This would allow pulmonary disease to develop earlier and exert systemic effects over a longer period, thereby more accurately reflecting the chronic nature of these diseases in human patients.

CS exposure is an intensive intervention in experimental COPD and weight loss is evident from as early as 2w. Furthermore, 1y old mice in an 8w model lost >15% body weight after only 6w of CS exposure. Adult mice were used in this model to better emulate the age of COPD onset in humans, however weight loss still occurred too quickly for it to reflect human COPD and was more reflective of exacerbation induced weight loss, though still too harsh. Thus, a longer-term model with less frequent CS exposure beginning in young mice and continuing for 1-1.5y would likely be more optima. However, feasibility may be an issue, as continuous, long-term exposure to CS could come with other health complications that confound results. Therefore, alternative models such as an elastase, or combined LPS and elastase-induced-COPD model may be appropriate.

In a modified asthma model, the moderate or severe asthma protocol could be conducted as usual but without dexamethasone treatment. Instead of concluding the study after 5w, the endpoint could be extended to 6-12m. This approach would better capture the long-term systemic effects of asthma and their impact on muscle wasting. Additionally, using adult mice could better represent the age at which muscle wasting is typically observed in asthma patients.

For models known to resolve over time, such as single i.n. dose bleomycin-induced IPF experimental models, administering multiple doses may be a viable approach to sustain the disease phenotype. Additionally, recurring challenges could be incorporated to simulate acute exacerbations, providing a more comprehensive representation of the disease's progression and episodic nature. The inclusion of pulmonary infections in these models also provides an excellent opportunity to understand their impact on disease in tandem to the effect of skeletal muscle,

allowing for multiple lines of enquiry within the same model that could maximise the use of tissues and animal lives.

To monitor disease progression and systemic effects, mice could be weighed daily, and monthly tail bleeds performed to track changes in circulating leukocytes, inflammatory markers, and therapeutic intervention concentrations in the blood. Such a model could also be applied to older mice (>1y old) to simulate acute exacerbations in an older patient. This approach would provide a more realistic framework for studying the interplay between chronic pulmonary diseases and systemic muscle loss.

Further investigations into the role of mitochondrial health and mitophagy in COPD:

Histological analysis of lung or skeletal muscle tissues, including staining for autophagosomes in experimental COPD models, particularly in H-151 or UA treated mice, could offer a static perspective on autophagy in COPD. This could be complemented by protein quantification of autophagy markers (e.g., LC3-I/-II ratio, p62) and mitophagy markers (e.g., PARKIN, PINK1, and BNIP3/NIX). Additionally, conducting an experimental COPD model in MitoQC mice could provide a more precise and controlled method for assessing mitophagic flux, as using MitoQC mice is considered the gold standard for evaluating mitophagy both *in vivo* and *ex vivo*.

Transmission electron microscopy (TEM) could further enhance these investigations by measuring mitochondrial abundance and providing insights into mitochondrial morphology, health, and turnover [391]. Mitochondrial respiration could also be assessed *ex vivo* using Seahorse real-time cell metabolic analysis. Integrating these complementary techniques in future models would offer a comprehensive overview of mitochondrial health, abundance, respiration, and mitophagy in experimental COPD.

The H-151 model did not halt disease progression in an experimental model of COPD and failed to prevent muscle mass loss. Whether this outcome reflects that cGAS-STING signaling is not essential for the progression of COPD remains unclear. Future experiments should focus on quantifying cytoplasmic mtRNA and mtDNA using RT-qPCR and qPCR, respectively. These analyses could help determine whether mitochondrial health is compromised in specific tissues and provide insights into PRR sensing of endogenous nucleotides in compromised skeletal muscle in COPD.

In this study, it was hypothesized that cGAS-mediated recognition of mtDNA results in STING activation, triggers local inflammation, and drives muscle atrophy in the skeletal muscle of experimental COPD models. However, it is also plausible that RIG-I-like receptor (RLR) sensing of double-stranded mtRNA may induce inflammation and contribute to atrophy through activation of TBK1 [392-394]. However, its role in skeletal muscle dysfunction or wasting has not been investigated. Exploring this pathway could open new avenues for understanding muscle atrophy mechanisms in COPD.

Lastly, the availability of online publicly available data sets provided excellent avenues of enquiry and supported many of the lines of questioning in this study. Future studies may include publicly available data from the skeletal muscle of patients to support transcriptome data. Ideally, patients with COPD-induced cachexia could be recruited and biopsies processed for proteomic or metabolic analyses.

Conclusion

In conclusion, the experimental murine models of IPF and asthma tested in this study did not demonstrate significant weight loss and are therefore unlikely to be suitable for future investigations into cachexia in these conditions. In contrast, CS exposure impaired skeletal muscle growth in young mice and induced skeletal muscle atrophy in adult mice in experimental COPD models. Across three COPD models in young female C57BL/6 mice, CS exposure was associated with a reduction in signaling through the protein synthesis pathway, mitochondrial dysfunction, and reflected microarray data from COPD patient quadriceps.

Efforts to directly target mitochondrial dysfunction or its downstream effector, STING, using UA or the STING inhibitor H-151, respectively, did not prevent skeletal muscle loss or improve lung function in experimental COPD. However, H-151 demonstrated a potential metabolic regulatory role in skeletal muscle by reducing ATP sensitivity and complex I-driven proton leak. Similarly, UA showed an ability to modulate mitochondrial respiration, dendritic cell induction, and prevent significant MFA decrease in response to CS exposure.

Thus, my hypothesis that skeletal muscle mitochondrial dysfunction and inflammation contribute to cachexia in pulmonary disease, requires further investigation and though these findings were preliminary, they highlight the need for follow-up experiments to fully elucidate the effects of these interventions. The potential efficacy of UA, H-151, or similar therapeutics in the context of COPD-induced cachexia remains to be fully determined, and these interventions may hold promise for providing symptom relief and improving the quality of life for COPD patients.

Bibliography

1. Evans, W.J., et al., *Cachexia: a new definition.* Clin Nutr, 2008. **27**(6): p. 793-9.
2. Ali, S. and J.M. Garcia, *Sarcopenia, cachexia and aging: diagnosis, mechanisms and therapeutic options - a mini-review.* Gerontology, 2014. **60**(4): p. 294-305.
3. Santilli, V., et al., *Clinical definition of sarcopenia.* Clin Cases Miner Bone Metab, 2014. **11**(3): p. 177-80.
4. Howard, E.E., et al., *Skeletal Muscle Disuse Atrophy and the Rehabilitative Role of Protein in Recovery from Musculoskeletal Injury.* Advances in Nutrition, 2020. **11**(4): p. 989-1001.
5. Gordon, B.S., A.R. Kelleher, and S.R. Kimball, *Regulation of muscle protein synthesis and the effects of catabolic states.* Int J Biochem Cell Biol, 2013. **45**(10): p. 2147-57.
6. Sartori, R., V. Romanello, and M. Sandri, *Mechanisms of muscle atrophy and hypertrophy: implications in health and disease.* Nature Communications, 2021. **12**(1): p. 330.
7. Petermann-Rocha, F., et al., *Global prevalence of sarcopenia and severe sarcopenia: a systematic review and meta-analysis.* J Cachexia Sarcopenia Muscle, 2022. **13**(1): p. 86-99.
8. Bock, J.-O., et al., *Associations of frailty with health care costs – results of the ESTHER cohort study.* BMC Health Services Research, 2016. **16**(1): p. 128.
9. Ye, C., et al., *Sarcopenia and catastrophic health expenditure by socio-economic groups in China: an analysis of household-based panel data.* J Cachexia Sarcopenia Muscle, 2022. **13**(3): p. 1938-1947.
10. Farkas, J., et al., *Cachexia as a major public health problem: frequent, costly, and deadly.* J Cachexia Sarcopenia Muscle, 2013. **4**(3): p. 173-8.
11. Bruyère, O., et al., *The health economics burden of sarcopenia: a systematic review.* Maturitas, 2019. **119**: p. 61-69.
12. Joglekar, S., P.N. Nau, and J.J. Mezhir, *The impact of sarcopenia on survival and complications in surgical oncology: A review of the current literature.* J Surg Oncol, 2015. **112**(5): p. 503-9.
13. Wan, S.N., et al., *Incident sarcopenia in hospitalized older people: A systematic review.* PLoS One, 2023. **18**(8): p. e0289379.
14. Goates, S., et al., *Economic Impact of Hospitalizations in US Adults with Sarcopenia.* J Frailty Aging, 2019. **8**(2): p. 93-99.
15. von Haehling, S. and S.D. Anker, *Cachexia as a major underestimated and unmet medical need: facts and numbers.* J Cachexia Sarcopenia Muscle, 2010. **1**(1): p. 1-5.
16. Sanders, K.J., et al., *Cachexia in chronic obstructive pulmonary disease: new insights and therapeutic perspective.* J Cachexia Sarcopenia Muscle, 2016. **7**(1): p. 5-22.
17. Wagner, P.D., *Possible mechanisms underlying the development of cachexia in COPD.* Eur Respir J, 2008. **31**(3): p. 492-501.
18. Barreiro, E. and A. Jaitovich, *Muscle atrophy in chronic obstructive pulmonary disease: molecular basis and potential therapeutic targets.* J Thorac Dis, 2018. **10**(Suppl 12): p. S1415-s1424.
19. Kwan, H.Y., et al., *The prognostic significance of weight loss in chronic obstructive pulmonary disease-related cachexia: a prospective cohort study.* J Cachexia Sarcopenia Muscle, 2019. **10**(6): p. 1330-1338.
20. Ito, Y., et al., *Skeletal muscle atrophy and short-term mortality in patients with acute exacerbation of idiopathic pulmonary fibrosis: an observational cohort study.* Respir Investig, 2023. **61**(4): p. 371-378.
21. Suzuki, Y., et al., *Cause of mortality and sarcopenia in patients with idiopathic pulmonary fibrosis receiving antifibrotic therapy.* Respirology, 2021. **26**(2): p. 171-179.

22. Bernardinello, N., et al., *Loss of muscle mass in Idiopathic Pulmonary Fibrosis.* European Respiratory Journal, 2022. **60**(suppl 66): p. 3406.
23. Li, J., et al., *Prevalence and risk factors of sarcopenia in idiopathic pulmonary fibrosis: a systematic review and meta-analysis.* Frontiers in Medicine, 2023. **10**.
24. Sridhar, M., et al., *Association of musculoskeletal involvement with lung function and mortality in patients with idiopathic pulmonary fibrosis.* Respiratory Research, 2024. **25**(1): p. 81.
25. Suzuki, Y., et al., *Distinct profile and prognostic impact of body composition changes in idiopathic pulmonary fibrosis and idiopathic pleuroparenchymal fibroelastosis.* Sci Rep, 2018. **8**(1): p. 14074.
26. Hu, Z., et al., *Associations between sarcopenia with asthmatic prevalence, lung function and comorbidity.* BMC Geriatrics, 2022. **22**(1): p. 703.
27. Visser, E., et al., *Muscle Function in Moderate to Severe Asthma: Association With Clinical Outcomes and Inflammatory Markers.* J Allergy Clin Immunol Pract, 2023. **11**(5): p. 1439-1447.e3.
28. Khan, B., et al., *Emerging Mechanisms of Skeletal Muscle Homeostasis and Cachexia: The SUMO Perspective.* Cells, 2023. **12**(4).
29. Argilés, J.M., et al., *Skeletal Muscle Regulates Metabolism via Interorgan Crosstalk: Roles in Health and Disease.* J Am Med Dir Assoc, 2016. **17**(9): p. 789-96.
30. Langen, R.C., et al., *Triggers and mechanisms of skeletal muscle wasting in chronic obstructive pulmonary disease.* Int J Biochem Cell Biol, 2013. **45**(10): p. 2245-56.
31. McLeod, M., et al., *Live strong and prosper: the importance of skeletal muscle strength for healthy ageing.* Biogerontology, 2016. **17**(3): p. 497-510.
32. Jensen, J., et al., *The role of skeletal muscle glycogen breakdown for regulation of insulin sensitivity by exercise.* Front Physiol, 2011. **2**: p. 112.
33. Adeva-Andany, M.M., et al., *Glycogen metabolism in humans.* BBA Clin, 2016. **5**: p. 85-100.
34. Smith, J.A.B., et al., *Exercise metabolism and adaptation in skeletal muscle.* Nature Reviews Molecular Cell Biology, 2023. **24**(9): p. 607-632.
35. Dejong, C.H., N.E. Deutz, and P.B. Soeters, *Intestinal glutamine and ammonia metabolism during chronic hyperammonaemia induced by liver insufficiency.* Gut, 1993. **34**(8): p. 1112-9.
36. He, Y., et al., *Glutamine synthetase in muscle is required for glutamine production during fasting and extrahepatic ammonia detoxification.* J Biol Chem, 2010. **285**(13): p. 9516-9524.
37. Weston, A.R., et al., *Skeletal muscle buffering capacity and endurance performance after high-intensity interval training by well-trained cyclists.* Eur J Appl Physiol Occup Physiol, 1997. **75**(1): p. 7-13.
38. Hollidge-Horvat, M.G., et al., *Effect of induced metabolic alkalosis on human skeletal muscle metabolism during exercise.* Am J Physiol Endocrinol Metab, 2000. **278**(2): p. E316-29.
39. Soeters, P.B., et al., *The anabolic role of the Warburg, Cori-cycle and Crabtree effects in health and disease.* Clin Nutr, 2021. **40**(5): p. 2988-2998.
40. Hoffmann, C. and C. Weigert, *Skeletal Muscle as an Endocrine Organ: The Role of Myokines in Exercise Adaptations.* Cold Spring Harb Perspect Med, 2017. **7**(11).
41. Iizuka, K., T. Machida, and M. Hirafuji, *Skeletal muscle is an endocrine organ.* J Pharmacol Sci, 2014. **125**(2): p. 125-31.
42. Lee, J.H. and H.S. Jun, *Role of Myokines in Regulating Skeletal Muscle Mass and Function.* Front Physiol, 2019. **10**: p. 42.

43. Severinsen, M.C.K. and B.K. Pedersen, *Muscle-Organ Crosstalk: The Emerging Roles of Myokines.* Endocr Rev, 2020. **41**(4): p. 594-609.
44. Engelen, M.P., et al., *Factors contributing to alterations in skeletal muscle and plasma amino acid profiles in patients with chronic obstructive pulmonary disease.* Am J Clin Nutr, 2000. **72**(6): p. 1480-7.
45. Romanick, M., L.V. Thompson, and H.M. Brown-Borg, *Murine models of atrophy, cachexia, and sarcopenia in skeletal muscle.* Biochim Biophys Acta, 2013. **1832**(9): p. 1410-20.
46. Morgan, J. and T. Partridge, *Skeletal muscle in health and disease.* Dis Model Mech, 2020. **13**(2).
47. Saxton, R.A. and D.M. Sabatini, *mTOR Signaling in Growth, Metabolism, and Disease.* Cell, 2017. **168**(6): p. 960-976.
48. Tatebe, H. and K. Shiozaki, *Evolutionary Conservation of the Components in the TOR Signaling Pathways.* Biomolecules, 2017. **7**(4).
49. van Putten, M., et al., *Mouse models for muscular dystrophies: an overview.* Dis Model Mech, 2020. **13**(2).
50. Baek, K.W., et al., *Rodent Model of Muscular Atrophy for Sarcopenia Study.* J Bone Metab, 2020. **27**(2): p. 97-110.
51. Wang, B.Y.-H., et al., *Is dexamethasone-induced muscle atrophy an alternative model for naturally aged sarcopenia model?* Journal of Orthopaedic Translation, 2023. **39**: p. 12-20.
52. Christian, C.J. and G.M. Benian, *Animal models of sarcopenia.* Aging Cell, 2020. **19**(10): p. e13223.
53. Ji, Y., et al., *Inflammation: Roles in Skeletal Muscle Atrophy.* Antioxidants (Basel), 2022. **11**(9).
54. Dalle, S. and K. Koppo, *Is inflammatory signaling involved in disease-related muscle wasting? Evidence from osteoarthritis, chronic obstructive pulmonary disease and type II diabetes.* Exp Gerontol, 2020. **137**: p. 110964.
55. Cai, D., et al., *IKKbeta/NF-kappaB activation causes severe muscle wasting in mice.* Cell, 2004. **119**(2): p. 285-98.
56. Nunes, E.A., et al., *Disuse-induced skeletal muscle atrophy in disease and nondisease states in humans: mechanisms, prevention, and recovery strategies.* Am J Physiol Cell Physiol, 2022. **322**(6): p. C1068-c1084.
57. Landi, F., et al., *Muscle loss: The new malnutrition challenge in clinical practice.* Clin Nutr, 2019. **38**(5): p. 2113-2120.
58. Owens, D.J., *Nutritional Support to Counteract Muscle Atrophy.* Adv Exp Med Biol, 2018. **1088**: p. 483-495.
59. Ahmed, S.T., et al., *Diagnosis and Treatment of Mitochondrial Myopathies.* Neurotherapeutics, 2018. **15**(4): p. 943-953.
60. Zhou, M., et al., *Activation of cGAS-STING pathway - A possible cause of myofiber atrophy/necrosis in dermatomyositis and immune-mediated necrotizing myopathy.* J Clin Lab Anal, 2022. **36**(10): p. e24631.
61. Cisterna, B.A., et al., *Active acetylcholine receptors prevent the atrophy of skeletal muscles and favor reinnervation.* Nature Communications, 2020. **11**(1): p. 1073.
62. Bongers, K.S., et al., *Skeletal muscle denervation causes skeletal muscle atrophy through a pathway that involves both Gadd45a and HDAC4.* Am J Physiol Endocrinol Metab, 2013. **305**(7): p. E907-15.
63. Carnio, S., et al., *Autophagy Impairment in Muscle Induces Neuromuscular Junction Degeneration and Precocious Aging.* Cell Reports, 2014. **8**(5): p. 1509-1521.

64. Ascenzi, F., et al., *Effects of IGF-1 isoforms on muscle growth and sarcopenia.* Aging Cell, 2019. **18**(3): p. e12954.
65. Schakman, O., et al., *Glucocorticoid-induced skeletal muscle atrophy.* Int J Biochem Cell Biol, 2013. **45**(10): p. 2163-72.
66. Sato, A.Y., et al., *Glucocorticoids Induce Bone and Muscle Atrophy by Tissue-Specific Mechanisms Upstream of E3 Ubiquitin Ligases.* Endocrinology, 2017. **158**(3): p. 664-677.
67. De Theije, C.C., et al., *Hypoxia-induced muscle atrophy and impaired regulation of protein turnover are partially dependent on muscle glucocorticoid receptor signaling.* European Respiratory Journal. **46**(suppl 59): p. PA4893.
68. Naruse, M., S. Trappe, and T.A. Trappe, *Human skeletal muscle-specific atrophy with aging: a comprehensive review.* J Appl Physiol (1985), 2023. **134**(4): p. 900-914.
69. Furrer, R. and C. Handschin, *Muscle Wasting Diseases: Novel Targets and Treatments.* Annu Rev Pharmacol Toxicol, 2019. **59**: p. 315-339.
70. Domaniku, A., S.N. Bilgic, and S. Kir, *Muscle wasting: emerging pathways and potential drug targets.* Trends Pharmacol Sci, 2023. **44**(10): p. 705-718.
71. Remels, A.H.V., et al., *The mechanisms of cachexia underlying muscle dysfunction in COPD.* Journal of Applied Physiology, 2012. **114**(9): p. 1253-1262.
72. De Brandt, J., et al., *Update on the Etiology, Assessment, and Management of COPD Cachexia: Considerations for the Clinician.* Int J Chron Obstruct Pulmon Dis, 2022. **17**: p. 2957-2976.
73. Hosseini, M., et al., *Global prevalence of asthma-COPD overlap (ACO) in the general population: a systematic review and meta-analysis.* Respir Res, 2019. **20**(1): p. 229.
74. GOLD, *Global Initiative for Chronic Obstructive Pulmonary Disease (GOLD) report 2024*. 2024, Global Initiative for Chronic Obstructive Pulmonary Disease.
75. GOLD, *GLOBAL STRATEGY FOR PREVENTION, DIAGNOSIS AND MANAGEMENT OF COPD: 2025 Report*. 2024.
76. Doucet, M., et al., *Muscle atrophy and hypertrophy signaling in patients with chronic obstructive pulmonary disease.* Am J Respir Crit Care Med, 2007. **176**(3): p. 261-9.
77. Cruthirds, C.L., et al., *A low postabsorptive whole body protein balance is associated with markers of poor daily physical functioning in Chronic Obstructive Pulmonary Disease.* Clin Nutr, 2022. **41**(4): p. 885-893.
78. Engelen, M.P., et al., *Enhanced levels of whole-body protein turnover in patients with chronic obstructive pulmonary disease.* Am J Respir Crit Care Med, 2000. **162**(4 Pt 1): p. 1488-92.
79. Ubhi, B.K., et al., *Metabolic profiling detects biomarkers of protein degradation in COPD patients.* European Respiratory Journal, 2011. **40**(2): p. 345-355.
80. Guo, Y., et al., *Autophagy in locomotor muscles of patients with chronic obstructive pulmonary disease.* Am J Respir Crit Care Med, 2013. **188**(11): p. 1313-20.
81. Puig-Vilanova, E., et al., *Oxidative stress, redox signaling pathways, and autophagy in cachectic muscles of male patients with advanced COPD and lung cancer.* Free Radic Biol Med, 2015. **79**: p. 91-108.
82. Alers, S., et al., *Role of AMPK-mTOR-Ulk1/2 in the regulation of autophagy: cross talk, shortcuts, and feedbacks.* Mol Cell Biol, 2012. **32**(1): p. 2-11.
83. Zong, Y., et al., *Mitochondrial dysfunction: mechanisms and advances in therapy.* Signal Transduction and Targeted Therapy, 2024. **9**(1): p. 124.
84. Wu, W., et al., *Advances in metabolomics of chronic obstructive pulmonary disease.* Chinese Medical Journal Pulmonary and Critical Care Medicine, 2023. **1**(4): p. 223-230.

85. WHO, *Chronic obstructive pulmonary disease (COPD)*. 2024, WHO: https://www.who.int/news-room/fact-sheets/detail/chronic-obstructive-pulmonary-disease-(copd).
86. Willemse, B.W.M., et al., *The impact of smoking cessation on respiratory symptoms, lung function, airway hyperresponsiveness and inflammation.* European Respiratory Journal. **23**(3): p. 464-476.
87. Lee, J.H., et al., *COPD Risk Factor Profiles in General Population and Referred Patients: Potential Etiotypes.* Int J Chron Obstruct Pulmon Dis, 2023. **18**: p. 2509-2520.
88. Zhang, Y., et al., *More to Explore: Further Definition of Risk Factors for COPD - Differential Gender Difference, Modest Elevation in PM(2).(5), and e-Cigarette Use.* Front Physiol, 2021. **12**: p. 669152.
89. Holtjer, J.C.S., et al., *Identifying risk factors for COPD and adult-onset asthma: an umbrella review.* Eur Respir Rev, 2023. **32**(168).
90. Tu, X., et al., *Asthma-COPD overlap: current understanding and the utility of experimental models.* Eur Respir Rev, 2021. **30**(159).
91. Barnes, P.J., *Inflammatory endotypes in COPD.* Allergy, 2019. **74**(7): p. 1249-1256.
92. Myronenko, O., et al., *Endotyping COPD: hypoxia-inducible factor-2 as a molecular "switch" between the vascular and airway phenotypes?* European Respiratory Review, 2023. **32**(167): p. 220173.
93. Christenson, S.A., et al., *Chronic obstructive pulmonary disease.* Lancet, 2022. **399**(10342): p. 2227-2242.
94. Ham, J., et al., *The Dynamic Contribution of Neutrophils in the Chronic Respiratory Diseases.* Allergy Asthma Immunol Res, 2022. **14**(4): p. 361-378.
95. Shapiro, S.D., *The macrophage in chronic obstructive pulmonary disease.* Am J Respir Crit Care Med, 1999. **160**(5 Pt 2): p. S29-32.
96. Fujii, W., et al., *Alveolar macrophage transcriptomic profiling in COPD shows major lipid metabolism changes.* ERJ Open Res, 2021. **7**(3).
97. Silver, J.S., et al., *Inflammatory triggers associated with exacerbations of COPD orchestrate plasticity of group 2 innate lymphoid cells in the lungs.* Nat Immunol, 2016. **17**(6): p. 626-35.
98. Bal, S.M., et al., *IL-1β, IL-4 and IL-12 control the fate of group 2 innate lymphoid cells in human airway inflammation in the lungs.* Nat Immunol, 2016. **17**(6): p. 636-45.
99. Chung, K.F. and I.M. Adcock, *Multifaceted mechanisms in COPD: inflammation, immunity, and tissue repair and destruction.* European Respiratory Journal, 2008. **31**(6): p. 1334-1356.
100. Belchamber, K.B.R., et al., *Defective bacterial phagocytosis is associated with dysfunctional mitochondria in COPD macrophages.* European Respiratory Journal, 2019. **54**(4): p. 1802244.
101. Hsu, A.T., et al., *The Role of Innate Lymphoid Cells in Chronic Respiratory Diseases.* Front Immunol, 2021. **12**: p. 733324.
102. Tashkin, D.P. and M.E. Wechsler, *Role of eosinophils in airway inflammation of chronic obstructive pulmonary disease.* Int J Chron Obstruct Pulmon Dis, 2018. **13**: p. 335-349.
103. Singh, D., et al., *Eosinophilic inflammation in COPD: prevalence and clinical characteristics.* Eur Respir J, 2014. **44**(6): p. 1697-700.
104. Abdulai, R.M., et al., *Deterioration of Limb Muscle Function during Acute Exacerbation of Chronic Obstructive Pulmonary Disease.* Am J Respir Crit Care Med, 2018. **197**(4): p. 433-449.
105. Mason, S.E., et al., *Respiratory exacerbations are associated with muscle loss in current and former smokers.* Thorax, 2021. **76**(6): p. 554-560.

106. Rennard, S.I. and S.G. Farmer, *Exacerbations and progression of disease in asthma and chronic obstructive pulmonary disease.* Proc Am Thorac Soc, 2004. **1**(2): p. 88-92.
107. Mathioudakis, A.G., et al., *Acute exacerbations of chronic obstructive pulmonary disease: in search of diagnostic biomarkers and treatable traits.* Thorax, 2020. **75**(6): p. 520-527.
108. Ghorani, V., et al., *Experimental animal models for COPD: a methodological review.* Tob Induc Dis, 2017. **15**: p. 25.
109. Yun, J.H., et al., *Transcriptomic Analysis of Lung Tissue from Cigarette Smoke-Induced Emphysema Murine Models and Human Chronic Obstructive Pulmonary Disease Show Shared and Distinct Pathways.* Am J Respir Cell Mol Biol, 2017. **57**(1): p. 47-58.
110. Rangasamy, T., et al., *Cigarette smoke-induced emphysema in A/J mice is associated with pulmonary oxidative stress, apoptosis of lung cells, and global alterations in gene expression.* Am J Physiol Lung Cell Mol Physiol, 2009. **296**(6): p. L888-900.
111. Beckett, E.L., et al., *A new short-term mouse model of chronic obstructive pulmonary disease identifies a role for mast cell tryptase in pathogenesis.* J Allergy Clin Immunol, 2013. **131**(3): p. 752-62.
112. Obeidat, M., et al., *The Overlap of Lung Tissue Transcriptome of Smoke Exposed Mice with Human Smoking and COPD.* Sci Rep, 2018. **8**(1): p. 11881.
113. Fricker, M., et al., *Chronic cigarette smoke exposure induces systemic hypoxia that drives intestinal dysfunction.* JCI Insight, 2018. **3**(3).
114. Serré, J., et al., *Enhanced lung inflammatory response in whole-body compared to nose-only cigarette smoke-exposed mice.* Respir Res, 2021. **22**(1): p. 86.
115. Luo, L., et al., *Chronic obstructive pulmonary disease and the airway microbiome: A review for clinicians.* Respir Med, 2024. **225**: p. 107586.
116. Wang, Z., et al., *Inflammatory Endotype-associated Airway Microbiome in Chronic Obstructive Pulmonary Disease Clinical Stability and Exacerbations: A Multicohort Longitudinal Analysis.* Am J Respir Crit Care Med, 2021. **203**(12): p. 1488-1502.
117. Li, N., et al., *Gut microbiota dysbiosis contributes to the development of chronic obstructive pulmonary disease.* Respir Res, 2021. **22**(1): p. 274.
118. Sulaiman, I., et al., *Lower Airway Dysbiosis Augments Lung Inflammatory Injury in Mild-to-Moderate Chronic Obstructive Pulmonary Disease.* American Journal of Respiratory and Critical Care Medicine, 2023. **208**(10): p. 1101-1114.
119. Bowerman, K.L., et al., *Disease-associated gut microbiome and metabolome changes in patients with chronic obstructive pulmonary disease.* Nature Communications, 2020. **11**(1): p. 5886.
120. Vandivier, R.W. and M. Ghosh, *Understanding the Relevance of the Mouse Cigarette Smoke Model of COPD: Peering through the Smoke.* Am J Respir Cell Mol Biol, 2017. **57**(1): p. 3-4.
121. Rodrigues Brandao-Rangel, M.A., et al., *Exercise Inhibits the Effects of Smoke-Induced COPD Involving Modulation of STAT3.* Oxid Med Cell Longev, 2017. **2017**: p. 6572714.
122. Balnis, J., et al., *Deaccelerated Myogenesis and Autophagy in Genetically Induced Pulmonary Emphysema.* Am J Respir Cell Mol Biol, 2022. **66**(6): p. 623-637.
123. Lüthje, L., et al., *Exercise intolerance and systemic manifestations of pulmonary emphysema in a mouse model.* Respir Res, 2009. **10**(1): p. 7.
124. WHO, *Asthma.* World Health Organisation, 2024.
125. Stern, J., J. Pier, and A.A. Litonjua, *Asthma epidemiology and risk factors.* Semin Immunopathol, 2020. **42**(1): p. 5-15.
126. CDC, *Asthma as the Underlying Cause of Death*. 2018, Centre for Disease Control.
127. Mortimer, K., et al., *The burden of asthma, hay fever and eczema in adults in 17 countries: GAN Phase I study.* Eur Respir J, 2022. **60**(3).

128. Wadhwa, R., et al., *Cellular mechanisms underlying steroid-resistant asthma.* Eur Respir Rev, 2019. **28**(153).
129. Hekking, P.W., et al., *The prevalence of severe refractory asthma.* J Allergy Clin Immunol, 2015. **135**(4): p. 896-902.
130. Wang, W., et al., *Potential therapeutic targets for steroid-resistant asthma.* Curr Drug Targets, 2010. **11**(8): p. 957-70.
131. Barnes, P.J. and I.M. Adcock, *Glucocorticoid resistance in inflammatory diseases.* Lancet, 2009. **373**(9678): p. 1905-17.
132. Kuruvilla, M.E., F.E. Lee, and G.B. Lee, *Understanding Asthma Phenotypes, Endotypes, and Mechanisms of Disease.* Clin Rev Allergy Immunol, 2019. **56**(2): p. 219-233.
133. Pembrey, L., et al., *Understanding asthma phenotypes: the World Asthma Phenotypes (WASP) international collaboration.* ERJ Open Res, 2018. **4**(3).
134. Bara, I., et al., *Pathophysiology of bronchial smooth muscle remodelling in asthma.* Eur Respir J, 2010. **36**(5): p. 1174-84.
135. Schmidt, D. and K.F. Rabe, *Immune mechanisms of smooth muscle hyperreactivity in asthma.* J Allergy Clin Immunol, 2000. **105**(4): p. 673-82.
136. Kavanagh, J., D.J. Jackson, and B.D. Kent, *Over- and under-diagnosis in asthma.* Breathe (Sheff), 2019. **15**(1): p. e20-e27.
137. Akindele, A., et al., *Qualitative study of practices and challenges when making a diagnosis of asthma in primary care.* NPJ Prim Care Respir Med, 2019. **29**(1): p. 27.
138. GINA, *Global Strategy for Asthma Management and Prevention (2024 update).* GINA, 2024.
139. McCracken, J.L., et al., *Diagnosis and Management of Asthma in Adults: A Review.* Jama, 2017. **318**(3): p. 279-290.
140. Kaur, R. and G. Chupp, *Phenotypes and endotypes of adult asthma: Moving toward precision medicine.* J Allergy Clin Immunol, 2019. **144**(1): p. 1-12.
141. Maspero, J., et al., *Type 2 inflammation in asthma and other airway diseases.* ERJ Open Res, 2022. **8**(3).
142. Froidure, A., et al., *Asthma phenotypes and IgE responses.* Eur Respir J, 2016. **47**(1): p. 304-19.
143. Kips, J.C., et al., *Murine models of asthma.* European Respiratory Journal, 2003. **22**(2): p. 374-382.
144. Carroll, O.R., et al., *Advances in respiratory physiology in mouse models of experimental asthma.* Front Physiol, 2023. **14**: p. 1099719.
145. Aun, M.V., et al., *Animal models of asthma: utility and limitations.* J Asthma Allergy, 2017. **10**: p. 293-301.
146. Woo, L.N., et al., *A 4-Week Model of House Dust Mite (HDM) Induced Allergic Airways Inflammation with Airway Remodeling.* Sci Rep, 2018. **8**(1): p. 6925.
147. Tu, X., et al., *Airway and parenchyma transcriptomics in a house dust mite model of experimental asthma.* Respir Res, 2023. **24**(1): p. 32.
148. Kim, D.I., M.K. Song, and K. Lee, *Comparison of asthma phenotypes in OVA-induced mice challenged via inhaled and intranasal routes.* BMC Pulm Med, 2019. **19**(1): p. 241.
149. Casaro, M., et al., *OVA-Induced Allergic Airway Inflammation Mouse Model.* Methods Mol Biol, 2019. **1916**: p. 297-301.
150. Kim, R.Y., et al., *Role for NLRP3 Inflammasome-mediated, IL-1β-Dependent Responses in Severe, Steroid-Resistant Asthma.* Am J Respir Crit Care Med, 2017. **196**(3): p. 283-297.
151. Pinkerton, J.W., et al., *Relationship between type 2 cytokine and inflammasome responses in obesity-associated asthma.* Journal of Allergy and Clinical Immunology, 2022. **149**(4): p. 1270-1280.

152. Raghu, G., et al., *An official ATS/ERS/JRS/ALAT statement: idiopathic pulmonary fibrosis: evidence-based guidelines for diagnosis and management.* Am J Respir Crit Care Med, 2011. **183**(6): p. 788-824.
153. Nalysnyk, L., et al., *Incidence and prevalence of idiopathic pulmonary fibrosis: review of the literature.* Eur Respir Rev, 2012. **21**(126): p. 355-61.
154. Martinez, F.J., et al., *Idiopathic pulmonary fibrosis.* Nat Rev Dis Primers, 2017. **3**: p. 17074.
155. Maher, T.M., et al., *Global incidence and prevalence of idiopathic pulmonary fibrosis.* Respir Res, 2021. **22**(1): p. 197.
156. Vancheri, C., et al., *Idiopathic pulmonary fibrosis: a disease with similarities and links to cancer biology.* Eur Respir J, 2010. **35**(3): p. 496-504.
157. Abramson, M.J., et al., *Occupational and environmental risk factors for idiopathic pulmonary fibrosis in Australia: case-control study.* Thorax, 2020. **75**(10): p. 864-869.
158. Raghu, G., et al., *Diagnosis of Idiopathic Pulmonary Fibrosis. An Official ATS/ERS/JRS/ALAT Clinical Practice Guideline.* Am J Respir Crit Care Med, 2018. **198**(5): p. e44-e68.
159. Raghu, G., et al., *Idiopathic Pulmonary Fibrosis (an Update) and Progressive Pulmonary Fibrosis in Adults: An Official ATS/ERS/JRS/ALAT Clinical Practice Guideline.* Am J Respir Crit Care Med, 2022. **205**(9): p. e18-e47.
160. Selman, M., A. Pardo, and A.U. Wells, *Usual interstitial pneumonia as a stand-alone diagnostic entity: the case for a paradigm shift?* Lancet Respir Med, 2023. **11**(2): p. 188-196.
161. Upagupta, C., et al., *Matrix abnormalities in pulmonary fibrosis.* Eur Respir Rev, 2018. **27**(148).
162. Glass, D.S., et al., *Idiopathic pulmonary fibrosis: Molecular mechanisms and potential treatment approaches.* Respir Investig, 2020. **58**(5): p. 320-335.
163. Warheit-Niemi, H.I., et al., *Fibrotic Lung Disease Alters Neutrophil Trafficking and Promotes Neutrophil Elastase and Extracellular Trap Release.* Immunohorizons, 2022. **6**(12): p. 817-834.
164. Achaiah, A., et al., *Neutrophil levels correlate with quantitative extent and progression of fibrosis in IPF: results of a single-centre cohort study.* BMJ Open Respir Res, 2023. **10**(1).
165. Parker, J.M., et al., *A Phase 2 Randomized Controlled Study of Tralokinumab in Subjects with Idiopathic Pulmonary Fibrosis.* Am J Respir Crit Care Med, 2018. **197**(1): p. 94-103.
166. King, T.E., Jr., et al., *Effect of interferon gamma-1b on survival in patients with idiopathic pulmonary fibrosis (INSPIRE): a multicentre, randomised, placebo-controlled trial.* Lancet, 2009. **374**(9685): p. 222-8.
167. Shenderov, K., et al., *Immune dysregulation as a driver of idiopathic pulmonary fibrosis.* J Clin Invest, 2021. **131**(2).
168. Collard, H.R., et al., *Acute Exacerbation of Idiopathic Pulmonary Fibrosis. An International Working Group Report.* Am J Respir Crit Care Med, 2016. **194**(3): p. 265-75.
169. Liu, T., F.G. De Los Santos, and S.H. Phan, *The Bleomycin Model of Pulmonary Fibrosis.* Methods Mol Biol, 2017. **1627**: p. 27-42.
170. Moore, B.B. and C.M. Hogaboam, *Murine models of pulmonary fibrosis.* Am J Physiol Lung Cell Mol Physiol, 2008. **294**(2): p. L152-60.
171. Walters, D.M. and S.R. Kleeberger, *Mouse models of bleomycin-induced pulmonary fibrosis.* Curr Protoc Pharmacol, 2008. **Chapter 5**: p. Unit 5.46.
172. Chang, A., P.M. Van Ry, and G. Raghu, *Idiopathic pulmonary fibrosis: aligning murine models to clinical trials in humans.* Lancet Respir Med, 2023. **11**(11): p. 953-955.
173. Izbicki, G., et al., *Time course of bleomycin-induced lung fibrosis.* Int J Exp Pathol, 2002. **83**(3): p. 111-9.

174. Kobayashi, H., A. Tachi, and S. Hagita, *Time course of histopathology of bleomycin-induced pulmonary fibrosis using an intratracheal sprayer in mice.* Exp Anim, 2024. **73**(1): p. 41-49.
175. Peng, R., et al., *Bleomycin induces molecular changes directly relevant to idiopathic pulmonary fibrosis: a model for "active" disease.* PLoS One, 2013. **8**(4): p. e59348.
176. Redente, E.F., et al., *Age and sex dimorphisms contribute to the severity of bleomycin-induced lung injury and fibrosis.* Am J Physiol Lung Cell Mol Physiol, 2011. **301**(4): p. L510-8.
177. Stout-Delgado, H.W., et al., *Age-Dependent Susceptibility to Pulmonary Fibrosis Is Associated with NLRP3 Inflammasome Activation.* Am J Respir Cell Mol Biol, 2016. **55**(2): p. 252-63.
178. Tashiro, J., et al., *Exploring Animal Models That Resemble Idiopathic Pulmonary Fibrosis.* Front Med (Lausanne), 2017. **4**: p. 118.
179. Redente, E.F., et al., *Persistent, Progressive Pulmonary Fibrosis and Epithelial Remodeling in Mice.* Am J Respir Cell Mol Biol, 2021. **64**(6): p. 669-676.
180. Franzén, L., et al., *Mapping spatially resolved transcriptomes in human and mouse pulmonary fibrosis.* Nat Genet, 2024. **56**(8): p. 1725-1736.
181. Schaefer, C.J., et al., *Antifibrotic activities of pirfenidone in animal models.* Eur Respir Rev, 2011. **20**(120): p. 85-97.
182. Wollin, L., et al., *Antifibrotic and anti-inflammatory activity of the tyrosine kinase inhibitor nintedanib in experimental models of lung fibrosis.* J Pharmacol Exp Ther, 2014. **349**(2): p. 209-20.
183. Vanoirbeek, J.A., et al., *Noninvasive and invasive pulmonary function in mouse models of obstructive and restrictive respiratory diseases.* Am J Respir Cell Mol Biol, 2010. **42**(1): p. 96-104.
184. Barreiro, T.J. and I. Perillo, *An approach to interpreting spirometry.* Am Fam Physician, 2004. **69**(5): p. 1107-14.
185. Taillandier, D. and C. Polge, *Skeletal muscle atrogenes: From rodent models to human pathologies.* Biochimie, 2019. **166**: p. 251-269.
186. Wang, X. and C.G. Proud, *The mTOR pathway in the control of protein synthesis.* Physiology (Bethesda), 2006. **21**: p. 362-9.
187. Riquelme, M.A., et al., *Mechanotransduction via the coordinated actions of integrins, PI3K signaling and Connexin hemichannels.* Bone Research, 2021. **9**(1): p. 8.
188. Di-Luoffo, M., et al., *PI3K functions as a hub in mechanotransduction.* Trends Biochem Sci, 2021. **46**(11): p. 878-888.
189. Bower, N.I. and I.A. Johnston, *Transcriptional regulation of the IGF signaling pathway by amino acids and insulin-like growth factors during myogenesis in Atlantic salmon.* PLoS One, 2010. **5**(6): p. e11100.
190. Tato, I., et al., *Amino Acids Activate Mammalian Target of Rapamycin Complex 2 (mTORC2) via PI3K/Akt Signaling*.* Journal of Biological Chemistry, 2011. **286**(8): p. 6128-6142.
191. Li, J., et al., *Structural basis of the activation of type 1 insulin-like growth factor receptor.* Nature Communications, 2019. **10**(1): p. 4567.
192. Luo, M., et al., *Phosphorylation of Human Insulin Receptor Substrate-1 at Serine 629 Plays a Positive Role in Insulin Signaling.* Endocrinology, 2007. **148**(10): p. 4895-4905.
193. Liao, Z., et al., *Comprehensive insulin receptor phosphorylation dynamics profiled by mass spectrometry.* Febs j, 2022. **289**(9): p. 2657-2671.
194. He, W., et al., *Interaction of insulin receptor substrate-2 (IRS-2) with the insulin and insulin-like growth factor I receptors. Evidence for two distinct phosphotyrosine-dependent interaction domains within IRS-2.* J Biol Chem, 1996. **271**(20): p. 11641-5.

195. Luo, J., et al., *The p85 regulatory subunit of phosphoinositide 3-kinase down-regulates IRS-1 signaling via the formation of a sequestration complex.* J Cell Biol, 2005. **170**(3): p. 455-64.
196. Ragupathi, A., C. Kim, and E. Jacinto, *The mTORC2 signaling network: targets and cross-talks.* Biochem J, 2024. **481**(2): p. 45-91.
197. Alessi, D.R., et al., *Mechanism of activation of protein kinase B by insulin and IGF-1.* Embo j, 1996. **15**(23): p. 6541-51.
198. Guertin, D.A., et al., *Ablation in mice of the mTORC components raptor, rictor, or mLST8 reveals that mTORC2 is required for signaling to Akt-FOXO and PKCalpha, but not S6K1.* Dev Cell, 2006. **11**(6): p. 859-71.
199. Panwar, V., et al., *Multifaceted role of mTOR (mammalian target of rapamycin) signaling pathway in human health and disease.* Signal Transduction and Targeted Therapy, 2023. **8**(1): p. 375.
200. Fraser, C.S., *Quantitative studies of mRNA recruitment to the eukaryotic ribosome.* Biochimie, 2015. **114**: p. 58-71.
201. Osterman, I.A., et al., *Comparison of mRNA features affecting translation initiation and reinitiation.* Nucleic Acids Res, 2013. **41**(1): p. 474-86.
202. Lyons, E.F., et al., *Translation elongation as a rate limiting step of protein production.* bioRxiv, 2024.
203. Milan, G., et al., *Regulation of autophagy and the ubiquitin–proteasome system by the FoxO transcriptional network during muscle atrophy.* Nature Communications, 2015. **6**(1): p. 6670.
204. Stitt, T.N., et al., *The IGF-1/PI3K/Akt pathway prevents expression of muscle atrophy-induced ubiquitin ligases by inhibiting FOXO transcription factors.* Mol Cell, 2004. **14**(3): p. 395-403.
205. Bodine, S.C., et al., *Identification of ubiquitin ligases required for skeletal muscle atrophy.* Science, 2001. **294**(5547): p. 1704-8.
206. Sandri, M., et al., *Foxo transcription factors induce the atrophy-related ubiquitin ligase atrogin-1 and cause skeletal muscle atrophy.* Cell, 2004. **117**(3): p. 399-412.
207. Castets, P., et al., *Sustained activation of mTORC1 in skeletal muscle inhibits constitutive and starvation-induced autophagy and causes a severe, late-onset myopathy.* Cell Metab, 2013. **17**(5): p. 731-44.
208. Castets, P., et al., *mTORC1 and PKB/Akt control the muscle response to denervation by regulating autophagy and HDAC4.* Nature Communications, 2019. **10**(1): p. 3187.
209. Castets, P. and M.A. Rüegg, *MTORC1 determines autophagy through ULK1 regulation in skeletal muscle.* Autophagy, 2013. **9**(9): p. 1435-7.
210. Kaiser, M.S., et al., *Dual roles of mTORC1-dependent activation of the ubiquitin-proteasome system in muscle proteostasis.* Communications Biology, 2022. **5**(1): p. 1141.
211. Gomes, M.D., et al., *Atrogin-1, a muscle-specific F-box protein highly expressed during muscle atrophy.* Proc Natl Acad Sci U S A, 2001. **98**(25): p. 14440-5.
212. Jogo, M., S. Shiraishi, and T.A. Tamura, *Identification of MAFbx as a myogenin-engaged F-box protein in SCF ubiquitin ligase.* FEBS Lett, 2009. **583**(17): p. 2715-9.
213. Tintignac, L.A., et al., *Degradation of MyoD mediated by the SCF (MAFbx) ubiquitin ligase.* J Biol Chem, 2005. **280**(4): p. 2847-56.
214. Csibi, A., et al., *MAFbx/Atrogin-1 controls the activity of the initiation factor eIF3-f in skeletal muscle atrophy by targeting multiple C-terminal lysines.* J Biol Chem, 2009. **284**(7): p. 4413-21.

215. Heras, G., et al., *Muscle RING-finger protein-1 (MuRF1) functions and cellular localization are regulated by SUMO1 post-translational modification.* J Mol Cell Biol, 2019. **11**(5): p. 356-370.
216. Cussonneau, L., et al., *Induction of ATF4-Regulated Atrogenes Is Uncoupled from Muscle Atrophy during Disuse in Halofuginone-Treated Mice and in Hibernating Brown Bears.* Int J Mol Sci, 2022. **24**(1).
217. Ebert, S.M., et al., *Biology of Activating Transcription Factor 4 (ATF4) and Its Role in Skeletal Muscle Atrophy.* J Nutr, 2022. **152**(4): p. 926-938.
218. Glass, D.J., *Skeletal muscle hypertrophy and atrophy signaling pathways.* Int J Biochem Cell Biol, 2005. **37**(10): p. 1974-84.
219. Brown, A.K. and A.E. Webb, *Regulation of FOXO Factors in Mammalian Cells.* Curr Top Dev Biol, 2018. **127**: p. 165-192.
220. Santos, B.F., et al., *FOXO family isoforms.* Cell Death & Disease, 2023. **14**(10): p. 702.
221. Tzivion, G., M. Dobson, and G. Ramakrishnan, *FoxO transcription factors; Regulation by AKT and 14-3-3 proteins.* Biochim Biophys Acta, 2011. **1813**(11): p. 1938-45.
222. Ehmsen, J.T., et al., *GADD45A is a protective modifier of neurogenic skeletal muscle atrophy.* JCI Insight, 2021. **6**(13).
223. Thyss, R., et al., *NF-kappaB/Egr-1/Gadd45 are sequentially activated upon UVB irradiation to mediate epidermal cell death.* Embo j, 2005. **24**(1): p. 128-37.
224. Ebert, S.M., et al., *Stress-induced skeletal muscle Gadd45a expression reprograms myonuclei and causes muscle atrophy.* J Biol Chem, 2012. **287**(33): p. 27290-301.
225. Marcotte, G.R., et al., *GADD45A is a mediator of mitochondrial loss, atrophy, and weakness in skeletal muscle.* JCI Insight, 2023. **8**(22).
226. Zeman, R.J., et al., *Differential skeletal muscle gene expression after upper or lower motor neuron transection.* Pflugers Arch, 2009. **458**(3): p. 525-35.
227. Palomer, X., et al., *GADD45A: With or without you.* Med Res Rev, 2024. **44**(4): p. 1375-1403.
228. Webster, J.M., et al., *Inflammation and Skeletal Muscle Wasting During Cachexia.* Front Physiol, 2020. **11**: p. 597675.
229. Trendelenburg, A.U., et al., *TAK-1/p38/nNFκB signaling inhibits myoblast differentiation by increasing levels of Activin A.* Skelet Muscle, 2012. **2**(1): p. 3.
230. Ladner, K.J., M.A. Caligiuri, and D.C. Guttridge, *Tumor necrosis factor-regulated biphasic activation of NF-kappa B is required for cytokine-induced loss of skeletal muscle gene products.* J Biol Chem, 2003. **278**(4): p. 2294-303.
231. Gallay, L., et al., *Involvement of Type I Interferon Signaling in Muscle Stem Cell Proliferation During Dermatomyositis.* Neurology, 2022. **98**(21): p. e2108-e2119.
232. De Luna, N., et al., *Hypoxia triggers IFN-I production in muscle: Implications in dermatomyositis.* Scientific Reports, 2017. **7**(1): p. 8595.
233. Ladislau, L., et al., *JAK inhibitor improves type I interferon induced damage: proof of concept in dermatomyositis.* Brain, 2018. **141**(6): p. 1609-1621.
234. Chen, Z., et al., *Exercise mimetics and JAK inhibition attenuate IFN-γ–induced wasting in engineered human skeletal muscle.* Science Advances, 2021. **7**(4): p. eabd9502.
235. Huang, Z., et al., *Inhibition of IL-6/JAK/STAT3 pathway rescues denervation-induced skeletal muscle atrophy.* Ann Transl Med, 2020. **8**(24): p. 1681.
236. Moresi, V., S. Adamo, and L. Berghella, *The JAK/STAT Pathway in Skeletal Muscle Pathophysiology.* Front Physiol, 2019. **10**: p. 500.
237. Arora, G., et al., *JAK Inhibitors Suppress Cancer Cachexia-Associated Anorexia and Adipose Wasting in Mice.* JCSM Rapid Commun, 2020. **3**(2): p. 115-128.

238. Baig, M.H., et al., *Myostatin and its Regulation: A Comprehensive Review of Myostatin Inhibiting Strategies.* Front Physiol, 2022. **13**: p. 876078.
239. Trendelenburg, A.U., et al., *Myostatin reduces Akt/TORC1/p70S6K signaling, inhibiting myoblast differentiation and myotube size.* Am J Physiol Cell Physiol, 2009. **296**(6): p. C1258-70.
240. Wu, C., et al., *TRAF6-mediated ubiquitination of AKT in the nucleus is a critical event underlying the desensitization of G protein-coupled receptors.* Cell Communication and Signaling, 2024. **22**(1): p. 213.
241. Suissa, S., et al., *Inhaled corticosteroids in COPD and the risk of serious pneumonia.* Thorax, 2013. **68**(11): p. 1029-36.
242. Raghu, G., et al., *An Official ATS/ERS/JRS/ALAT Clinical Practice Guideline: Treatment of Idiopathic Pulmonary Fibrosis. An Update of the 2011 Clinical Practice Guideline.* Am J Respir Crit Care Med, 2015. **192**(2): p. e3-19.
243. Richeldi, L., et al., *Efficacy and safety of nintedanib in idiopathic pulmonary fibrosis.* N Engl J Med, 2014. **370**(22): p. 2071-82.
244. Salehian, B. and K. Kejriwal, *Glucocorticoid-Induced Muscle Atrophy: Mechanisms And Therapeutic Strategies.* Endocrine Practice, 1999. **5**(5): p. 277-281.
245. Gupta, A. and Y. Gupta, *Glucocorticoid-induced myopathy: Pathophysiology, diagnosis, and treatment.* Indian J Endocrinol Metab, 2013. **17**(5): p. 913-6.
246. Klein, G.L., *THE EFFECT OF GLUCOCORTICOIDS ON BONE AND MUSCLE.* Osteoporos Sarcopenia, 2015. **1**(1): p. 39-45.
247. Wu, M., C. Liu, and D. Sun, *Glucocorticoid-Induced Myopathy: Typology, Pathogenesis, Diagnosis, and Treatment.* Horm Metab Res, 2024. **56**(5): p. 341-349.
248. Schakman, O., H. Gilson, and J.P. Thissen, *Mechanisms of glucocorticoid-induced myopathy.* J Endocrinol, 2008. **197**(1): p. 1-10.
249. Braun, T.P. and D.L. Marks, *The regulation of muscle mass by endogenous glucocorticoids.* Front Physiol, 2015. **6**: p. 12.
250. Jaitovich, A. and E. Barreiro, *Skeletal Muscle Dysfunction in Chronic Obstructive Pulmonary Disease. What We Know and Can Do for Our Patients.* Am J Respir Crit Care Med, 2018. **198**(2): p. 175-186.
251. Ruwanpura, S.M., B.J. Thomas, and P.G. Bardin, *Pirfenidone: Molecular Mechanisms and Potential Clinical Applications in Lung Disease.* Am J Respir Cell Mol Biol, 2020. **62**(4): p. 413-422.
252. Zanotti, S., et al., *Anti-fibrotic effect of pirfenidone in muscle derived-fibroblasts from Duchenne muscular dystrophy patients.* Life Sciences, 2016. **145**: p. 127-136.
253. Wollin, L., et al., *Mode of action of nintedanib in the treatment of idiopathic pulmonary fibrosis.* Eur Respir J, 2015. **45**(5): p. 1434-45.
254. Tomioka, H. and T. Fujikawa, *Trajectory of bodyweight and skeletal muscle mass in patients treated with nintedanib for idiopathic pulmonary fibrosis.* Clinical Nutrition Open Science, 2024. **58**: p. 13-20.
255. Ikeda, S., et al., *Negative impact of anorexia and weight loss during prior pirfenidone administration on subsequent nintedanib treatment in patients with idiopathic pulmonary fibrosis.* BMC Pulmonary Medicine, 2019. **19**(1): p. 78.
256. Piñol-Jurado, P., et al., *Nintedanib decreases muscle fibrosis and improves muscle function in a murine model of dystrophinopathy.* Cell Death Dis, 2018. **9**(7): p. 776.
257. Groarke, J.D., et al., *Ponsegromab for the Treatment of Cancer Cachexia.* N Engl J Med, 2024.

258. Cloonan, S.M., et al., *Mitochondrial dysfunction in lung ageing and disease.* European Respiratory Review, 2020. **29**(157): p. 200165.
259. Pokharel, M.D., et al., *Mitochondrial network dynamics in pulmonary disease: Bridging the gap between inflammation, oxidative stress, and bioenergetics.* Redox Biol, 2024. **70**: p. 103049.
260. Ryter, S.W., et al., *Mitochondrial Dysfunction as a Pathogenic Mediator of Chronic Obstructive Pulmonary Disease and Idiopathic Pulmonary Fibrosis.* Ann Am Thorac Soc, 2018. **15**(Suppl 4): p. S266-s272.
261. Qian, L., et al., *Mitochondria signaling pathways in allergic asthma.* J Investig Med, 2022. **70**(4): p. 863-882.
262. Runtsch, M.C., et al., *Itaconate and itaconate derivatives target JAK1 to suppress alternative activation of macrophages.* Cell Metab, 2022. **34**(3): p. 487-501.e8.
263. Ashmore, R., et al., *Investigating mitochondrial dysfunction in asthma.* European Respiratory Journal. **46**(suppl 59): p. OA1775.
264. Mabalirajan, U. and B. Ghosh, *Mitochondrial dysfunction in metabolic syndrome and asthma.* J Allergy (Cairo), 2013. **2013**: p. 340476.
265. Rangarajan, S., K. Bernard, and V.J. Thannickal, *Mitochondrial Dysfunction in Pulmonary Fibrosis.* Ann Am Thorac Soc, 2017. **14**(Supplement_5): p. S383-s388.
266. Ling, N.X.Y., et al., *mTORC1 directly inhibits AMPK to promote cell proliferation under nutrient stress.* Nat Metab, 2020. **2**(1): p. 41-49.
267. Smiles, W.J., et al., *New developments in AMPK and mTORC1 cross-talk.* Essays Biochem, 2024. **68**(3): p. 321-336.
268. Palmieri, M., et al., *Characterization of the CLEAR network reveals an integrated control of cellular clearance pathways.* Hum Mol Genet, 2011. **20**(19): p. 3852-66.
269. Malik, N., et al., *Induction of lysosomal and mitochondrial biogenesis by AMPK phosphorylation of FNIP1.* Science, 2023. **380**(6642): p. eabj5559.
270. Poulsen, N.S., et al., *Growth and differentiation factor 15 as a biomarker for mitochondrial myopathy.* Mitochondrion, 2020. **50**: p. 35-41.
271. Yatsuga, S., et al., *Growth differentiation factor 15 as a useful biomarker for mitochondrial disorders.* Ann Neurol, 2015. **78**(5): p. 814-23.
272. Ost, M., et al., *Muscle-derived GDF15 drives diurnal anorexia and systemic metabolic remodeling during mitochondrial stress.* EMBO reports, 2020. **21**(3): p. e48804.
273. Montero, R., et al., *GDF-15 Is Elevated in Children with Mitochondrial Diseases and Is Induced by Mitochondrial Dysfunction.* PLoS One, 2016. **11**(2): p. e0148709.
274. Decout, A., et al., *The cGAS-STING pathway as a therapeutic target in inflammatory diseases.* Nat Rev Immunol, 2021. **21**(9): p. 548-569.
275. Dvorkin, S., et al., *New frontiers in the cGAS-STING intracellular DNA-sensing pathway.* Immunity, 2024. **57**(4): p. 718-730.
276. Kim, J., H.-S. Kim, and J.H. Chung, *Molecular mechanisms of mitochondrial DNA release and activation of the cGAS-STING pathway.* Experimental & Molecular Medicine, 2023. **55**(3): p. 510-519.
277. Dobbs, N., et al., *STING Activation by Translocation from the ER Is Associated with Infection and Autoinflammatory Disease.* Cell Host Microbe, 2015. **18**(2): p. 157-68.
278. Ishikawa, H. and G.N. Barber, *STING is an endoplasmic reticulum adaptor that facilitates innate immune signalling.* Nature, 2008. **455**(7213): p. 674-8.
279. Yum, S., et al., *TBK1 recruitment to STING activates both IRF3 and NF-κB that mediate immune defense against tumors and viral infections.* Proc Natl Acad Sci U S A, 2021. **118**(14).

280. Hou, Y., et al., *Non-canonical NF-κB Antagonizes STING Sensor-Mediated DNA Sensing in Radiotherapy.* Immunity, 2018. **49**(3): p. 490-503.e4.
281. Haag, S.M., et al., *Targeting STING with covalent small-molecule inhibitors.* Nature, 2018. **559**(7713): p. 269-273.
282. Lin, I.C., et al., *Absorption and Metabolism of Urolithin A and Ellagic Acid in Mice and Their Cytotoxicity in Human Colorectal Cancer Cells.* Evid Based Complement Alternat Med, 2023. **2023**: p. 8264716.
283. Zhao, H., et al., *Pharmacological Effects of Urolithin A and Its Role in Muscle Health and Performance: Current Knowledge and Prospects.* Nutrients, 2023. **15**(20).
284. Rogovskii, V.S., *The Therapeutic Potential of Urolithin A for Cancer Treatment and Prevention.* Curr Cancer Drug Targets, 2022. **22**(9): p. 717-724.
285. Ryu, D., et al., *Urolithin A induces mitophagy and prolongs lifespan in C. elegans and increases muscle function in rodents.* Nat Med, 2016. **22**(8): p. 879-88.
286. Hou, Y., et al., *Urolithin A improves Alzheimer's disease cognition and restores mitophagy and lysosomal functions.* Alzheimers Dement, 2024. **20**(6): p. 4212-4233.
287. Ballesteros-Álvarez, J., et al., *Urolithin A reduces amyloid-beta load and improves cognitive deficits uncorrelated with plaque burden in a mouse model of Alzheimer's disease.* Geroscience, 2023. **45**(2): p. 1095-1113.
288. Chen, P., et al., *Methylated urolithin A, mitigates cognitive impairment by inhibiting NLRP3 inflammasome and ameliorating mitochondrial dysfunction in aging mice.* Neuropharmacology, 2024. **252**: p. 109950.
289. Saleem, A. and D.A. Hood, *Acute exercise induces tumour suppressor protein p53 translocation to the mitochondria and promotes a p53-Tfam-mitochondrial DNA complex in skeletal muscle.* J Physiol, 2013. **591**(14): p. 3625-36.
290. Liu, S., et al., *Effect of Urolithin A Supplementation on Muscle Endurance and Mitochondrial Health in Older Adults: A Randomized Clinical Trial.* JAMA Netw Open, 2022. **5**(1): p. e2144279.
291. Singh, A., et al., *Urolithin A improves muscle strength, exercise performance, and biomarkers of mitochondrial health in a randomized trial in middle-aged adults.* Cell Rep Med, 2022. **3**(5): p. 100633.
292. Chen, P., et al., *Activation of the miR-34a-Mediated SIRT1/mTOR Signaling Pathway by Urolithin A Attenuates D-Galactose-Induced Brain Aging in Mice.* Neurotherapeutics, 2019. **16**(4): p. 1269-1282.
293. Totiger, T.M., et al., *Urolithin A, a Novel Natural Compound to Target PI3K/AKT/mTOR Pathway in Pancreatic Cancer.* Mol Cancer Ther, 2019. **18**(2): p. 301-311.
294. Luo, C., et al., *Interactions between Gut Microbiota and Polyphenols: New Insights into the Treatment of Fatigue.* Molecules, 2022. **27**(21).
295. Tan, W.S.D., H.M. Shen, and W.S.F. Wong, *Dysregulated autophagy in COPD: A pathogenic process to be deciphered.* Pharmacol Res, 2019. **144**: p. 1-7.
296. Barnes, P.J., J. Baker, and L.E. Donnelly, *Autophagy in asthma and chronic obstructive pulmonary disease.* Clin Sci (Lond), 2022. **136**(10): p. 733-746.
297. Zhang, Y., J. Zhang, and Z. Fu, *Role of autophagy in lung diseases and ageing.* European Respiratory Review, 2022. **31**(166): p. 220134.
298. García-Prat, L., et al., *Autophagy maintains stemness by preventing senescence.* Nature, 2016. **529**(7584): p. 37-42.
299. Le Grand, F. and M.A. Rudnicki, *Skeletal muscle satellite cells and adult myogenesis.* Curr Opin Cell Biol, 2007. **19**(6): p. 628-33.

300. Doyle, A., et al., *Toll-like receptor 4 mediates lipopolysaccharide-induced muscle catabolism via coordinate activation of ubiquitin-proteasome and autophagy-lysosome pathways.* Faseb j, 2011. **25**(1): p. 99-110.
301. Leduc-Gaudet, J.P. and S.N.A. Hussain, *Muscle Wasting in Chronic Obstructive Pulmonary Disease: Not Enough Autophagy?* Am J Respir Cell Mol Biol, 2022. **66**(6): p. 587-588.
302. Kim, R.Y., et al., *Elucidating novel disease mechanisms in severe asthma.* Clin Transl Immunology, 2016. **5**(7): p. e91.
303. Willis-Owen, S.A.G., et al., *COPD is accompanied by co-ordinated transcriptional perturbation in the quadriceps affecting the mitochondria and extracellular matrix.* Scientific Reports, 2018. **8**(1): p. 12165.
304. McDonald, M.N., et al., *It's more than low BMI: prevalence of cachexia and associated mortality in COPD.* Respir Res, 2019. **20**(1): p. 100.
305. Sankari, A., K. Chapman, and S. Ullah, *Idiopathic Pulmonary Fibrosis*, in *StatPearls*. 2025, StatPearls Publishing

306. Sul, B., et al., *Volumetric characteristics of idiopathic pulmonary fibrosis lungs: computational analyses of high-resolution computed tomography images of lung lobes.* Respir Res, 2019. **20**(1): p. 216.
307. Kolb, P., et al., *The importance of interventional timing in the bleomycin model of pulmonary fibrosis.* European Respiratory Journal, 2020. **55**(6): p. 1901105.
308. Zhang, J., et al., *The role of cGAS-STING signaling in pulmonary fibrosis and its therapeutic potential.* Front Immunol, 2023. **14**: p. 1273248.
309. Ou, L., et al., *Targeting STING-mediated pro-inflammatory and pro-fibrotic effects of alveolar macrophages and fibroblasts blunts silicosis caused by silica particles.* J Hazard Mater, 2023. **458**: p. 131907.
310. Song, S., et al., *Decreased expression of STING predicts poor prognosis in patients with gastric cancer.* Scientific Reports, 2017. **7**(1): p. 39858.
311. Lohinai, Z., et al., *Loss of STING expression is prognostic in non-small cell lung cancer.* J Surg Oncol, 2022. **125**(6): p. 1042-1052.
312. Raaby Gammelgaard, K., et al., *cGAS-STING pathway expression as a prognostic tool in NSCLC.* Transl Lung Cancer Res, 2021. **10**(1): p. 340-354.
313. Fallon, P.G. and C. Schwartz, *The high and lows of type 2 asthma and mouse models.* Journal of Allergy and Clinical Immunology, 2020. **145**(2): p. 496-498.
314. Al-Kharashi, L.A., et al., *BALB/c and C57BL/6 mice differ in oxidant and antioxidant responses in innate and adaptive immune cells in an asthma model induced by cockroach allergens.* International Immunopharmacology, 2023. **124**: p. 110892.
315. Picado, C., J. Montserrat, and A. Agusti-Vidal, *Muscle atrophy in severe exacerbation of asthma requiring mechanical ventilation.* Respiration, 1988. **53**(3): p. 201-3.
316. Bouredji, Z., A. Argaw, and J. Frenette, *The inflammatory response, a mixed blessing for muscle homeostasis and plasticity.* Front Physiol, 2022. **13**: p. 1032450.
317. Laveneziana, P. and P. Palange, *Physical activity, nutritional status and systemic inflammation in COPD.* European Respiratory Journal. **40**(3): p. 522-529.
318. Sinden, N.J. and R.A. Stockley, *Systemic inflammation and comorbidity in COPD: a result of 'overspill' of inflammatory mediators from the lungs? Review of the evidence.* Thorax, 2010. **65**(10): p. 930-6.
319. Barnes, P.J. and B.R. Celli, *Systemic manifestations and comorbidities of COPD.* Eur Respir J, 2009. **33**(5): p. 1165-85.

320. Ninfali, C., et al., *Regulation of muscle atrophy-related genes by the opposing transcriptional activities of ZEB1/CtBP and FOXO3.* Nucleic Acids Res, 2018. **46**(20): p. 10697-10708.
321. Cooney, R.N., S.R. Kimball, and T.C. Vary, *Regulation of skeletal muscle protein turnover during sepsis: mechanisms and mediators.* Shock, 1997. **7**(1): p. 1-16.
322. Gingras, A.C., et al., *Hierarchical phosphorylation of the translation inhibitor 4E-BP1.* Genes Dev, 2001. **15**(21): p. 2852-64.
323. Fletcher, C.M., et al., *4E binding proteins inhibit the translation factor eIF4E without folded structure.* Biochemistry, 1998. **37**(1): p. 9-15.
324. Meyuhas, O., *Ribosomal Protein S6 Phosphorylation: Four Decades of Research.* Int Rev Cell Mol Biol, 2015. **320**: p. 41-73.
325. Mitchell, P., *Chemiosmotic coupling in oxidative and photosynthetic phosphorylation. 1966.* Biochim Biophys Acta, 2011. **1807**(12): p. 1507-38.
326. Nolfi-Donegan, D., A. Braganza, and S. Shiva, *Mitochondrial electron transport chain: Oxidative phosphorylation, oxidant production, and methods of measurement.* Redox Biol, 2020. **37**: p. 101674.
327. Gnaiger, E., *Mitochondrial Pathways*

and Respiratory Control

An Introduction to OXPHOS Analysis, I. OROBOROS INSTRUMENTS Corp, Austria, Editor. 2014: Mitochondr Physiol Network 19.12 OROBOROS MiPNet Publications 2014.
328. Walsh, M.A., et al., *A practical perspective on how to develop, implement, execute, and reproduce high-resolution respirometry experiments: The physiologist's guide to an Oroboros O2k.* Faseb j, 2023. **37**(12): p. e23280.
329. Nanayakkara, G.K., H. Wang, and X. Yang, *Proton leak regulates mitochondrial reactive oxygen species generation in endothelial cell activation and inflammation - A novel concept.* Arch Biochem Biophys, 2019. **662**: p. 68-74.
330. Jastroch, M., et al., *Mitochondrial proton and electron leaks.* Essays Biochem, 2010. **47**: p. 53-67.
331. Holloway, G.P., et al., *Age-Associated Impairments in Mitochondrial ADP Sensitivity Contribute to Redox Stress in Senescent Human Skeletal Muscle.* Cell Rep, 2018. **22**(11): p. 2837-2848.
332. Miotto, P.M. and G.P. Holloway, *Exercise-induced reductions in mitochondrial ADP sensitivity contribute to the induction of gene expression and mitochondrial biogenesis through enhanced mitochondrial H2O2 emission.* Mitochondrion, 2019. **46**: p. 116-122.
333. Pharaoh, G., et al., *Reduced adenosine diphosphate sensitivity in skeletal muscle mitochondria increases reactive oxygen species production in mouse models of aging and oxidative stress but not denervation.* JCSM Rapid Commun, 2021. **4**(1): p. 75-89.
334. Scialò, F., D.J. Fernández-Ayala, and A. Sanz, *Role of Mitochondrial Reverse Electron Transport in ROS Signaling: Potential Roles in Health and Disease.* Front Physiol, 2017. **8**: p. 428.
335. Robb, E.L., et al., *Control of mitochondrial superoxide production by reverse electron transport at complex I.* J Biol Chem, 2018. **293**(25): p. 9869-9879.
336. Casey, A.M., et al., *Pro-inflammatory macrophages produce mitochondria-derived superoxide by reverse electron transport at complex I that regulates IL-1β release during NLRP3 inflammasome activation.* Nature Metabolism, 2025. **7**(3): p. 493-507.
337. Kasai, S., et al., *Regulation of Nrf2 by Mitochondrial Reactive Oxygen Species in Physiology and Pathology.* Biomolecules, 2020. **10**(2).

338. Swanson, K.V., M. Deng, and J.P.Y. Ting, *The NLRP3 inflammasome: molecular activation and regulation to therapeutics.* Nature Reviews Immunology, 2019. **19**(8): p. 477-489.
339. Shimada, K., et al., *Oxidized mitochondrial DNA activates the NLRP3 inflammasome during apoptosis.* Immunity, 2012. **36**(3): p. 401-14.
340. Guo, H., J.B. Callaway, and J.P. Ting, *Inflammasomes: mechanism of action, role in disease, and therapeutics.* Nat Med, 2015. **21**(7): p. 677-87.
341. Laird, B.J., et al., *The Emerging Role of Interleukin 1β (IL-1β) in Cancer Cachexia.* Inflammation, 2021. **44**(4): p. 1223-1228.
342. Cheung, W.W., et al., *The role of IL-1 in adipose browning and muscle wasting in CKD-associated cachexia.* Scientific Reports, 2021. **11**(1): p. 15141.
343. McDonald, J.J., D.C. McMillan, and B.J.A. Laird, *Targeting IL-1α in cancer cachexia: a narrative review.* Curr Opin Support Palliat Care, 2018. **12**(4): p. 453-459.
344. Kalinkovich, A. and G. Livshits, *The cross-talk between the cGAS-STING signaling pathway and chronic inflammation in the development of musculoskeletal disorders.* Ageing Res Rev, 2024. **104**: p. 102602.
345. Li, Y., et al., *mtDNA release promotes cGAS-STING activation and accelerated aging of postmitotic muscle cells.* Cell Death & Disease, 2024. **15**(7): p. 523.
346. Mukai, K., et al., *Activation of STING requires palmitoylation at the Golgi.* Nature Communications, 2016. **7**(1): p. 11932.
347. White, R.B., et al., *Dynamics of muscle fibre growth during postnatal mouse development.* BMC Dev Biol, 2010. **10**: p. 21.
348. Givan, C.V., *Regulation of glycolysis by adenosine diphosphate in Pisum sativum.* Phytochemistry, 1974. **13**(9): p. 1741-1745.
349. O'Neill, L.A., R.J. Kishton, and J. Rathmell, *A guide to immunometabolism for immunologists.* Nat Rev Immunol, 2016. **16**(9): p. 553-65.
350. Everts, B., et al., *TLR-driven early glycolytic reprogramming via the kinases TBK1-IKKε supports the anabolic demands of dendritic cell activation.* Nat Immunol, 2014. **15**(4): p. 323-32.
351. Ando, M., et al., *Interleukin 6 enhances glycolysis through expression of the glycolytic enzymes hexokinase 2 and 6-phosphofructo-2-kinase/fructose-2,6-bisphosphatase-3.* J Nippon Med Sch, 2010. **77**(2): p. 97-105.
352. O'Carroll, S.M., F.D.R. Henkel, and L.A.J. O'Neill, *Metabolic regulation of type I interferon production.* Immunol Rev, 2024. **323**(1): p. 276-287.
353. Schmid, M., et al., *The interplay between autophagy and cGAS-STING signaling and its implications for cancer.* Front Immunol, 2024. **15**: p. 1356369.
354. Library, T.J., *Body Weight Information for B6 (000664)*.
355. Vassallo, R., et al., *Cigarette smoke promotes dendritic cell accumulation in COPD; a Lung Tissue Research Consortium study.* Respir Res, 2010. **11**(1): p. 45.
356. Tsoumakidou, M., et al., *Dendritic cells in chronic obstructive pulmonary disease: new players in an old game.* Am J Respir Crit Care Med, 2008. **177**(11): p. 1180-6.
357. Davidyan, A., et al., *Maintenance of muscle mass in adult male mice is independent of testosterone.* PLoS One, 2021. **16**(3): p. e0240278.
358. Svartberg, J. and R. Jorde, *Endogenous testosterone levels and smoking in men. The fifth Tromsø study.* Int J Androl, 2007. **30**(3): p. 137-43.
359. Wang, W., et al., *Cigarette smoking has a positive and independent effect on testosterone levels.* Hormones (Athens), 2013. **12**(4): p. 567-77.
360. ENGLISH, K.M., et al., *Effect of cigarette smoking on levels of bioavailable testosterone in healthy men.* Clinical Science, 2001. **100**(6): p. 661-665.

361. Brown, D., et al., *Mouse model of testosterone-induced muscle fiber hypertrophy: involvement of p38 mitogen-activated protein kinase-mediated Notch signaling.* J Endocrinol, 2009. **201**(1): p. 129-39.
362. Serra, C., et al., *Testosterone Improves the Regeneration of Old and Young Mouse Skeletal Muscle.* The Journals of Gerontology: Series A, 2012. **68**(1): p. 17-26.
363. Anzueto, A., *Impact of exacerbations on COPD.* Eur Respir Rev, 2010. **19**(116): p. 113-8.
364. Vermeeren, M.A., A.M. Schols, and E.F. Wouters, *Effects of an acute exacerbation on nutritional and metabolic profile of patients with COPD.* Eur Respir J, 1997. **10**(10): p. 2264-9.
365. Spruit, M.A., et al., *Muscle force during an acute exacerbation in hospitalised patients with COPD and its relationship with CXCL8 and IGF-I.* Thorax, 2003. **58**(9): p. 752-6.
366. Schols, A.M., et al., *Nutritional assessment and therapy in COPD: a European Respiratory Society statement.* European Respiratory Journal, 2014. **44**(6): p. 1504-1520.
367. Pitta, F., et al., *Physical activity and hospitalization for exacerbation of COPD.* Chest, 2006. **129**(3): p. 536-44.
368. Yde, S.K., et al., *Unintentional weight loss is reflected in worse one-year clinical outcomes among COPD outpatients.* Clinical Nutrition, 2023. **42**(11): p. 2173-2180.
369. Shu, J., et al., *Comparison and evaluation of two different methods to establish the cigarette smoke exposure mouse model of COPD.* Scientific Reports, 2017. **7**(1): p. 15454.
370. Yu, X., et al., *Causal role of immune cells in muscle atrophy: mendelian randomization study.* Scientific Reports, 2024. **14**(1): p. 25878.
371. Huang, B., et al., *CD8(+)CD57(+) T cells exhibit distinct features in human non-small cell lung cancer.* J Immunother Cancer, 2020. **8**(1).
372. Bonomo, A.C., et al., *Crosstalk Between Innate and T Cell Adaptive Immunity With(in) the Muscle.* Front Physiol, 2020. **11**: p. 573347.
373. Ng, S.K., et al., *The protective effect of cannabinoids against colorectal cancer cachexia through modulation of inflammation and immune responses.* Biomed Pharmacother, 2023. **161**: p. 114467.
374. Zhang, J., et al., *CD8 T Cells Are Involved in Skeletal Muscle Regeneration through Facilitating MCP-1 Secretion and Gr1high Macrophage Infiltration.* The Journal of Immunology, 2014. **193**(10): p. 5149-5160.
375. Liu, P., et al., *PtdIns(3,4,5)P3-Dependent Activation of the mTORC2 Kinase Complex.* Cancer Discov, 2015. **5**(11): p. 1194-209.
376. Czech, M.P., *PIP2 and PIP3: Complex Roles at the Cell Surface.* Cell, 2000. **100**(6): p. 603-606.
377. Liu, Y.B., et al., *The Role of Mitochondrial Quality Control in Chronic Obstructive Pulmonary Disease.* Lab Invest, 2024. **104**(2): p. 100307.
378. Wang, Y., et al., *Skeletal Muscle Mitochondrial Dysfunction in Chronic Obstructive Pulmonary Disease: Underlying Mechanisms and Physical Therapy Perspectives.* Aging Dis, 2023. **14**(1): p. 33-45.
379. Gifford, J.R., et al., *Altered skeletal muscle mitochondrial phenotype in COPD: disease vs. disuse.* J Appl Physiol (1985), 2018. **124**(4): p. 1045-1053.
380. Haji, G., et al., *Mitochondrial dysfunction in airways and quadriceps muscle of patients with chronic obstructive pulmonary disease.* Respiratory Research, 2020. **21**(1): p. 262.
381. Frazier, A.E. and D.R. Thorburn, *Biochemical analyses of the electron transport chain complexes by spectrophotometry.* Methods Mol Biol, 2012. **837**: p. 49-62.
382. Neikirk, K., et al., *Call to action to properly utilize electron microscopy to measure organelles to monitor disease.* Eur J Cell Biol, 2023. **102**(4): p. 151365.

383. Neel, B.A., Y. Lin, and J.E. Pessin, *Skeletal muscle autophagy: a new metabolic regulator.* Trends Endocrinol Metab, 2013. **24**(12): p. 635-43.
384. Halling, J.F. and H. Pilegaard, *PGC-1α-mediated regulation of mitochondrial function and physiological implications.* Appl Physiol Nutr Metab, 2020. **45**(9): p. 927-936.
385. Kang, I., C.T. Chu, and B.A. Kaufman, *The mitochondrial transcription factor TFAM in neurodegeneration: emerging evidence and mechanisms.* FEBS Lett, 2018. **592**(5): p. 793-811.
386. Ramanjulu, J.M., et al., *Design of amidobenzimidazole STING receptor agonists with systemic activity.* Nature, 2018. **564**(7736): p. 439-443.
387. Holm, K.E., et al., *The impact of age on outcomes in chronic obstructive pulmonary disease differs by relationship status.* J Behav Med, 2014. **37**(4): p. 654-63.
388. Vinciguerra, M., *Urolithin A improves physical performance in middle age.* Nature Aging, 2022. **2**(6): p. 460-460.
389. Wen, Y., et al., *MyoVision: software for automated high-content analysis of skeletal muscle immunohistochemistry.* J Appl Physiol (1985), 2018. **124**(1): p. 40-51.
390. Bergmeister, K.D., et al., *Automated muscle fiber type population analysis with ImageJ of whole rat muscles using rapid myosin heavy chain immunohistochemistry.* Muscle Nerve, 2016. **54**(2): p. 292-9.
391. Chakraborty, J., et al., *Investigating mitochondrial autophagy by routine transmission electron microscopy: Seeing is believing?* Pharmacol Res, 2020. **160**: p. 105097.
392. Dalrymple, N.A., V. Cimica, and E.R. Mackow, *Dengue Virus NS Proteins Inhibit RIG-I/MAVS Signaling by Blocking TBK1/IRF3 Phosphorylation: Dengue Virus Serotype 1 NS4A Is a Unique Interferon-Regulating Virulence Determinant.* mBio, 2015. **6**(3): p. e00553-15.
393. Rehwinkel, J. and M.U. Gack, *RIG-I-like receptors: their regulation and roles in RNA sensing.* Nature Reviews Immunology, 2020. **20**(9): p. 537-551.
394. Stok, J.E., M.E. Vega Quiroz, and A.G. van der Veen, *Self RNA Sensing by RIG-I–like Receptors in Viral Infection and Sterile Inflammation.* The Journal of Immunology, 2020. **205**(4): p. 883-891.